Linear and Nonlinear Optical Characterization of BaTiO₃ Nanoparticles and their Applications in Two-Photon Photothermal Microscopy

THESIS

Submitted in partial fulfillment
of the requirements for the degree of
DOCTOR OF PHILOSOPHY

by

BIJEESH M. M.

Under the Supervision of
Prof. P. Nandakumar

BIRLA INSTITUTE OF TECHNOLOGY AND SCIENCE, PILANI

2018

BIRLA INSTITUTE OF TECHNOLOGY AND SCIENCE, PILANI

CERTIFICATE

This is to certify that the thesis entitled **"Linear and Nonlinear Optical Characterization of BaTiO$_3$ Nanoparticles and their Applications in Two-Photon Photothermal Microscopy"** and submitted by <u>**Bijeesh M. M.**</u> ID No <u>**2010PHXF0812G**</u> for award of Ph.D. of the Institute embodies original work done by him under my supervision.

Signature of the Supervisor:

Name in capital block letters: **Prof. P. NANDAKUMAR**

Designation: Associate Professor

Date: 20/4/2018

i

DECLARATION

I, **Bijeesh M M** hereby declare that this thesis entitled **"Linear and Nonlinear Optical Characterization of BaTiO₃ Nanoparticles and their Applications in Two-Photon Photothermal Microscopy"** submitted by me under the guidance and supervision of **Prof. P. Nandakumar** is a bonafide research work. I also declare that it has not been submitted previously in part or in full to this University or any other University or Institution for the award of any degree.

Signature of the Student:

Name: **BIJEESH M. M.**

Reg. No.: 2010PHXF0812G

Date: 20-11-2018

DEDICATED TO

My beloved parents

My lovely wife
    &

My little daughter

Acknowledgements

On the occasion of completion of this thesis it is my pleasure to express my sincere thanks to all the support, love, encouragement and guidance that made my research journey much easier and successful. The first person who deserves my sincere gratitude is my supervisor **Prof. P Nandakumar.** It is a difficult task for me to express my deep gratitude to him by writing some words. He is an excellent scientist with wide knowledge and great experimental skill. He has given me full freedom to do whatever I am interested in and gave support whenever I need, and I greatly appreciate that freedom. I feel always it has been an honor to be his first student and I am truly grateful to him for such a peaceful and pleasant research environment he created for me. I am always thankful to him for introducing me into such an exciting field of nonlinear optics. The attempts I made for answering his divergent questions, in our lengthy never ending discussions, always helped me in improving my critical reasoning ability. There were numerous occasions where I got stuck and depressed in my research journey but a meeting with him will always make me a peaceful man. His positive outlook and confidence in me were the inspiration and the driving force for the successful completion of my Ph.D.

I would like to acknowledge my warmest thanks to my Doctoral Advisory Committee members, **Dr. Teny Theresa John** and **Dr. Ram Shanker Patel.** I am very grateful to their interest in my work and for always being helpful. Thank you for investing time and providing interesting and valuable feedback for my thesis work.

The thesis becomes incomplete without acknowledging **Dr. Geetha K Varier**. She is a brilliant scientist with full of new interesting ideas and a respectable woman with great human values. I would like to thank her dedicated scientific guidance, consistent support and encouragement throughout the duration of my Ph.D. I would also like to thank for her friendship, patience, kindness and great sense of humor.

A sincere thanks to my M.Sc teacher **Prof. Titus K Mathew** for encouraging me to do research. I also express my gratitude towards (late) **Prof. Suresh Ramaswamy** (Former Dean) for the motivation he has given me and being a good teacher to me. I am thankful to (late) Prof. **Sanjeev K. Agarwal** (former Director) for being such a wonderful leader and the care, support and motivation towards Ph.D students were really appreciable.

*In this thesis I would like to use the term **'We'** instead of **'I'** because during a Ph.D thesis work one is usually supported by other persons, in particular the supervisor and lab members. However, the experiments described in this thesis and writing were essentially done by myself.*

Table of Contents

List of figures

List of tables

LIST OF SYMBOLS AND ABBREVATIONS

AFM — Atomic Force Microscope

ANOVA — Analysis of Variance

AOM — Acousto Optic Modulator

AR — Analytical Reagent

Ar^+ — Argon ion

Au — Gold

$Ba(CH_3COO)_2$ — Barium Acetate

$BaTiO_3$ — Barium Titanate

BPF — Band Pass Filter

CARS — coherent Anti-Stokes Raman Scattering

CdS — Cadmium Sulphide

cm — Centimeter

CO_2 — Carbon dioxide

Cu — Copper

CW — Continuous Wave

DAQ — Data Acquisition

DMEM — Dulbecco's Modified Eagles Medium

DMSO — Dimethyl Sulphoxide

EDS — Energy Dispersive X-ray Spectroscopy

esu — Electrostatic Unit

ev — Electron Volt

FBS — Fetal Bovine Serum

fs — Femtosecond

FWHM — Full Width Half Maximum

g — Gram

GFP — Green Fluorescent Protein

GW — Gigawatt

$HAuCl_4$ — Chloroauric acid

HeLa — Henrietta Lacks

He-Ne — Helium- Neon

HRTEM — High Resolution Transmission Electron Microscopy

I/O — Input/output

ICDD — International center for diffraction data

kHz — Kilohertz

kV — Kilovolt

LIA — Lock-in Amplifier

m — Meter

mA — Milliampere

mg — Milligram

MHz — Megahertz

min — Minute

mm — Millimeter

mmol — Millimol

mW — Milliwatt

NA — Numerical Aperture

NAD(P)H — Nicotinamide adenine dinucleotide phosphate

Nd:YAG — Neodymium: Yttrium Aluminum Garnet

NDF — Neutral Density Filter

nm — Nanometer

ns — Nanosecond

OD — Optical Density

OKE — Optical Kerr Effect

PBS — Phosphate Buffered Saline

PLD   - Pulsed Laser Deposition

PLL   - Poly-L-Lysine

RFP   - Red Fluorescent Protein

RPM   - Rotation Per Minute

s   - Second

SAED   - Selected area electron
diffraction

SEM   - Scanning Electron
Microscope

SHG   - Second Harmonic
Generation

SNR   - Signal to Noise Ratio

$SrTiO_3$ - Strontium Titanate

TEM   - Transmission Electron
Microscope

THG   - Third Harmonic Generation

Ti   - Titanium

TPEF   - Two-photon excited
fluorescence

UV- VIS- NIR   - Ultraviolet- Visible-
Near Infrared

W   - Watt

XRD   - X- ray diffraction

YFP   - Yellow Fluorescent Protein

μl   - Microliter

μm   - Micrometer

μM   - Micromolar

μs   - Microsecond

^0C - Degree Celsius

2D   - Two- Dimensional

3D   - Three- Dimensional

Abstract

Fluorescence based microscopic techniques play an important role in biology research. The fluorescence microscopy relies on external labeling of the area of interest with a fluorescent probe to achieve high contrast in imaging. The photobleaching and phototoxicity of the dye labels is a major challenge in fluorescence microscopy that limits long time observation of a biological system. This has prompted the development of many new labels and alternate imaging methodologies. Metallic and dielectric nanoparticles are a class of promising nonfluorescent labels from the point of view of photostability and biocompatibility. Multiphoton absorption based nonlinear optical techniques provide a powerful approach to detect such nanoparticle labels using infrared excitation. Nonlinear optical microscopy is inherently confocal due to the nature of interaction and provides three-dimensional optical sectioning capability. It allows one to make use of excitation wavelengths in the infrared region of the spectrum which is away from the optical absorption bands of biological tissues. The use of infrared wavelengths also provides for deeper penetration of the radiation in biological tissues.

In this work we examine the nonlinear optical properties of $BaTiO_3$ nanoparticles belonging to the perovskite family from the point of view of applications in the area of biomolecular imaging. $BaTiO_3$ nanoparticles are a potential biomolecular label having high photostability and possess many attractive optical and dielectric properties including large values of third order nonlinear optical susceptibility. In this work we synthesize and characterize $BaTiO_3$ nanoparticles having different sizes, study their linear and nonlinear optical properties and explore the means to enhance their nonlinear optical properties. Further we make use of their high third order optical nonlinearity to develop a nonlinear optical microscope based on two-photon absorption induced photothermal effect using infrared excitation at high repetition rates.

The $BaTiO_3$ nanoparticles are synthesized by a room temperature sol-gel technique using barium acetate and titanium IV butoxide as the base materials. Monodisperse $BaTiO_3$ nanoparticles having average size ranging from 12 nm to 90 nm are prepared by varying the annealing temperature from 500^oC to 1000^oC. Particle size of nanoparticles are controlled by varying this single synthesis parameter. Local electric field effects near the nanoparticle can have an enabling effect on the nonlinear optical properties of nanoparticles. In this work we further explored the potential of this

property to enhance the nonlinear optical absorption of $BaTiO_3$ nanoparticles by incorporating small amount of gold nanoparticles in the $BaTiO_3$ nanoparticle lattice. For this purpose, $Au/BaTiO_3$ nanocomposite films with different molar ratio of Au/Ba are prepared by sol-gel technique. Crystal structure of $BaTiO_3$ nanoparticles and $Au/BaTiO_3$ nanoparticle films are characterized by X-ray diffraction. Transmission electron microscope is used to study the morphology, shape, crystal structure and to determine the particle size. The linear optical properties are studied using a UV-VIS NIR spectrophotometer.

The nonlinear optical properties of $BaTiO_3$ nanoparticles and $Au/BaTiO_3$ nanoparticle films are studied using a single beam Z-scan Technique. Nanoparticles samples for the study are prepared by dispersing them in ethylene glycol and experiments are carried out in a quartz cuvette. The two-photon absorption coefficient of the nanoparticles, an important property from the point of view of application in nonlinear optical microscopy, is estimated from the Z-scan transmittance curve. The two-photon absorption coefficient of the $BaTiO_3$ nanoparticle is of the order of 10^{-11} m/W and is found to increase with decreasing size of $BaTiO_3$ nanoparticles. The two-photon absorption coefficient of the $Au/BaTiO_3$ nanoparticle films increases linearly with gold nanoparticle concentration and significant enhancement of nonlinear optical absorption is observed in qualitative agreement with that predicted for the Maxwell-Garnet geometry. This ability to fine tune the nonlinear optical coefficients of $Au/BaTiO_3$ films would be handy in optical device applications.

Characterization of nanocomposite films using optical techniques is a challenge and often requires careful examination of transmission electron microscopy images. In this work we developed a photothermal microscope capable of detecting gold nanoparticles having size as small as 5 nm to characterize $Au/BaTiO_3$ nanocomposite films. The capability of the method, whose potential is already demonstrated in biomolecular imaging applications, is further expanded to detect gold nanoparticles and their distribution $Au/BaTiO_3$ nanocomposite films. We used the method to study the distribution of gold nanoparticles in $Au/BaTiO_3$ films synthesized with different Au/Ba molar ratio in the precursor solution. The study shows that the distribution of gold nanoparticles in the film concurs with our assumption of Maxwell-Garnet geometry for the composite film. It is observed that the number density of gold nanoparticle increases with higher Au/Ba molar ratio in the precursor solution as expected.

Finally, in the last chapter of this thesis we explore the application potential of $BaTiO_3$ nanoparticles in biomolecular imaging based on the results of our investigations on various properties on these nanoparticles. We indeed found that these photostable and biocompatible nanoparticles could be successfully employed as a biomolecular label in nonlinear optical microscopy. A new nonlinear optical microscopic technique, named two-photon photothermal microscopy, capable of detecting individual nonfluorescent nanoparticles with high sensitivity is developed to detect and image $BaTiO_3$ nanoparticles. The method which is inherently confocal makes use of near infrared excitation at high repetition rates and would be of interest in deep tissue imaging. The applicability of the technique in biology is demonstrated by imaging $BaTiO_3$ nanoparticles internalized in HeLa cells at fast time scales with a pixel dwell time of 80 μs. In order to check the cell viability after addition of $BaTiO_3$ nanoparticle, a cytotoxicity measurement using (3-(4,5- dimethylthiazole-2-yl)-2,5-diphenyl tetrazolium bromide) (MTT) assay was carried out in HeLa cells. Here we note that the technique developed makes use of the third order nonlinear optical properties of the samples and hence can be employed to detect even nanoparticle having inversion symmetry.

Chapter 1: Introduction

1.1 Introduction

Optical microscopy has emerged as an indispensable tool in modern biology research. The evolution of optical microscopy is driven by the desire to achieve contrast and resolution to image single cells and probe internal cellular structure. Different types of optical microscopes such as phase contrast microscope, polarizing microscope and differential interference contrast microscopes have been developed over the years to address the specific needs of biological community. Though all these techniques are employed by biologists, fluorescence based microscopy is the most promising and sought after imaging technique due to its improved contrast and functionality. In fluorescent microscopy the area of interest or the specimen is labeled with a fluorescent probe and the fluorescent light emitted from the probe is used to provide better contrast between the area of interest and the surrounding scattering media. Confocal fluorescence microscopy, where the sample is excited by a laser light provides high spatial resolution and three-dimensional sectioning capabilities through confocal detection of signal from only the focal region [1–3].

The success of fluorescence based microscopy relies heavily on the availability of appropriate fluorescent probes or the dye labels. The photobleaching and phototoxicity of dye labels have been a major challenge in fluorescence microscopy [1,2]. Photobleaching and phototoxicity put limits on the long term observation of a biological system and quantitative analysis of data becomes difficult in situations that require monitoring of the system for long durations.

Another particularly attractive approach employed in biological imaging is nonlinear optical microscopy where fluorescence excitation of the dye label is achieved through multiphoton absorption [4–7]. The nonlinear optical absorption requires large electric field strengths, available only at the focal region of the laser beam and the fluorescence excitation occurs mostly at the focus of the objective. Thus, nonlinear optical microscopy is inherently confocal and provides three-dimensional sectioning capability. Multiphoton absorption allows one to make use of excitation wavelengths in the infrared region which is away from the optical absorption bands of biological tissues. The use of infrared wavelengths also provides for deeper penetration of the radiation in

biological tissues. Multiphoton fluorescence microscopy has become a popular microscopic technique in biology, especially in studies involving deep tissue imaging.

Nonlinear optical microscopy minimizes photobleaching to some extent by limiting the volume of excitation. However, the photobleaching of the dye label at the focal spot is still a challenge faced by the current techniques. Many new types of optical labels, and altogether new experimental strategies are being developed in recent years to address the issue of photobleaching in fluorescence imaging [8–12]. Among these various new labels, metallic and dielectric nanoparticles are promising from the point of view of photostability and biocompatibility. However many of these nanoparticles are nonfluorescent or weakly fluorescent and fluorescence based techniques are not appropriate to detect them. Alternative imaging methodologies for detecting nonfluorescent nanoparticles using photothermal microscopy have been demonstrated recently [13–16]. Multiphoton absorption based nonlinear optical techniques provide powerful approach to detect such nanoparticles using infrared excitation.

This thesis is set in this context to explore the nonlinear optical properties of a model dielectric nanoparticle system from the point of view of applications in biomolecular imaging. $BaTiO_3$ nanoparticles, belonging to the perovskite family are used as a representative system having high optical nonlinearity. $BaTiO_3$ nanoparticles are synthesized by a sol-gel method and characterized using different techniques such as X-ray diffraction, scanning electron microscopy, transmission electron microscopy, and optical absorption. The third order nonlinear optical properties are studied by the well-known single beam Z–scan technique. The thesis also explores the possibility of enhancing or fine tuning the nonlinear optical coefficients of $BaTiO_3$ nanoparticle films through the addition of gold nanoparticles. Photothermal microscopy is employed to characterize the distribution of gold nanoparticles and the nonlinear absorption coefficients of $Au/BaTiO_3$ having different Au/Ba molar ratios are compared. The thesis further makes use of the large third order optical nonlinearity of these nanoparticles in developing a new nonlinear optical imaging technique that can detect and image $BaTiO_3$ nanoparticle labels with high sensitivity. The microscope, named two-photon photothermal microscope, is inherently confocal. $BaTiO_3$ nanoparticles are biocompatible and highly photostable making the microscope employing them as label attractive in biomolecular imaging. The applicability of this microscopic technique, in biomolecular imaging is demonstrated by imaging $BaTiO_3$ nanoparticle incorporated HeLa cells.

In this introductory chapter, we start with a brief discussion on the interaction of light with linear and nonlinear media and then discuss the different effects arising from the third order optical nonlinearity of a material. After that we discuss various approaches to optical microscopy, including nonlinear optical microscopy and recent advances. The literature on BaTiO$_3$ nanoparticles and the current status of biomolecular imaging using these nanoparticles is also presented in this chapter. A short section deals with the investigations on the biocompatibility of these labels. We conclude the chapter by discussing the objectives and giving a brief outline of the thesis.

1.2 Interaction of light with matter

The linear optical interaction of light with an atom can be understood from a simple classical model where the atom is approximated to a harmonic oscillator. A dielectric material can be approximated to a collection of electrons bound to the positive ion cores through electromagnetic interaction. When light interacts with a material these negative and positive charges experience the Lorentz force,

$$F = -e[E(t) + v \, \mathrm{X} \, B(t)]$$
(1.1)

where $E(t)$ and $B(t)$ represent the electric and magnetic fields of the incident light. The effect of optical magnetic field on the atom is much weaker than that of the electric field and we may ignore the second term in the above equation. Also, since the ion cores are much heavier than the electrons, at optical frequencies the motion of the electron is more significant than that of the ion cores. Thus, upon interaction with light, effectively the electrons experience a force,

$$F(t) = -eE(t)$$
(1.2)

which causes the center of the electron cloud to shift away from the positive core. However this motion of the electron cloud is transitory due to the restoring force from the positive ion core. Thus, when an incident light interacts with an atom an induced electric dipole is created in the medium. If the applied electric filed is of the form $E(t) = E_0 e^{-i\omega t} + c.c.$, oscillating with a frequency ω, then the induced dipole also oscillates at the same frequency (*c.c.* – Complex conjugate).

The Lorentz model of atom assumes that the restoring force depends linearly on the displacement of the electron cloud. If we use a simplistic analogy, we can consider this situation identical to a charge on a spring with mass m. If the spring is ideal, providing a linear restoring force, it describes the regime of linear optics. Most of the commonly observed optical phenomena are well described by the Lorentz model. If the amplitude of the electric field $E(t)$ is high, then the spring is distorted and the restoring force is no longer linear. Nonlinear optics is the regime in which the spring deviates from linearity, or in other words the nonlinear optical effects become important if the interaction potential is anharmonic. Though a complete understanding of nonlinear optical interaction of light with matter requires a quantum mechanical treatment, the above model gives a good description of the nonlinear optical effects in the case of nonresonant interaction where the frequency of the incident light is much lower than that of atomic resonances. In the following we give a brief description of linear and nonlinear optical interaction of light.

1.2.1 Linear optics

In the linear regime the restoring force is linearly proportional to the displacement of the center of electron cloud $x(t)$. This is true for a spring mass system with small displacements. The restoring force may be written as

$$F_s = -m\omega_0^2 x(t) \tag{3.3}$$

where m is the mass of the electrons and ω_0 is the natural frequency of 'the harmonic oscillator'. We may also consider a damping force of the form

$$F_d = -m\gamma \frac{dx(t)}{dt} \tag{1.4}$$

where γ is the damping constant. The applied electric field $E(t)$ gives a driving force -eE(t) which forces the electrons to oscillate at the frequency ω. The equation of motion of this forced, damped harmonic oscillator is,

$$m\frac{d^2x(t)}{dt^2} + m\gamma \frac{dx(t)}{dt} + m\omega_0^2 x(t) = -eE(t) \tag{1.5}$$

The steady solution of this equation is $x(t) = x_0 e^{-i\omega t}$ where x_0 the amplitude of oscillation is,

$$x_0 = -\frac{e}{m} \frac{E_0}{(\omega_0^2 - \omega^2) - i\gamma\omega} \tag{1.6}$$

The induced dipole moment due to this displacement is $p(t) = -ex(t)$. For a system of N atoms, the average dipole moment per unit volume, or the polarization is,

$$P(t) = -Nex(t)$$

$$= \frac{Ne^2}{m} \frac{E_0 e^{-i\omega t}}{(\omega_0^2 - \omega^2) - i\gamma\omega} \tag{1.7}$$

$$= \varepsilon_0 \chi^{(1)} \vec{E}(t)$$

where, $\chi^{(1)} = \frac{Ne^2}{\varepsilon_0 m} \frac{1}{(\omega_0^2 - \omega^2) - i\gamma\omega}$ is defined as the linear optical susceptibility of the medium. Here ε_0 is the permittivity of free space. Thus, the electric dipoles in this case oscillate at the same frequency as that of the incident electric field. This oscillating polarization in the medium will result in the emission radiation at the same frequency and modify the way in which the wave propagates. The electric displacement $D = \varepsilon_0 E + P = \varepsilon_0(1 + \chi^{(1)})E$ and thus the dielectric constant of the medium is $1 + \chi^{(1)}$. The complex refractive index of the medium is given by the square root of dielectric constant. The losses in the medium due to absorption arise from the imaginary part of the susceptibility.

1.2.2 Nonlinear optics

The harmonic restoring force considered in the analysis of the previous section is almost always an approximation and is valid only over a limited range of displacements. For large displacements of electrons from its equilibrium position, the restoring force is a nonlinear function of the displacement x. In our analogy with the spring mass system, the spring is now distorted. The restoring force now depends on various powers of x,

$$F_s = -m\omega_0^2 x(t) - max^2(t) - mbx^3(t) - \cdots \tag{1.8}$$

where $a, b \ldots$ are constants which determines the strength of the nonlinearity.

Depending on the strength of the nonlinearity of the medium and the electric field we may restrict the number of terms in the above force equation. For example, we may assume that only terms up to quadratic in x is significant giving rise to second order nonlinearity. In this case

$$F_s = -m\omega_0^2 x(t) - max^2(t) \tag{1.9}$$

and the equation of motion becomes

$$m\frac{d^2x(t)}{dt^2} + m\gamma\frac{dx(t)}{dt} + m\omega_0^2 x(t) + max^2(t) = -eE(t) \tag{1.10}$$

If we include second and third order nonlinearity the equations of motion is

$$m\frac{d^2x(t)}{dt^2} + m\gamma\frac{dx(t)}{dt} + m\omega_0^2 x(t) + max^2(t) + mbx^3(t) = -eE(t) \tag{1.11}$$

and so on.

To solve this equation, we may use the approach of perturbation theory and replace $E(t)$ by $\lambda E(t)$, where λ is a parameter whose value can be continuously varied between zero and one. Now we can solve the above nonlinear equation by considering a power series expansion in the strength of λ and the perturbation of the form,

$$x(t) = \lambda x_1 + \lambda^2 x_2 + \lambda^3 x_3 + \cdots \tag{1.12}$$

For the solution to be valid, each term in the solution should satisfy the equation separately. Substituting each term in the equation and putting $\lambda = 1$, we will get,

$$m\frac{d^2x_1(t)}{dt^2} + m\gamma\frac{dx_1(t)}{dt} + m\omega_0^2 x_1(t) = -eE(t) \tag{1.13}$$

$$m\frac{d^2x_2(t)}{dt^2} + m\gamma\frac{dx_2(t)}{dt} + m\omega_0^2 x_2(t) + ax_1^2(t) = 0 \tag{1.14}$$

$$m\frac{d^2x_3(t)}{dt^2} + m\gamma\frac{dx_3(t)}{dt} + m\omega_0^2 x_3(t) + 2ax_1(t)x_2(t) + bx_1^3(t) = 0 \tag{1.15}$$

The first equation is same as the equation of motion in linear regime. The solution of the first equation is given by,

$$x_1(t) = x_0 e^{-i\omega t} \tag{1.16}$$

$$\text{where, } x_0 = -\frac{e}{m}\frac{E_0}{(\omega_0^2-\omega^2)-i\gamma\omega}$$

Once we know the solution for first equation, we can substitute for $x_1{}^2(t)$ in the second equation. It can be seen that the second equation contains a source term which depends on the square of the

electric field. And again, once we know $x_1(t)$ and $x_2(t)$ the third equation can be solved. From the expansion of $x(t)$, it automatically follows that the polarization, $P(t) = -Nex(t)$ is also a power series in $E(t)$. We can write

$$\tilde{P}(t) \equiv \tilde{P}^{(1)}(t) + \tilde{P}^{(2)}(t) + \tilde{P}^{(3)}(t) + \cdots \tag{1.17}$$

$\tilde{P}^{(1)}(t)$ is the linear polarization, $\tilde{P}^{(2)}(t)$ is the second order polarization and so on.

In the case of linear optics, the higher order terms in the electric field can be neglected and the induced polarization is given by,

$$\tilde{P}^1(t) = \epsilon_0 \chi^1 \tilde{E}(t) \tag{1.18}$$

where $\tilde{E}(t)$ is the incident electric field ϵ_0 is the permittivity of free space, χ^1 is the linear susceptibility. Here for simplicity, we are considering electric field, polarization, and susceptibility as scalars. When we consider vector nature of electric field and polarization, susceptibility would be a tensor. For the linear case χ^1 is a tensor of rank two. In the case of nonlinear optical interaction, the induced polarization may be written as,

$$\tilde{P}(t) = \epsilon_0 [\chi^{(1)} \tilde{E}(t) + \chi^{(2)} \tilde{E}^2(t) + \chi^{(3)} \tilde{E}^3(t) + \cdots] \tag{1.19}$$

or

$$\tilde{P}(t) \equiv \tilde{P}^{(1)}(t) + \tilde{P}^{(2)}(t) + \tilde{P}^{(3)}(t) + \cdots$$

where, $\chi^{(2)}$ and $\chi^{(3)}$ are the second and third order nonlinear optical susceptibilities. They are third and fourth rank tensors respectively. $\tilde{P}^{(2)}(t) = \epsilon_0 \chi^{(2)} \tilde{E}^2(t)$ is the second order nonlinear polarization and $\tilde{P}^{(3)}(t) = \epsilon_0 \chi^{(3)} \tilde{E}^3(t)$ is the third order nonlinear polarization. So briefly, $\chi^{(1)}$ describes linear optical process, $\chi^{(2)}$ describes second order nonlinear optical process and $\chi^{(3)}$ describes third order nonlinear optical process.

We may express the polarization as sum of linear and nonlinear contributions

$$\tilde{P}(t) \equiv \tilde{P}^{(1)}(t) + \tilde{P}^{NL}(t) \tag{1.20}$$

and the wave equation for a nonlinear optical media can be expressed as,

$$\nabla^2 \tilde{E} - \frac{n^2}{c^2} \frac{\partial^2 \tilde{E}}{\partial t^2} = \frac{1}{\epsilon_0 c^2} \frac{\partial^2 \tilde{P}^{NL}}{\partial t^2} \tag{1.21}$$

where n is linear refractive index and c is speed of light in vacuum. According to this, the nonlinear polarization $\tilde{P}^{NL}$ which depends on higher powers of electric field will lead to the generation of radiation at new frequencies as the time varying polarization will act as the source of new frequencies.

1.3 Effects due to second order nonlinear optical susceptibility

The examples of process involving second order nonlinear optical susceptibility are second harmonic generation, sum and difference frequency generation, optical parametric oscillation and optical parametric amplification.

If we consider two distinct frequency ω_1 and ω_2 present in the incident wave.

$$\tilde{E}(t) = E_1 e^{-i\omega_1 t} + E_2 e^{-i\omega_2 t} + c.c. \tag{1.22}$$

Then the nonlinear polarization $\tilde{P}^{(2)}$ can be written as,

$$\tilde{P}^{(2)}(t) = \epsilon_0 \chi^{(2)} \tilde{E}^2(t)$$

$$= \epsilon_0 \chi^{(2)} \left[E_1^2 e^{-2i\omega_1 t} + E_2^2 e^{-2i\omega_2 t} + 2E_1 E_2 e^{-i(\omega_1 + \omega_2)t} + 2E_1 E_2^* e^{-i(\omega_1 - \omega_2)t} \right. \tag{1.23}$$
$$\left. + c.c. \right] + 2\epsilon_0 \chi^{(2)} \left[E_1 E_1^* + E_2 E_2^* \right]$$

The complex amplitude of the various frequency components can be written as

$$P(2\omega_1) = \epsilon_0 \chi^{(2)} E_1^2$$
$$P(2\omega_2) = \epsilon_0 \chi^{(2)} E_2^2$$
$$P(\omega_1 + \omega_2) = 2\epsilon_0 \chi^{(2)} E_1 E_2 \tag{1.24}$$
$$P(\omega_1 - \omega_2) = 2\epsilon_0 \chi^{(2)} E_1 E_2^*$$
$$P(0) = 2\epsilon_0 \chi^{(2)} (E_1 E_1^* + E_2 E_2^*)$$

New frequencies are generated due to each of the second order polarization term. Each term represents a physical process. The last term $P(0)$ represents the DC term and this process is called optical rectification. In general, it is convenient to represent $\tilde{P}^{(2)}(t)$ as a sum of the contribution from different frequency components,

$$\tilde{P}^{(2)}(t) = \sum_{n} P(\omega_n)e^{-i\omega_n t} \tag{1.25}$$

and the second order polarization will lead to generation of radiation at different frequencies given by the sums and differences of ω_n's. Here we may also note that the materials having a center of symmetry would have zero magnitude for second order susceptibility and would not show any second order effects.

1.3.1 Second harmonic generation

The process in which a nonlinear optical medium interacts with a pump wave of frequency, ω and generates a wave of double the frequency 2ω is called second harmonic generation or frequency doubling. The polarization amplitudes for second harmonic generation is $P(2\omega) = \epsilon_0 \chi^{(2)} E_1^2$. We can consider light beam with electric field, $\tilde{E}(t) = E e^{-i\omega t} + C.C.$ is incident on a material which is having a non-zero second order susceptibility $\chi^{(2)}$. Then the nonlinear polarization due to $\chi^{(2)}$ is given by,

$$\tilde{P}(2\omega) = \epsilon_0 \chi^{(2)}(2\omega, \omega, \omega)\tilde{E}^2(\omega) \tag{1.26}$$

where the frequency dependence of $\chi^{(2)}$ is explicitly indicated. This nonlinear polarization consists of a DC term (zero frequency) and a contribution at 2ω.

The wave equation for a nonlinear optical media having second order nonlinearity is given by,

$$\nabla^2 \tilde{E} - \frac{n^2}{c^2}\frac{\partial^2 \tilde{E}}{\partial t^2} = \frac{1}{\epsilon_0 c^2}\frac{\partial^2 \tilde{P}^{(2)}}{\partial t^2} \tag{1.27}$$

According to this the second term in the nonlinear polarization, $\tilde{P}^{(2)}$ will lead to the generation of radiation at 2ω which is a second harmonic frequency. Figure 1.1 (a) gives a schematic of the interaction of incident wave having frequency ω with a material having non-zero second order susceptibility and production of a new wave having frequency 2ω. Figure 1.1 (b) shows the energy level diagram representing second harmonic generation.
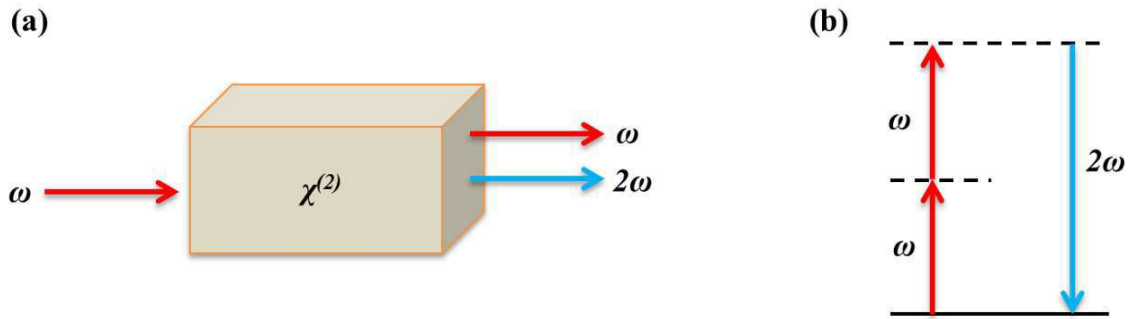
Fig. 1.1 Second harmonic generation (a) Interaction of an incident light wave with frequency ω with a medium having a nonzero second order nonlinear optical susceptibility. (b) Energy level diagram.

1.3.2 Sum and difference frequency generation
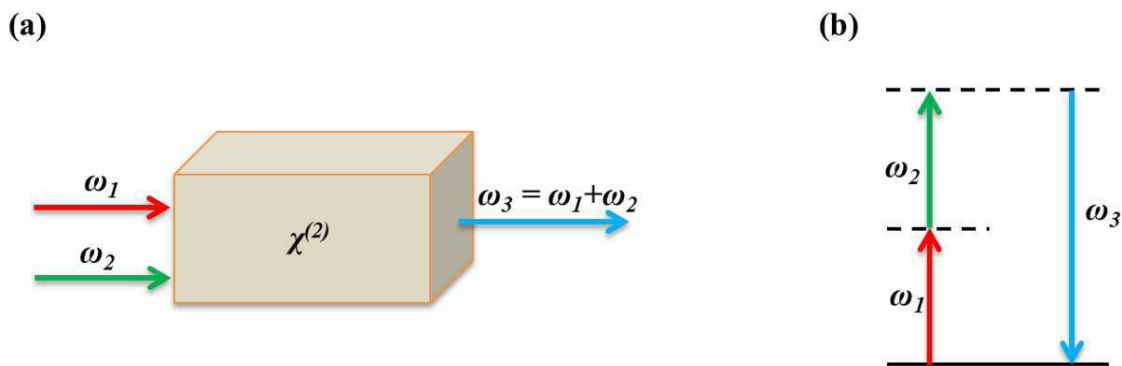
Fig. 1.2 Sum frequency generation (a) Interaction of an incident light wave with frequencies ω_1 and ω_2 with a medium having a nonzero second order nonlinear optical susceptibility. (b) Energy level diagram.

When two beams of different frequencies are incident on a nonlinear medium with a non-zero second order nonlinear optical susceptibility, $\chi^{(2)}$, it leads to the generation of new frequencies as sum of the incident frequency or difference of the incident frequencies. The terms $P(\omega_1 + \omega_2)$ represents sum frequency generation. $P(\omega_1 - \omega_2)$ represents difference frequency generation in which new frequency is generated at the difference of the incident frequencies. This process can be used for generating tunable radiation. Figures 1.2 (a) and (b) represents interaction geometry and energy level diagram for the sum frequency generation process. Figure 1.3 (a) and (b)

represents interaction geometry and energy level diagram for difference frequency generation process.
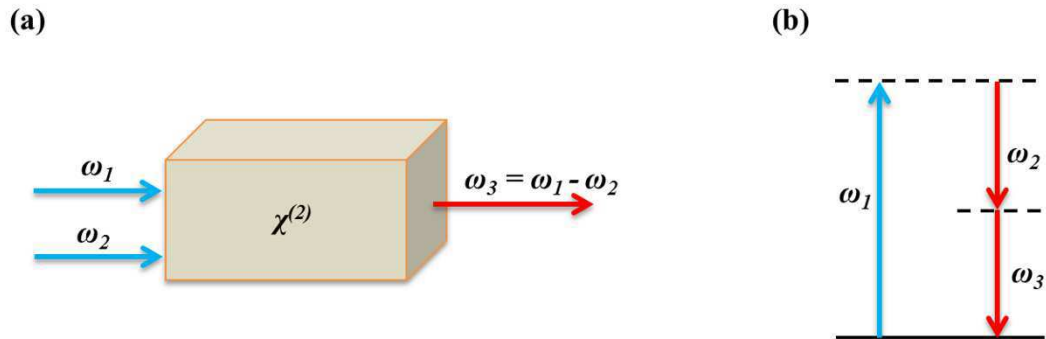
Fig. 1.3 Difference frequency generation (a) Interaction of an incident light wave with frequencies ω_1 and ω_2 with a medium having a nonzero second order nonlinear optical susceptibility. (b) Energy level diagram.

1.3.3 Parametric oscillation and parametric amplification
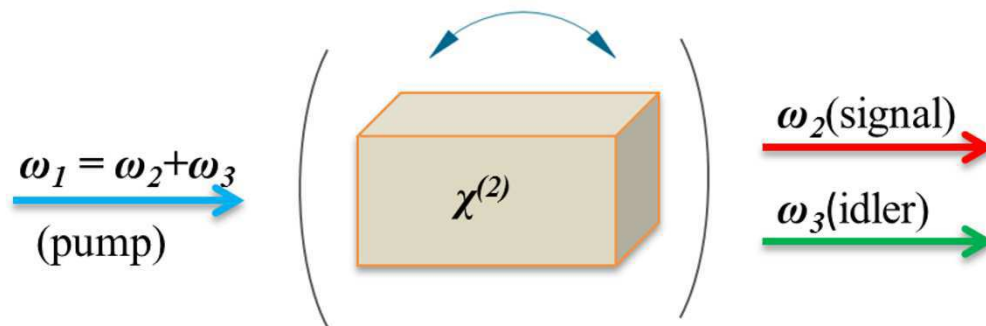
Fig. 1.4 Optical parametric oscillator

In a parametric process the initial and final quantum mechanical states involved in a transition are identical. The life time of population inversion in a virtual level is given by $\hbar/\delta E$ where δE is the energy difference between the virtual level and nearest real level. In a nonparametric process the transition of population inversion happens between two real levels. In difference frequency generation one atom absorbs a photon with frequency ω_1 and emits a frequency $\omega_3 = \omega_1 - \omega_2$ in the presence of a photon of frequency ω_2. Or in other words, a photon with frequency ω_1 is annihilated and two photons of frequency ω_2 and ω_3 are created in the presence of ω_2 frequency.

This process can even happen if the ω_2 frequency is not present. This process is known as parametric fluorescence and the generated field intensity will be weaker. In this case if the nonlinear crystal is kept inside an optical resonator one can amplify the generated fields ω_2 or ω_3. The output frequency $\omega_3 = \omega_1 - \omega_2$ can be controlled by adjusting the orientation of the crystal (phase matching condition) and can be used to generate tunable radiation. In this process ω_1 is called the pump frequency, desired output frequency is called signal frequency ω_s and the other output frequency is called idler frequency ω_i. Figure 1.4 shows a schematic of optical parametric oscillator.

1.4 Effects due to third order nonlinear optical susceptibility

The third order nonlinear polarization can lead to various effects such as third-harmonic generation (THG), two-photon absorption, Kerr effect, self-phase modulation, self-focusing, four-wave mixing, stimulated Brillouin scattering, stimulated Raman scattering, optical solitons, optical bistability. In this section, we will briefly discuss some of these processes.

1.4.1 Third harmonic generation
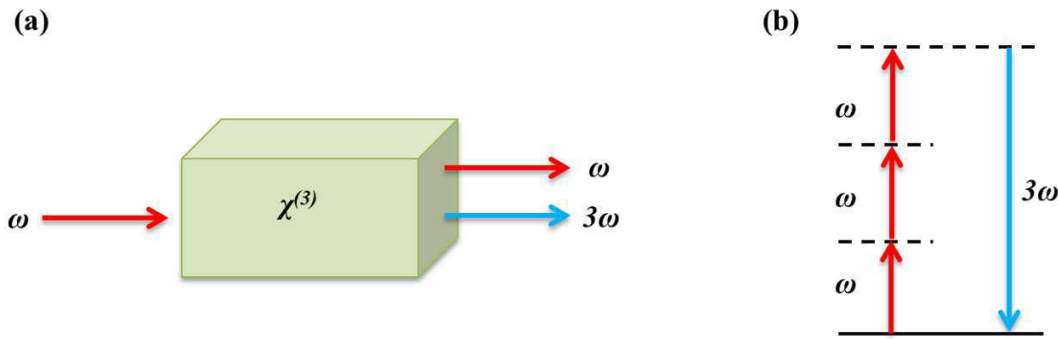
Fig. 1.5 (a) Interaction of an incident light wave with frequency ω with a medium having a nonzero third order nonlinear optical susceptibility (b) Energy level diagram showing the generation of third harmonic generation.

The nonlinear polarization due to $\chi^{(3)}$ is given by,

$$\tilde{P}^{(3)}(t) = \epsilon_0 \chi^{(3)} \tilde{E}(t)^3 \tag{1.28}$$

In a medium having nonzero third order susceptibility, $\tilde{P}^{(3)}(t)$ generates new frequencies which are sum of three input frequencies. In third harmonic generation process, three photons of the same frequency, ω is used to create a single photon of frequency, 3ω which is three times the frequency of incident photons. The third harmonic generation process is illustrated in figure 1.5 (a) and (b).

1.4.2 Intensity dependent refractive index

Apart from quenching new frequencies, the third order polarization can result other effects such as intensity dependent refractive index, saturable absorption and multiphoton absorption. In this section we will derive the mechanism behind intensity dependent refractive index. For simplicity we will assume the incident light is monochromatic. The third order polarization, $\tilde{P}^{(3)}(t)$ induced by a field $\tilde{E}(t) = E_0 \cos \omega t$ is,

$$
\begin{aligned}
\tilde{P}^{(3)}(t) &= \epsilon_0 \chi^{(3)} E_0{}^3 \cos^3 \omega t \\
&= \epsilon_0 \chi^{(3)} E_0{}^3 (\frac{1}{4} \cos 3\omega t + \frac{3}{4} \cos \omega t) \\
&= \frac{1}{4} \epsilon_0 \chi^{(3)} E_0{}^3 \cos 3\omega t + \frac{3}{4} \epsilon_0 \chi^{(3)} E_0{}^3 \cos \omega t
\end{aligned}
\tag{1.29}
$$

The first term in the above expression results in third harmonic generation. The second term is responsible for intensity dependent refractive index. The second term, the source term for the frequency ω can be written as,

$$
\tilde{P}_\omega^{(3)}(t) = \frac{3}{4} \epsilon_0 \chi^{(3)} E_0{}^3 \cos \omega t = (\frac{3}{4} \epsilon_0 \chi^{(3)} E_0{}^2) \tilde{E}(t)
\tag{1.30}
$$

If we assume $\chi^{(1)}$ and $\chi^{(3)}$ are non-zero, then there are two sources for generation of frequency ω. The linear polarization, $\tilde{P}_\omega^{(1)}(t)$ and $\tilde{P}_\omega^{(3)}(t)$

Then the total source term for the frequency ω will be

$$
\begin{aligned}
\tilde{P}^{(1)}(t) + \tilde{P}_\omega^{(3)}(t) &= \epsilon_0 \chi^{(1)} \tilde{E}(t) + (\frac{3}{4} \epsilon_0 \chi^{(3)} E_0{}^2) \tilde{E}(t) \\
&= \epsilon_0 \left[\chi^{(1)} + \frac{3}{4} \chi^{(3)} E_0{}^2 \right] \tilde{E}(t) = \epsilon_0 \chi_{eff} \tilde{E}(t)
\end{aligned}
\tag{1.31}
$$

where $\chi_{eff} = \chi^{(1)} + \frac{3}{4}\chi^{(3)}E_0^2$ is the effective susceptibility.

The electric displacement is $D = \epsilon_0(1 + \chi_{eff})E$ and the effective real part of refractive index can be calculated by,

$$n = \sqrt{Re(\epsilon)} \tag{1.32}$$

where $\epsilon = 1 + \chi_{eff}$ is the effective dielectric constant.

$$n = \sqrt{Re(1 + \chi_{eff})} = \sqrt{Re\left(1 + \chi^{(1)} + \frac{3}{4}\chi^{(3)}E_0^2\right)}$$

$$n = \sqrt{1 + Re(\chi^{(1)}) + \frac{3Re(\chi^{(3)})}{4}E_0^2}$$

$$n \approx \sqrt{1 + Re(\chi^{(1)})} + \frac{3Re(\chi^{(3)})}{8\sqrt{1 + Re(\chi^{(1)})}}E_0^2$$

$$n \approx n_0 + \frac{3Re\left(\chi^{(3)}\right)}{8n_0}E_0^2 = n_0 + \bar{n}_2 E_0^2 \tag{1.33}$$

where $n_0 = \sqrt{1 + Re(\chi^{(1)})}$ and $\bar{n}_2 = \frac{3Re\left(\chi^{(3)}\right)}{8n_0}$

We can write the refractive index in terms of intensity, $I = \frac{1}{2}n_0\epsilon_0 c E_0^2$ as,

$$n = n_0 + n_2 I \tag{1.34}$$

where, $n_2 = \frac{2\bar{n}_2}{n_0\epsilon_0 c} = \frac{3}{4n_0^2\epsilon_0 c}Re\left(\chi^{(3)}\right)$ is the intensity dependent refractive index.

Intensity dependent refractive index can lead to a process called self-focusing. For example, let us consider a Gaussian beam propagating through a nonlinear crystal with non-zero values of n_2. Then since the transverse intensity of the Gaussian beam decreases away from the center of the beam,

the axial region of the beam will see a higher refractive index (for positive nonlinearity) and the intensity dependent refractive index makes the crystal to act as a convex lens and focus the beam. This effect is termed as self-focusing. Self-phase modulation also happens as a result of the intensity dependent refractive index. When the light wave passes through a nonlinear crystal with $n_2 > 0$, then n_2 creates changes in the phase of the incident light wave. In four wave mixing the interaction of two or three waves inside a nonlinear crystal produces new wavelengths through degenerate and nondegenerate four wave mixing.

1.4.3 Two-photon absorption

If we consider a complex index of refraction by including the real and imaginary part of the susceptibility, then we can write,

$$\tilde{n}(\omega) = n(\omega) + iK(\omega) = \sqrt{\epsilon(\omega)} \tag{1.35}$$

where the real part of the complex refractive index is the usual refractive index n and the imaginary part of the complex refractive index, K is the extinction coefficient, which is responsible for absorption. If we follow a similar approach as in the previous section for the imaginary part of the effective susceptibility, $\chi_{eff} = \chi^{(1)} + \frac{3}{4}\chi^{(3)}E_0{}^2$ we can express the extinction coefficient also as sum of real and imaginary parts as in the case of nonlinear refractive index,

$$K = K_0 + K_2 I \tag{1.36}$$

where K_2 is given by $K_2 = \frac{3}{4n_0^2\epsilon_0 c} Im(\chi^{(3)})$

$$K = K_0 + \frac{3}{4n_0^2\epsilon_0 c} Im(\chi^{(3)})I \tag{1.37}$$

The linear absorption coefficient is defined as $\alpha_0 = 2\frac{\omega}{c}K_0$. We can write the above equation in terms of absorption coefficient as,

$$\alpha = \alpha_0 + \alpha_2 I \tag{1.38}$$

where α_2 is the two-photon absorption coefficient

$$\alpha_2 = \frac{3\omega}{2n_0^2\epsilon_0 c^2} Im((\chi^{(3)})) \tag{1.39}$$

In a two-photon absorption process, an atom makes its transition from ground state to its excited state by absorbing two photons simultaneously. The nonlinear absorption cross section describing this process is given by,

$$\sigma = \sigma^{(2)}I \tag{1.40}$$

The absorption cross section is no longer a constant material property, but it increases linearly with the intensity of light.

The atomic transition rate R due to the two-photon absorption process is

$$R = \frac{\sigma I}{\hbar\omega} \tag{1.41}$$

$$R = \frac{\sigma_{2p}I^2}{\hbar\omega} \tag{1.42}$$

1.4.4 Saturable absorption

Saturable absorption is a nonparametric nonlinear optical process in which the absorption coefficient of the material decreases with increasing intensity of incident light. This happens when the material is exposed to intense light, so that all the atoms are excited, and the ground state is depleted. The dependence of the absorption coefficient of the material on the incident laser intensity in this case is given by,

$$\alpha = \frac{\alpha_0}{1 + I/I_s} \tag{1.43}$$

where α_0 is the linear absorption coefficient and I_s is the saturation intensity.

1.5 Optical Microscopy

One of the major focus of this thesis is on developing new and improved optical microscopic techniques by making use of the large third order nonlinear optical absorption observed in perovskite nanoparticles. In this section we give a brief review of existing optical microscopic techniques, its salient features and drawbacks.

The optical microscope also known as light microscope uses a combination of lenses and visible light to image small objects at greater magnification than the human eye can perceive [1,17].

Optical microscopy is the most widely used and important imaging tool employed in life science [1,2,18]. Other than life sciences optical microscopy finds application in various fields such as electronics, material science and photonics [1–3,17,19–21]. Figure 1.6 depicts the basic principle of image formation in a compound microscope in a self-explanatory manner.
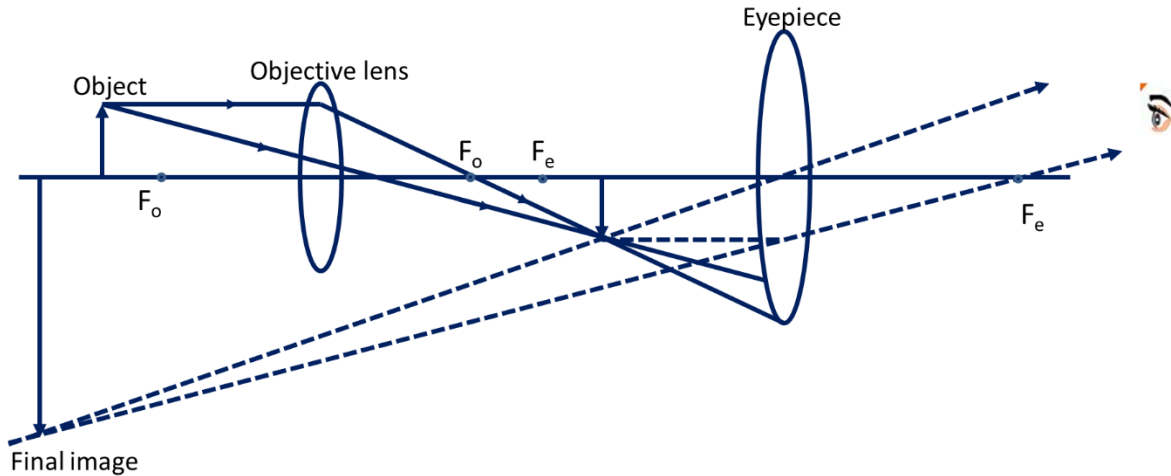
Fig. 1.6 Image formation in a compound optical microscope

One of the simplest optical microscopes is the bright field microscope. In bright field imaging the sample is illuminated with a broadband (white) light source and the image is formed from the transmitted/reflected light [3,20]. Usually a condenser lens is used to focus the light on the specimen and the transmitted/reflected light is collected by another lens which is termed as the objective lens. The objective lens in combination with the ocular (eyepiece) lens forms an enlarged image of the specimen. Figure 1.7 shows the schematic of a wide field microscope. The quality of the image in an optical microscope is decided by two parameters, resolution and contrast. Resolution is a measure of the shortest distance between two closely spaced objects that can be seen resolved in the image [17]. The resolution of an optical microscope is limited by the diffraction of light which is a fundamental limitation [17,22]. Imaging a small point object forms an Airy disc pattern which consists of a central bright spot surrounded by bright and dark circular rings. According to Rayleigh criterion, two point sources are just resolvable when the maximum of the Airy intensity pattern of one point source falls on the minimum of the second point source's Airy intensity pattern [17,22]. Figure 1.8 illustrates the Airy disc pattern of two point sources in three different situations: (a) when the two points are well resolved (b) when the two points are no longer resolvable and (c) when the two points are just resolvable. According to Rayleigh criterion,

the lateral resolution is the distance from the central maximum to the first minimum of the airy pattern and is given by the equation,

$$\text{Lateral Resolution, } r = \frac{1.22\lambda}{NA_{Obj}+NA_{cond}}$$

where λ is the wavelength of light and NA is the numerical aperture of the lenses used. Numerical aperture is given by the equation, $NA = n\,sin\alpha$, where n is the refractive index of the medium and α is the half the angle of the light acceptance cone of the lens [17,22]. Thus, the image resolution depends on the numerical aperture of the objective and condenser, and wavelength of light used.

One of the challenges in using bright field microscopy is to separate the image from the scattering environment [1,19]. In general, the optical contrast comes from the difference in the optical properties of structures within the sample and the neighboring medium. In bright field transmission imaging, the light is passed through a semi-transparent medium and the differences in the transmitted light intensity between neighboring points provide the image contrast. Different approaches have been tried out in conventional optical microscopy to improve image contrast. This include dark field microscopy [19,20,23], polarization based microscopy [24], and phase contrast imaging [23]. In dark field imaging, the light from the unscattered region of the specimen is excluded and the field around the specimen becomes dark. This is achieved by blocking the central light rays along the optical axis of the microscope. This forms a hollow light cone incident on the sample which makes an oblique angle with the sample and image is formed with the scattered light. In dark field microscopy, the contrast is created by a bright specimen on a dark background. This will help in imaging outlines, edges and boundaries clearly. In a polarized light microscopy, the illumination beam is polarized to image a birefringent sample to enhance the contrast. This is achieved by keeping a polarizer between condenser and sample and an analyzer in the path of light rays to the detector after the sample. Polarization microscopy can be used to extract information about anisotropic materials. In phase contrast microscopy the change in phase of the light beam when passed through the sample is converted into intensity variation to increase the contrast in the image. In phase contrast microscopy an annular aperture is used in the focal plane of the condenser and a phase plate is kept at the rear focal plane of the objective. The phase plate is also an annular ring with a phase altering material. The light passing through the condenser annular aperture passes through the specimen. The rays which do not deviate from the specimen pass through the phase

plate where the phase altering material is present and the phase is altered. The light rays which are scattered from the sample pass through the phase plate through the regions where the phase altering material is not covered and its phase remains unchanged. This creates a difference in phase between transmitted and scattered light and thus would give better contrast. Phase contrast microscopy can be used to image transparent optical samples.

Lamp

Path of light

Condenser lens

Specimen

Objective lens

Eyepiece

Final image
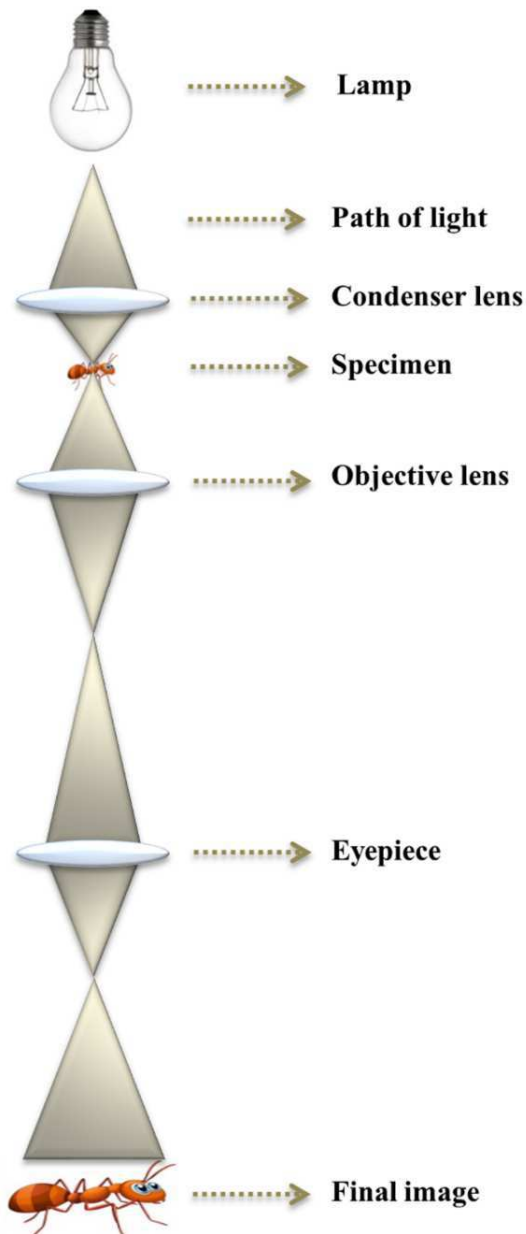
Fig. 1.7 The schematic of a bright field microscope.
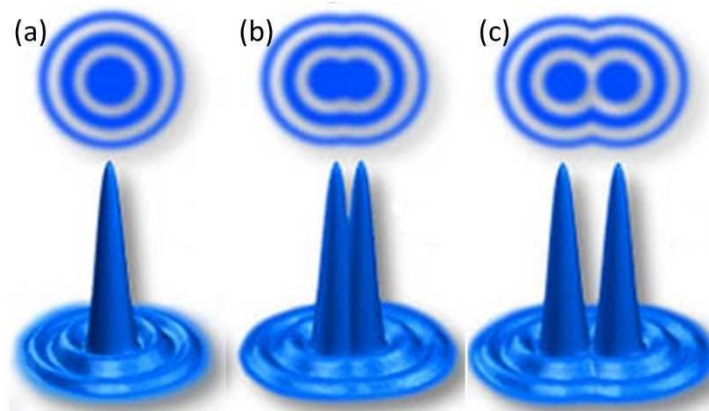
Fig. 1.8 Airy disc pattern of two closely spaced point sources when the two points are (a) unresolved (b) just resolved and (c) well resolved

Though these techniques such as dark field microscope, polarization microscope, and phase contrast microscope have improved the contrast compared to conventional bright field microscope, still large-scale improvement is necessary to provide quantitative information on biological process. This is especially true since the contrast and signal to background ratio is limited due to the relatively small difference in the refractive indices of the desired biological objects to be imaged and that of the surroundings. A novel approach employed to overcome this difficulty is fluorescence microscopy where desired region of the specimen is labeled with fluorescent dye. The fluorescence emission from the dye labels forms the contrast in imaging [21]. Fluorescence microscopy has helped in improving the signal to background ratio considerably in the biological imaging [21]. The molecules which emit fluorescence when irradiated are called fluorophores. Fluorescence microscopy allows one to label proteins and other biological molecules of interest inside the cell by specific fluorophores and image them with better contrast and resolution. In conventional fluorescence microscopy, the fluorescent label in the specimen is illuminated by monochromatic radiation filtered out from a broad band light source and the resulted fluorescence is collected by an objective lens and sent to a detector through appropriate filters to form the image of the specimen. Signal to noise ratio is improved significantly in this method of imaging [21]. Since we can label a specific desired structure inside a complex specimen by fluorophores, fluorescence microscopy enables targeted imaging of specific regions inside a biological system [21].

The excitation wavelength, extinction coefficient, emission wavelength, fluorescence quantum yield, fluorescence lifetime and the stock shift in wavelength are important parameters for selecting fluorophores as labels. The wavelength of the light source in fluorescence microscopy is selected to coincide with the excitation band of the fluorophores. The extinction coefficient is the measure of the amount of absorption of the fluorophores at a particular wavelength. Fluorescence quantum yield is the ratio of number of photons emitted by the molecule to the number of photons absorbed by the molecule. Fluorescence lifetime is inversely proportional to the width of the excitation energy level. Normally for fluorescence process, the lifetime is of the order of microseconds to nanoseconds, so the absorption and emission are almost instantaneous. The smaller is the lifetime, lesser is the data acquisition time. Traditionally used fluorophores are natural or synthetic dyes. The most popular among them are the ones corresponding to the excitation wavelength of the Ar^+ laser lines 488 nm, 510 nm, 540 nm. Another category of dyes is nucleic acid dyes. Hoechst and DAPI are examples of nucleic acid dyes. To improve the imaging capabilities of fluorescence microscope many new markers are been developed in recent years. One major development in the field of a biomarker is the discovery of fluorescent proteins such as green fluorescent protein (GFP) found in some of the living organisms. GFP absorbs blue or violet light and emits green fluorescence. Similarly, yellow fluorescent protein (YFP) and red fluorescent protein (RFP) are also used as fluorescent markers.

Several different approaches are applied in a conventional microscopy to improve the resolution and contrast for specific imaging needs. We briefly discuss these microscopic techniques and their limitation in the following section.

1.5.1 Confocal Fluorescence Microscopy

One of the major development in optical microscopy is the invention of confocal fluorescence microscopy by Marvin Minsky in 1955. Marvin Minsky proposed that by adding a pinhole in the confocal backplane of the objective lens one can reduce out of focus light reaching the detector [2,3,25]. In conventional fluorescence microscopy, the fluorescence emitted from the sample above and below of the focal plane are also collected by the objective and send to the detector. This out of focus light when it reaches the detector reduces the contrast of the signal from the focus. In confocal microscopy the pinhole used in the path of the fluorescence light eliminate out of focus light from the specimen. The pinhole placed in the confocal plane acts like a spatial filter

and removes the out of focus light from the sample. In other words, the pinhole enables to collect the light only from the desired depth of field in the specimen. This gives the confocal microscope better axial resolution. It also provides the capability to collect serial Z- sections of the sample, or the Z- sectioning capability [2,3,25]. These optical sections can be combined to form a high resolution three-dimensional image of the specimen. Figure 1.9 illustrates the use of pinhole and path of light rays in a confocal microscope to eliminate out of focus light in confocal microscope.

The invention of the confocal microscope was not noticed much until the invention of lasers. The invention of lasers augmented the use of microscopy in different fields. The monochromaticity and directionality of lasers allows tight focusing of the beam to small diffraction limited spot, thereby improving the resolution of the microscope considerably. In confocal fluorescence microscopy, since the laser is focused into a small spot in the sample, one has to either raster scan the beam over the sample or move the sample in the XY (lateral) plane to acquire a two-dimensional image. The scanning of the sample can be done by moving the stage where the sample is attached while keeping the laser position fixed (stage scanning), or by scanning the laser beam using a galvanometric mirror while keeping the sample fixed (laser scanning). In our studies, we have employed a laser scanning microscope. The advantage of laser scanning is the fast acquisition of images in few seconds. After the invention of lasers, the confocal microscope became popular among the imaging systems. Sensitivity, spatial resolution, and three-dimensional sectioning capabilities make it an ideal microscope in the study of biological systems such as membranes, tissues, and cells [2,3,5,25].

1.5.2 Nonlinear optical microscopy

Most of the available fluorophores employed so far in confocal fluorescence microscopy use visible light to excite the fluorophores. This wavelength is not ideal for biomolecular imaging, especially in an experiment that involves deep tissue imaging considering the absorption in biological tissues, which ranges from 350 nm to 650 nm. Further, the CW excitation can result in heating up of the sample even at low powers reducing the viability of the technique in many systems. Another approach made to overcome these limitations is the nonlinear optical microscopy.
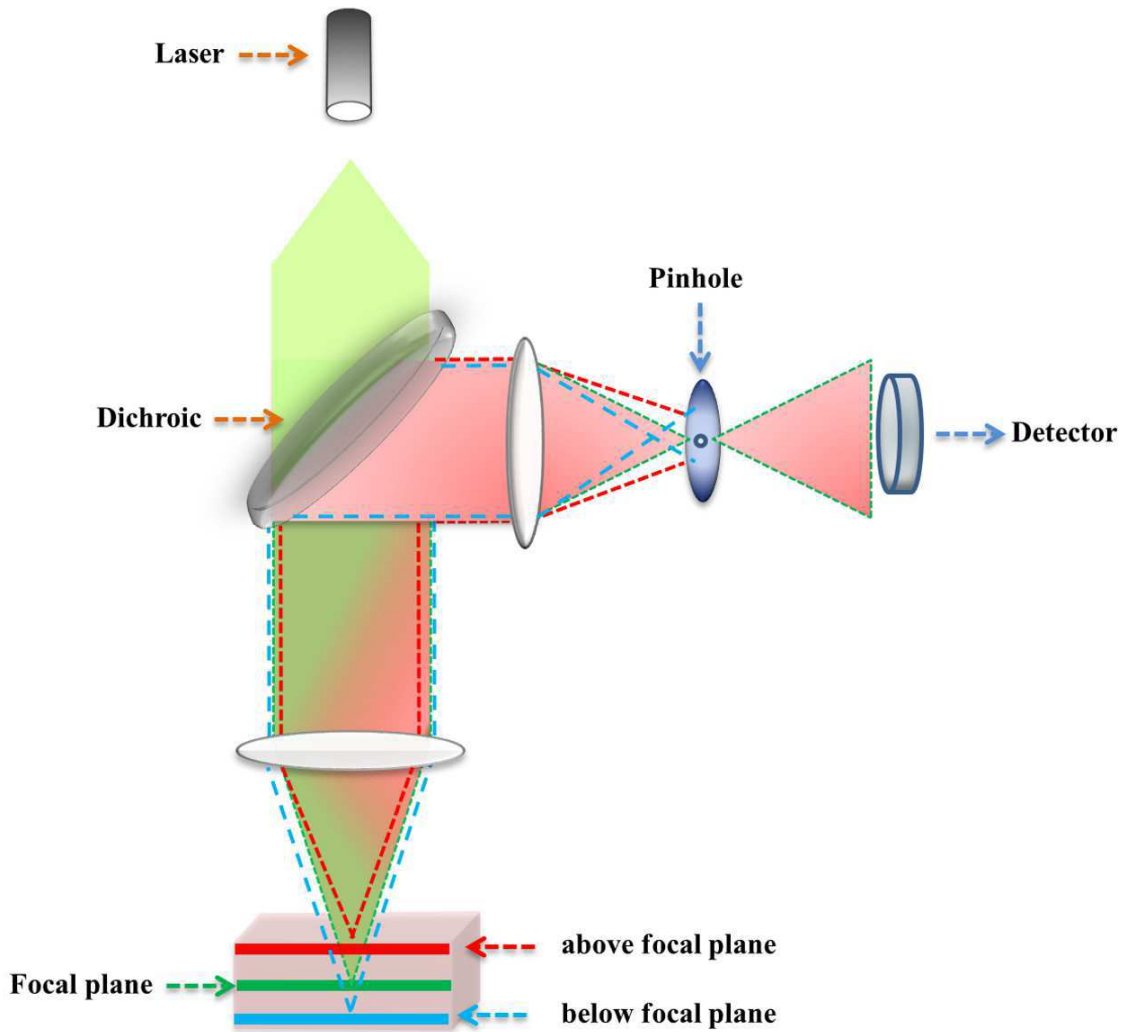
Fig. 1.9 Schematic of confocal microscopy.

In a conventional optical microscope, the image contrast is given by the linear interaction of the incident radiation field intensity with the sample, namely absorption and scattering. In a linear optical process, the polarization induced by light-matter interaction is varying linearly with the incident intensity. In a nonlinear optical process, the induced polarization is dependent upon higher powers of the incident radiation field. Two-photon absorption, three-photon absorption and second harmonic generation are some of the examples of nonlinear optical processes used in microscopy. These nonlinear optical processes can be used to create contrast in optical microscopy. Advances in the field of laser technology has strengthened the application potential of nonlinear optical microscopic techniques as a successful tool in biomedical research [4,6,7,26]. Two-photon

absorption, described in the previous section, is a third order nonlinear optical phenomenon which involves the transition of a system from the ground state to a higher lying state by the simultaneous absorption of two photons from an incident radiation field. The nonlinear absorption is proportional to the square of the instantaneous intensity I and the optical loss due to absorption is described by the differential equation

$$\frac{dI}{dz} = -\alpha I - \alpha_2 I^2 \tag{1.44}$$

where α is the linear absorption coefficient, which in this case arises only from the impurities present if any. The two-photon absorption coefficient α_2 in this expression is a macroscopic parameter characterizing the material and is related to the imaginary part of the third order nonlinear optical susceptibility $\chi^{(3)}$ by the relation,

$$\alpha_2 = \frac{3\omega}{2n_0^2 \epsilon_0 c^2} Im(\chi^{(3)})$$

If N is the number density of the molecules involved in the interaction, the transition rate due to the two-photon absorption process, $R = \sigma_2 I^2 / \hbar\omega$ where $\sigma_2 = \hbar\omega\alpha_2 / N$ is defined as the two-photon absorption cross-section. Two-photon excited fluorescence (TPEF) microscopy is one of the well-developed nonlinear optical microscopes. Some of the other nonlinear microscopy techniques are second harmonic generation (SHG) microscopy and third harmonic generation (THG) microscopy, and coherent anti-Stokes Raman scattering (CARS) microscopy.

The success of all the above mentioned fluorescence microscopies relies heavily on the availability of suitable fluorophores that can be used to stain the biomolecules of interest. A key issue faced by most biologists employing fluorescence microscopy is the phototoxicity and photobleaching of available fluorophores [2,21,25]. A fluorophore loses its ability to fluorescence permanently due to photon induced chemical damage called photobleaching. This limits the use of fluorophores for longer excitation time. Repeated exposure of the fluorescently labeled cells to laser radiation is a major cause for phototoxicity. When excited with lasers the fluorophores will go to higher excited state. In the excited state, they can react with oxygen or other molecules to damage cells. While phototoxicity of the fluorophore is inherently harmful to the biological system under observation, photobleaching hinders the use of the technique in studies that require long observation times.

Many live cell imaging studies, for example, experiments that involve cytoplasmic and nuclear transport require continuous monitoring for long periods of time. The search for photostable labels which resist photobleaching for a longer duration than conventional fluorescent dyes have resulted in the development of many new fluorescent probes such as semiconductor quantum dots. Though these efforts partly succeeded in developing many new photostable labels, they are often accompanied by newer challenges. Semiconductor quantum dots, for example, is a promising new biological label that satisfies the requirement of long-term photo-stability, but their irregular photo blinking (fluorescent intermittency) is a major drawback that has prevented the usage of them as biological labels [27]. These inherent limitations of confocal fluorescence microscopy have stimulated an intense research effort on developing new imaging techniques and labels.

Instead of molecular fluorophores one of the potential label experimented is fluorescent nanoparticles. Fluorescent nanoparticles include fluorescently doped silica nanoparticles [8,28,29], polymer nanoparticles [9,30], carbon dots [31–33] and intrinsically fluorescent semiconductor quantum dots [10,34,35] and noble metal nanoparticles [11,36]. Nanoparticle labels possess certain advantages over traditional molecular probes. Nanoparticle labels are often less cytotoxic and highly photostable, unlike molecular fluorophores. Binding a molecular fluorophore with a protein can cause change in the optical properties of both. Most of the dye labeled nanoparticles or the intrinsically fluorescent nanoparticles are generally inert and do not interact with the biological protein or specimen. Most importantly the optical properties of the nanoparticles are not affected by the binding biomolecular specimen. Depending upon the charge of the nanoparticles it can be easily internalized into cells and can attach with the desired structure of the cells. Nanoparticle labels can be used for fluorescence image and targeted image analysis. However, the nanoparticle labels have not become popular due to their weak fluorescence and blinking effects.

Another very important recent development, is the detection of gold nanoparticles with photothermal microscopy, [13,14,16,37] from the point of application as biological labels. Photothermal microscopy is a pump probe microscopy which is free from photobleaching and blinking and can be used to collect images for longer duration without any degradation in the signal. In the following section, we will discuss in detail about the photothermal microscopy and their applications.

1.5.3 Photothermal microscope

Nanoparticles are a potential alternative to conventional dye labels in biomolecular imaging. Fluorescence from the nanoparticles is negligible and most nanoparticles are not suitable for fluorescence imaging. Conventional optical microscope makes use of the scattered light from the sample or the structures inside the sample to form an image of the specimen. According to Mie theory, the scattering cross section of a spherical particle whose radius R is much smaller than the wavelength of light decreases as R^6 while absorption decreases only as R^3. As a result, for smaller particles absorption based detection methods are more sensitive compared to scattering based techniques. Considering the drawback of fluorescent probes, the absorption based detection of non-luminescent nano size particles become promising. Upon optical excitation of a non-luminescent particle, most of the absorbed energy is transferred to the lattice through nonradiative relaxation process and thus causes a temperature change in the nanoparticle and its immediate surroundings. This change can be detected using an appropriate sensor or a second probe beam. This method of detection of nano size objects, generally termed photothermal detection, is free from photobleaching or blinking effects.

Photothermal microscopy is a pump probe detection technique. Pump beam or the excitation beam is selected in the resonance absorption band of the target molecule/nanoparticle. The nanoparticle is excited with the modulated pump beam. The energy absorbed by the nanoparticle is released locally as thermal energy. Since the pump beam generates thermal energy it is also called as the heating beam. Due to the resonance absorption of the modulated pump beam, the nanoparticles act as point heat sources with a modulation frequency of the pump beam. The locally released heat generates changes in the refractive index of the surroundings which varies with the modulation frequency. A probe beam is scattered due to change in refractive index. The probe is filtered at the modulation frequency by using a lock-in amplifier and is used to obtain the image of the nanoparticle. Normally Acousto Optic Modulator (AOM) is used to modulate the pump beam and a lock-in amplifier is used to filter the probe beam.

Detection of gold nanoparticles using photothermal microscopy has been reported recently [13,14,16,37]. Berciaud *et al.* have succeeded in the detection of a gold nanoparticle of size as small as 1.4 nm with photothermal heterodyne imaging [37]. Mostafa A. El-Sayed *et al.* successfully implemented cancer cell imaging and selective photothermal cancer therapy using

gold nanorod in in-vitro conditions [15]. This method of detection of gold nanoparticles is free from photobleaching and high signal to noise ratio (SNR) images can be acquired at fast timescales suitable for biological imaging. These studies show that photothermal effect based microscopy has a high potential to be a viable alternative to confocal fluorescence microscopy. However, the photothermal microscopy of gold nanoparticles reported so far relies on linear optical absorption and makes use of a continuous wave (CW) laser as pump beam. Hence the technique is not inherently confocal and usage of gold nanoparticles as label necessitates the use of visible light having wavelength around 500 nm as the pump beam. This wavelength is not ideal for biomolecular imaging, especially in an experiment that involves deep tissue imaging considering the absorption in biological tissues, which ranges from 350 nm to 650 nm. Further, the CW excitation can result in heating up of the sample even at low powers reducing the viability of the technique in many systems.

Thus, it would be better if we can have an appropriate photostable and biocompatible label that can be detected and imaged using infrared excitation. A two-photon excited photothermal microscopy, for example, would retain all the advantages of photothermal technique and nonlinear microscopy such as inherent confocality. Another potential candidate for biomolecular imaging is $BaTiO_3$ nanoparticles. In the present work, we explore the potential of $BaTiO_3$ nanoparticles, a widely popular dielectric nanoparticle having high nonlinear optical susceptibilities as a biomolecular label. We employ a two-photon absorption induced photothermal effect for detection of the nanoparticle. In the following section, we give a detailed review of the existing literature on $BaTiO_3$ and discuss its viability as a biomarker.

1.6 Barium Titanate (BaTiO₃)

Barium Titanate ($BaTiO_3$) is a well-known dielectric material having high melting point, low thermal expansion, and good chemical resistance. Ever since its first discovery by Wainer and Solomon during the second world war as a potential replacement for oxide dielectrics, $BaTiO_3$ has attracted huge interest because of its unique characteristics. Its high dielectric constant, low dielectric loss and chemical stability make it an ideal candidate for capacitors in electrical and electronics industry. $BaTiO_3$ is a sought after ferroelectric material, and its photorefractive and piezoelectric properties are used in different applications. During the last couple of decades, the bulk properties of $BaTiO_3$ are well studied and different groups have engineered its structure to

suit specific applications [38–42]. BaTiO$_3$ exists as white powders and transparent crystals. The structure of BaTiO$_3$ comes in the perovskite family with a chemical formula of the form *ABO$_3$*. The perovskite structure of BaTiO$_3$ is shown in figure 1.10. Perovskites exhibit unique material properties that have potential applications in various scientific fields. In particular, applications of both bulk and nanoparticle forms of BaTiO$_3$ have been demonstrated in fields such as high density optical data storage, in phase conjugate mirrors and lasers, nonlinear optical devices, optical computing, optical image processing, piezoelectric devices, pyroelectric sensors, semi-conductive ceramics varistors, electro-optic devices, holography, dielectric amplifiers, nano transducers, micro capacitors, nanoscale electronic devices, detectors, capacitors, positive temperature coefficient thermistors, multilayer ceramic capacitors, and sensors [12,38,39,41–54].

The property of perovskite structures to accommodate a large number of dopants is used for varying BaTiO$_3$ properties by doping with different materials of interest. The dielectric constant of BaTiO$_3$ is related to its ferroelectric properties which depend on the crystal structure, morphological parameters and the nature of doping material. The changes in the properties of BaTiO$_3$ due to doping with different rare earth metals such as Lanthanum, Erbium, Samarium, Neodymium, and Cerium are studied by different groups [55–61]. The doping results in a shift in Curie temperature, the phase transition temperature corresponding to the transition from ferroelectric phase to paraelectric phase of BaTiO$_3$.

In the last few decades, several new methods of the synthesis of BaTiO$_3$ have been developed. Some of the commonly used methods for the preparation of BaTiO$_3$ are solid state reaction method, hydrothermal method [62–65], sol-gel processing [66–69], spray pyrolysis [70] and polymeric precursor method . Large scale synthesis of BaTiO$_3$ mostly uses solid-state reaction method which is a low-cost method. One disadvantage of this method is the high temperature calcinations required for forming BaTiO$_3$. Further, in this method, subsequent processing is needed to form smaller size particle of BaTiO$_3$ from aggregates.

Depending upon the final application various methods are developed for the synthesis of BaTiO$_3$ nanoparticles. These include the popular hydrothermal method, solvothermal method and sol-gel preparation method. Different groups have successfully employed a hydrothermal method for the synthesis of BaTiO$_3$ nanoparticles [62–65,71,72]. M. L. Moreira *et al.* have tried a new approach,

hydrothermal microwave method for the synthesis of BaTiO₃ nanoparticles [73]. Solvothermal method is used for the preparation of BaTiO₃ nanoparticles by a few groups [74,75]. The sol-gel method is also a popular method employed [66–69,76]. Stephen O'Brien *et al.* synthesized BaTiO₃ nanoparticles of size varying from 6 nm to 12 nm by sol-gel method [77]. Co-precipitation from solution, [78–81], catecholate process [82], combined solid-state polymerization and pyrolysis [83], spray pyrolysis [70], chemical vapor method [84] and combination of above methods [85–89] are some of the other methods employed for the synthesis of BaTiO₃ nanoparticles. Room temperature biosynthesis method is also used in BaTiO₃ nanoparticle preparation [90]. The recent surge in the interest of BaTiO₃ nanoparticles is primarily due to its applications in nanoelectronic devices and biomolecular imaging. Though very many methods were developed, synthesis of monodisperse BaTiO₃ nanoparticles with controlled size are still a challenge to be achieved in material chemistry.
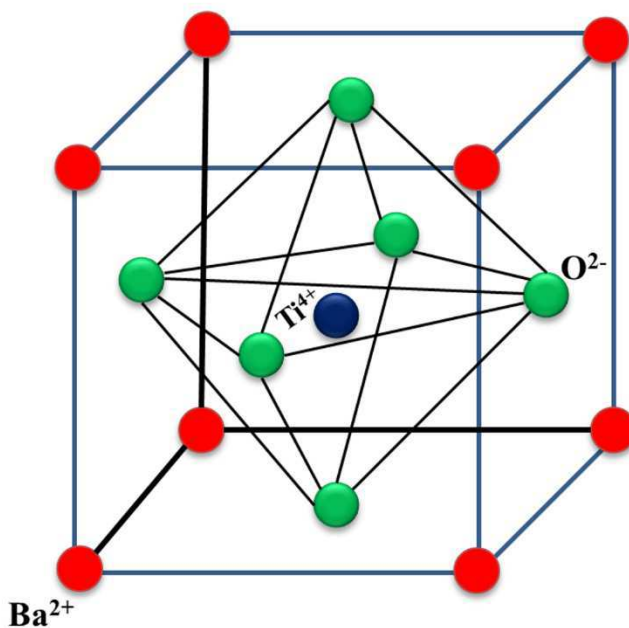
Fig.1.10: Perovskite structure of BaTiO₃

Biomedical and biomolecular imaging is another recent promising area of application of BaTiO₃ nanoparticles. The desired criteria for a good biomarker are biocompatibility, bioconjugation, specific selectivity of the target molecules, chemical stability, photostability and high signal response to the imaging technique in the desired wavelength suitable for imaging. BaTiO₃ nanoparticles satisfy most of the desired properties of biomarkers. This surged the number of studies carried out on BaTiO₃ nanoparticles as a biomarkers [43,44,91–95]. BaTiO₃ nanoparticles

can be easily conjugated with biomolecules of interest and its potential as nanocarriers for drug delivery is being explored seriously [28,91,93,95]. $BaTiO_3$ nanoparticles exhibit large nonlinear optical susceptibilities near infrared region which can be utilized for different nonlinear imaging techniques such as second harmonic generation imaging, third harmonic generation imaging and two-photon absorption based imaging. Studies have been reported on the use of $BaTiO_3$ as nanoprobes in second harmonic generation imaging technique [93,96–99].

Ciofani *et al.* have studied the cell internalization of $BaTiO_3$ nanoparticles and its biocompatibility by using both quantitative and qualitative assays [92]. Christopher Dempsey *et al.* studied the cellular uptake of $BaTiO_3$ nanoparticles and employed surface coating with polyethylenimine to improve the cellular uptake [100]. They have achieved an improved gene delivery with polyethyleneimine coated $BaTiO_3$ nanoparticles conjugated DNA. Bagchi A *et al.* successfully employed ceramic nanoparticles ($BaTiO_3$, $CaTiO_3$, $SrTiO_3$) nanoparticles in polymer composites for bone tissue regeneration. Addition of ceramic nanoparticles enhanced the mechanical properties such as tensile strength and modulus of the composite which is a desired property in bone tissue engineering [101]. Ball *et al.* have tested the biocompatibility of porous $BaTiO_3$ micrometer sized particle and their application in orthopedic tissue engineering [102]. Ciofani *et al.* suggested the use of $BaTiO_3$ nanoparticles for cancer therapy [91,103]. They have shown the efficiency of the chemotherapy drug, doxorubicin increases with the addition of $BaTiO_3$ nanoparticles to it. Hsieh *et al.* have performed specific labeling of $BaTiO_3$ nanocrystals by surface functionalization and bioconjugation of immunoglobulin G antibody for second harmonic imaging [93]. This provides a promising method of imaging membrane proteins of live biological cells *in vitro*. Farrokh Takin *et al.* proposed a promising application of Barium titanate core-gold shell nanoparticles as a photothermal agent for hyperthermia (thermal therapy) treatment against cancer cells [104]. Jelena Cˇulic´-Viskota *et al.* used $BaTiO_3$ as photostable SHG nanoprobe for long-term in vivo imaging in living zebrafish embryos [96]. Hsieh *et al.* demonstrated imaging through turbid media by using $BaTiO_3$ nanoparticles as second harmonic imaging with the help of digital phase conjugation microscopy [97]. Rachel Grange *et al.* successfully demonstrated the use of $BaTiO_3$ as a biomarker in living tissues [98]. They have detected the $BaTiO_3$ biomarker through a thickness of 50 μm and 120 μm by using second harmonic generation signal from $BaTiO_3$. Ye Pu *et al.* have developed a new holographic principle for imaging, named harmonic holography [105]. In this method, the digital hologram is made by using the coherent second harmonic signal from

an ensemble of $BaTiO_3$ nanocrystals and frequency doubled reference beam. Eugene Kim *et al.* have investigated the second harmonic signal from single $BaTiO_3$ nanoparticles down to 22 nm particle size and imaged it [106]. Ronan Le Dantec *et al.* have used Hyper-Rayleigh Scattering (HRS) combined with dynamic light scattering to find hyperpolarizabilities and nonlinear coefficients of the material [107]. They have used a second harmonic generation microscopy to image individual nanoparticles and further studied the second harmonic signal as a function of incident light polarization.

Ramakanth *et al.* have studied the magnetic and nonlinear optical properties of $BaTiO_3$ nanoparticles [108]. Ganeev *et al.* have studied the third order and higher order nonlinear optical properties of $BaTiO_3$ nanoparticles dispersed in ethylene glycol [109]. Enhancement of third-order nonlinear optical properties of $BaTiO_3$ nanoparticles and films with different dopants are studied by different groups. Nonlinear absorption coefficient (α_2) and nonlinear refractive index (n_2) of $BaTiO_3$ films doped with cerium [57,110], rhodium [111,112], silver [113–115], gold [116–122] and iron [123,124] are studied and most of these studies have found an increase in the nonlinear optical coefficients compared to pure $BaTiO_3$. This is generally assigned to the localized electric field of the dopants which can change the nonlinear response of the material. However the mechanism of nonlinearity in nanoparticle and its size dependence is still not well understood.

Apart from the above detailed, $BaTiO_3$ nanoparticles have found applications in many other related fields. Zhibo Yan *et al.* have studied the possibility of high-performance programmable memory devices based on copper doped $BaTiO_3$ nanoparticle [45]. Schlag *et al.* have studied the size driven phase transition in $BaTiO_3$ [125]. Holtmann *et al.* demonstrated the light induced photovoltaic effects in $BaTiO_3$ for the recording of holography [46]. Yanyan Fan has studied the enhanced dielectric properties of core–shell structured biopolymer doped $BaTiO_3$ nanoparticles and suggested their application in energy storage [47].

In summary, the properties of $BaTiO_3$ bulk and nanoparticles and their composites have found applications in different fields as follows. Ferroelectric properties found application in computer information storage or memory devices [38,45,48,126]. High dielectric constant found applications in capacitors [41,47,49,127,128]. Piezoelectric property can be used to form different sensors such as microphones, accelerometers and hydrophones and actuators, ultrasonic

generators, resonators, filters [50]. The pyroelectric properties of $BaTiO_3$ can be utilized in making infrared detectors [51,129,130]. Electro-optic effects can be utilized in laser Q-switches, optical shutters, and integrated optical (photonic) devices. Nonlinear optical properties have found applications in laser frequency doubling, optical mixing, including four-wave mixing and holographic information storage. Medical and biomolecular imaging of $BaTiO_3$ nanoparticles is emerging area of interest.

1.7 Objectives

The main objectives of the present thesis can be summarized as:

- Size controlled synthesis and characterization of $BaTiO_3$ nanoparticles and $Au/BaTiO_3$ nanocomposite films
- Linear and nonlinear optical characterization of $BaTiO_3$ nanoparticles and $Au/BaTiO_3$ nanocomposite films
- Development of methodologies for enhancing and tuning the nonlinear optical coefficients for specific applications
- Development of alternate imaging techniques such as photothermal microscopy which are useful for biomolecular imaging as well as for characterization of nanocomposite films
- Development of nonlinear optical microscopic techniques by making use of the large third order optical nonlinearity of $BaTiO_3$ nanoparticles.
- Detection and imaging of single $BaTiO_3$ nanoparticles using nonlinear optical microscopy.
- Exploring the potential of $BaTiO_3$ nanoparticle as a biomarker in nonlinear optical microscopy.

1.8 Organization/ Thesis Outline

The thesis work is organized into 7 chapters. In chapter 1 we introduce the topic of research and give a brief introduction to the nonlinear optics, present a detailed literature review on $BaTiO_3$ and discuss the objectives and scope of the work. Different optical microscopic techniques and their uses and limitations in biomolecular imaging are also discussed in the chapter 1. In chapter 2 we start with a brief review of the characterization techniques used in the present study. Then we discuss the methods employed for the synthesis of $BaTiO_3$ nanoparticles, $BaTiO_3$ thin films, and

Au/BaTiO$_3$ nanocomposite thin films. Results of the synthesis and characterization in correlation to synthesis parameters are presented. A detailed description of Z-scan technique used for nonlinear optical studies of the sample is given in chapter 3. Chapter 3 also covers the nonlinear optical studies performed on the BaTiO$_3$ nanoparticles. Chapter 4 explore the possibility of enhancing and tuning the nonlinear optical properties of Au/BaTiO$_3$ nanocomposite thin films. In chapter 5, we discuss the development of photothermal microscopy as a characterization tool for Au/BaTiO$_3$ nanocomposite films and present images of gold nanoparticles which throw light on their distribution in the film. The development of a two-photon photothermal microscope and applications of the microscope in biomolecular imaging is given in chapter 6. Summary, conclusions and future scope of research is given in chapter 7.

Chapter 2: Synthesis and characterization of BaTiO$_3$ nanoparticles and Au/BaTiO$_3$ thin films

2.1 Introduction

BaTiO$_3$ nanoparticles possess many attractive optical and dielectric properties which makes them a promising candidate material for device applications in the area of photonics and nanoelectronics [12,43,49,53,54,131–134]. In addition to this, BaTiO$_3$ nanoparticles find potential applications in different fields such as biomedical engineering and biomolecular imaging [44,91,92,94,99,135–137]. The morphological properties of BaTiO$_3$ nanoparticles depend on the synthesis methods employed. There are several different approaches available for the synthesis of BaTiO$_3$ nanoparticles apart from the traditional solid-state synthesis employed in industrial production. These include hydrothermal method [62,64,65,69,71,72,138], sol-gel processing [66–68,139], polymeric precursor method [76,140–142]. Though each of these methods have its own advantages, the synthesis of monodisperse BaTiO$_3$ nanoparticles having a desired size and shape is still a challenge. It has long been observed that the annealing temperature affects the particle size [62,63,143–146]. Different groups have made use of this synthesis parameter to control the size and shape of the particles formed [62,63,143–146]. However, so far there is no unique process identified to achieve monodisperse particles of desired size. In this work, we successfully synthesized monodisperse BaTiO$_3$ nanoparticles of varying average sizes in the size range of 12 nm to 90 nm by employing sol-gel method. We could achieve this by varying a single synthesis parameter namely, the annealing temperature, and keeping all other synthesis parameters unchanged. We are able to reproduce the results repeatedly by maintaining the same synthesis parameters. BaTiO$_3$ thin films and Au/BaTiO$_3$ composite thin films containing monodisperse particles of different concentrations are also prepared by the same method. The method of synthesis and characterization of BaTiO$_3$ nanoparticles and Au/BaTiO$_3$ nanocomposites employed in this work are detailed in this chapter. We begin the chapter, by giving a brief overview of the various sample characterization techniques employed in the study.

2.2 Overview of characterization techniques

$BaTiO_3$ nanoparticles, $BaTiO_3$ thin films, and $Au/BaTiO_3$ composite films are characterized using X-ray diffractometer, UV-VIS-NIR absorption spectrometer, scanning electron microscope, transmission electron microscope and atomic force microscope. The crystalline structure and crystallite size are studied by X-ray diffractometer. UV-VIS-NIR spectrometer is used to study the linear optical properties of the samples. Scanning electron microscope and transmission electron microscope are used to study particle size, particle size distribution, morphology and chemical nature of the molecules. Atomic force microscope is used to study the topography of the thin films. The surface quality of the film is investigated by an optical microscope.

2.2.1 X-ray Diffraction (XRD)

XRD is a powerful nondestructive technique for characterization of the crystalline materials. It can be used to find crystalline structure and crystallite size of the materials. The powder X-ray diffractometer employed by us consists of an X-ray source, a rotating sample holder and a detector. Monochromatic X-rays filtered from the X-ray source is collimated and directed towards the sample and the diffracted beam is collected by the detector. Figure 2.1 shows the schematic arrangement of X-ray diffractometer. Normally when the sample is rotated by an angle Θ, the detector is to be rotated by an angle 2Θ to measure the scattered X-rays. The diffracted intensity of X-rays from the sample as a function of angle Θ is recorded by the detector. For those angles that satisfy the Bragg's condition, constructive interference of the reflected rays from different crystal planes occur which corresponds to a peak in the diffractogram. These peaks are characteristics of the sample crystal structure and can be used to identify crystal structure of an unknown material. In our studies, we used a Rigaku Miniflex II Desktop X-ray Diffractometer using Copper K_α radiation operated at 30 kV and 15 mA.

In the Bragg's condition for constructive interference, we assume that the crystal is having infinite dimensions. But in the actual experimental situation, the crystal size is finite, and this can lead to imperfections in the obtained diffraction peaks. A finite number of crystal planes involved in the diffraction process leads to a reduction in the peak height and thus broadening of the diffraction peaks. Thus, the grain size, or the crystallite size can be found from the width of the XRD peaks.

According to Scherrer equation the mean crystallite size is given by, $d = \frac{K\lambda}{\beta cos\Theta}$ where λ is the wavelength of X-ray radiation used, β is the full width at half the maximum (FWHM) of the diffraction peak in radians and Θ is the Bragg's angle corresponding to the diffraction peak. K is a dimensionless shape factor. Normally for spherically shaped particles K is taken as 0.94. There are several other factors such as monochromaticity of the incident X-rays, crystal lattice distortions such as stress and strain of the sample and other instrumental effects that can produce broadening of the diffraction peaks but are normally small compared to size effect.
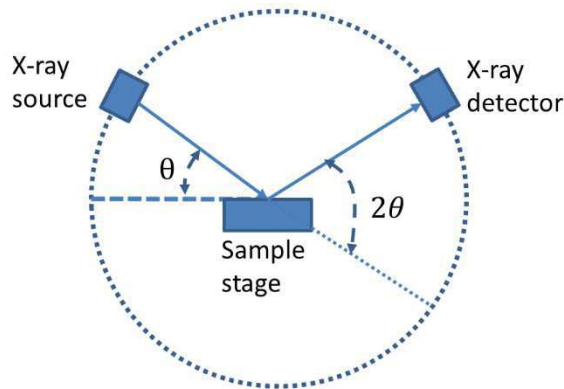
Fig. 2.1: Schematic of X-ray diffractometer

2.2.2 UV-VIS-NIR absorption spectroscopy

UV-VIS-NIR absorption spectroscopy is used to study the linear optical absorption properties of materials in the ultraviolet, visible and near infrared radiation of the electromagnetic spectrum. When a radiation of particular frequency with intensity I_o is incident on the sample of thickness, t, then the transmitted light, I can be written as,

$$I = I_o e^{-\alpha t} \tag{2.1}$$

where α is the absorption coefficient of the material. Absorption coefficient gives a measure of distance up to which radiation having a particular wavelength can penetrate inside the material before it is absorbed completely.

The transmittance,

$$T = \frac{I}{I_0} \tag{2.2}$$

The measure of the light absorbed by the material is given by the absorbance, A of the material. Absorbance can be written as

$$A = 1 - T = 1 - \frac{I}{I_0} \tag{2.3}$$

and absorption coefficient α is,

$$\alpha = \frac{-\ln(A)}{t} \tag{2.4}$$

where ln denotes natural logarithm.
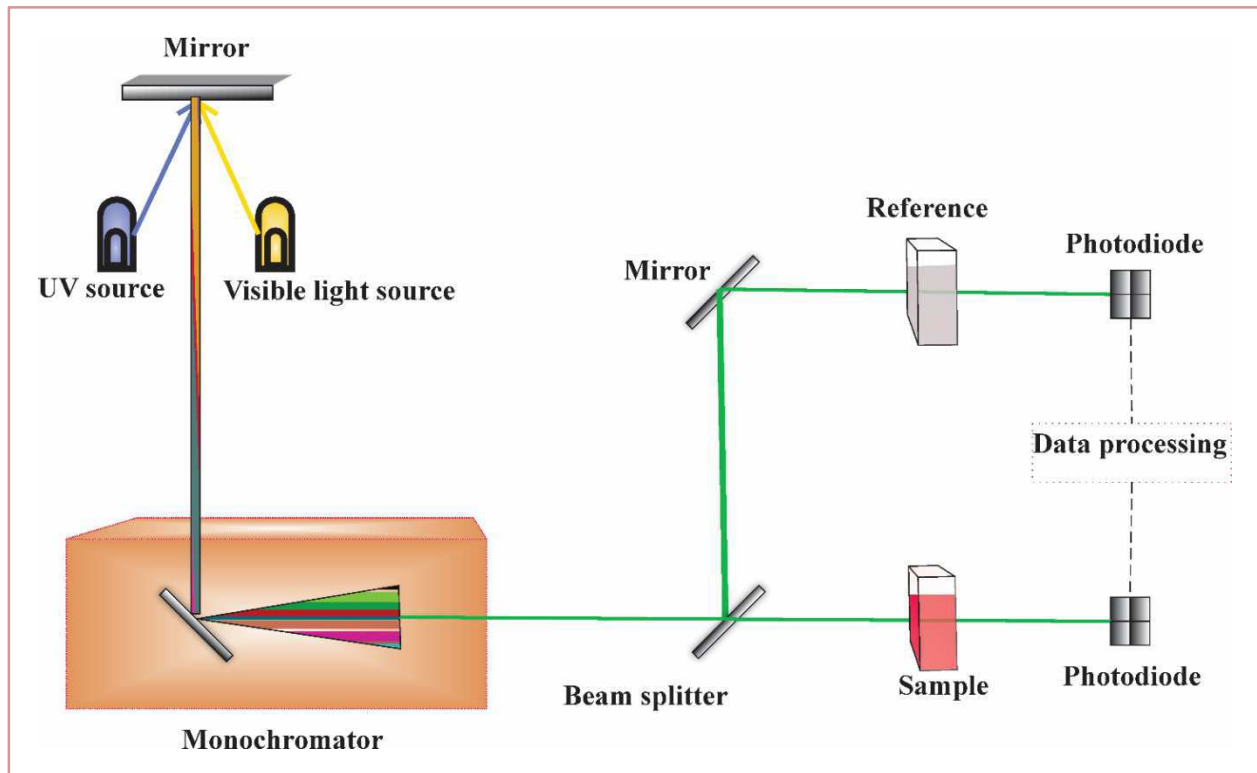
Fig. 2.2: The schematic of UV-VIS-NIR absorption spectrometer.

A broadband light source is used in UV-VIS-NIR absorption spectrometer and a grating is used to select the desired wavelength of light. A particular wavelength of known intensity is passed through the sample of known thickness and the transmitted/reflected radiation intensity is measured. The absorbance measured is plotted against the wavelength of light used to give the absorption spectrum of the sample. The absorption spectrum can be used to study the absorption coefficient as a function of wavelength and thus to determine the band gap of the materials. A Tauc plot, which is a plot of $(\alpha h v)^2$ against $h v$, where h is planks constant and v is the frequency of the

radiation, is used to find energy band gap of the material by extrapolating the absorption edge to the X (*hv*) axis. Figure 2.2 shows the schematic of an absorption spectrometer. The absorption spectra of all samples reported in this thesis are measured by UV-VIS-NIR scanning spectrometer, model JASCO V-570 UV-VIS-NIR in the 400 nm - 800 nm wavelength range.

2.2.3 Scanning Electron Microscope
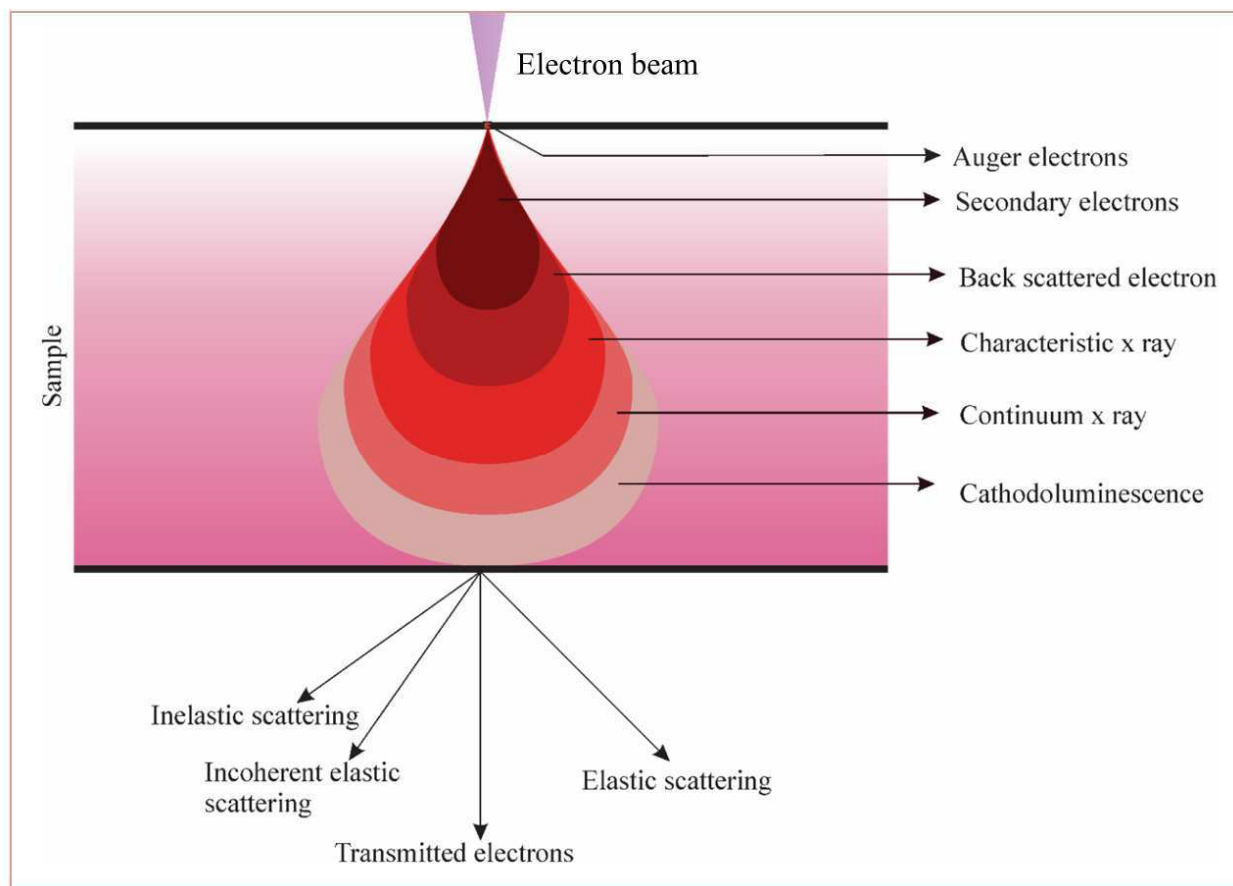
Fig. 2.3: Interaction volume of the electron beam in the sample. Various signals arising from the electron sample interaction is shown in the figure.

Scanning electron microscope (SEM) is an imaging tool having nanometer resolution which can give information about morphology, chemical composition and crystalline structure of materials. SEM consists of an electron gun source which produces high energy electron beam which is accelerated and focused on the sample using electromagnetic field and electromagnetic lenses. The beam passes through a pair of scanning coil which helps to deflect the beam in the x and y-direction

for scanning the sample. Figure 2.4(c) shows the schematic image of SEM. A number of different signals are produced due to the electron and sample interaction and they are helpful to reveal various information about the sample. The commonly used signal includes secondary electron, backscattered electron, X-rays, diffracted backscattered electron, visible light and heat. Secondary electrons are used for getting morphology and topography of the sample. Backscattered electrons are used to find chemical compositional information. X- rays are used for the elemental analysis of the sample. Diffracted backscattered electrons can also be used to examine micro fabric and crystallographic orientation in materials. Figure 2.3 shows the interaction volume of the electron with the sample and the process associated with the interaction.
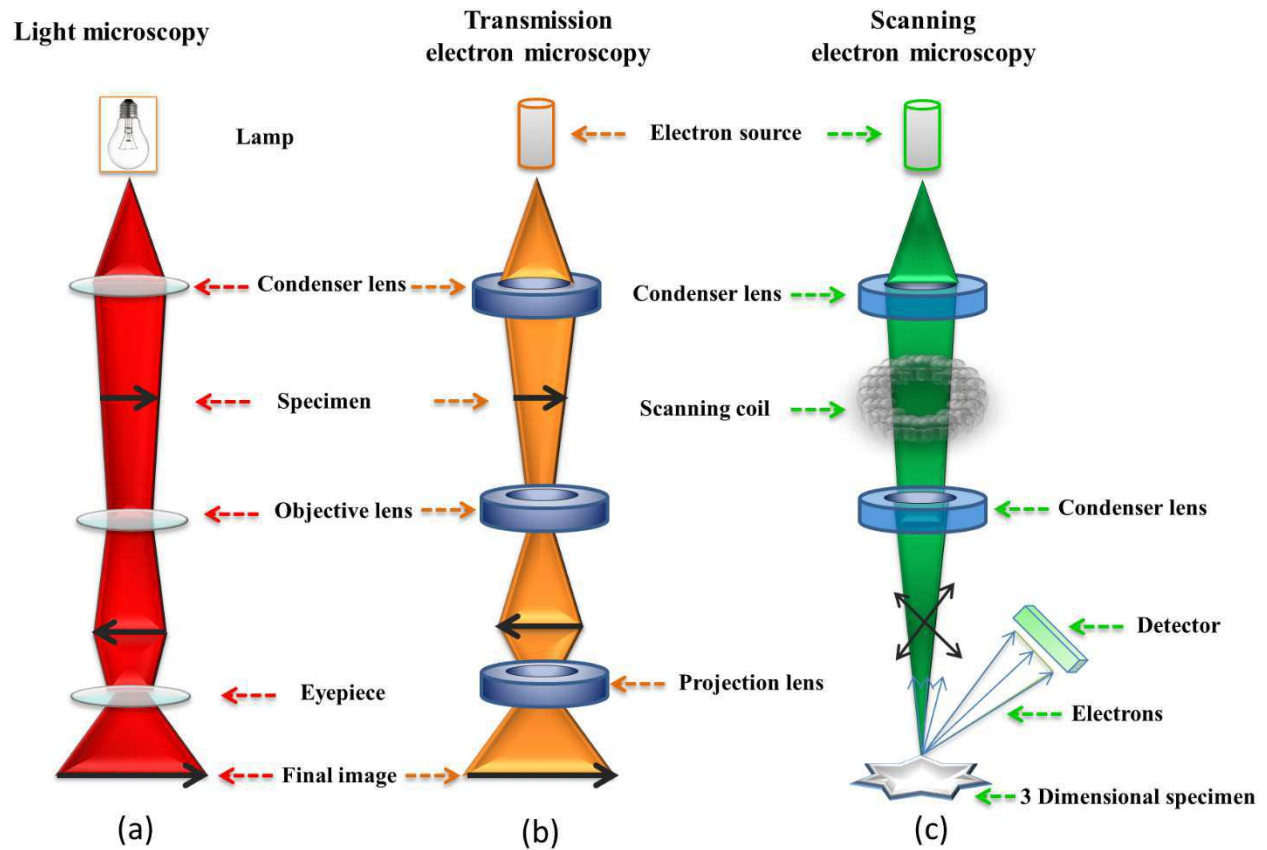
Fig. 2.4: (a) Schematic of optical microscope (b) Schematic of transmission electron microscope (c) Schematic of scanning electron microscope.

2.2.4 Transmission Electron Microscope

Transmission electron microscope (TEM) makes use of electrons transmitted through the specimen for imaging. Transmitted electrons are used in TEM to provide image contrast and resolution. TEM can be used to study morphological, compositional and crystallographic information of the sample. The electron beam is produced by an electron gun and is accelerated by applying a high voltage across the beam and then focused on the sample by electrostatic and electromagnetic lenses. Figure 2.4(b) shows a schematic of a TEM. Figure 2.3 shows the interaction volume of the electrons with the sample. Elastically scattered electrons collected are used for high-resolution imaging of electron diffraction rings from the atoms, which reveal the compositional and structural information of the sample.

2.2.5 Atomic Force Microscope

Atomic Force Microscope (AFM) is a scanning probe microscope having a resolution of the order of few angstroms. AFM makes use of a cantilever with a very sharp tip to scan the sample surface. When the sharp tip of the cantilever reaches near the sample, the interaction between the atoms in the sample and cantilever tip causes the cantilever to deflect. The deflection of the cantilever is mapped and is used to form a high resolution image of the sample. AFM is used to acquire three-dimensional topographic information of the specimen at the nanoscale. AFM can be used in contact mode, non-contact mode and tapping mode. In contact mode, the cantilever tip touches the sample while moving. This can be used for hard samples and is a destructive technique. In noncontact mode the cantilever tip goes very near to the sample but do not touch it and thus is a non-destructive imaging technique. Tapping mode is an in-between mode that gives higher resolution without damaging the sample surface. The three-dimensional topographic information on samples in our study is obtained in the tapping mode of the AFM. Figure 2.5 shows the schematic diagram of AFM.
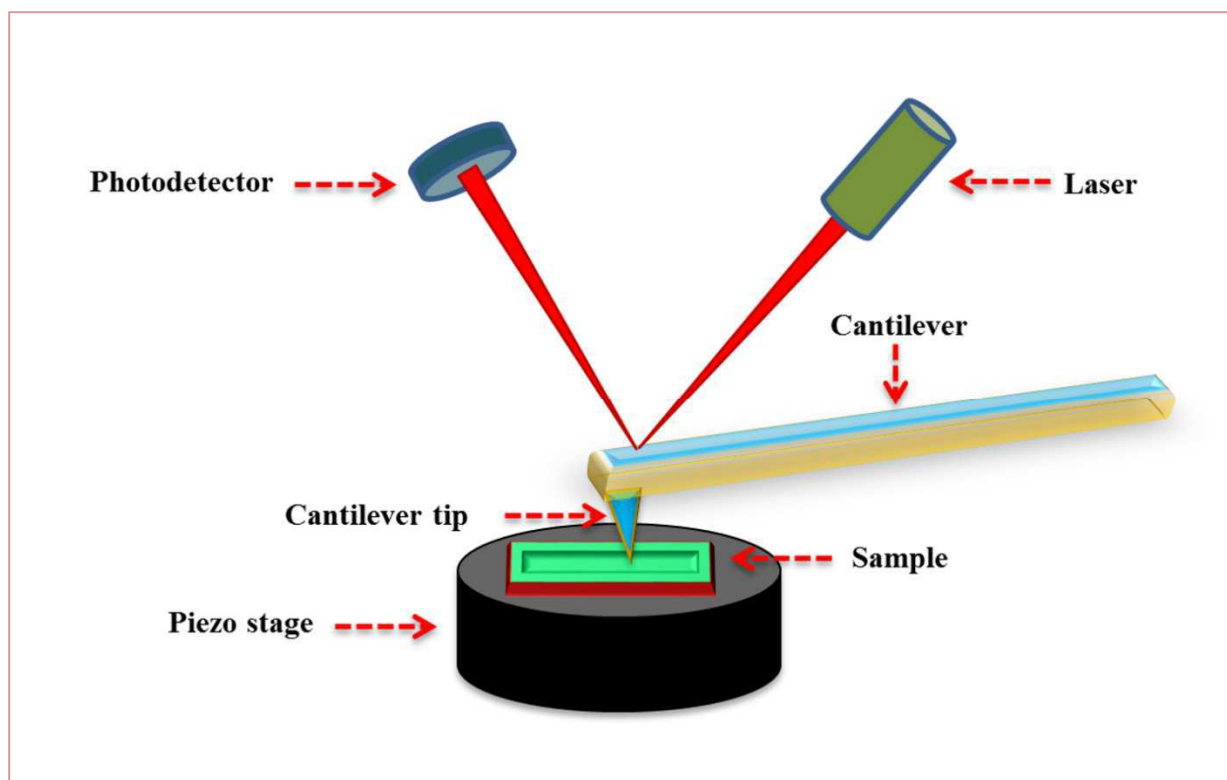
Fig. 2.5: Schematic of AFM

2.3 BaTiO₃ nanoparticle preparation

Sol-gel method is one of the well-known solution based chemical methods that is used for synthesizing BaTiO₃ nanoparticles. Sol is a stable dispersion of colloidal particles in a solvent and gel is a three-dimensional cross-linked particle in a liquid. In sol-gel method, a precursor solution is first made by adding the primary reagents into a solvent, namely sol. The sol transforms into a gel in a gelation process. Finally, the crystallographic transformation of the compound is accomplished by heat treating at high temperatures. The homogeneity of the precursor solution ensures the phase purity and homogeneity of the compound prepared [66,68]. Additionally, the sol-gel method is environmental friendly and cost effective. In the present work BaTiO₃ nanoparticles and BaTiO₃ thin films are prepared by sol-gel technique. A flow chat of the method employed for the synthesis of BaTiO₃ nanoparticles are given in the figure 2.6. Barium Acetate and Titanium Butoxide are used as the primary reagents for the preparation of BaTiO₃ nanoparticles. We have used high purity analytical reagent (AR) grade barium acetate and titanium butoxide for the synthesis. The chemicals used for synthesis, their analytical grade, and the brand

are given in table 2.1. The BaTiO₃ nanoparticles are prepared in three steps. First, a precursor solution of the BaTiO₃ is formed by mixing the reagents. The solution is then dried using the evaporation method. In the third step, the solid obtained by the drying process is annealed at high temperatures to form BaTiO₃ nanoparticles.
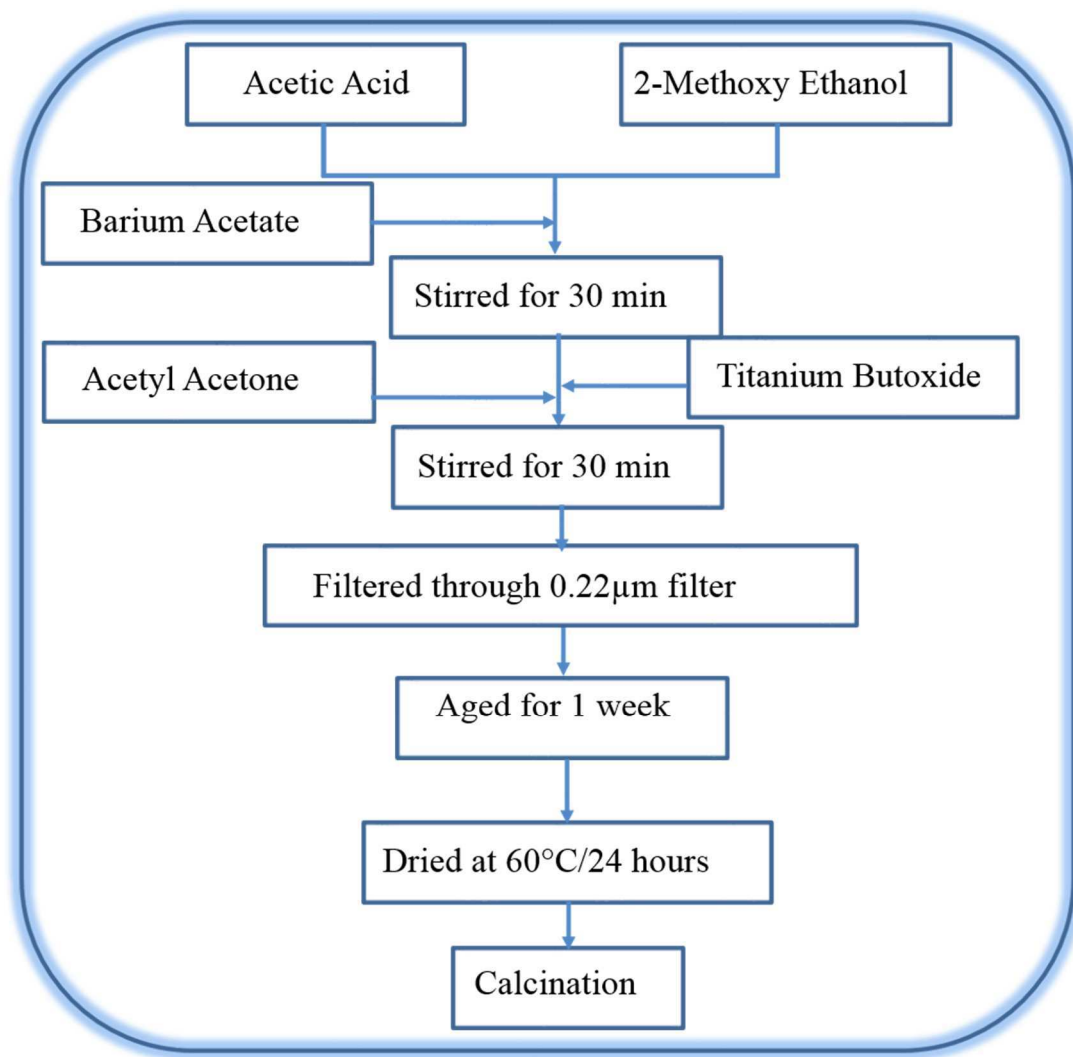
Fig. 2.6: Flow chart for the preparation of BaTiO₃ nanoparticles.

2.3.1 Preparation of BaTiO₃ precursor solution

An aqueous solution of acetic acid and 2-methoxy ethanol is first prepared by mixing them at room temperature. 10 ml of acetic acid and 10 ml of 2-methoxy ethanol are added in a beaker and stirred using a magnetic stirrer to mix them properly. 2.55 g Barium Acetate [Ba(CH₃COO)₂] (10 mmol)

is added to the stirring aqueous solution. The solution is stirred for 30 minutes at room temperature. After mixing them properly an appropriate amount of acetylacetone is added to stabilize the solution. The acetylacetone is added in drops till a change in the color of the solution from yellow to reddish yellow, indicating the formation of Barium sol, is observed. After stabilizing the solution, 3.4 ml of Titanium butoxide is added to the solution and stirred for another 30 min. Finally, the solution is filtered through 0.22 µm filter paper to remove any solidified impurities and then aged for one week. The solution is transferred into a covered petridish and kept inside an oven for drying. The drying is carried out at 60 ℃ and it takes 24-48 hours for complete drying.

Chemical	Company name	Grade
Barium Acetate	S D Fine Chemical Limited	AR
Acetic Acid	Sigma Aldrich	Technical Grade
2-Methoxy Ethanol	BASF- India	AR
Acetyl Acetone	S D Fine Chemical Limited	AR
Titanium Butoxide	Sigma Aldrich	AR
Chloroauric Acid	Sigma Aldrich	Technical Grade
Trisodium Citrate	S D Fine Chemical Limited	AR
Sodium Borohydride	S D Fine Chemical Limited	AR
Ethanol	S D Fine Chemical Limited	AR

Table 2.1: Chemicals used for synthesis and their analytical grade

2.3.2 Annealing at high temperature

Fig. 2.7: Furnace used for annealing the samples.

The well-dried samples from the oven are transferred to an alumina boat and kept inside a tube furnace for annealing in nitrogen atmosphere. The annealing is carried out at a temperature above 500 ºC. Different annealing temperatures in the range 500-1000 ºC in steps of 100 ºC is tried out to make particles of different sizes. Nitrogen atmosphere is employed to eliminate carbonate impurities. The nitrogen gas is passed through silicone oil at both ends of the furnace as shown in figure 2.7. The continuous flow of nitrogen throughout the experiment is ensured by monitoring the bubbles in the silicone oil. Experiments are repeated to empirically optimize annealing temperature, annealing time and annealing cycle to get monodisperse single crystalline phase $BaTiO_3$ nanoparticles. Furnace takes 20 minutes to reach the desired annealing temperature and the annealing is carried out for 2 hours. After annealing, the sample is taken out only after the

furnace temperature has reached room temperature, which typically takes 4-5 hours. The white colored powder formed is taken out and grinded properly to form fine powders. The effect of annealing temperature on particle size, shape, and the crystal structure is studied by different characterization methods as detailed below.

2.4 Characterizations of the BaTiO$_3$ nanoparticles

2.4.1 Characterization by UV-VIS-NIR absorption spectroscopy

The absorption spectrum of the BaTiO$_3$ nanoparticle is taken in the reflection mode by making use of the integrating sphere attachment of the UV-VIS-NIR spectrophotometer (JASCO V-570). The powder sample is kept inside the sample holder and pressed to form a pellet of 1 mm thickness. Figure 2.8 shows the absorption spectrum of BaTiO$_3$ nanoparticles prepared by annealing at temperatures, (a) 650 $^{\circ}$C (b) 700 $^{\circ}$C (c) 800 $^{\circ}$C (d) 900 $^{\circ}$C and (e) 1000 $^{\circ}$C respectively. The absorption spectra show an absorption edge below 400 nm wavelength. Figure 2.9 show the Tauc plot of the data. The absorption edges and the bandgap estimated from the absorption spectra and Tauc plot of the different samples is given in table 2.

Annealing temperature ($^{\circ}$C)	Band gap (eV)
650	3.31
700	3.29
800	3.26
900	3.24
1000	3.21

Table 2.2: Absorption edge and band gap of BaTiO$_3$ nanoparticles prepared by annealing at different temperatures.
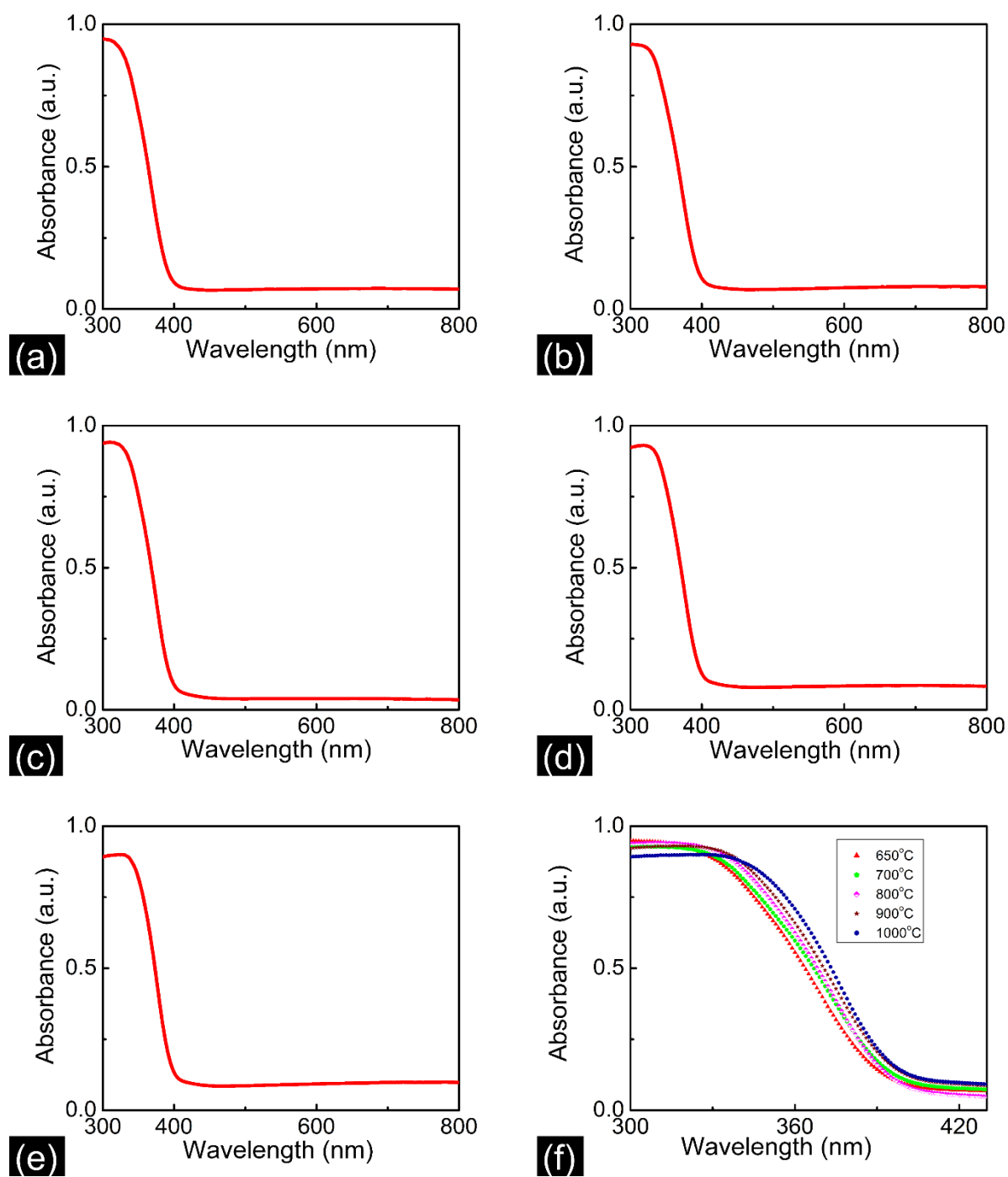
Fig. 2.8: Absorption spectrum of BaTiO$_3$ nanoparticles prepared by annealing at temperatures (a) 650 °C (b) 700 °C (c) 800 °C (d) 900 °C (e) 1000 °C. (f) Comparison of absorption edge for different heat-treated samples.
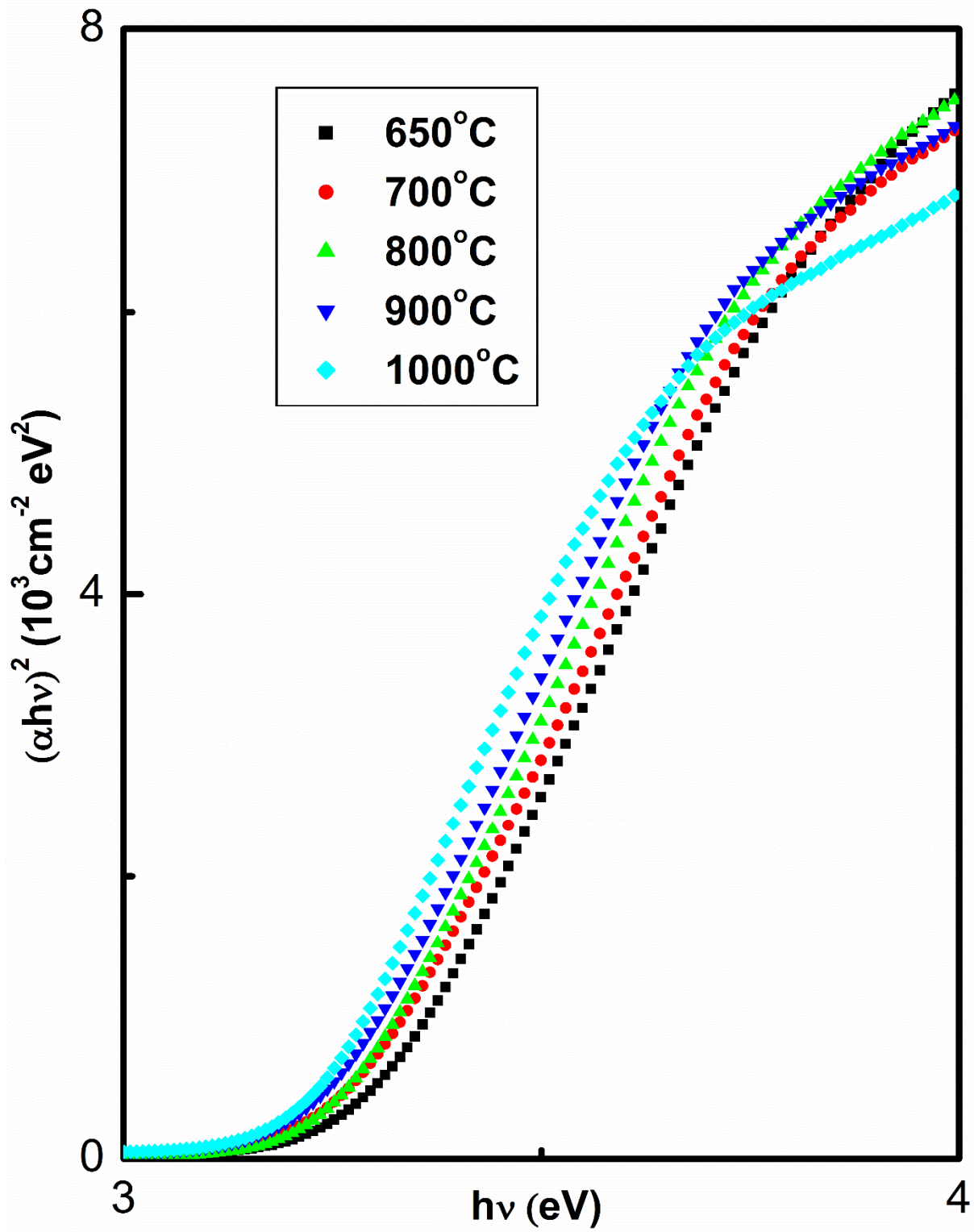
Fig. 2.9: Tauc plot for BaTiO₃ nanoparticles prepared by different annealing temperatures.

2.4.2 Characterization of BaTiO₃ nanoparticles by X-ray diffraction

The crystal structure of the $BaTiO_3$ nanoparticles synthesized is analyzed by X-ray diffraction. For the XRD analysis, fine powder of $BaTiO_3$ nanoparticles synthesized is added into a 0.5 mm deep well sample holder. The upper surface is levelled by pressing the powder with a glass plate and excess powder around the well is cleaned off. The XRD is recorded for the detector angles, 2Θ varying from 20° to 80°. The scanning speed is set at 2° per minute and total scanning time is 30 minutes. The X-ray source used is Cu. Anode voltage and anode emission current are set at 30 kV and 15 mA respectively.

The range of annealing temperature is selected based on XRD analysis of the crystalline structure of the sample. The $BaTiO_3$ precursor powder annealed at 500 ^{o}C for 20 min is white in color and the XRD pattern shows, characteristic peaks of crystalline $BaTiO_3$ corresponding to (001), (101), (002) and (211) planes. However, these sample showed some impurity peaks also, as shown in the figure 2.10(a). Impurity peaks are also present in samples annealed for longer time duration of 2 hours (figure 2.10(b)). Hence these sample are discarded, and fresh samples are prepared at higher temperature. Based on this analysis of XRD patterns, it is observed that pure $BaTiO_3$ nanoparticles are formed at annealing temperatures in the range of 650 ^{o}C to 1000 ^{o}C and an annealing duration of 2 hours.
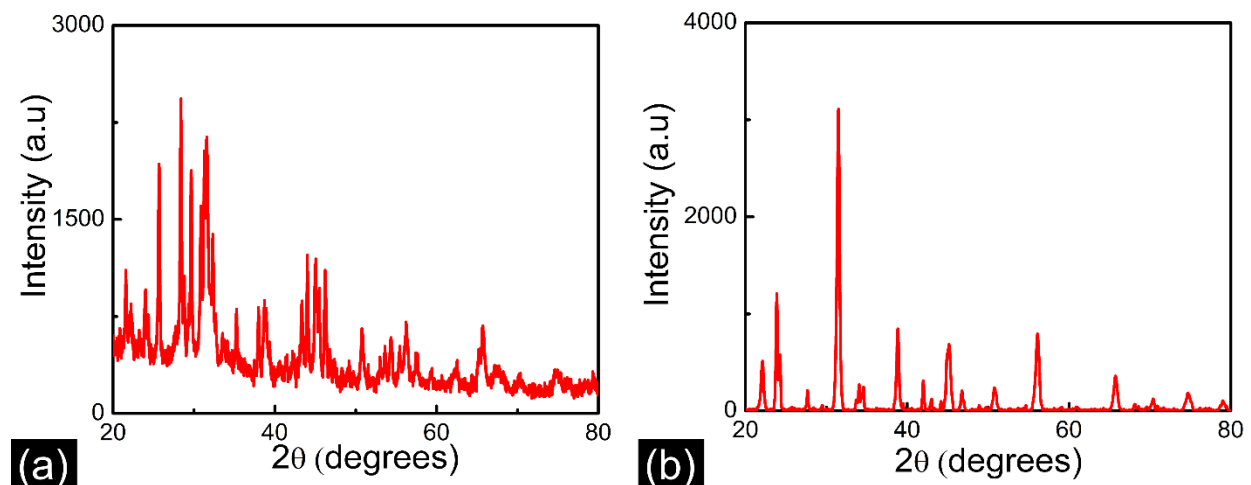
Fig. 2.10: XRD patterns of $BaTiO_3$ precursor powder annealed at (a) 500 ^{o} C for 20 minutes and (b) 500 ^{o}C for 2 hours.

Figure 2.11 shows the XRD patterns of $BaTiO_3$ nanoparticles annealed at temperatures (a) 650 °C (b) 700 °C (c) 800 °C (d) 900 °C and (e) 1000 °C. The peaks are identified and compared with the reference data from the International Centre for Diffraction Data (ICDD) catalogue. The planes (001), (101), (110), (111), (002), (200), (102), (211), (202), (212), (301) and (311), which are characteristic of tetragonal phase crystalline $BaTiO_3$, are identified and marked in the XRD pattern. The crystalline peaks were matching with the reference data from the ICDD for catalog number 72-0138. Figure 2.11(f) shows an expanded view of the 100% intensity peak at 31.5° which shows the combination of twin peaks corresponding to (101) and (110) planes at 31.5° and 31.6°. Green, red and blue line shows the corresponding Gaussian peak fit. The crystallite sizes of all samples are measured by the Scherrer formula. We have considered only the well isolated peak at 38.89° corresponding to (111) planes for the calculation of crystallite size. The crystallite sizes measured for all the $BaTiO_3$ powder samples prepared at different annealing temperature are given in the table 2.3.

Annealing temperature (°C)	Crystallite size (nm)
650	19 ± 5
700	24 ± 7
800	35 ± 8
900	46 ± 7
1000	74 ± 12

Table 2.3: The crystallite size of the $BaTiO_3$ nanoparticles measured from the XRD graphs by using Scherrer formula
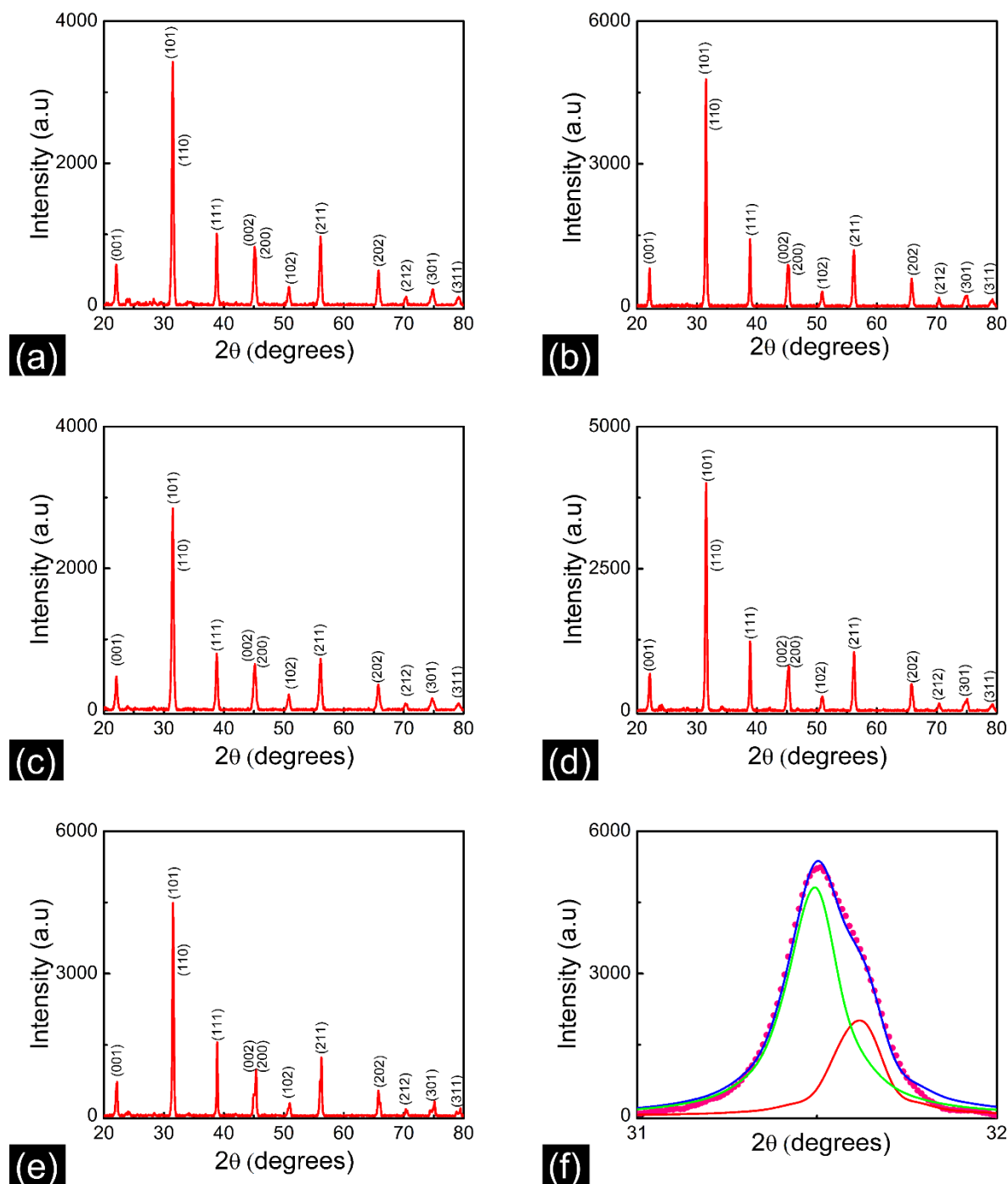
Fig. 2.11: XRD patterns of the BaTiO$_3$ nanoparticles heat treated at different temperatures. (a) 650 °C (b) 700 °C (c) 800 °C (d) 900 °C (e) 1000 °C. (f) Expanded view of the peak at 31.5° which shows the combination of twin peaks (101) and (110) at 31.5° and 31.6°. Green, red and blue line shows the corresponding Gaussian peak fit.

2.4.3 Characterization of BaTiO$_3$ nanoparticles by transmission electron microscope

TEM is used to study the morphology and crystalline structure of BaTiO$_3$ nanoparticles. Samples for TEM imaging are prepared as follows. BaTiO$_3$ nanoparticles are dispersed in ethanol to form a clear solution. To avoid the formation of aggregates, the nanoparticle dispersed solution is sonicated for 20 min at room temperature. A few microliters of solution prepared is drop cast on the copper grid. Solution drop cast copper grid is kept for drying in infrared light for 10 min and loaded in the imaging chamber of TEM. Images of dispersed nanoparticles are obtained. Figure 2.12 shows the TEM images of BaTiO$_3$ nanoparticles prepared by annealing at temperatures (a) 650 ºC (b) 700 ºC (c) 800 ºC (d) 900 ºC (e) 1000 ºC. Size of the BaTiO$_3$ nanoparticles are measured from the TEM images using ImageJ software. A size distribution histogram is plotted with the measured sizes and the average size is estimated from a Gaussian fit to the size distribution histogram. Figure 2.13 shows the size distribution histogram of BaTiO$_3$ nanoparticles prepared with annealing temperature (a) 650 ºC (b) 700 ºC (c) 800 ºC (d) 900 ºC (e) 1000 ºC. The red line shows the gaussian fit. Figure 2.13(f) shows the variation in size of BaTiO$_3$ nanoparticles with annealing temperature. The mean size of the BaTiO$_3$ nanoparticles measured from the size distribution histogram corresponding to different annealing temperature is given in table 2.4. Figure 2.14 shows the selected area electron diffraction (SAED) pattern from BaTiO$_3$ nanoparticles. The crystallographic planes corresponding to diffraction rings in the SAED pattern are identified and marked in the image. The measured interplanar distance, d from the image is compared with the standard values for tetragonal phase crystalline BaTiO$_3$ from the ICDD catalogue (Card No. 72-0138). Table 2.5 shows the comparison of theoretical d values and the d values obtained from SAED patterns.
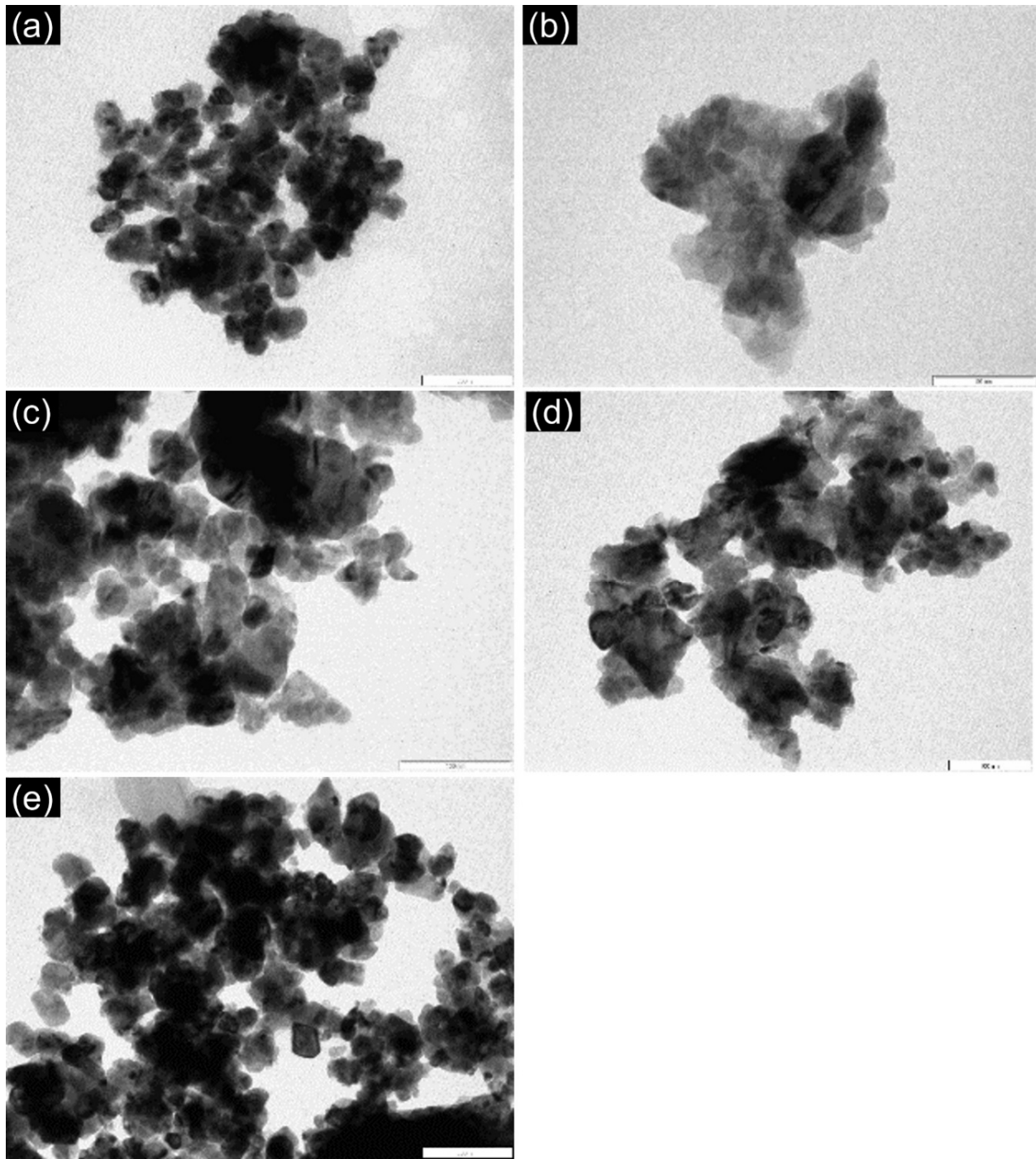
Fig. 2.12: TEM images of BaTiO$_3$ nanoparticles prepared by annealing at temperatures (a) 650 ^{o}C (b) 700 ^{o}C (c) 800 ^{o}C (d) 900 ^{o}C (e) 1000 ^{o}C.
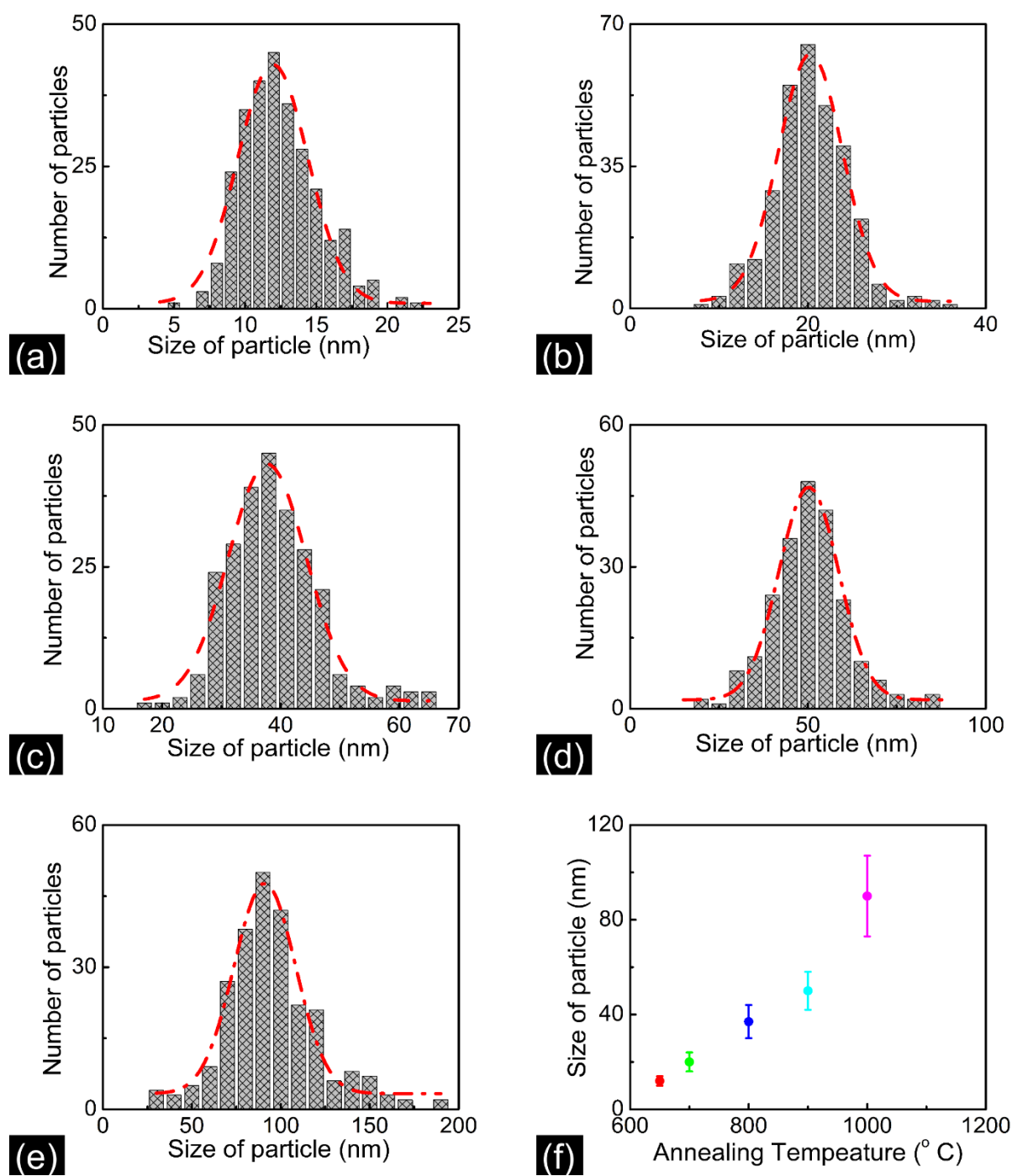
Fig.2.13: Size distribution histogram of BaTiO₃ nanoparticles prepared by annealing at temperatures (a) 650 °C (b) 700 °C (c) 800 °C (d) 900 °C and (e) 1000 °C measured from the TEM images. Red line shows the Gaussian fit. (f) Variation of size of BaTiO₃ nanoparticle with annealing temperature.

Annealing temperature (ºC)	Estimated size (nm)
650	12 ± 2
700	20 ± 4
800	37 ± 7
900	50 ± 8
1000	90 ± 17

Table 2.4: Size of $BaTiO_3$ nanoparticles estimated from the size distribution histogram plotted from TEM images.

Ring identification				
	Radius [1/nm]		d-spacing [nm]	
Plane	theor.	measured	theor.	measured
(1 1 0)	3.518	3.679	0.284	0.272
(1 1 1)	4.309	4.517	0.232	0.221
(0 0 2)	4.975	5.191	0.201	0.193
(1 1 2)	6.093	6.357	0.164	0.157
(0 0 3)	7.463	7.322	0.134	0.137
(1 1 3)	8.250	8.160	0.121	0.123
(2 0 3)	8.969	8.925	0.111	0.112

Table 2.5: Comparison of theoretical d values from the ICDD catalogue No. 72-0138 and the d-values obtained from SAED patterns.
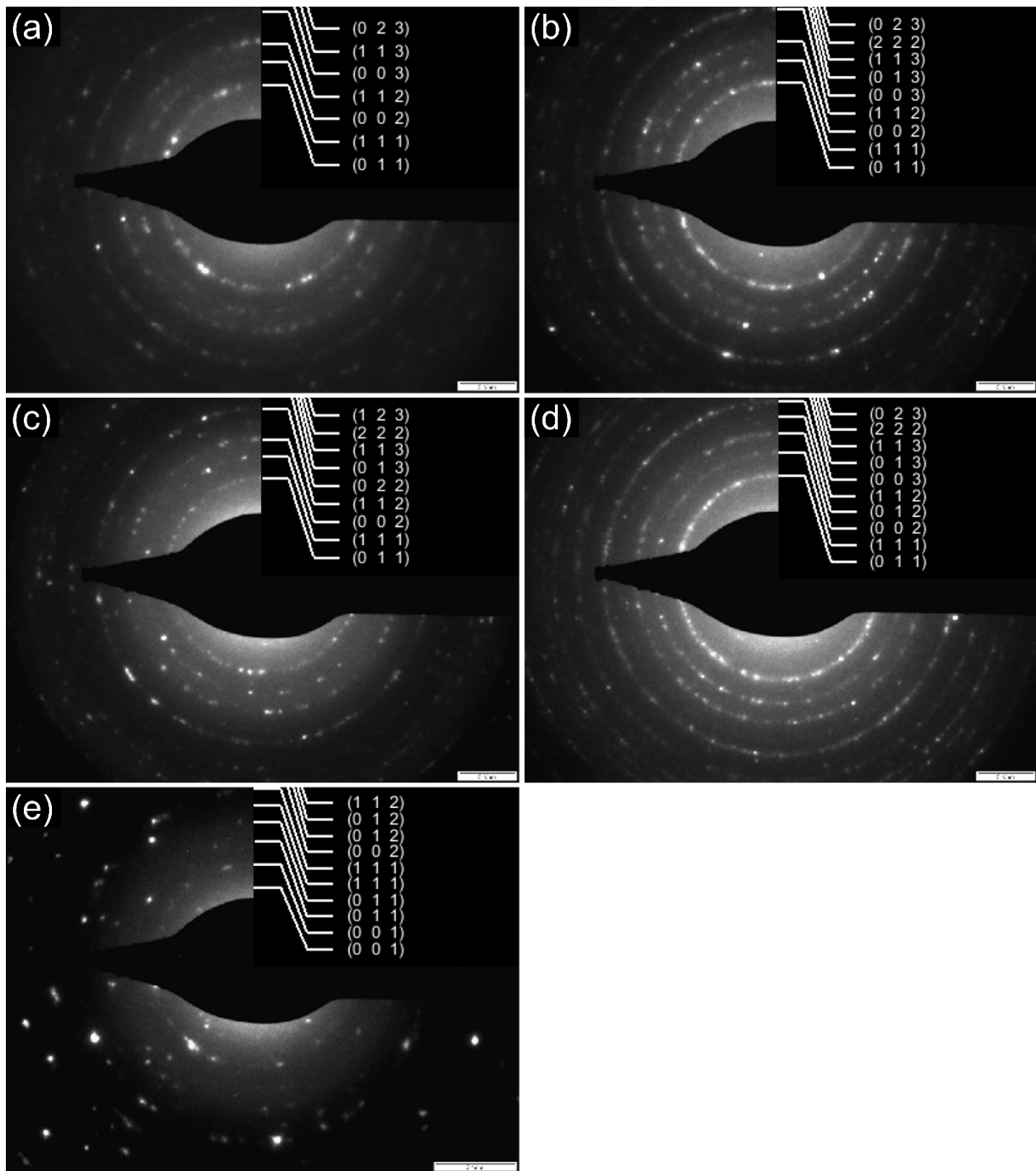
Fig. 2.14: Selected area electron diffraction pattern from the BaTiO$_3$ crystal planes prepared by annealing at temperatures (a) 650 ºC (b) 700 ºC (c) 800 ºC (d) 900 ºC (e) 1000 ºC. The inset in the figures shows the crystallographic planes identified corresponding to the rings.

2.5 Preparation of BaTiO$_3$ and Au/BaTiO$_3$ thin films.

There are several techniques available for the preparation of BaTiO$_3$ nanostructured films. Radio frequency sputtering[147,148], pulsed laser deposition [148,149], molecular beam epitaxy [150], flash evaporation technique [151,152], chemical vapor deposition [153], hydrothermal method [64,154], electrochemical technique [64], and sol-gel technique [155–158] are some of the techniques used for the preparation of BaTiO$_3$ thin. Sol-gel technique is one of the simple and cost-effective methods among them [155–157,159]. In sol-gel technique it is easy to incorporate metal or ceramic nanoparticles inside BaTiO$_3$ thin films to form nanocomposite film[160]. BaTiO$_3$ thin films can be prepared by either drop casting or spin coating the BaTiO$_3$ precursor solution on an appropriate substrate. In drop casting method, few drops of BaTiO$_3$ precursor solution is added to a cleaned quartz slide. Due to gravity, the solution spreads on the quartz slide and gets dried in about 48 hours at room temperature. After drying the films are annealed at 800 ^{o}C for 2 hours. However, the films prepared by drop casting method shows poor surface uniformity. Moreover there is no proper method for controlling the thickness of the sample in this method. Hence in this work we have used spin coating method for preparing the films. BaTiO$_3$ thin films are prepared from the BaTiO$_3$ precursor solution by spin coating on a quartz substrate and subsequent annealing at 800 ^{o}C. The microscopic quartz slides are cleaned in potassium dichromate solution and washed in running water followed by distilled water and dried. Importantly soap solution is not used to avoid the formation of soap films on the substrate surface.

2.5.1 Preparation of BaTiO$_3$ thin films

Preparation of BaTiO$_3$ precursor solution is discussed in detail in section 2.3.1. The stabilizing agent acetylacetone is used to control the viscosity of the precursor solution which is useful in controlling the thickness of the films formed. Spin coating is done by HO-TH-05 (Holmarc) model spin coating unit. In the spin coating method, the substrate is held tightly inside the spin coater by creating a vacuum in between the substrate and the holder. 1 to 2 ml of BaTiO$_3$ precursor solution is dropped on the quartz slide and thin films coated by spinning the slide at high rotation per minute (rpm). The spin speed and time are optimized by trial and error to obtain films of desired thickness. Thus, optimized spin speed of 2000 rpm and 60 s spin time is used to prepare all the samples reported in this thesis. The films formed by spin coating of BaTiO$_3$ precursor solution on quartz

slide is dried in an oven at 60 ^{0}C for 10 minutes. The BaTiO$_3$ precursor films formed are then annealed at 800 ^{o}C for 2 hours to obtain thin transparent films of BaTiO$_3$ nanoparticles.

2.5.2 Preparation and characterization of gold colloids
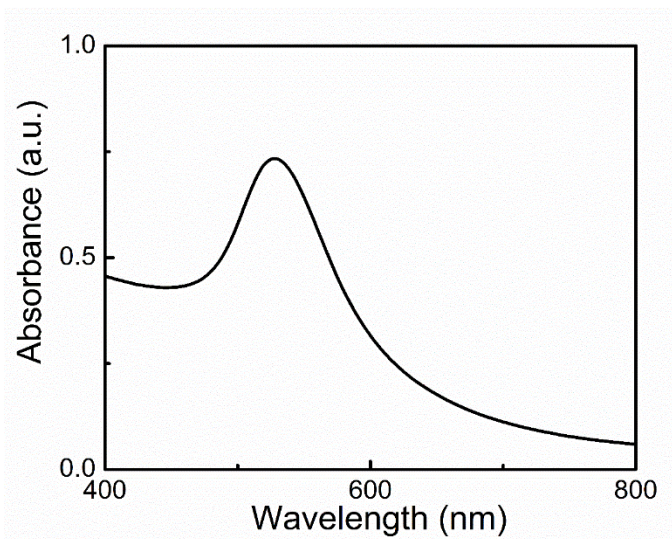
Fig. 2.15: Absorption spectra of gold nanoparticles prepared by NaBH$_4$ reduction method. The absorption peak is found at 530 nm.
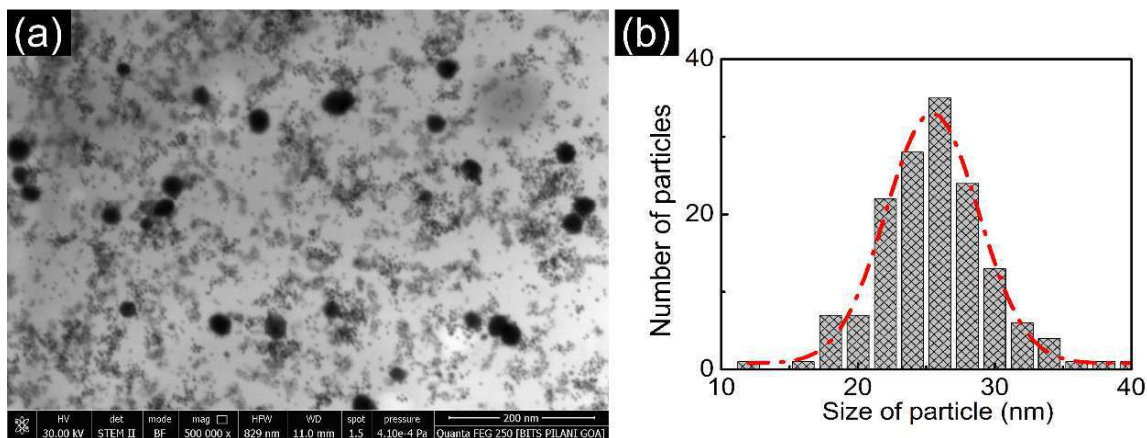
Fig. 2.16: (a) SEM image of the gold nanoparticle prepared by NaBH$_4$ reduction method. (b) The particle size distribution measured from SEM image. The red line indicates the Gaussian fit. The particle size measured is 25 ± 4 nm.

Gold colloids are prepared by NaBH$_4$ reduction method. 4 ml of 24.3 mM chloroauric acid in ethanol solution is added to 100 ml of 1.0 mM trisodium citrate in water. Trisodium citrate acts as a stabilizing chemical reagent for gold nanoparticles and could prevent the gold nanoparticles from growing and aggregating. 1 ml solution of 0.2 M NaBH$_4$ in water solution is then added to the mixed solution and the color of the solution turned from a dark purplish-red to blackish-red color quickly indicating the formation of gold nanoparticles. The solution is concentrated to 20 ml under vacuum. The gold nanoparticles so prepared are characterized by UV-VIS-NIR absorption spectroscopy and SEM. Figure 2.15 shows the absorption spectra of gold nanoparticles prepared by NaBH$_4$ reduction method. The gold nanoparticles are diluted in distilled water and taken in quartz cuvette for recording absorption spectra. Distilled water in quartz cuvette is used as a reference. The absorption spectrum shows the characteristic plasmon resonance absorption peak of gold nanoparticles at 530 nm. For characterization using SEM the gold nanoparticle solution is diluted in ethanol and sonicated for 20 minutes. The solution is then drop casted on a silicon wafer by using a micropipette to form well dispersed gold nanoparticles. Silicon wafer is used because SEM requires a conducting surface. Figure 2.16 (a) shows the SEM image of gold nanoparticles prepared by the above method. The particle size of the gold nanoparticle is measured from SEM images using ImageJ. Figure 2.16 (b) shows the particle size histogram of the gold nanoparticle obtained from the analysis of the SEM images. The particle size histogram is fitted with a Gaussian profile to estimate the mean particle size and the spread in the mean particle size. The mean size of gold nanoparticle thus estimated is 25 ± 4 nm.

2.5.3 Preparation of Au/BaTiO$_3$ Films

Au/BaTiO$_3$ nanocomposite precursor solution is prepared by injecting gold nanoparticles into the BaTiO$_3$ precursor solution slowly with different molar ratios of Au/Ba. To distribute the gold nanoparticles uniformly in the solution, the Au/BaTiO$_3$ composite precursor solution is mixed well in a cyclomixer. The molar ratio of Au in the films is adjusted by varying the amount of gold solution added to the BaTiO$_3$ precursor solution. The Au/BaTiO$_3$ thin film is prepared by spin coating. The spin speed used is 2000 rpm for 60 s. The films are dried at 60 °C for 10 min and heat treated at 800 °C. Controlled Nitrogen atmosphere is used while heat treatment for better surface quality. Figure 2.17 shows the flowchart for the preparation of Au/BaTiO$_3$ thin films. It may be noted that one cannot prepare films with arbitrary high gold nanoparticle concentration by this

method. When the amount of gold increases inside the acidic precursor solution, Au atoms change to Au^{3+} ions and forms a precipitate in the solution. This limits the amount of the gold nanoparticle that can be added to the acidic solution. Thus, the molar ratio of Au/Ba was limited to less than 5/100 in our samples. Au/BaTiO$_3$ composite films with Au/Ba molar ratios 1.6/100, 2.5/100 and 4.8/100 are prepared.
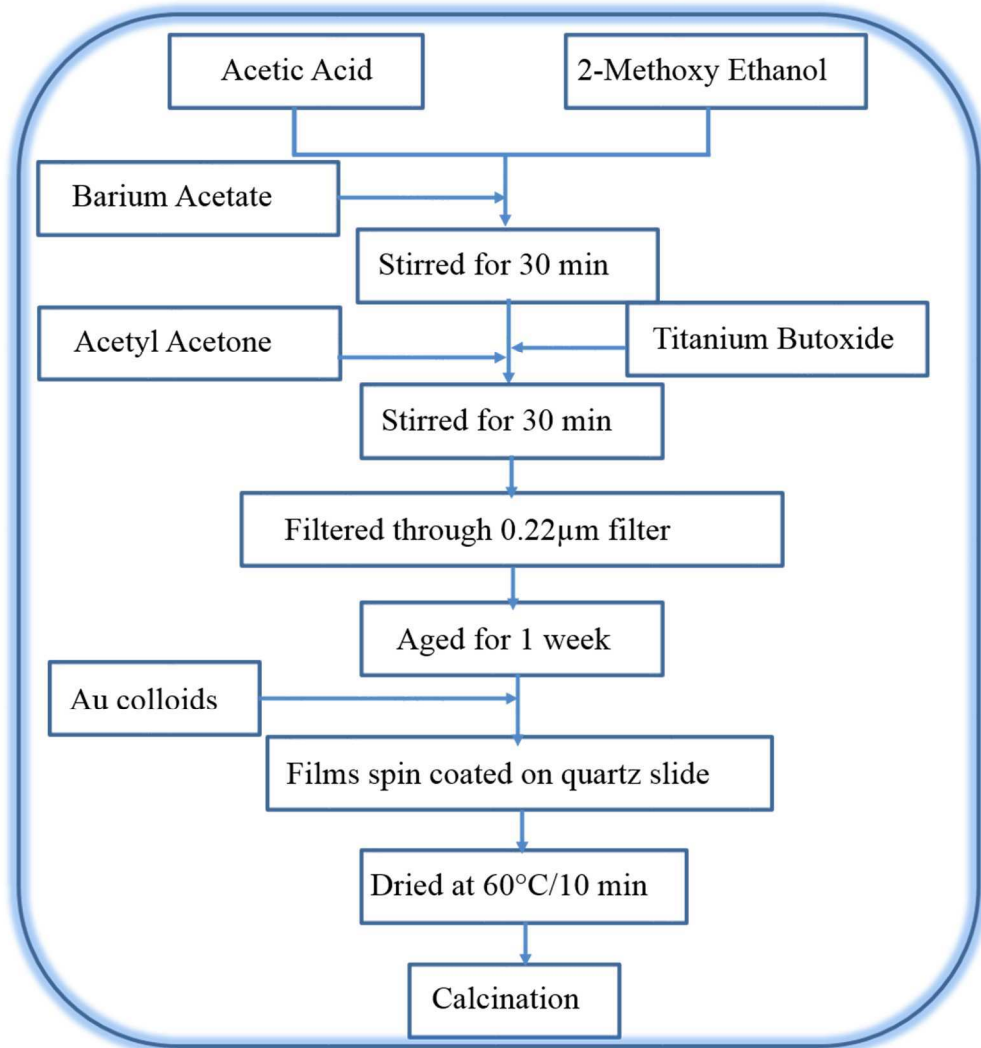
Fig. 2.17: Flowchart for the preparation of Au/BaTiO$_3$ thin films.

2.6 Characterizations of the BaTiO₃ and Au/BaTiO₃ thin films

The Au/BaTiO$_3$ thin films prepared are characterized by UV-VIS-NIR absorption spectra, XRD, SEM, TEM and AFM.

2.6.1 Characterization by X-ray diffraction

Figure 2.18 shows the XRD pattern of Au/BaTiO$_3$ thin films with Au/Ba molar ratio 4.8/100, annealed at 800 °C for 2 hours. The crystallographic planes (001), (101), (111), (002), (201), (211), (202), (212), (301), and (311) corresponding to the tetragonal phase crystalline BaTiO$_3$ are identified and marked in the XRD pattern. It confirms the formation of tetragonal phase BaTiO$_3$. Since the Au (111) and Au (200) diffraction peaks are overlapping with the BaTiO$_3$ (111) and BaTiO$_3$ (002) diffraction peaks, it is not possible to separate out gold diffraction peaks from BaTiO$_3$ diffraction peaks in the XRD pattern.
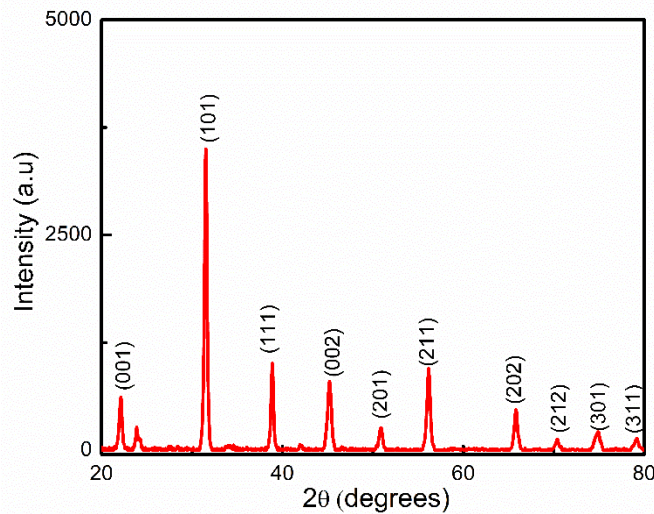
Fig 2.18: X-Ray Diffraction pattern of Au/BaTiO$_3$ thin film with Au/Ba molar ratio of 4.8/100, coated on quartz slide and annealed at 750 °C for 1hr in nitrogen atmosphere. The X-ray diffraction pattern of Au/BaTiO$_3$ thin film confirms the formation of tetragonal phase BaTiO$_3$.

2.6.2 Characterization by UV-VIS-NIR absorption

Figure 2.19 shows the Absorption spectra of Au/BaTiO$_3$ thin films with Au/Ba molar ratio of 4.8/100, coated on quartz slide and annealed at 750 °C for 1hr in nitrogen atmosphere. Plane quartz slide is used for the baseline correction. The figure shows the plasmon resonance absorption of gold nanoparticles at 568 nm and the characteristic absorption edge of BaTiO$_3$ at around 370 nm. The inset shows an expanded view of 568 nm plasmon absorption.
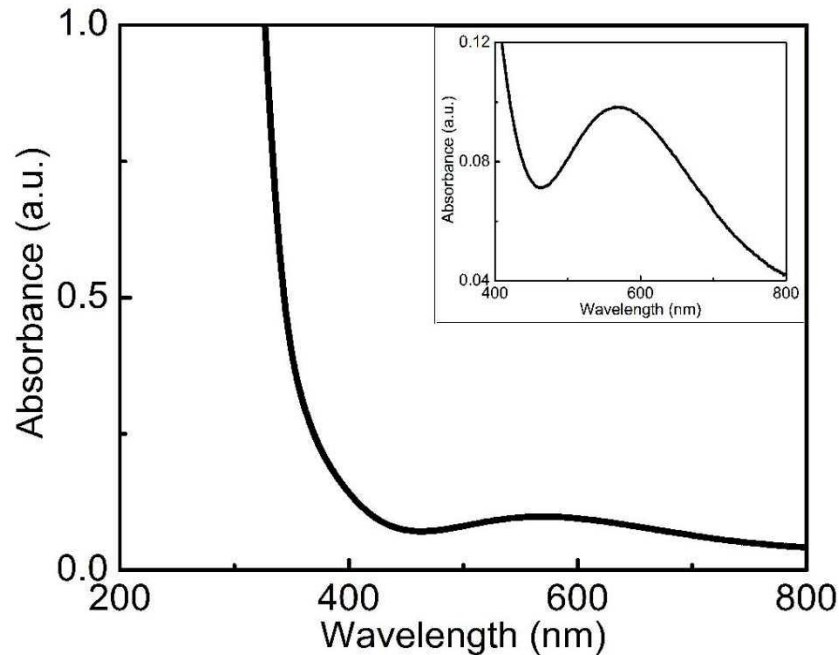
Fig. 2.19: Absorption spectra of Au/BaTiO$_3$ thin films coated on quartz slide and annealed at 750 ^{0}C for 1hr in nitrogen atmosphere. The figure shows the plasmon resonance absorption of gold nanoparticles at 568 nm and the characteristic absorption edge of BaTiO$_3$ at around 370 nm. The inset shows an expanded view of 568 nm plasmon absorption.

2.6.3 Characterization by transmission electron microscope

The high-resolution transmission electron microscope (HRTEM) images of BaTiO$_3$ and Au/BaTiO$_3$ are taken by an FEI make Tecnai G2, F30 machine. A small portion of the films is peeled off from the centre of the films and used to make sample for HRTEM. The peeled off films portion is dispersed in ethanol and drop casted on top of copper grid for imaging in HRTEM. Figure 2.20(a) shows the HRTEM image of BaTiO$_3$ thin films heat treated at 750 ^{o}C. The average particle size is measured to be 15 nm from the HRTEM. Figure 2.20(b) shows the convergent beam electron diffraction images of BaTiO$_3$. The pattern exhibits sharp diffraction rings corresponding to (001), (110), (111), (200) and (112) planes characteristic of crystalline BaTiO$_3$ having tetragonal phase. Figure 2.20(c) shows the HRTEM image of Au/BaTiO$_3$ thin films. The figure shows two distinct lattice planes having interplanar distances of 0.24 nm and 0.41 nm as indicated. The planes having interplanar distance of 0.24 nm is attributed to the (111) plane of gold and the planes having interplanar distance of 0.41 nm is attributed to (001) plane of BaTiO$_3$. The SAED pattern of

Au/BaTiO$_3$ thin films, shown in figure 2.20(d), also exhibits sharp diffraction rings characteristic of crystalline BaTiO$_3$ having tetragonal phase, confirming the findings from XRD analysis. The average size of gold nanoparticle is estimated to be 10 nm and that of BaTiO$_3$ nanoparticles is 20 nm. Figure 2.21 shows the Energy-dispersive X-ray spectroscopy (EDS) image of Au/BaTiO$_3$ thin film heat-treated at 750 ^{o}C for 2 hour with Au/Ba molar ratio of 4.8/100. The Au/Ba molar ratio found from the EDS spectrum is 4.4/100 which is close to the estimated value from the sample preparation.
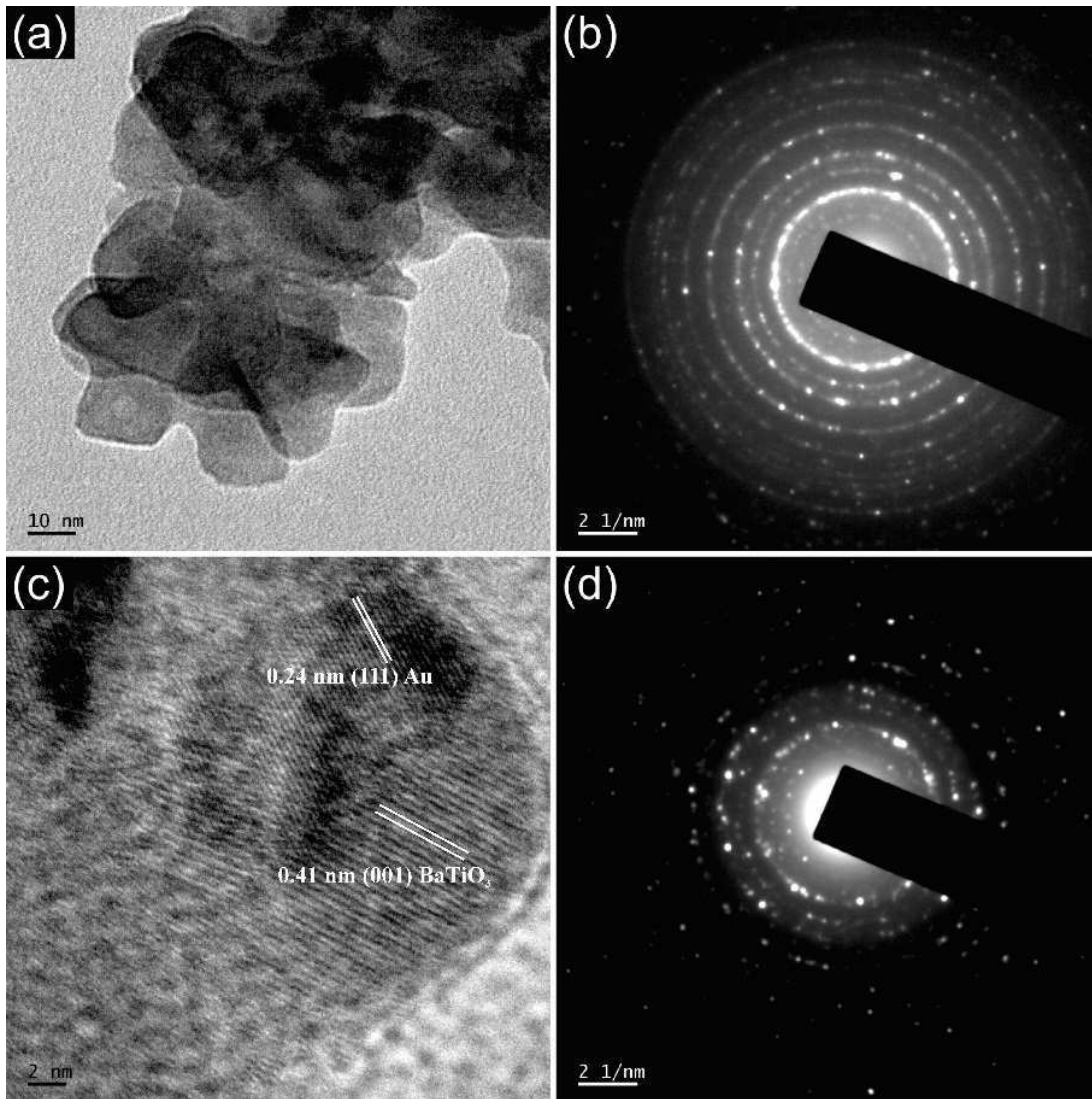
Fig. 2.20: (a) HRTEM image of BaTiO$_3$ thin film. (b) Combined beam electron diffraction pattern of BaTiO$_3$ thin film. (c) HRTEM image of Au/BaTiO$_3$ thin film. (d) SAED pattern of Au/BaTiO$_3$ thin film.
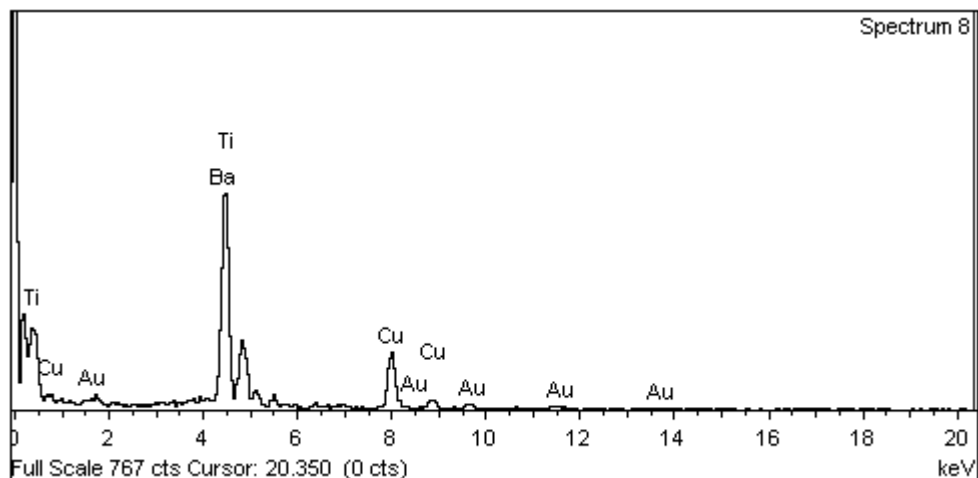
Fig.2.21: Energy-dispersive X-ray spectroscopy (EDS) image of Au/BaTiO$_3$ thin film heat-treated at 750 ^{o}C for 2 hours with Au/Ba molar ratio of 4.8/100.

2.6.4 Characterization by atomic force microscope

The surface quality and topography of the BaTiO$_3$ thin film prepared are studied by Atomic force microscopy (AFM). Figure 2.22 (a) shows the 3D topography and (b) 2D topography image of the BaTiO$_3$ thin film prepared on quartz slide and annealed at 750 ^{o}C for 2 hours.

(a)

(b)
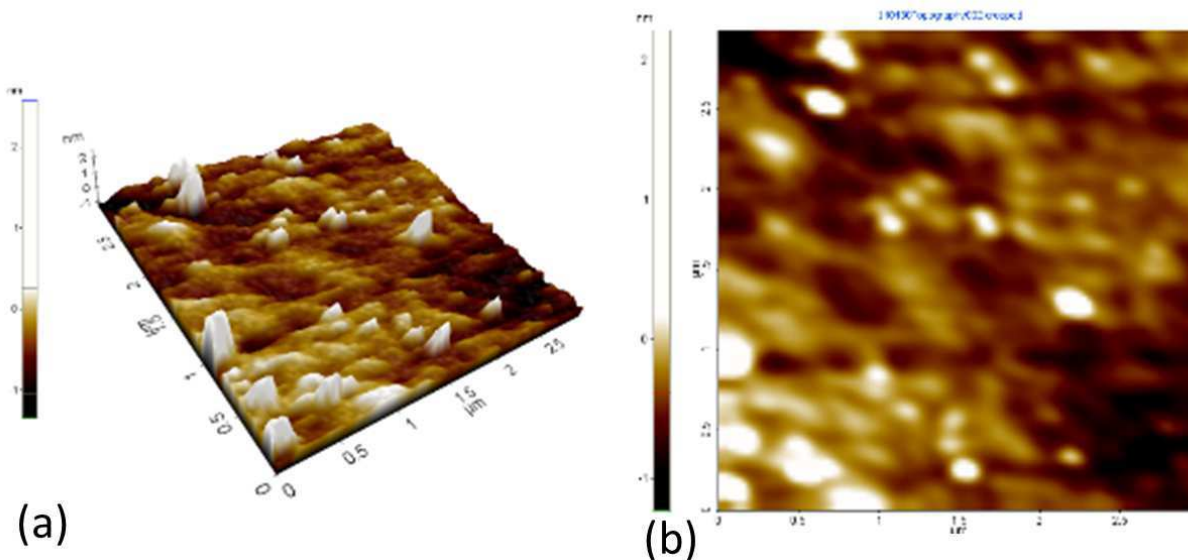
Fig. 2.22: (a) The 3D topography and (b) 2D topography image of the BaTiO$_3$ thin film prepared on quartz slide and annealed at 750 ^{o}C for 2 hours.

2.7 Summary

Monodisperse $BaTiO_3$ nanoparticles of different average sizes, 12 nm, 20 nm, 37 nm, 50 nm and 90 nm are successfully prepared by sol-gel technique and characterised by UV-VIS-NIR absorption spectrometer, X-ray diffractometer and transmission electron microscopy. The size of $BaTiO_3$ nanoparticles are controlled by varying the annealing temperature. The linear optical absorption edge and bandgap are estimated from absorption spectra and Tauc plot. A small but systematic increase in the bandgap of the nanoparticles with decreasing size is observed. This could be due to the band structure modification arising from quantum confinement effects. Tetragonal crystal structure of $BaTiO_3$ is identified from the X-ray diffraction. The size of the $BaTiO_3$ nanoparticles is estimated from transmission electron microscope images. $BaTiO_3$ thin films and $Au/BaTiO_3$ thin films are also prepared by sol-gel technique and characterised by UV-VIS-NIR absorption spectrometer, X-ray diffractometer, transmission electron microscope and atomic force microscope.

Chapter 3: Nonlinear optical absorption in BaTiO$_3$ nanoparticles

3.1 Introduction

Materials possessing large values of nonlinear optical susceptibilities have potential applications in different areas of quantum optics [108,109,132,161]. The application of nanoparticles with large nonlinear optical susceptibilities in diverse fields such as quantum computing and information processing, ultra-cold atoms, plasma physics, particle accelerators, biomedicine and biomedical engineering has been recognized in recent years [95,108,109,132,135,136,161–163]. In addition to large nonlinear optical susceptibility, nonlinear optical materials should have different properties specific to the applications. For example, in all optical implementation of quantum information processing or in all optical switching the material should have fast response times and high optical damage thresholds. Biomolecular imaging or biomedical engineering applications will require the material to be biocompatible and photostable in addition to having large nonlinear optical coefficients. The search for an ideal nonlinear material having all the required properties is far from over and there is a sustained effort to develop new and novel materials with promising applications. BaTiO$_3$ nanoparticles, the focus of our investigation in this thesis, are highly photostable and biocompatible and thus have good potential to be employed as a biomolecular label in nonlinear optical microscopy. In this chapter we examine the nonlinear optical absorption in BaTiO$_3$ nanoparticles from the point of view of applications in the area of biomolecular imaging. The well-established Z-scan technique is developed in the laboratory to study the third order optical nonlinearity of materials and is employed to determine the nonlinear optical absorption coefficient (α_2) of the nanoparticles, nanoparticle films and Au/BaTiO$_3$ composite films. We first briefly discuss the Z-scan technique and the details of the experimental set up before presenting the results of the studies on BaTiO$_3$ nanoparticles and composite films.

3.2 Z-scan technique

In 1989 M Sheik- Bahae, A. A. Said and E. W. Van Stryland developed a sensitive experimental technique for determining the third order nonlinear optical coefficients of bulk samples [164]. The method, generally termed the Z-scan method, is one of the simplest and most popular experimental techniques to estimate the third order nonlinear optical coefficient of materials. In Z-scan

technique a laser beam is focused by a lens into a thin sample, such that changes in the beam diameter within the sample due to either diffraction or nonlinear refraction can be neglected, is moved through the focus of the lens along the propagation direction (Z). The transmitted intensity is measured at different sample positions along the laser beam path. Analysis of the transmittance intensity curve against the sample position thus plotted provides the third order nonlinear optical susceptibility of the material. The far field intensity is measured either with an aperture in front of the detector (closed aperture Z-scan) or without an aperture (open aperture Z-scan). Since the sample is moved along the propagation direction (Z) of the laser beam, this method is termed as Z-scan. This single beam measurement technique gained wide acceptance because of the simple experimental set up employed as well as the straight forward determination of the third order nonlinear optical coefficients from the transmittance intensity curve. In most Z-scan experiments the sign and magnitude of nonlinear absorption coefficient and nonlinear refractive index can be directly estimated from the transmittance intensity curve without performing a tedious theoretical fitting.

3.2.1 Closed aperture Z-scan technique
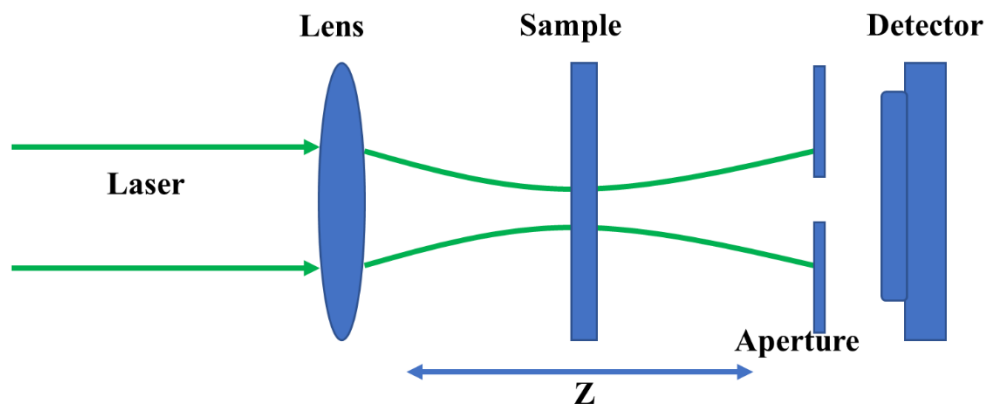
Fig. 3.1: Schematic of closed aperture Z-scan set up

Figure 3.1 shows a typical experimental set up employed for closed aperture Z-scan measurement. In closed aperture Z-scan an aperture is placed in the far field in between the sample and the detector as shown in the figure. The closed aperture Z-scan data can be qualitatively understood by considering the effect of a focused Gaussian beam on a material having a refractive nonlinearity ($n_2 \neq 0$). If $n_2 \neq 0$, the effective refractive index of the material at a point on the sample will

depend on the intensity of the incident light at that point. If the material has positive third order optical nonlinearity $(n_2 > 0)$ the higher intensity regions will have high refractive index compared to lower intensity regions. Since a Gaussian beam has maximum intensity at the center, the center of the focal spot will see maximum refractive index and there will be a gradation of refractive index as you move away from the center. This implies that if $n_2 > 0$, the sample will act like a convex lens. Thus for a focused Gaussian beam, the far field transmittance of a material having positive nonlinearity would be equivalent to the transmittance of a combination of two convex lenses. Moving the sample along the axis of the focused laser beam is thus equivalent to moving of a convex lens. If the sample is kept before the focal point of the lens, then it causes the beam to focus to a point before the natural focus of the lens. This results in stronger divergence of the beam in the far field and the detector will show a lower intensity. If the sample is kept after the focal point of the lens, then the sample causes the beam to focus to a point after the natural focus of the lens, and hence the detector records a higher intensity. In the transmittance curve, first a valley occurs corresponding to the sample position just before the focus of the lens followed by a peak corresponding to the sample position just after the focus of the lens. Figure 3.2(a) shows a typical closed aperture Z-scan transmittance curve for positive third order nonlinear refraction. Similarly, if the sample having negative third order refractive nonlinearity $(n_2 < 0)$, there will be a gradual increase in the refractive index, with higher refractive index at the edges and lower refractive index at the center (axial point). Thus samples having $n_2 < 0$ acts like a concave lens when exposed to a focused Gaussian beam. The nature of the transmittance curve for materials with a negative refractive nonlinearity is illustrated in figure 3.2(b).
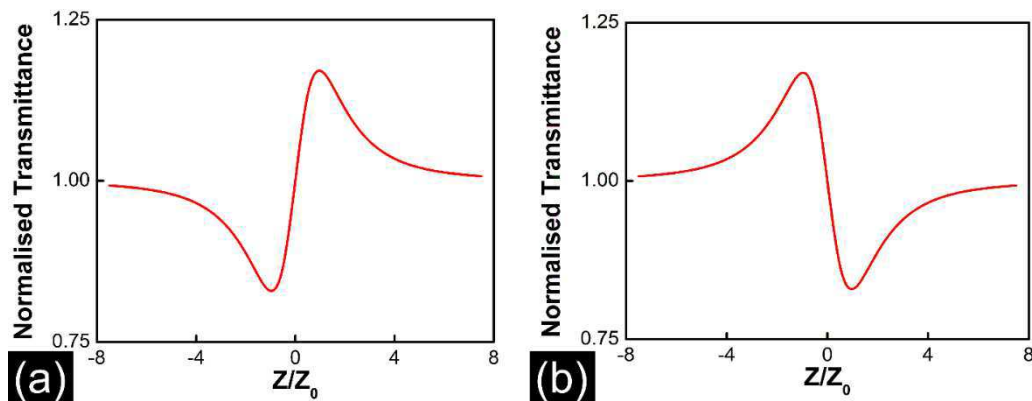
Fig. 3.2: A typical closed aperture Z-scan transmittance curve for (a) positive and (b) negative third order nonlinear refraction.

In order to quantitatively understand the transmittance curve, one has to compute the intensity at the aperture as a function of the sample position. Two effects have to be taken into account while estimating this intensity: one, the decrease in intensity of the beam at the sample due to linear and nonlinear absorption and two, the change in the phase due to nonlinear refraction at the sample. The rate of change of intensity due to absorption inside the sample is given by

$$\frac{dI(\xi)}{d\xi} = -[\alpha_0 + \alpha_2 I(\xi)]I(\xi) \tag{3.1}$$

where $I(\xi)$ is the intensity at position ξ in the sample. If we consider only cubic nonlinearity, the above expression can be integrated to give the intensity

$$I(\xi) = I_0 e^{-\alpha_0 \xi} \left[1 + I_0 \alpha_2 \left(\frac{1 - e^{-\alpha_0 \xi}}{\alpha_0}\right)\right]^{-1} \tag{3.2}$$

Now if we define an 'effective length' L_{eff} by $L_{eff} = \frac{1 - e^{-\alpha_0 L}}{\alpha_0}$, the intensity at the exit face of the sample is

$$I(\xi = L) = \frac{I_0 e^{-\alpha_0 L}}{1 + I_0 \alpha_2 L_{eff}} \tag{3.3}$$

The nonlinear phase acquired by the beam while travelling through a distance $d\xi$ in a medium with cubic nonlinearity is $(2\pi n_2/\lambda)I(\xi)d\xi$, where λ is the free space wavelength. The total nonlinear phase accumulated at the exit of the sample is

$$\Delta\varphi_{NL} = \int_0^L \frac{2\pi n_2}{\lambda} I(\xi)d\xi \tag{3.4}$$

$$\Delta\varphi_{NL} = \frac{2\pi n_2}{\alpha_2 \lambda} \ln\left[1 + I_0 \alpha_2 \left(\frac{1 - e^{-\alpha_0 L}}{\alpha_0}\right)\right]$$

$$\Delta\varphi_{NL} = \frac{2\pi n_2}{\alpha_2 \lambda} \ln\left[1 + I_0 \alpha_2 L_{eff}\right] \tag{3.5}$$

Let us consider a Gaussian beam having a beam waist w_0 travelling along the positive Z-direction incident on a nonlinear sample. The magnitude of the electric field can written as

$$|E_{in}(z, r, t)| = |E_0(t)| \frac{w_0}{w(z)} e^{-r^2/w^2(z)} \tag{3.6}$$

where $w^2(z) = w_0{}^2(1 + z^2/z_0^2)$ is the beam radius at z, $z_o = kw_0{}^2/2$ is the diffraction length (Rayleigh Length) of the beam, $k=2\pi/\lambda$ is the free space wave vector, λ is the wavelength and r is the radial distance from the center. $E_0(t)$ is the on-axis electric field and contains the temporal envelope of the laser pulse. For a CW excitation the envelope can be taken to be a square function, and for pulsed excitation the envelope will be a Gaussian in time. If we denote the incident intensity at sample position z by $I_{in}(z,r,t)$, then from equation (3.3), intensity at the exit face of a sample kept at z will be,

$$I_{exit}(z,r,t) = \frac{I_{in}(z,r,t)\,e^{-\alpha_0 L}}{1 + q(z,r,t)} \qquad (3.7)$$

where $q(z,r,t) = I_{in}(z,r,t)\alpha_2 L_{eff}$. The nonlinear phase acquired is

$$\Delta\phi(z,r,t) = \frac{k_0 n_2}{\alpha_2}\,ln[1 + q(z,r,t)] \qquad (3.8)$$

In this analysis it is assumed that the thickness (L) of the sample is small so that changes in the beam diameter due to diffraction or nonlinear refraction can be neglected within the sample. This assumption implies that the interaction of the sample with the laser pulse takes place only at one plane, not spread out over entire length, and the self-refraction process is referred to external self-refraction. The sample thickness L $< z_0$ is a good approximation to consider the sample to be 'thin' [164]. Under the above assumption the electric field at the exit plane is

$$E_{exit}(z,r,t) = E_{in}(z,r,t)e^{-\alpha_0 L/2}e^{-i\Delta\varphi(z,r,t)} \qquad (3.9)$$

$$E_{exit}(z,r,t) = \frac{E_{in}(z,r,t)\,e^{-\alpha_0 L/2}}{[1 + q(z,r,t)]^{1/2}}\,[1 + q(z,r,t)]^{ikn_2/\alpha_2} \qquad (3.10)$$

In order to quantitatively reproduce the Z-scan transmittance curve one has to find the total intensity at the aperture as function of the z position of the sample. The electric filed at the aperture plane E_a (z, r, t) can be determined from the field at the exit plane of the sample using the Huygen's principle through a zeroth order Hankel transform [164]. This is achieved by considering the complex field at the exit plane as a superposition of Gaussian beams through a Taylor series expansion of the nonlinear phase term $e^{i\Delta\varphi(z,r,t)}$ (Gaussian decomposition) and propagating each Gaussian beam to the aperture [165].

If the nonlinear absorption is negligible, $\Delta\phi$ can be expressed in simpler symmetric form. Taking the limit α_2 going to zero in equation (3.8)

$$\Delta\phi(z, r, t) = k_0 I(z, r, t) n_2 L_{eff} \tag{3.11}$$

Substituting $I(z, r, t) = \frac{c\epsilon_0 n}{2} |E(z, r, t)|^2$,

$$\Delta\phi(z, r, t) = \Delta\varphi_0(z, t) e^{-2r^2/w^2(z)} \tag{3.12}$$

with $\Delta\phi_0(z, t) = \frac{\Delta\varphi_0(t)}{1+z^2/z_0^2}$ where $\Delta\varphi_0(t) = k_0 n_2 I_0(t) L_{eff}$ is the on-axis face shift at the focus, $I_0(t)$ being the on-axis irradiance at the focus. Thus, if the nonlinear absorption is negligible, the nonlinear phase shift at the exit surface follow the Gaussian shape of the pulse across the cross section of the beam.

$$e^{i\Delta\phi(z,r,t)} = \sum_{m=0}^{\infty} \frac{[i\Delta\phi_0(z, t)]^m}{m!} e^{-2mr^2/w^2(z)} \tag{3.13}$$

The electric field at the aperture plane is given by,

$$E_a(r, t) = E(z, r = 0, t) e^{-\alpha_0 L/2} \sum_{m=0}^{\infty} \frac{[i\Delta\phi_0(z, t)]^m}{m!} \frac{w_{m0}}{w_m} e^{\left(-\frac{r^2}{w_m^2} - \frac{ikr^2}{2R_m} + i\theta_m\right)} \tag{3.14}$$

where,

$$w_{m0}^2 = \frac{w^2(z)}{2m + 1} \tag{3.15}$$

$$d_m = \frac{k w_{m0}^2}{2} \tag{3.16}$$

$$w_m^2 = w_{m0}^2 \left(g^2 + \frac{d^2}{d_m^2}\right) \tag{3.17}$$

$$R_m = d\left(1 - \frac{g}{g^2 + d^2/d_m^2}\right)^{-1} \tag{3.18}$$

$$\theta_m = tan^{-1}\left(\frac{d}{d_m g}\right) \tag{3.19}$$

and d is defined as the propagation distance from sample to the aperture in free space and g is defined by,

$$g = 1 + \frac{d}{R(z)}$$

(3.20)

The transmitted power $(P_r(\Delta\varphi_0(t)))$ through the aperture for an on axis phase shift of $\Delta\varphi_0(t)$ is obtained by spatially integrating electric field at the aperture plane $E_a (z, r, t)$ over the aperture plane.

$$P_T(\Delta\phi_0(t)) = c\epsilon_0 n_0 \pi \int_0^{r_a} |E_a(r,t)|^2 r dr$$

(3.21)

For pulsed excitation, the normalized Z-scan transmittance $T(z)$ can be calculated as

$$T(z) = \frac{\int_{-\infty}^{\infty} P_T(\Delta\phi_0(t))dt}{s \int_{-\infty}^{\infty} P_i(t)dt}$$

(3.22)

where $P_i(t) = \pi w_0^2 I_0(t)/2$ is the instantaneous input power within the sample and

$$s = 1 - e^{-2r_a^2/w_a^2}$$

(3.23)

is the aperture transmittance in the absence of any nonlinearity, w_a being the beam radius at the aperture.

Further simplifications occur for far field condition ($d \gg z_o$). If $\Delta\varphi_0$ is small, ie $|\Delta\varphi_0| \ll 1$ we can add only the first two terms in the Gaussian decomposition [165]. The Z-scan transmittance curve $T(z, \Delta\phi_0)$ defined by

$$T(z, \Delta\phi_0) = \frac{|E_a(z, r = 0, \Delta\phi_0)|^2}{|E_a(z, r = 0, \Delta\phi_0 = 0)|^2}$$

(3.24)

For far field conditions ($d \gg z_o$) a simple expression for transmittance can be found.

$$T(z, \Delta\phi_0) \cong 1 - \frac{4\Delta\phi_0 x}{(x^2 + 9)(x^2 + 1)}$$

(3.25)

with $x = z/z_0$.

The peak (maximum transmittance) and valley (minimum transmittance) corresponds to z positions at which derivative of the transmittance curve vanishes. For third order nonlinearity the

peak to valley separation is found to $1.7z_o$. The difference between normalized peak and valley transmittance $\Delta T_{p\text{-}v} = T_p - T_v$, a quantity normally measured in Z-scan experiment, is given by

$$\Delta T_{\mathrm{p-v}} = \frac{8|x_{p,v}|}{(x_{p,v}^2 + 9)(x_{p,v}^2 + 1)}\Delta\phi_0 \qquad (3.26)$$

$$\Delta T_{\mathrm{p-v}} = 0.406\Delta\phi_0 \qquad (3.27)$$

where, $x_{p,v} = x_p - x_v$ and it can be calculated by solving the differential equation $\frac{dT(z,\Delta\phi_0)}{dz} = 0$,

$$x_{p,v} = \pm\sqrt{\frac{\sqrt{52}-5}{3}} \cong 0.858$$

$\Delta T_{p\text{-}v}$ for different materials has been measured by Sheik-Bahae *et al.* [166] and is found to agree well with the above result. $\Delta T_{p\text{-}v}$ increases linearly with $\Delta\varphi_0$, and for a given value of $\Delta\varphi_0$ the magnitude and shape of the transmittance curve does not depend on the wavelength or geometry as long as the far field condition for the aperture plane is satisfied. Thus equation (3.26) provides a quick method to find the nonlinear refraction experiment employing low laser powers. However, if the power is high the nonlinear phase shift will be large and one has to use the full calculation as discussed earlier to determine the nonlinearity.

3.2.2 Open aperture Z-scan technique

Figure 3.3 shows the schematic of open aperture Z-scan technique employed to reveal the absorptive nonlinearity of the materials. The setup is essentially the same as the closed aperture Z-scan setup, except that the aperture in front of the detector is removed. The detector in this case detects all of the transmitted light. Hence the setup is not sensitive to nonlinear refraction and the Z-scan transmittance curve does not show any changes arising from refraction. However as the sample is moved along z-direction towards the focal point, there will be an increase in nonlinear absorption and maximum absorption will occur at the focal point. These changes in absorption will be recorded as a dip in the Z-scan transmittance curve with the maximum dip occurring when the sample is at the focal point. The depth in the transmittance intensity curve is directly proportional to the nonlinear absorption coefficient and thus the open aperture Z-scan measures the nonlinear absorption in a simple experimental setup. However it should be noted here that both two-photon

and other higher order multi-photon processes can contribute to the signal in open aperture z-scan. In the analysis described here we will restrict ourselves only to changes in the transmittance curve due to two-photon absorption, assuming that the contributions from higher order process will be comparatively weak.
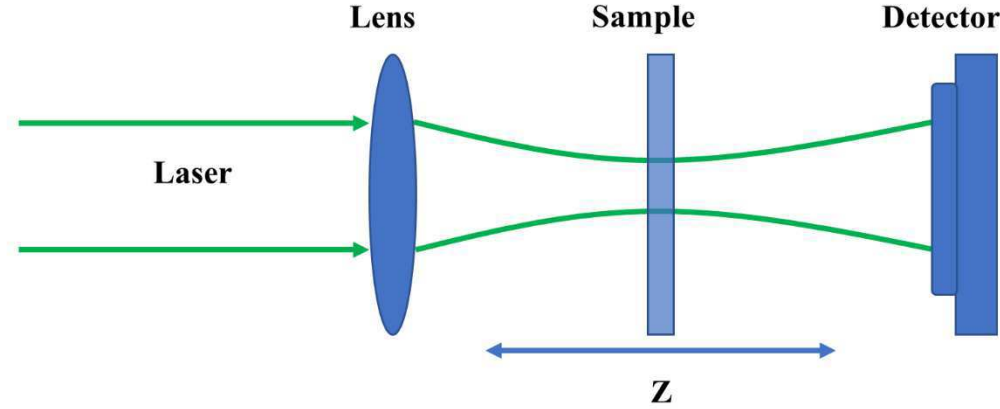
Fig. 3.3: Schematic of open aperture Z-scan technique

The nature of nonlinear absorption and absorption coefficient (α_2) is determined from the transmittance curve as explained in the following. For a Gaussian beam of the form,

$I_{in}(z, r, t) = \frac{2P(t)}{\pi w^2(z)} e^{-2r^2/w^2(z)}$ interacting with the sample. Here $P(t)$ is the instantaneous power of the beam at time t, for a Gaussian beam $P(t) = (\pi \omega_0^2/2)I_0$, with the peak (on axis intensity) $I_0 = \frac{c\epsilon_0 n}{2}|E|^2$. As defined earlier, $w^2(z) = w_0^2(1 + z^2/z_0^2)$ is the beam radius at z, $z_o = kw_0^2/2$ is the Rayleigh length, $k{=}2\pi/\lambda$ is the free space wave vector, λ is the wavelength of the laser and r is the radial coordinate. For a CW beam $P(t)$ is a constant, and for a pulsed laser beam $P(t)$ has a Gaussian time dependence. We further assume that the thickness (L) of the sample is small so that changes in the beam diameter due to diffraction or nonlinear refraction can be neglected.

Following our discussion in the previous section, the intensity at the exit face of a sample kept at z is given by equation (3.7).

$$I_{exit}(z, r, t) = \frac{I_{in}(z, r, t) \, e^{-\alpha_0 L}}{1 + I_{in}(z, r, t)\alpha_2 L_{eff})} \tag{3.28}$$

The total transmitted power $P(z, t)$ for the sample position z.

$$P(z, t) = 2\pi \int_0^\infty I_{exit}(z, r, t) \, r \, dr \tag{3.29}$$

$$P(z,t) = 2\pi \frac{2P(t)}{\pi w^2(z)} e^{-\alpha_0 L} \int_0^\infty \frac{e^{-\frac{2r^2}{w^2(z)}}}{1 + \alpha_2 L_{eff} \frac{2P(t)}{\pi w^2(z)} e^{-\frac{2r^2}{w^2(z)}}} \, r \, dr \qquad (3.30)$$

$$P(z,t) = P(t)e^{\alpha L} \frac{\ln[1 + q_0(z,t)]}{q_0(z,t)} \qquad (3.31)$$

Where,

$$q_0(z,t) = \alpha_2 L_{eff} I(z, r = 0, t) = \frac{2\alpha_2 L_{eff} I_0(t)}{1 + z^2/z_0^2} \qquad (3.32)$$

If we assume a Gaussian temporal profile for the beam, the normalized beam transmittance can be obtained by integrating the above expression over time, [164]

$$T(z) = \frac{1}{\sqrt{\pi} q_0(z)} \int_{-\infty}^\infty \ln\left[1 + q_0(z,0)e^{-\tau^2}\right] d\tau \qquad (3.33)$$

For $|q_0| < 1$, the transmittance equation can be rewritten in a summation form,

$$T(z) = \sum_{m=0}^\infty \frac{[-q_0(z)]^m}{(m+1)^{3/2}} \qquad (3.34)$$

and the summation can be restricted to m = 1. The nonlinear absorption coefficient is determined by fitting the equation (3.34) with $m = 1$ to the transmittance data of the open aperture Z-scan.

When the sample shows both absorptive and refractive nonlinearity, a combination of both open aperture Z-scan and closed aperture Z-scan can be used to extract the refractive nonlinearity. The third-order optical nonlinearity of the BaTiO$_3$ nanoparticles, BaTiO$_3$ thin films and Au/BaTiO$_3$ thin films synthesized are studied by the Z-scan method.

3.3 Results and Discussion

3.3.1 Design and standardization of Z-scan set up

Figure 3.4 shows the experimental setup employed for Z-scan measurements. For closed aperture Z-scan measurements, an aperture is used in front of the detector. The aperture size can be adjusted to pass desired fraction of incident laser intensity. Mirrors M1 and M2 are used to align the laser

beam parallel to a line on the optical table so that the beam is incident normally on the sample. Beam splitter (BS) and photo detector 1 (PD1) is used to measure the variations in the input laser beam. The lens L focuses laser beam. The sample is fixed on a translation stage (Holmarc model RCM TS-50-150-1) and is moved through the focus of the lens with the help of a stepper motor. Photodiode PD2 is used to measure the transmitted intensity as function of sample position. National Instrument LabVIEW software and NI DAQ 6009 is used to interface stepper motor and detectors.
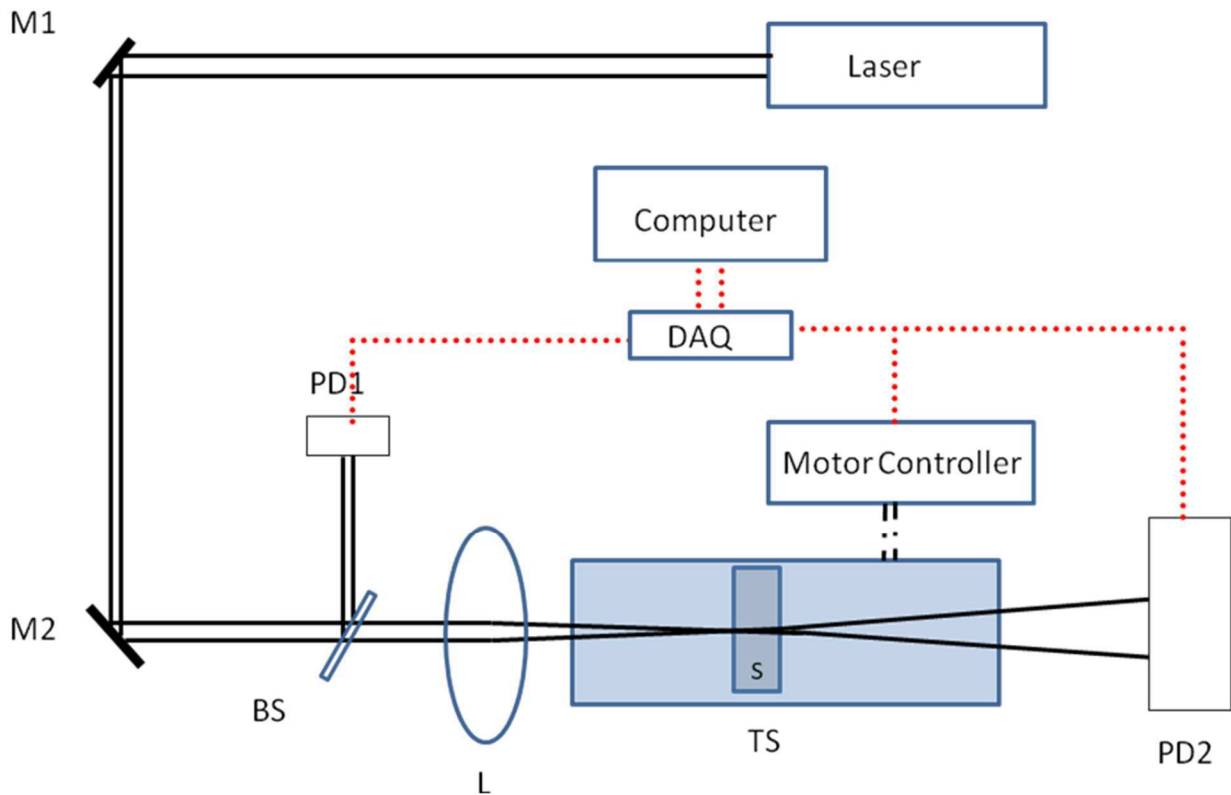
Fig. 3.4: Experimental setup for open aperture Z-scan. M1, M2- Mirrors, BS – Beam Splitter, PD1, PD2 - Photo detectors, L- Lens, TS –Translation Stage, S- Sample, DAQ- Data Acquisition Card.

Synchronised measurement of the transmitted intensity and the sample position is achieved with the help of a simple LabVIEW based program written for this purpose. The program controls stepper motor and records the intensity data from the photodiodes at each sample position and plots the transmittance curve. The digital output port of the multifunction I/O device NI USB 6009 is used to control the stepper motor of the translation stage. The step angle for the stepper motor

used is 1.8° and it gives 200 steps in one revolution in half step mode. The pitch of the screw associated with the translation stage used is 0.5 mm which corresponds to a least count of 2.5 μm (0.5mm /200 steps). In a typical experiment the translation stage moves by 250 μm and waits for a second to measure the output from both the photodiodes. The transmittance curve is plotted with distance on the X axis and intensity on Y axis in the front panel of the LabVIEW software. Figure 3.5 shows (a) front panel and (b) block diagram of the LabVIEW program.

To optimise the Z-scan setup, initial studies are done on Rhodamine-B dye solutions of different concentrations using the 543 nm wavelength beam from a He-Ne laser (Melles Griot, 25LGR). The Rhodamine-B dye solution is taken in a 1mm thick cuvette and nonlinear refractive index is measured by using the closed aperture Z-scan setup. Focal length of the lens used is 15 cm and the aperture size are kept as S = 0.5. Figure 3.6 shows the closed aperture Z-scan data of Rhodamine-B solution of 75 μM. The nonlinear refractive index is estimated from the Z-scan transmittance curve by fitting the data to the equation (3.26). The nonlinear refractive index measured for different concentration is given in the table 3.1. It is found that the nonlinear refractive index is negative, and the order of magnitude is 10^{-8} (cm^2/W).

Concentration Of Rho-B (μM)	Linear absorption coefficient	Effective length (cm)	Peak intensity in the sample (W/cm^2)	Third order nonlinear refractive index, n_2 (cm^2/W)
75	17.8905	0.0991	171.358	-2.19*10^-8
100	23.854	0.0988	171.358	-2.14*10^-8

Table. 3.1: Nonlinear refractive index calculated for two different concentration of rhodamine-B solution.
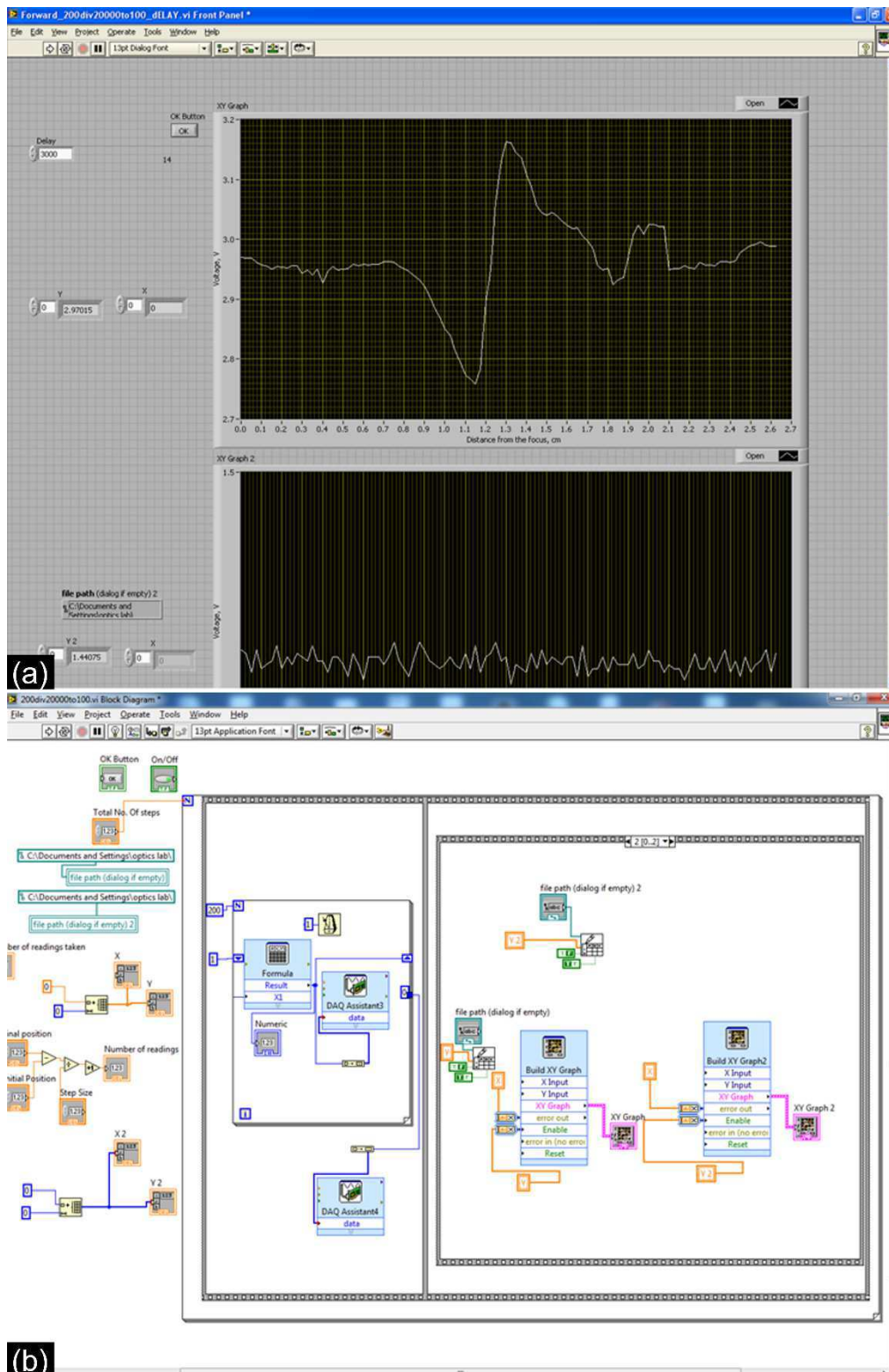
Fig. 3.5: (a) Front panel and (b) block diagram of the program used for the interface of the stepper motor and photodiodes for data acquisition of the Z-scan measurements.
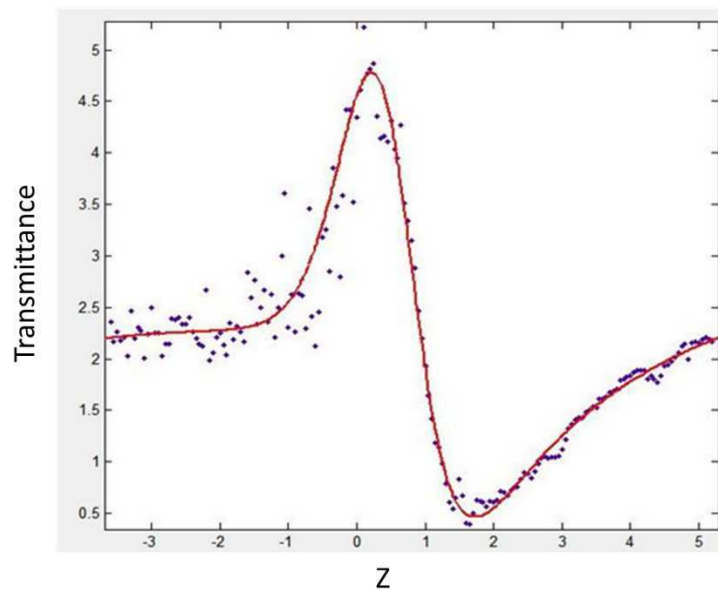
Fig. 3.6: Closed aperture Z-scan traces of Rhodamine-B solution of concentration 75 μM. Wavelength of laser used was 543 nm and with an aperture size of S = 0.5.

3.3.2 Nonlinear optical absorption of BaTiO₃ nanoparticles

The nonlinear optical absorption of BaTiO$_3$ nanoparticles is studied using Z-scan set up described in the previous section. The experiments are carried out in the open aperture geometry to extract the third order nonlinear optical absorption coefficient α_2 of the particles. Studies are carried on different set of samples having average size 12 nm, 20 nm, 37 nm, 50 nm, and 90 nm. This study provides information on dependence of particle size of BaTiO$_3$ nanoparticles on its nonlinear optical properties. The details of the sample preparation technique employed for synthesising BaTiO$_3$ nanoparticles of different sizes are given in the chapter 2. BaTiO$_3$ nanoparticles of different sizes are prepared by sol-gel method. The particle size determined by various characterisation techniques as reported in chapter 2 is reproduced here in Figure 3.7. The BaTiO$_3$ nanoparticles synthesized are grinded properly to form a fine powder. The sample for nonlinear optical studies are prepared by dispersing the finely grinded BaTiO$_3$ nanoparticles in ethylene glycol to form a uniform dispersion of the nanoparticles in solution. For this 1 mg of BaTiO$_3$ nanoparticles is added to 2 ml of ethylene glycol and sonication is carried out for 30 minutes. The solution is taken in a quartz cuvette and kept on the translation stage of the Z-scan apparatus for nonlinear characterisation.

The nonlinear optical absorption properties of BaTiO$_3$ nanoparticles in ethylene glycol solution are studied by the open aperture Z-scan technique. Figure 3.5 shows the schematic of the Z-scan set up used in this study. A femtosecond mode-locked Ti:sapphire laser system (Mira 900, Coherent) operating at 76 MHz is used for the Z-scan study. The wavelength of the laser is 800 nm. The pulse width of the laser, measured with an auto-correlator is 120 fs. The focal length of the lens used is 10 cm. The beam diameter before the lens is 2 mm and the radius at focus was 13 µm. The transmitted beam energy and the reference beam energy are measured directly using photodiodes and their ratio was taken to form the transmittance curve. The Z-scan curve is normalized by the transmittance value obtained with the sample kept far away from the focus. The thickness of the cuvette used is 1 mm. Linear transmission measured for different size nanoparticle solution for the same concentration in ethelene glycol.
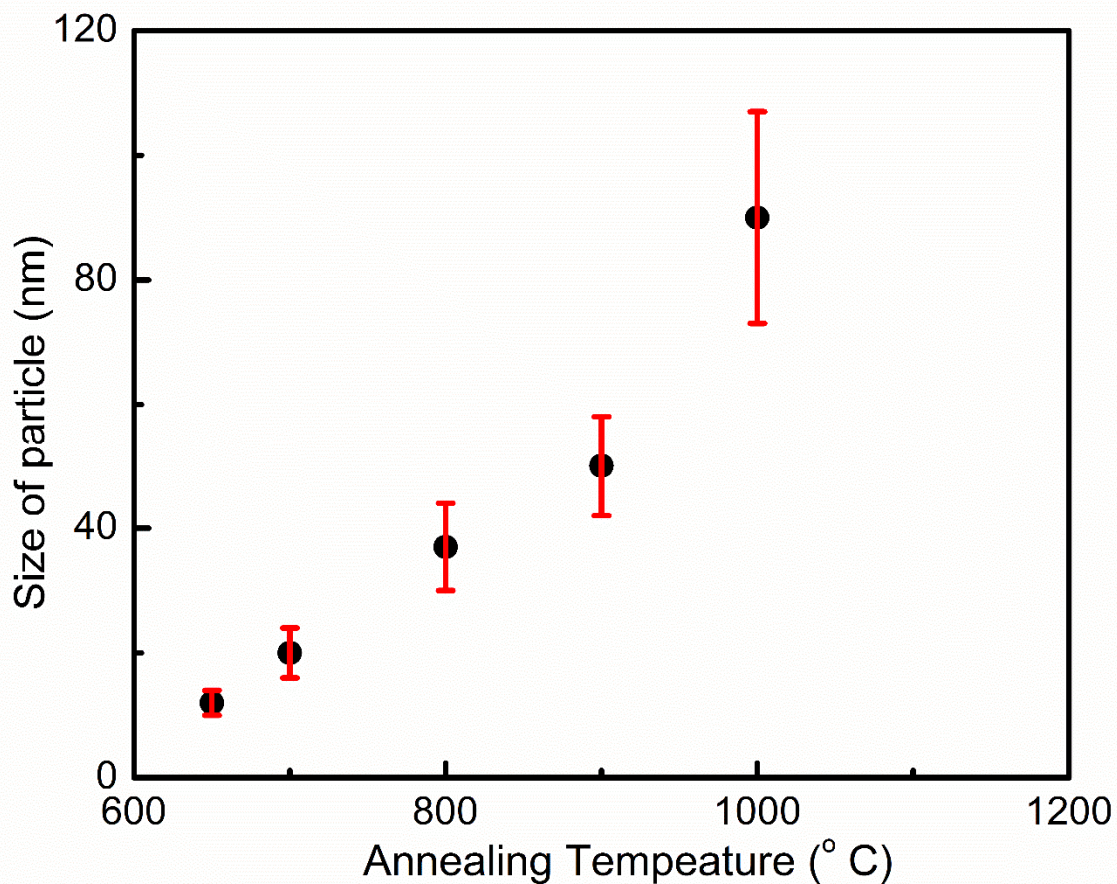
Fig. 3.7: Size of BaTiO$_3$ nanoparticles with the annealing temperature
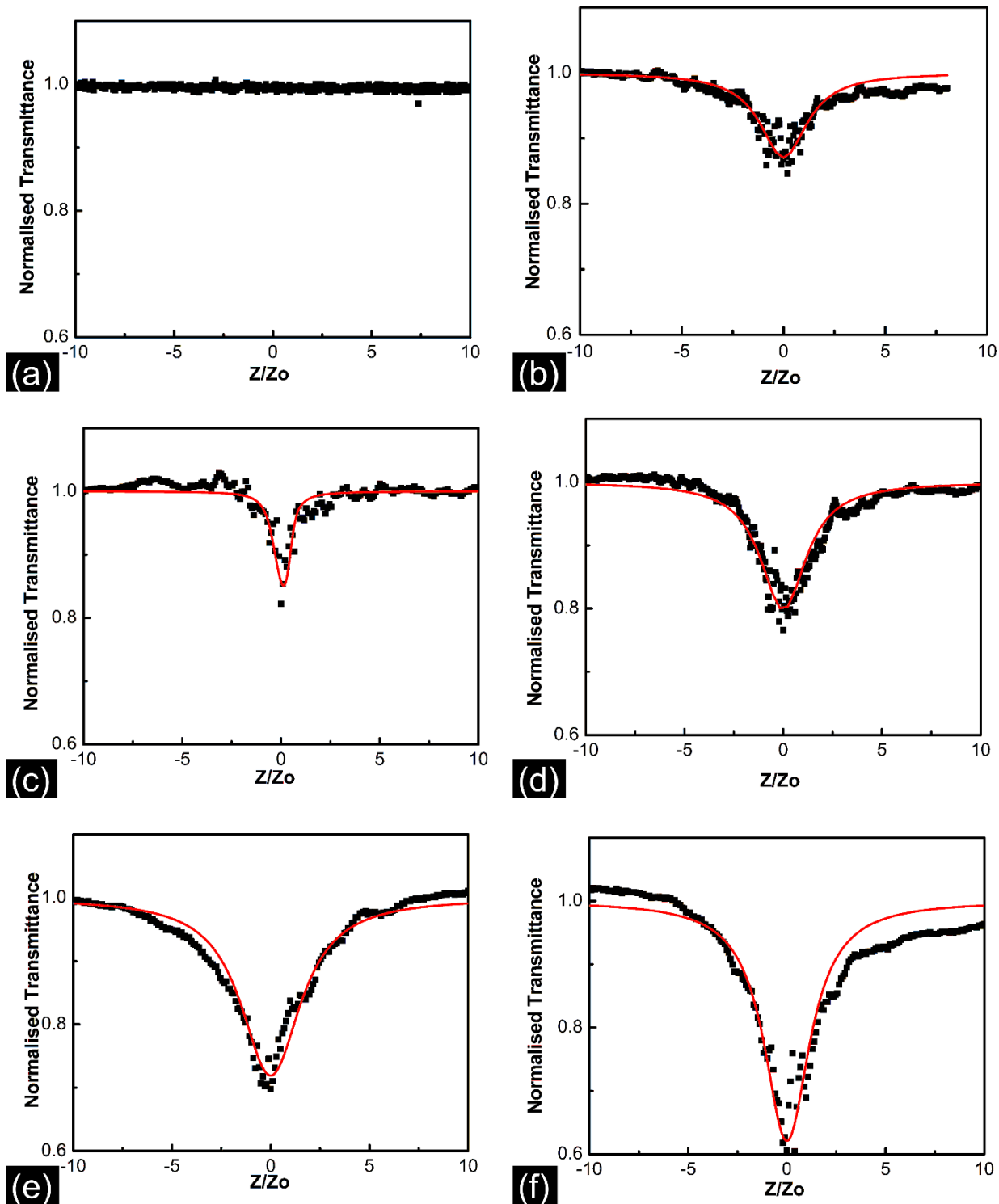
Fig. 3.8: Open Aperture Z-scan traces of solvent (a) and $BaTiO_3$ nanoparticles dispersed in ethelene glycol with average size (b) 90 nm (c) 50 nm (d) 37 nm (e) 20 nm (f) 12 nm.

Size of BaTiO$_3$ nanoparticles (nm)	Linear transmittance	Two-photon absorption coefficient (α_2) (x 10^{-11} m/W)
90 ± 17	59.8 %	3.68 ± 0.05
50 ± 8	58.9 %	5.65 ± 0.08
37 ± 7	59.3 %	6.50 ± 0.06
20 ± 4	60.4 %	8.20 ± 0.09
12 ± 2	60.0 %	11.00 ± 0.08

Table 3.2: Two-photon absorption coefficient of BaTiO$_3$ nanoparticles measured by open aperture Z-scan.

Figure 3.8 shows the open aperture Z-scan curve for solvent (a) and BaTiO$_3$ nanoparticles of average size (b) 90 nm (c) 50 nm (d) 37 nm (e) 20 nm and (f) 12 nm. The Z-scan traces of all the BaTiO$_3$ nanoparticles shows a reverse saturable absorption and the strength of nonlinear absorption increases as the size of the particles decreases. The Z-scan curves are further analysed by carrying out a theoretical fitting to equation (3.34) to extract the nonlinear absorption coefficients.   The Z-scan curves show a proper fitting for a two-photon absorption process confirming that the dominant contribution to absorption is two-photon absorption. The dark squares in the graph are experimental data points and the solid red lines are theoretical curve fit for a two-photon absorption process. The nonlinear absorption coefficient is measured from the Z-scan data by using equation (3.34). Table 3.2 shows the two-photon absorption coefficient measured for different size BaTiO$_3$ nanoparticles.

Figure 3.10 depicts the variation of two-photon absorption coefficient of BaTiO$_3$ nanoparticles with size. The figure clearly shows that the two-photon absorption coefficient of BaTiO$_3$ nanoparticles increases with decrease in the nanoparticle size. Influence of particle size on the dielectric properties of dielectric and semiconductor nanoparticles has been observed by many groups [108,167–171]. This size dependence is generally attributed to the quantum confinement

effects and surface effects. Nonlinear optical properties of dielectrics in the nonresonant regime can be well understood from anharmonic oscillator model. Quantum confinement of electrons in a dielectric material leads to modification of energy band structure of the dielectric material. Influence of particle size of $BaTiO_3$ nanoparticles on optical band gap is observed in the previous chapter. The modification of energy band structure will cause a variation in the dielectric constant. This will further lead to a size dependant linear and nonlinear optical property in nanoparticles. A full theoretical understanding of the mechanism of size dependent optical nonlinearity of dielectric would require further more detailed examination of different contributions to the nonlinearity and its temporal response.
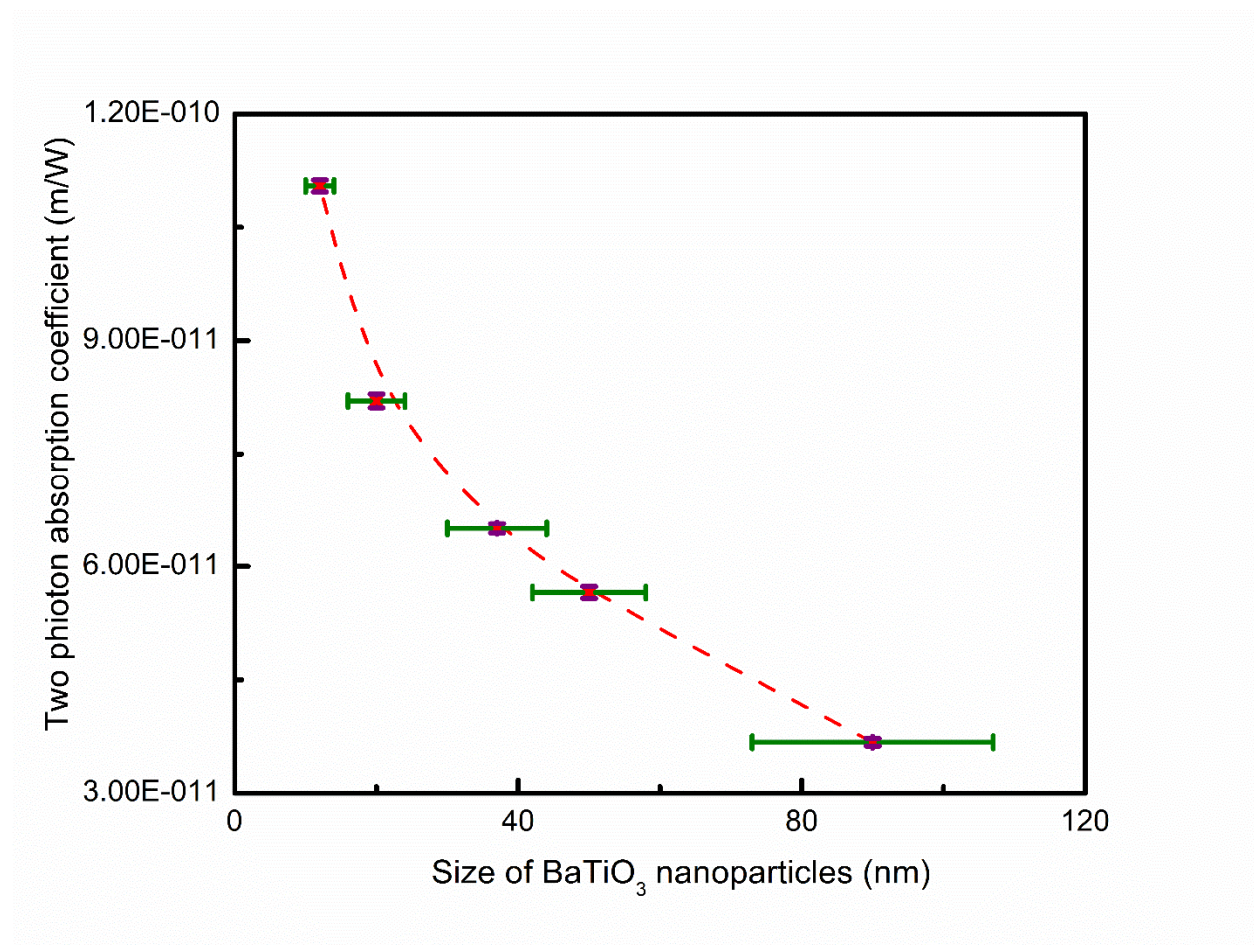
Fig. 3.9: Variation of two-photon absorption coefficient of $BaTiO_3$ nanoparticles with size. The red line over the points is a guide to eye.

3.4. Summary

An automated Z-scan measurement set up is developed in the laboratory and standardized by measuring the nonlinear refractive index of Rhodamine-B dye. Nonlinear absorption coefficient of $BaTiO_3$ nanoparticles of different sizes dispersed in ethylene glycol solution is determined from the open aperture Z-scan transmission curve. The results show an increase in the nonlinear optical absorption coefficient of $BaTiO_3$ nanoparticles with the decrease in size of the particles. Though an increase in the optical nonlinearity $BaTiO_3$ nanoparticles have been reported earlier, the present work presents systematic study of nonlinear absorption of nanoaprticles of different sizes carried out under identical conditions. The variation in the nonlinear optical coefficients of $BaTiO_3$ nanoparticles with size could be due the changes in the energy band structure due to the quantum confinement effects. More detailed investigations of the nonlinearity and its temporal response would be required to fully understand the mechanism of the nonlinearity and it size dependence.

Chapter 4: Tuning the nonlinear optical absorption in Au/BaTiO$_3$ nanocomposites with gold nanoparticle concentration

4.1. Introduction

Nanocomposites have attracted much interest in recent years due to their superior linear and nonlinear optical properties. When two materials are combined to form a nanocomposite it is often possible to choose the parameters in such a way that the composite possess properties superior to those of the constituent materials [172–174]. Maxwell Garnet [175] studied the linear optical properties of small amount of spherical inclusion materials in a host matrix and found that the effective dielectric constant of the composite depends on the fill fraction of the inclusion material and dielectric constants of both of the constituents. Sipe *et al.* predicted the conditions for nanocomposites in the Maxwell Garnet geometry to possess higher nonlinear susceptibility than the constituent materials [172,173]. This property of nanocomposites to modify its optical properties based on morphological parameters will be useful in a variety of fields such as laser technology, optical communication, data storage and medical diagnostics [176]. Optically transparent dielectric materials like BaTiO$_3$ form excellent host matrices for nanocomposites. BaTiO$_3$ is a highly photostable material having large nonlinear optical susceptibilities at the visible and infrared spectral region and thus have potential for applications in a variety of fields [132,161–163,177–179]. Applications of BaTiO$_3$ nanoparticles as potential biocompatible label has been demonstrated recently in second harmonic imaging [136,180,181] and photothermal imaging using infrared excitation [182]. Further, because of the intrinsic capability of the perovskite structures to host ions of different sizes, it is possible to accommodate a large number of dopants in the BaTiO$_3$ lattices. Metal nanoparticles are one of the promising inclusion materials in nanocomposites due to their unique nonlinear optical properties at the surface plasmon resonance wavelength. These nanoparticles can easily be incorporated in to the BaTiO$_3$ matrix by sol-gel method or pulsed laser deposition. Enhancement of nonlinear optical properties of amorphous BaTiO$_3$ matrix by the addition of different metal nanoparticles such as silver [113,115], iron [123], rhodium [111], cerium [183,184] and gold [23–27] are reported in the literature. These composites show interesting

nonlinear optical properties with the magnitude and sign of the nonlinearity depending critically on the fill fraction of the nanoparticle [115]. Among the various nanoparticle inclusions, gold nanoparticles are of particular interest from the point of view of applications in the field of nonlinear optics. Gold nanoparticles have plasmon resonance absorption in the visible region of the electromagnetic spectrum and Au/BaTiO$_3$ nanocomposites show fascinating optical properties when excited near this wavelength. Further the size and shape of gold nanoparticles can control the surface plasmon resonance wavelength and consequently the nonlinear optical properties [187–194].

Many groups have investigated the nonlinear properties of Au/BaTiO$_3$ nanocomposites by employing various experimental approaches such as Z-scan technique and optical Kerr effect (OKE) experiment with different excitation wavelengths and pulse durations [116–118,185,186]. Otsuki *et al.* investigated the effects of size and shape of gold nanoparticle on the third order optical nonlinearity of Au/BaTiO$_3$ thin films prepared by sol-gel method and reported a decrease in $\chi^{(3)}$ with increase in the annealing temperature [116]. The change in $\chi^{(3)}$ is attributed to the change in the size of gold nanoparticle and to structural changes in the BaTiO$_3$ matrix. At the same time Yang *et al.* observed an increase in $\chi^{(3)}$ values of Au/BaTiO$_3$ thin films with increase in annealing temperature and the samples showed ultrafast response with delay times of 150 fs [117]. Guohong *et al.* measured the third order nonlinear susceptibility of Au/BaTiO$_3$ through off-resonance femtosecond Kerr effect and modeled the particle size dependence of the nonlinearity using Mie scattering theory [185]. Liu *et al.* reported ultrafast response time and large third order susceptibility of Au core CdS shell nanoparticles embedded in BaTiO$_3$ thin films [186]. Ning *et al.* fabricated hexagon shaped Au nanoparticle arrays embedded in BaTiO$_3$ matrix by using double layer nanosphere lithography and pulsed laser deposition (PLD) and nonlinear optical properties of films are measured by a Z-scan technique [118]. W Wang *et al.* studied the nonlinear optical properties of two gold concentrations in the BaTiO$_3$ matrix prepared by PLD with Z-scan technique and found that at high metal concentration the coupling factor $(\text{Im}(\chi^{(3)})/\text{Re}(\chi^{(3)}))$ increases significantly [195]. In another work W Wang *et al.* reported the change in sign of nonlinear absorption and nonlinear refractive index for Au/BaTiO$_3$ samples with same gold concentration but with different morphology of gold and BaTiO$_3$ [122]. The large variation in the nonlinear optical susceptibility of Au/BaTiO$_3$ nanocomposites found in these experiments is

attributed to the enhancement of the local electric field near the metal nanoparticles by the presence of dielectric medium.

The nonlinear optical studies reported so far on Au/BaTiO$_3$ nanocomposites mostly deal with gold nanoparticles in amorphous BaTiO$_3$ matrix. The literature shows differing reports on the variation of nonlinear optical properties with annealing temperature and the dependence of the nonlinearity on particle size or fill fraction is still not well studied. In particular there is a glaring lack of data on the influence of molar ratio of Au/Ba in Au/BaTiO$_3$ composites on its nonlinear properties. The molar ratio of Au/Ba is a central parameter that would allow one to tune the nonlinear absorption in Au/BaTiO$_3$ nanocomposites, an important property useful in many device applications. In this work we synthesized pure BaTiO$_3$ nanoparticles and gold nanoparticles incorporated crystalline BaTiO$_3$ films having three different fill fractions using sol-gel technique in identical fashion. The third order nonlinear optical susceptibilities of the four sets of samples are measured using open aperture single beam Z-scan technique. The nature of nonlinear absorption and the absorption coefficient (β) is determined from the Z-scan transmittance curve and the dependence of β on the fill fraction of gold nanoparticles is compared to that predicted for nanocomposites in Maxwell Garnet geometry.

4.2. Nanocomposite geometry

The linear and nonlinear optical properties of nanocomposites, with length scales such as the size of the nanoparticle and distance between them are much smaller than the wavelength of light, can be modeled with an effective medium approach with an effective dielectric constant [172,173,175]. There are mainly three types of nanocomposite structures which comes under the criteria of effective medium approach [172]. They are Maxwell Garnett geometry, Brueggemann geometry and layered composite geometry.

4.2.1. Maxwell Garnett geometry

In Maxwell Garnett geometry small amount of spherical inclusions are embedded in a host matrix as shown in the figure 4.1. Maxwell Garnet studied the linear optical properties of small amount of spherical inclusion materials in a host matrix and confirmed the effective dielectric constant of the composite depends on the fill fraction of the inclusion material and dielectric constants of both constituents.
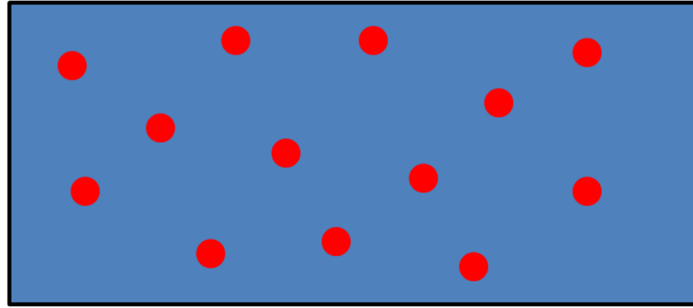
Fig. 4.1: Maxwell Garnett geometry

4.2.2. Brueggemann geometry

In Brueggemann geometry two components are intermixed to form a nanocomposite as shown in figure 4.2.
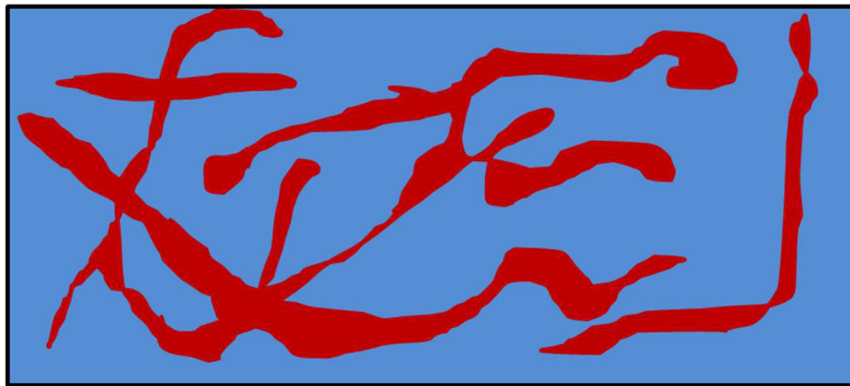
Fig. 4.2: Brueggemann geometry nanocomposites

4.2.3. Layered composite geometry

The layered geometry is formed with alternate layers of two different materials having different linear and nonlinear optical properties as shown in figure 4.3.
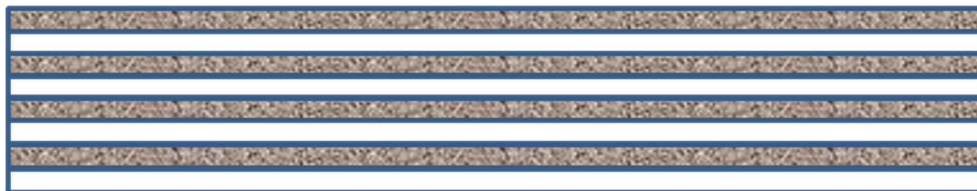
Fig. 4.3: Layered geometry nanocomposites

4.3 Effective medium model

Sipe *et al.* and Boyd *et al.* predicted the conditions for nanocomposites to possess higher nonlinear susceptibility than the constituent materials [172,173]. They have considered the nanocomposite as an effective medium with dielectric constant ε_{eff} for the calculation of propagation of light inside nanocomposite rather than with individual dielectric constants ε_i for inclusion material and ε_h for host matrix. This condition is valid since the size of the nanoparticle and their distances are much smaller than the wavelength of light and the scattering due to the inhomogeneous nature of the composite is insignificant. A typical system under consideration is a nanostructured composite in which a linear or nonlinear nanoparticle is embedded in a host medium which is of linear or nonlinear in nature. The inclusion particles inside the matrix create inhomogeneity in the matrix. This will generate sharp changes in the refractive indices inside the matrix around the inclusion particle. So, the electromagnetic field distribution in the nanocomposites will be completely different from that of the homogeneous matrix. Since the nonlinear polarization depends on the spatially inhomogeneous electric field, it will create changes in the nonlinear optical properties of the composite matrix. This can be explained in terms of local field effects. Local field is the effective field that acts to polarize an individual molecule [172]. Local field (E_{loc}) can be expressed as follows

$$E_{loc} = E + \frac{4\pi}{3} P \qquad (4.1)$$

where E is the macroscopic field and P is the polarization

The total response of the system can be found by performing spatial average over the total system. According Lorentz-Lorenz law

$$\varepsilon = 1 + 4\pi L N \alpha \qquad (4.2)$$

where ε is the linear dielectric constant, α is the atomic polarizability, L is the local field correction factor and N is the number density of molecule. The local field factor can be written as [172]

$$L = \frac{1}{1 - \frac{4}{3}\pi N\alpha} = \frac{\varepsilon + 2}{3} \qquad (4.3)$$

This model can be extended to find the nonlinear optical properties of nanocomposites. The nanocomposites we are interested is thin films in which metal nanoparticles are embedded in a dielectric matrix. The smaller concentration of nearly spherical metal nanoparticles inside dielectric matrix can be considered as Maxwell Garnet geometry. According to Maxwell Garnet the effective dielectric constant (ε_{eff}) of the composite film is given by, [173,175]

$$\varepsilon_{eff} = \varepsilon_h \left(\frac{1 + 2\beta f}{1 - \beta f} \right) \tag{4.4}$$

$$\text{where} \quad \beta = \frac{\varepsilon_i - \varepsilon_h}{\varepsilon_i + 2\varepsilon_h}$$

where f is fill fraction of inclusion material, ε_i and ε_h are the linear dielectric constants of the inclusion and host materials. If we consider that only the inclusion material is nonlinear, then the total displacement (D) for inclusion can be written as,

$$D_i = \varepsilon_i E_i + 4\pi P_i^{NL} \tag{4.5}$$

where P_i^{NL} is the nonlinear polarization for inclusion given by,

$$P_i^{NL} = A_i (E_i . E_i^*) E_i + \frac{B_i}{2} (E_i . E_i) E_i^* \tag{4.6}$$

Here A_i and B_i are the nonlinear response coefficients of the inclusion material. Similarly, using an effective medium concept, we can write similar equation for the composite also. The total displacement for the composite is,

$$D_{eff} = \varepsilon_{eff} E + 4\pi P_{eff}^{NL} \tag{4.7}$$

where, $\quad P_{eff}^{NL} = A_{eff}(E . E^*)E + \frac{B_{eff}}{2}(E . E)E^* \quad$ and ε_{eff} is the effective dielectric constant.

If we consider that only the inclusion material is nonlinear and the host matrix responds linearly to the optical field, the effective nonlinear coefficients for the composite film is given by [172],

$$A = f \left| \frac{\varepsilon + 2\varepsilon_h}{\varepsilon_i + 2\varepsilon_h} \right|^2 \left[\frac{\varepsilon + 2\varepsilon_h}{\varepsilon_i + 2\varepsilon_h} \right]^2 A_i \tag{4.8}$$

$$B = f \left| \frac{\varepsilon + 2\varepsilon_h}{\varepsilon_i + 2\varepsilon_h} \right|^2 \left[\frac{\varepsilon + 2\varepsilon_h}{\varepsilon_i + 2\varepsilon_h} \right]^2 B_i \tag{4.9}$$

where, A_i and B_i are the nonlinear response coefficients of the inclusion. In our sample selection the assumption, only the inclusion material is nonlinear is true for the fact that the dielectric host nonlinear response is very less compared to the inclusion material. Under this assumption, the third order optical nonlinearity of our samples may be written as [172,173]

$$\chi^3(-\omega; \omega, \omega, -\omega) = f \left| \frac{\varepsilon + 2\varepsilon_h}{\varepsilon_i + 2\varepsilon_h} \right|^2 \left(\frac{\varepsilon + 2\varepsilon_h}{\varepsilon_i + 2\varepsilon_h} \right)^2 \chi_m^3(-\omega; \omega, \omega, -\omega) \quad . \tag{4.10}$$

Similarly, one can derive the nonlinear coefficients for the nanocomposite structure where only the host response nonlinear to the incident electric field. In the case where both the host and inclusion material respond nonlinear to the incident optical field the effective nonlinear response coefficients for the composite can be obtained by summing the two contributions. From the equations it is clear that at certain conditions the effective nonlinear susceptibility of the composite can be higher than that of either of its constituents. It is evident from the experiments that the fill fraction or the concentration of metal nanoparticle plays an important role in the modification of nonlinear coefficients of the composites. This ability to tune nonlinear coefficients of metal nano-composites with metal nanoparticle concentration will be useful in many optical device applications.

4.4. Results and discussion

The synthesis and characterization of the BaTiO$_3$ thin films and Au/BaTiO$_3$ thin films explained in chapter 2 is briefly mentioned below. BaTiO$_3$ thin films and Au/BaTiO$_3$ thin films are prepared by sol-gel technique from precursor solutions of BaTiO$_3$ and gold nanoparticle prepared separately. 2.55 g of barium acetate is added in to a stirred mixed solution of acetic acid (10ml) and 2-methoxy ethanol (10ml). After 30 min of stirring, appropriate amount of acetyl acetone is added to stabilize

the solution. 3.4 ml of titanium butoxide is added to the solution and stirred for another 30 min. Finally, the solution is filtered through a 0.22 µm filter paper and aged for one week in vacuum to form $BaTiO_3$ precursor solution. Gold nanoparticles are prepared by citrate reduction method. 20 ml of 24.3 mM $HAuCl_4$ solution is prepared in distilled water and kept for stirred boiling. To the boiling solution quickly added 2 ml of 1% solution of trisodium citrate dehydrate. Stop boiling once the solution turns deep red. Desired amount of gold nanoparticle solution is injected in to the $BaTiO_3$ precursor solution and mixed well to form a uniform solution. $BaTiO_3$ thin films and $Au/BaTiO_3$ thin films are prepared on a microscopic quartz slide ($76 \times 26 \times 1$ mm) by spin coating. Spin coating is done by SCU-2007 (APEX Instruments co.) model spin coating unit. 1 ml of the mixed solution is poured on the quartz slide and coated by rotating at 1500 rpm for 30 s. The coated film is then dried at $60\,^0C$ for 10 minutes and successively heat treated at $750\,^0C$ for 1 hour in the nitrogen atmosphere.

The absorption spectra of the samples are measured by a UV-VIS absorption spectrophotometer (JASCO V-570 UV-VIS-NIR) in the 400-800 nm wavelength range. The crystal structure of the $BaTiO_3$ and $Au/BaTiO_3$ films was studied by X-Ray Diffraction (XRD) technique using Cu-Kα radiation (Rigaku Miniflex II Desktop X-Ray Diffractometer). The high-resolution transmission electron microscope (HRTEM) images of $BaTiO_3$ and $Au/BaTiO_3$ are taken by a FEI make Tecnai G2, F30 machine. The thin films were scratched out from the quartz slide and coated on top of a copper grid for taking HRTEM image.

4.4.1. Nonlinear absorption in $BaTiO_3$ thin films and $Au/BaTiO_3$ thin films

Nonlinear absorption of $Au/BaTiO_3$ thin films with different molar ratio of Au/Ba is studied by a single beam open aperture Z-scan technique. In these experiments the sample is moved along the focal region of a lens and the transmitted intensity is collected by a photodiode. The nature of nonlinear absorption and absorption coefficient (α_2) is determined from the transmittance curve. A frequency-doubled Q-Switched Nd:YAG laser having a pulse width of 5 ns at 532 nm wavelength is used for the open aperture Z-scan. A planoconvex lens of focal length 10.75 cm is used to focus the laser beam and the focal spot radius is 10 µm. The Rayleigh length is 0.6 mm and the on-axis peak intensity of the laser at the focus is 4.8 x 10^{13} W/m^2.

The nonlinear absorption of the quartz slide used as substrate is measured by open aperture Z-scan technique. The quartz slide does not show any nonlinear absorption at 532 nm for the energy selected for the measurements. The sample thickness is estimated from the absorption spectra to be 25 µm. Figure 4.4 (a), (b), (c) and (d) shows the open aperture Z-scan transmittance curve for BaTiO$_3$ and gold embedded BaTiO$_3$ nanoparticles with Au/Ba molar ratio of 1.6/100, 2.5/100 and 4.8/100 respectively. All graphs show a normalized transmittance valley which indicates the presence of nonlinear absorption in the samples. Assuming a Gaussian beam profile, the normalized beam transmittance in open aperture Z-scan can be written as [196],

$$T(z) = \frac{1}{\sqrt{\pi}q_0(z)} \int_{-\infty}^{\infty} \ln\left[1 + q_0(z)e^{-\tau^2}\right] d\tau \tag{4.11}$$

where,

$$q_0 = \frac{\alpha_2 I_0 L_{eff}}{1 + \frac{z^2}{z_0^2}} \tag{4.12}$$

α_2 is two-photon absorption coefficient, I_0 is peak on axis irradiance at the focus, z is position of the sample with respect to the focus of the lens, z_0 is Rayleigh length and L_{eff} is effective length of the sample.

$$L_{eff} = \frac{1 - e^{-\alpha L}}{\alpha} \tag{4.13}$$

where, L is actual length of the sample and α is linear absorption coefficient.

For $|q_0| < 1$, the transmittance equation can be rewritten in summation form,

$$T(z) = \sum_{m=0}^{\infty} \frac{[-q_0(z)]^m}{(m+1)^{3/2}} \tag{4.14}$$

and we may restrict the summation to m = 1. The nonlinear absorption coefficient is determined by fitting the equation (4.14) with $m = 1$ to the transmittance data of the open aperture Z-scan.
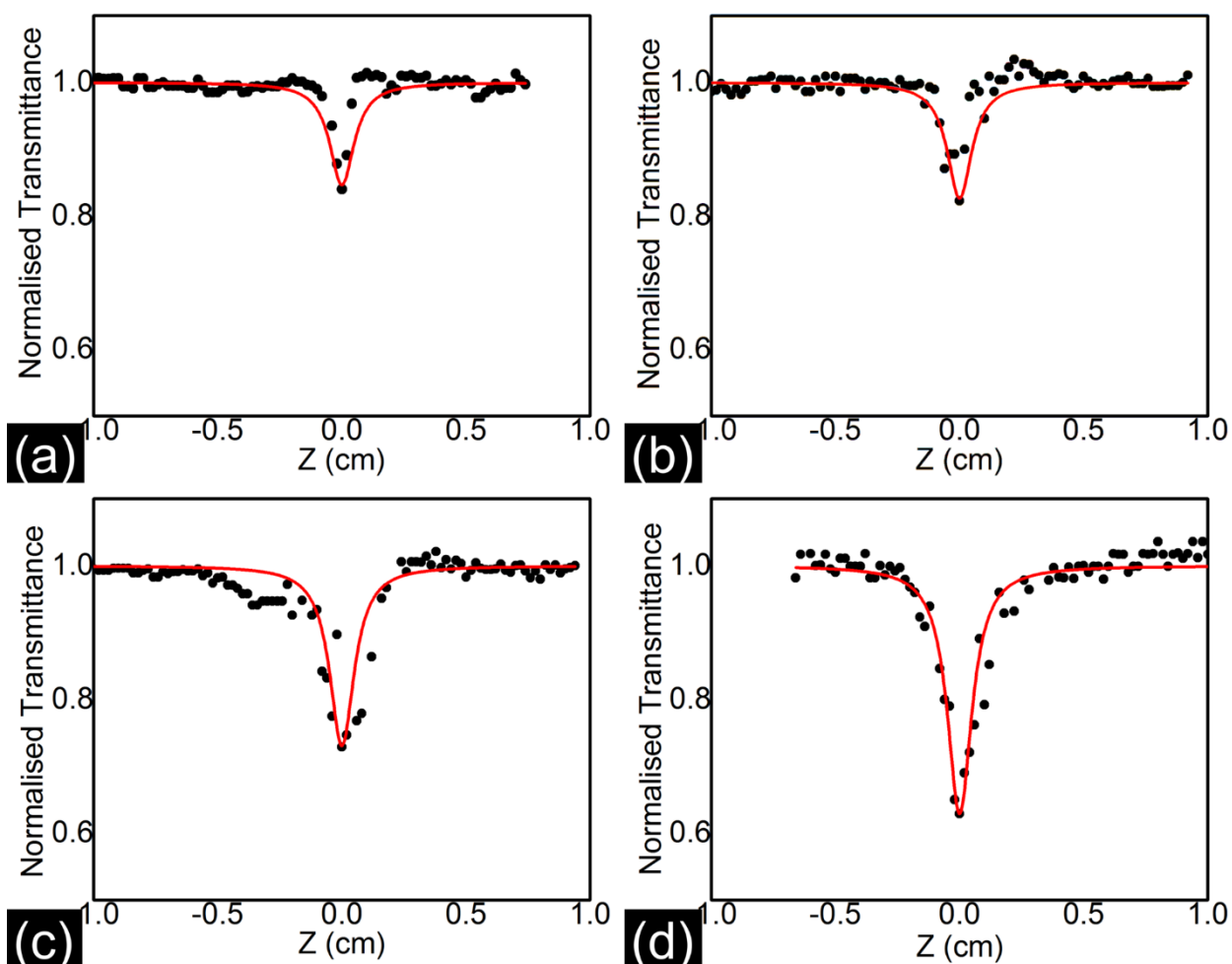
Fig.4.4: Open aperture Z-scan traces of (a) BaTiO₃ thin films and Au/ BaTiO₃ thin films having Au/Ba molar ratio of (b) 1.6/100 (c) 2.5/100 (d) 4.8/100.

The two-photon absorption coefficient estimated as described above for pure BaTiO$_3$ thin films is $(1.0 \pm 0.1) \times 10^{-9}$ m/W. The two-photon absorption coefficient measured for samples of 1.6/100, 2.5/100 and 4.8/100 Au/Ba molar ratio are $(1.5 \pm 0.2) \times 10^{-9}$ m/W, $(2.0 \pm 0.1) \times 10^{-9}$ m/W and $(3.2 \pm 0.2) \times 10^{-9}$ m/W respectively. Figure 4.5 shows the variation of two-photon absorption coefficient with gold concentration in the Au/BaTiO$_3$ films. The data shows an approximately linear increase of nonlinear absorption coefficient of Au/BaTiO$_3$ with the increase in volume concentration of gold nanoparticles. Since the concentration of nearly spherical gold nanoparticle in Au/BaTiO$_3$

films is low, we can consider the sample to be in Maxwell Garnet geometry. According to Maxwell Garnet [175] the effective dielectric constant of the composite film is given by,

$$\varepsilon_{eff} = \varepsilon_h \left(\frac{1+2\beta f}{1-\beta f} \right), \text{ Where } \beta = \frac{\varepsilon_i - \varepsilon_h}{\varepsilon_i + 2\varepsilon_h}$$

where f is fill fraction of inclusion material, ε_i and ε_h are the linear dielectric constants of the inclusion and host materials. The composition dependent nonlinear optical properties of nanocomposites have been theoretically analysed in detail by different groups [172–174,197]. The nature and magnitude of the nonlinearity depends critically on the nonlinear optical properties of the host as well as the inclusion materials. In the case where the host does not show nonlinear behavior, the third order nonlinear optical susceptibility $\chi^3(-\omega; \omega, \omega, -\omega)$ of the composite is given by,

$$\chi^3(-\omega; \omega, \omega, -\omega) = f \left| \frac{\varepsilon_{eff} + 2\varepsilon_h}{\varepsilon_i + 2\varepsilon_h} \right|^2 \left(\frac{\varepsilon_{eff} + 2\varepsilon_h}{\varepsilon_i + 2\varepsilon_h} \right)^2 \chi_m^3(-\omega; \omega, \omega, -\omega)$$

where $\chi_m^3(-\omega; \omega, \omega, -\omega)$ is the third order nonlinear optical susceptibility of the inclusion material. The third order optical nonlinearity of $BaTiO_3$ nanoparticles at 532 nm is of the order of 10^{-9} esu [113,179,183] while that of gold nanoparticle is of the order of 10^{-7} esu [119,191,193]. Hence for simplifying the analysis we may assume that the $BaTiO_3$ matrix show linear behavior in comparison to the nonlinearity of gold nanoparticles. Further since the fill fraction used in the experiment is very small, the effective dielectric constant will be approximately equal to that of the host. Under this assumption, the third order optical nonlinearity of our samples is expected to increase linearly with fill fraction in qualitative agreement with the behavior shown in figure 4.5.

Sample	Au/Ba Ratio (x 10^{-2})	α_2 (x 10^{-9}m/W)
1	0	1.0 ± 0.1
2	1.6	1.5 ± 0.2
3	2.5	2.0 ± 0.1
4	4.8	3.2 ± 0.2

Table 4.1: Dependence of Au/Ba molar ratio on the two-photon absorption coefficient of the Au/BaTiO3 nanocomposites.
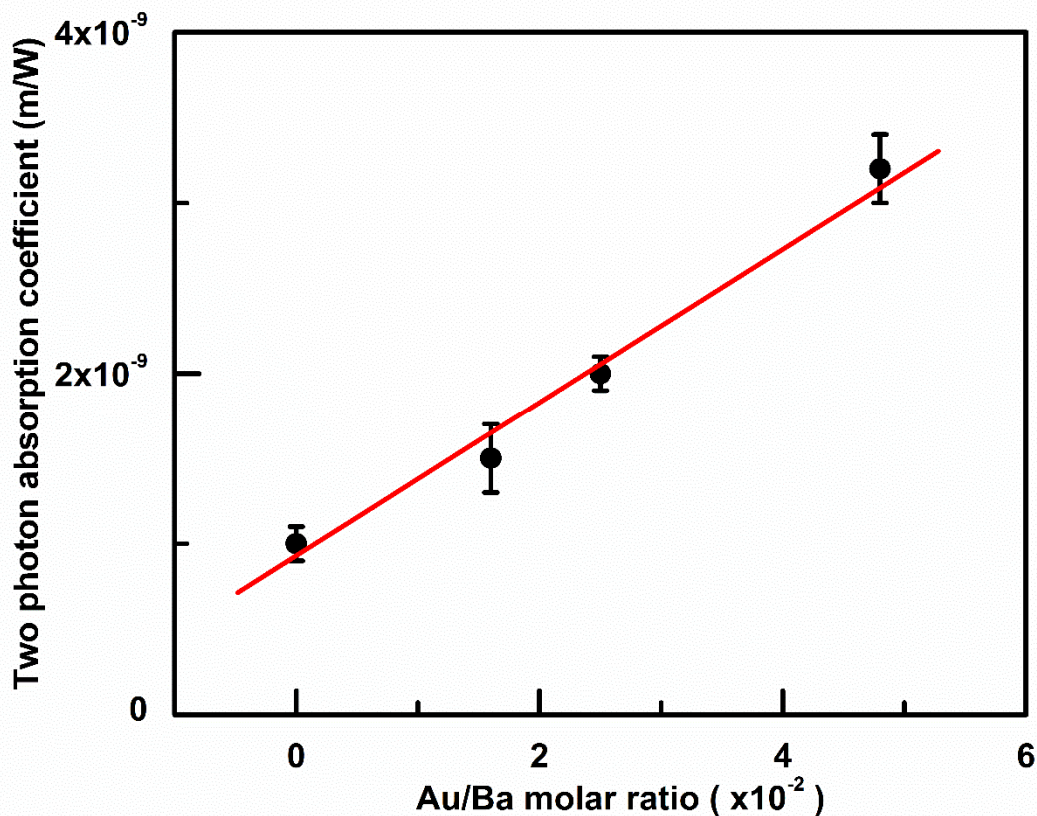
Fig.4.5: Variation of two-photon absorption coefficient with Au/Ba molar ratio in the Au/ BaTiO$_3$ nanocomposite films.

4.4.2 Nonlinear refraction in BaTiO$_3$ thin films

The nonlinear refractive index of BaTiO$_3$ thin film is measured by a closed aperture Z-scan geometry. A femtosecond mode-locked Ti:sapphire laser system (Mira 900, Coherent) operating at 76 MHz, wavelength 750 nm is used for the light source for the Z-scan. The laser pulse width measured by an autocorrelator is 120 fs. The focal length of the lens used is 50 mm. The beam diameter before the lens is 2 mm and the radius at focus was 11.65 µm. The transmitted beam energy and the reference beam energy are measured directly by using photodiodes and their ratio was taken. The Z- scan curve is normalized by using the transmittance when the sample is kept far away from the focus. The sample thickness is estimated from the absorption spectra to be 25 µm.

Figure 4.6 shows the closed aperture Z-scan curve of BaTiO$_3$ thin film. The Z-scan trace indicates positive nonlinear refractive index. Since a wavelength of 750 nm, away from the absorption edge is chosen the nonlinearity could be primarily of non-resonant origin.

For obtaining the nonlinear refractive index n$_2$, we fit the nonlinear refraction curve, by the formula,

$$T(z, \Delta\phi_0) \cong 1 - \frac{4\Delta\phi_0 x}{(x^2+9)(x^2+1)} \qquad , x = z/z_0$$

Here $T(z, \Delta\phi_0)$ is the normalized transmittance and z_0 is the Rayleigh length. Here it is assumed that the primary contribution to the nonlinearity arises from third order effects.
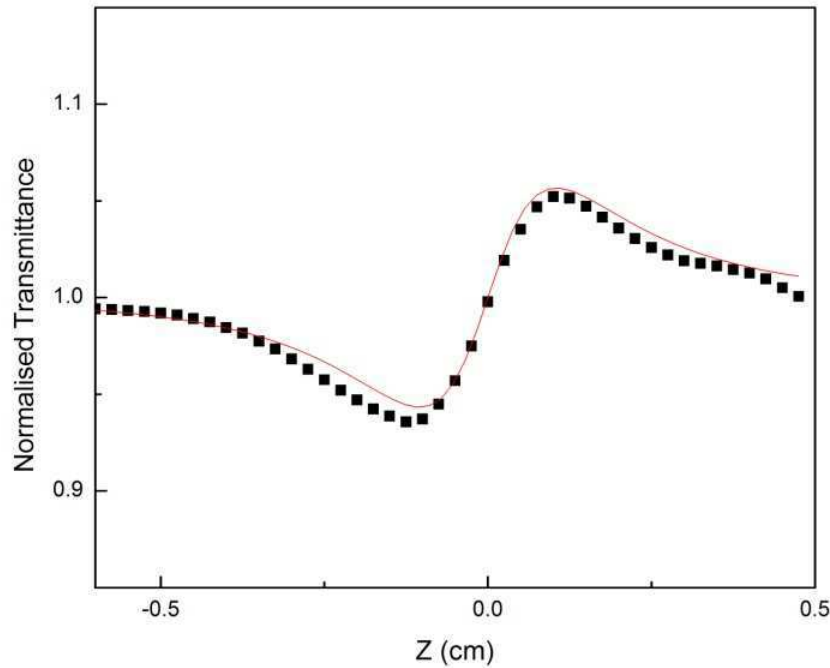
Fig. 4.6: Closed aperture Z -scan data for BaTiO$_3$ thin film. Solid line is the theoretical fit.

The transmitted beam energy and the reference beam energy are measured by two photo detectors. The linear transmittance of the far field aperture S, defined as the ratio of the pulse energy passing the aperture to the total energy, is measured to be 0.3. Peak power at the focus is calculated as 21 GW/cm^2 and the on axis nonlinear phase shift, $\Delta\Phi_0$ obtained from the theoretical fit was 0.35. The

nonlinear refractive index n_2 of the BaTiO$_3$ thin film calculated from the above data is 7.92×10^{-14} cm^2/W.

4.5 Conclusion

In summary BaTiO$_3$ and Au/BaTiO$_3$ thin films with different molar ratio of Au/Ba are prepared successfully by sol-gel method and characterized by X-ray powder diffraction, optical absorption spectroscopy and HRTEM. The two-photon absorption coefficient of the composite films is determined by the single beam open aperture Z-scan method at a wavelength of 532 nm using a 5 ns pulses from a frequency-doubled Q-Switched Nd:YAG laser. Au/BaTiO$_3$ nanocomposites shows enhanced nonlinear optical absorption with the increase of gold nanoparticle concentration in qualitative agreement with that predicted for the Maxwell-Garnet geometry. The property to tune the nonlinearity is important from the point of view of applications in many devices. In the present work we have restricted the fill fraction of gold nanoparticle to 4.8/100 due to coagulation of the sample which is a limitation of the current synthesis procedure. It is possible to further increase the fill fraction by suitably modifying sample preparation methods and efforts are on to achieve this.

Chapter 5: Photothermal characterization of Au/BaTiO$_3$ nanocomposite films

5.1 Introduction

In the previous chapter we discussed the nonlinear optical properties of Au/BaTiO$_3$ nanocomposite films. We presented the results on the nonlinear optical absorption and showed that the two-photon absorption coefficient of Au/BaTiO$_3$ nanocomposite films increases with increasing the concentration of gold nanoparticles in the film. In that work the increase in the concentration of gold nanoparticles was deduced from the Au/Ba molar ratio in the precursor solution from which the films were prepared. We confirmed the presence of gold nanoparticles in the film by analyzing the transmission microscopy images of the film, but we could not quantify the distribution of nanoparticles in the film. This was primarily due to non-availability of appropriate nondestructive characterization tools that can readily determine the distribution of gold nanoparticles in the films. Though scanning electron microscopy can, in principle characterize thin composite films, in practice it is a difficult task due to specific sample preparation requirements and the limited area of scanning possible. In comparison optical microscopic techniques provide a simple and readily available characterization tool that can achieve large area scanning with very little sample preparation. However, since gold nanoparticles are weekly fluorescent it is almost impossible to detect gold nanoparticles in a dielectric host using fluorescent microscopy. It is in this context that the recently developed photothermal microscopy [198–202] which is a promising technique to characterize nonluminescent nanoparticles received our attention. Photothermal microscopy has received enormous attention from researches in recent years due to its potential in bimolecular imaging [203–205]. This is particularly so because of the limitation of the widely popular confocal fluorescence microscopy due to the photostability and phototoxicity of dye labels employed [1,2]. Photothermal imaging using gold nanoparticles could very well be a successful alternative imaging technique in biology and biomedical research.

In this chapter we report on the development of an improved photothermal microscope to detect gold nanoparticles and extend the application of the technique to a hitherto unexplored area: characterization of metallic nanoparticle in a dielectric matrix. We first discuss the basic principles of photothermal microscopy, present experimental results on the detection of gold nanoparticles

having size as small 5 nm and demonstrate capabilities of the photothermal microscopy as a characterization technique for material science. The photothermal images of Au/BaTiO$_3$ nanocomposite films with different molar ratio of Au/Ba are taken and the density and distribution of gold nanoparticle in the films are compared. The method reported here provides a general nondestructive tool to test the presence of metallic nanoparticles in scattering background.

5.2 Photothermal microscopy

Mie theory predicts that the scattering cross section of spherical particles in the nanometer range decreases as R^6 while absorption cross section decreases only as R^3. As a result scattering based detection methods are ineffective in detecting nanoparticles having size much less than the wavelength of light. Absorption based detection methods are handy in such experiments. Photothermal microscopy, an absorption based imaging technique which relies on the thermal distribution around a nanoparticle to detect them, allows detection of single sub-resolution sized and non-luminescent nanoparticles with high sensitivity. This is because, in the absence of fluorescence, non-radiative relaxation processes dominates and excitation with an absorbing radiation results in a temperature change in the nanoparticle and its immediate surroundings. This change in temperature causes a refractive index gradient around the nanoparticle and can be detected using an appropriate sensor. Photothermal microscopy maps this refractive index gradient by employing a second non-resonant probe beam and monitoring the change in the scattered intensity of the probe beam. Photothermal microscopy is thus a pump-probe detection technique where one detects the pump induced temperature variation around a nanoparticle using a probe beam. This method of detection of nanoparticles is free from photobleaching or blinking effects, and thus can be potential alternative for fluorescent based microscopic techniques.

Gold nanoparticles are one of the promising candidates that can be used as a label in photothermal microscopy. This is primarily due to its unique optical properties exhibited near the plasmon resonance wavelength. Gold nanoparticles show strong absorption in the plasmon resonance wavelength, around green region of the spectrum. Since gold nanoparticles are weakly fluorescent, most of the absorbed energy is released as thermal energy, which is a highly desirable measure for a photothermal label. Detection of gold nanoparticles using photothermal microscopy has been reported recently [198–202]. Berciaud *et al.* have succeeded in the detection of gold nanoparticle of size as small as 1.4 nm with photothermal heterodyne imaging [202]. Photothermal effects in

gold nanorods have been successfully employed in cancer cell imaging and selective photothermal cancer therapy in *in vitro* conditions [203,205]. Applicability of photothermal microscopy using gold nanorods in biomolecular imaging has been demonstrated by Tong *et al.* [204,206].

Apart from its potential as a biomolecular imaging technique, photothermal microscopy can have potential applications in many other areas. For example, the technique can be used to detect uniformity and defects in metallic coating such as optical mirrors. It can also find applications in the characterization of semiconductor wafers by studying the thermal profile upon excitation. In the present work we employed photothermal microscopy to characterize gold nanoparticles in $Au/BaTiO_3$ composite films. We employed laser scanning method to raster scan the pump-probe beams over the sample and high signal to noise ratio images of gold nanoparticles in $Au/BaTiO_3$ nanocomposite are acquired at fast timescales with pixel dwell time of $80\,\mu s$. The method provides a nondestructive tool that would allow the detection and characterization of nanoparticles in a dielectric environment. The following sections discuss the sample preparation methods and the experimental setup employed for photothermal imaging.

5.3 Sample preparation

Three types of gold nanoparticles are studied by using photothermal microscope. The gold nanoparticles having an average size 5 nm (Product No. G1402) and 10 nm (Product NO. 1527) used for photothermal imaging are purchased from Sigma Aldrich. Third sample, gold nanoparticle having average size of 25 nm, is prepared in the laboratory by citrate reduction method and size is measured using scanning electron microscope. The samples are diluted by a factor of 1:10 using double distilled water and sonicated for 30 min. The samples for imaging are made on a clean microscopic coverslip of 22 mm x 22 mm area. The coverslips are cleaned by using chromic acid followed by running water and double distilled water. The gold nanoparticle on microscopic coverslip is made by spin coating. Approximately $20\,\mu l$ of the diluted gold nanoparticle solution is added on top of a microscopic coverslip fixed on the sample holder of spin coater and spin coated at 4000 rpm for 60 seconds. The samples are mounted on the microscopic stage of an inverted microscope. The spinning speed and concentration of gold nanoparticles are optimized in such a way that a uniform thin layer of isolated gold nanoparticles is formed on the coverslip. Water is added on the coverslip before taking the images. The $Au/BaTiO_3$ nanocomposite thin films prepared on quartz slide is kept upside down on the microscopic stage and protected with a

microscopic coverslip from the oil immersion objective of the inverted microscope for taking the photothermal images.

5.4 Experimental set up
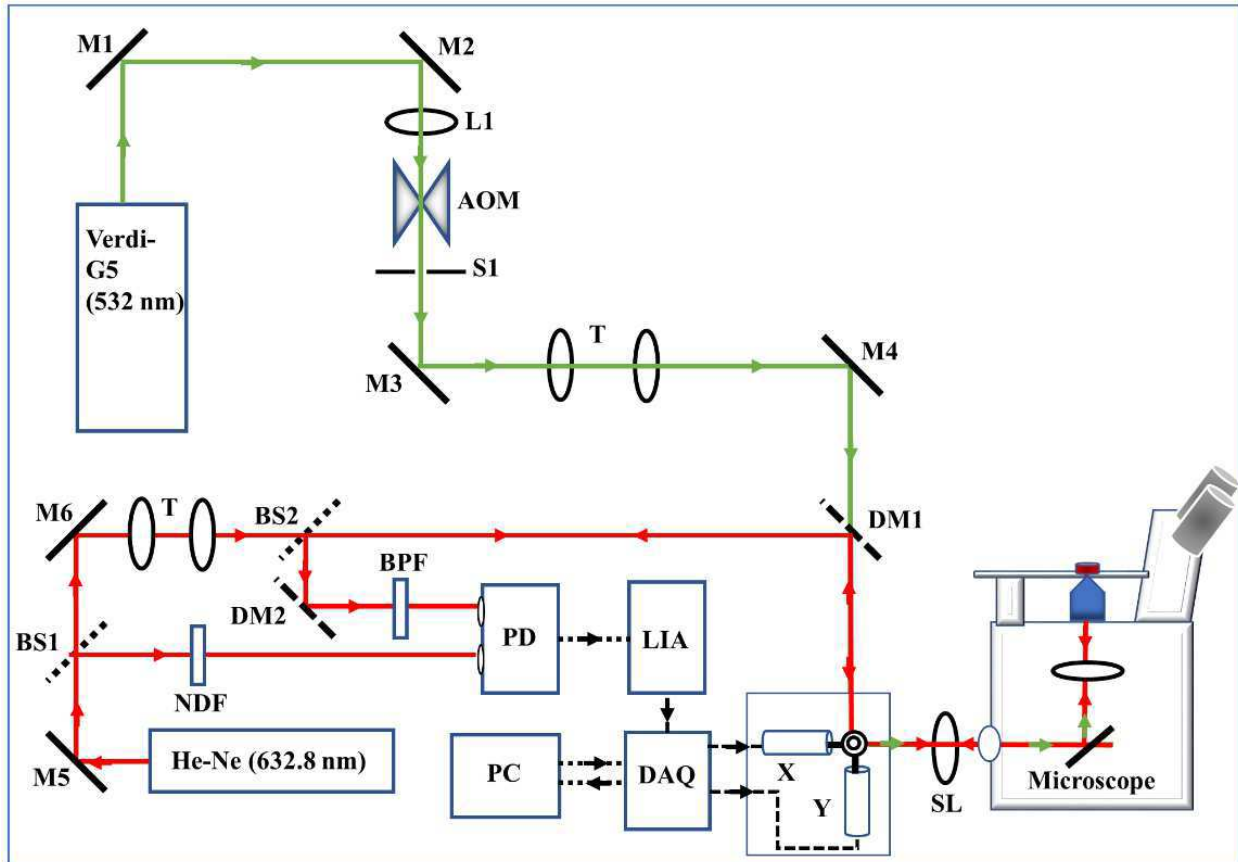
Fig. 5.1: Schematic of the Photothermal microscope. M1-M8: mirrors, BS1-BS2: beam splitters, AOM: Acousto-optic modulator, SL: scan lens, X,Y: scan mirrors, DAQ: data acquisition card, LIA: Lock-in amplifier, DM: Dichroic mirror, PD: photodiode, PC: computer, BPF: band pass filter, NDF: neutral density filter, S1: aperture, T: Telescope.

The experimental set up used for the photothermal microscope is depicted in the figure 5.1. The samples prepared for photothermal microscopy is fixed on a sample stage of an inverted optical microscope (IX 71 Olympus Corporation). A solid-state laser having a wavelength of 532 nm is

used as a pump beam and a He-Ne laser having a wavelength of 632 nm is used for the probe beam. An acousto-optic modulator is used to modulate the pump beam at desired frequencies. Pump modulation frequency used is 115 kHz in this experiment. Both pump and probe beams are made collinear and directed to the sample kept on microscope stage by using proper filters and mirrors. A galvanometric scanner consisting of X and Y mirrors are used to raster scan the beam over a desired area on the sample. X and Y mirrors of the galvanometric scanner oscillated with certain frequencies of sawtooth waves to scan the beam. The backscattered probe beam descanned by the galvanometric scan mirrors is filtered and directed to the detector. A balanced photo diode is used as the detector and the detected signal is given to a lock in amplifier. Pump induced small variation in the probe beam intensity locked at the modulation frequency is detected by the lock in amplifier. National instruments data acquisition card 6251 is used for controlling the scan mirrors and collecting the output signals from the lock-in amplifier. NI-LabVIEW software platform is used for interfacing the scan mirrors and detectors. The data acquision rate used is 1.25 MHz. A 512 pixels x 512 pixels images are acquired in seconds employing 80 μs integration time.

5.5 Results and discussion

Photothermal images of free standing gold nanoparticles in water are first acquired to standardize the set up and make sure that we are detecting single gold nanoparticles. Figure 5.2 (a) shows photothermal images of gold nanoparticles with an average size of 10 nm and 15% distribution in size, spin coated on a microscopic coverslip. A 512 pixels x 512 pixels image is acquired in 20 seconds corresponding to a pixel dwell time of 80 μs. The pixel size used is ≈ 50 nm. The images are acquired using pump power of 2 mW and probe power of 1 mW. Double distilled water is added to the sample before taking the images. Water is a good photothermal medium and it helps in removing scattering from the glass air interface. The signal to noise ratio (SNR) in the image is 43. The SNR is measured as the ratio of the photothermal peak intensity to the standard deviation of the background. While taking each of the images it was verified that the photothermal signal disappears when either of the beams is blocked thereby making sure that no spurious scattered image is detected. Figure 5.2 (b) shows the pseudo 3D image of one of the particle shown in the figure 5.2 (a). Figure 5.2 (c) shows the photothermal signal profile of one of the particle in the figure 5.2 (a). The FWHM of the plot profile gives the resolution of the photothermal microscope. The FWHM measured is 190 nm. In order to further confirm that we are indeed detecting single

nanoparticles, we compared the intensity distribution of the particles in the image to that of the size distribution of the gold nanoparticles. Since the photothermal intensity should scale with the volume of the particles, the corresponding photothermal intensity distribution is expected to be three times that of the particle size distribution. Figure 5.2 (d) shows the photothermal intensity histogram of 10 nm gold nanoparticle with a size distribution of 15 %. The percentage distribution in intensity is 47±6 % in agreement with expected value. We further tested the capability of the photothermal microscope to detect a smaller size gold nanoparticle, 5 nm. Figure 5.3 (a) shows the photothermal image of gold nanoparticles having an average size of 5 nm with a size distribution of 15 % prepared on a microscopic coverslip by spin coating at 4000 rpm for 30 s. The pump and probe powers used at the sample is 3 mW and 1 mW respectively. The SNR in the image shown is 38. Figure 5.3 (b) depicts the pseudo 3D image of one of the gold nanoparticle having an average size of 5 nm corresponding to the thermal profile generated. Figure 5.3 (c) shows the photothermal signal profile for a 5 nm single gold nanoparticle. The FWHM of the plot profile is 170 nm. Figure 5.3 (d) shows the photothermal intensity histogram of 5 nm gold nanoparticle. As expected the percentage distribution in intensity is found to be 51±9 %.
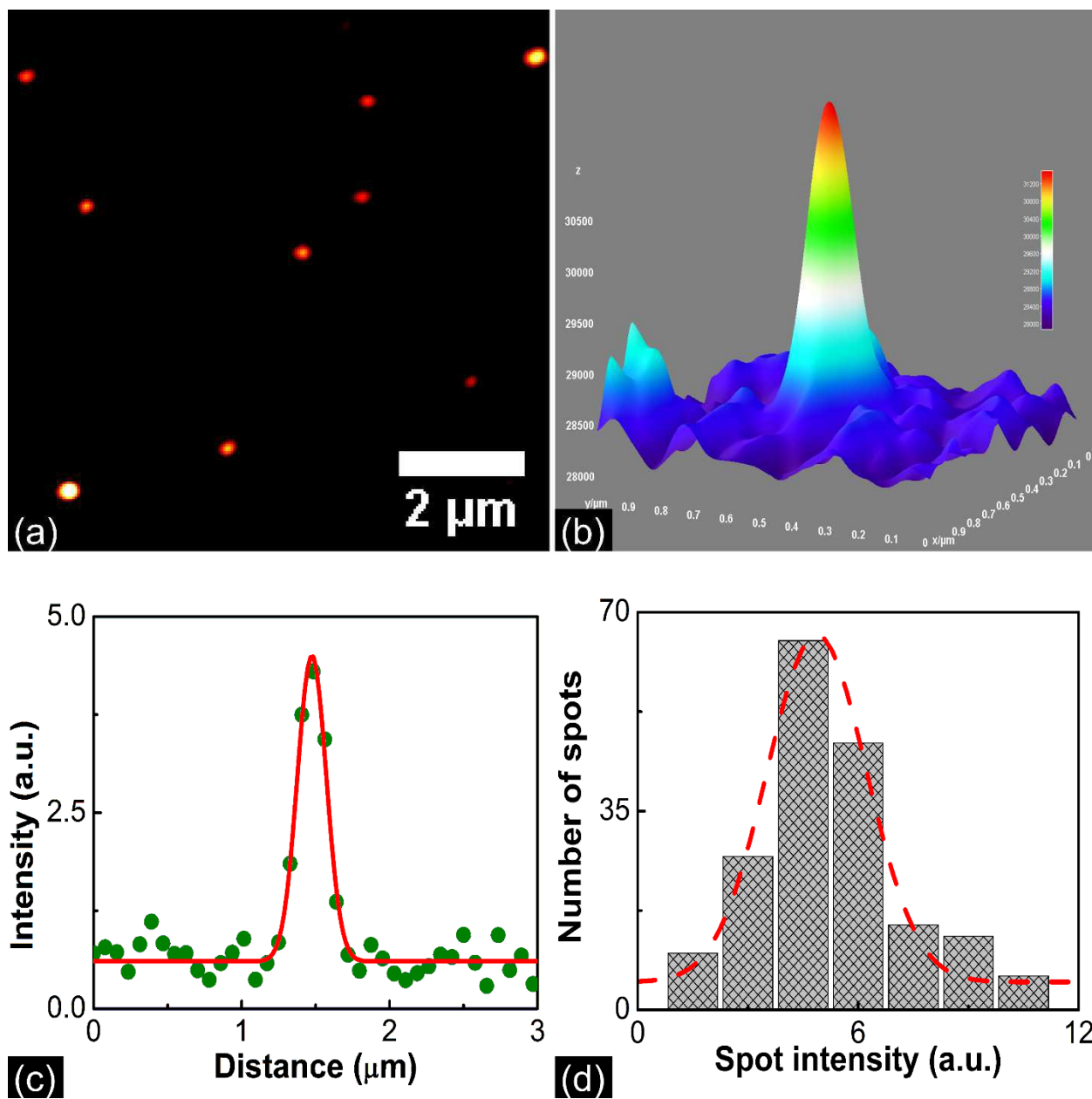
Fig. 5.2: (a) Photothermal image of gold nanoparticle having an average size of 10 nm with a 15% distribution in size spin coated on a microscopic coverslip at 4000 rpm for 30 s. The pump and probe powers employed for taking images are 2 mW and 1 mW respectively. Water added on coverslip act as the photothermal medium. The SNR of the images is 43. (b) Pseudo 3D image of one of the gold nanoparticle shown in (a) corresponding to the thermal profile generated. (c) Photothermal signal profile of one of the 10 nm gold nanoparticle in figure (a). The FWHM of plot profile is 190 nm. (d) Photothermal intensity histogram of gold nanoparticle of 10 nm. The percentage distribution in intensity is 47 ± 6 %.
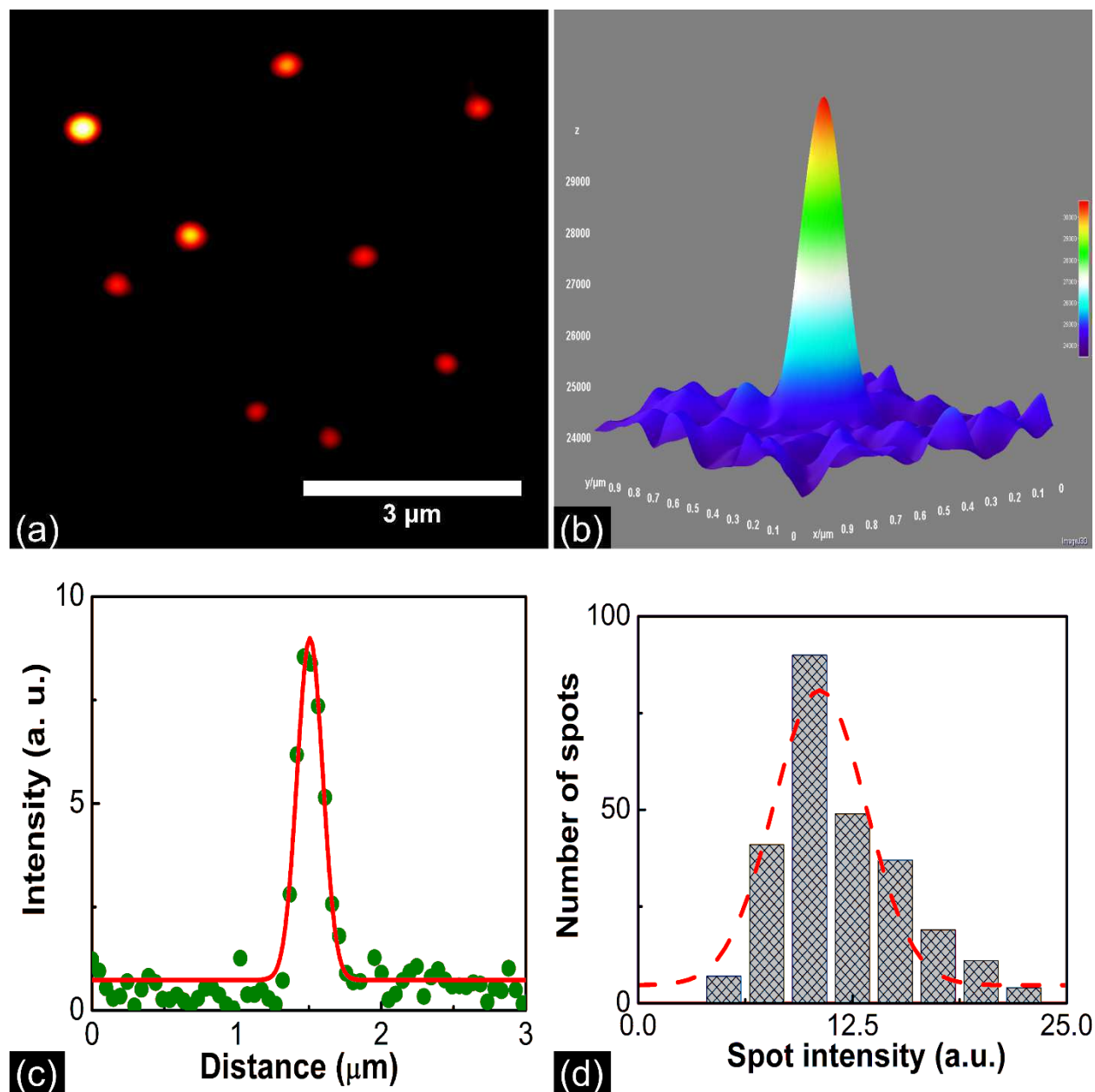
Fig. 5.3: (a) Photothermal image of gold nanoparticle with average size 5 nm and a distribution of 15% in size, spin coated on a microscopic coverslip at 4000 rpm for 30 s. The SNR in the image shown is 38. (b) Pseudo 3D image of single gold nanoparticle corresponding to the thermal profile generated. (c) Photothermal signal profile of single gold nanoparticle in the photothermal image. The FWHM is measured is 170 nm. (d) Photothermal intensity distribution histogram of gold nanoparticles with a 5 nm average particle size. The percentage distribution in intensity is 51±9%. Since the photothermal intensity scale with volume of particle, the intensity distribution is expected to be three times that of the particle size distribution.

The gold nanoparticles used in the study of Au/BaTiO$_3$ nanocomposite is further investigated with photothermal microscope. The gold nanoparticle is synthesized by citrate reduction method and characterized by scanning electron microscopy. The average particle size measured from SEM images is 25 ± 4 nm. The figure 2.16 (a) showing the SEM image and (b) particle size distribution is reproduced as figure 5.4 (a) and (b).
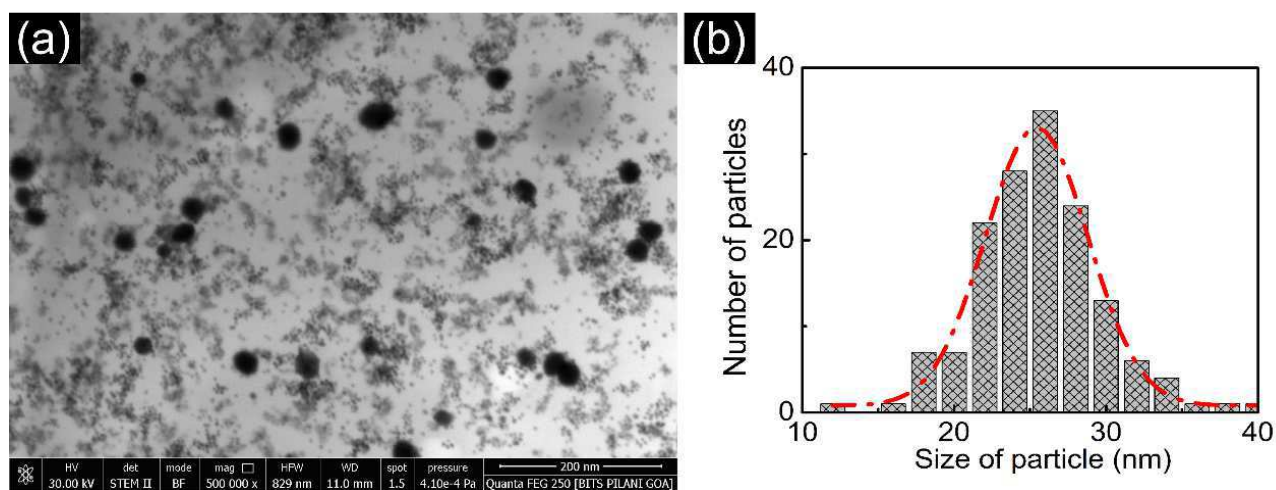
Fig. 5.4: (a) SEM image of the gold nanoparticle prepared by NaBH$_4$ reduction method. (b) Shows the particle size distribution measured from SEM image. The red line indicates the Gaussian fit. The particle size measured is 25 nm ± 4 nm.

Figure 5.5 (a) shows the photothermal image of gold nanoparticles having an average size of 25 nm synthesized by citrate reduction method. A thin films of gold nanoparticle is prepared on a microscopic coverslip by spin coating at 4000 rpm for 30 s. The pump and probe powers used for the study are 2 mW and 1 mW respectively. The SNR of the images shown is 56. Figure 5.5 (b) depicts the pseudo 3D image of single 25 nm gold nanoparticle corresponding to the thermal profile generated. Figure 5.5 (c) shows he photothermal signal intensity profile corresponding to a single gold nanoparticle. The FWHM of photothermal intensity profile is 200 nm. Figure 5.5 (d) shows the photothermal intensity distribution histogram. The percentage of distribution in intensity is found to be 89±9 %, which is in accordance with the expected value.
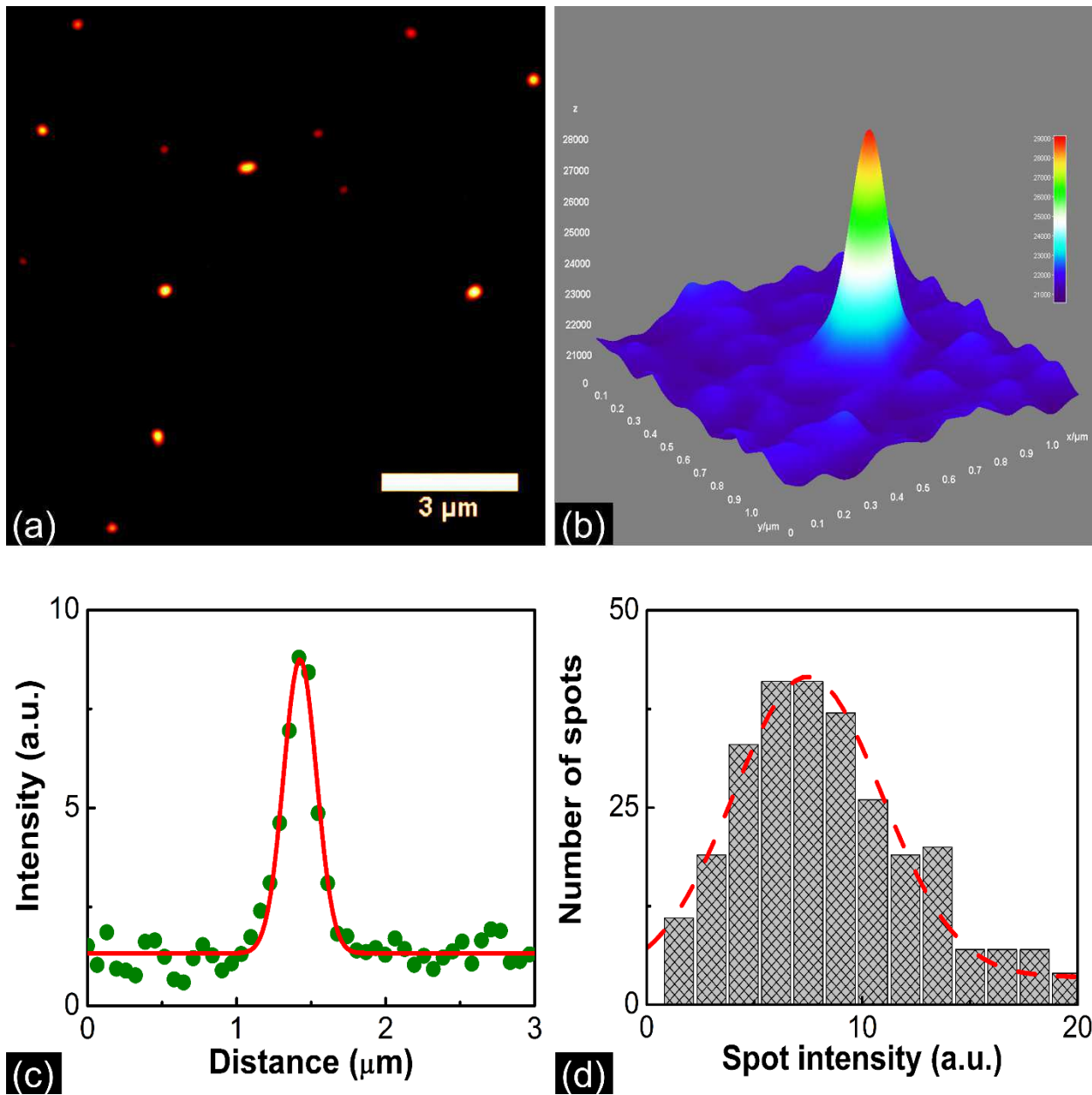
Fig. 5.5: (a) Photothermal image of gold nanoparticle of average size 25 nm synthesized by citrate reduction method spin coated on a microscopic coverslip at 4000 rpm for 30 s. The pump and probe powers used for imaging are 2 mW and 1 mW respectively. The SNR in the images shown is 56. (b) pseudo 3D image of single 25 nm gold nanoparticle corresponding to the thermal profile generated. (c) photothermal signal intensity profile corresponding to a single gold nanoparticle. The FWHM of photothermal intensity profile is 200 nm. (d) shows the photothermal intensity distribution histogram. The percentage of distribution in intensity is found to be 89±9 %, which is in accordance with the expected value.

Au/BaTiO$_3$ nanocomposite films with different Au/Ba molar ratio are prepared by sol-gel technique and characterized by X-ray diffractometer, UV-VIS-NIR absorption spectrophotometer and high-resolution transmission electron microscope. The details of the preparation and characterization of Au/BaTiO$_3$ nanocomposite films is given in chapter 2, section 2.5. Au/BaTiO$_3$ nanocomposites having Au/Ba molar ratios, 1.6/100, 2.5/100 and 4.8/100 are imaged by photothermal microscopy. Photothermal images of the three sets of samples are acquire as detailed above. In all samples, images of 40 μm x 40 μm area of the sample is acquired. A 512 pixel x 512 pixel image is acquired in 20 s with a pixel integration time of 80 μs. The pixel size used is 80 nm. Figure 5.6 shows the photothermal image of Au/BaTiO$_3$ nanocomposite thin film having Au/Ba molar ratio of 1.6/100. From the images it is clear that the distribution of gold nanoparticles is not uniform in the films. Moreover, it was looking like a cluster of gold nanoparticles at some particular area surrounded by an area devoid of gold nanoparticles. This was due to the fact that injected gold nanoparticles in the BaTiO$_3$ precursor solution was not mixed well due to the high viscosity of the precursor solution. In order to improve the uniformity of the sample we further improved the sample preparation. We controlled the viscosity of the precursor solution by varying the amount of acetyl acetone added. The gold nanoparticle injected BaTiO$_3$ precursor solution is mixed well in a cyclomixer. This helps in preparation of films with better uniformity. Figure 5.7 (a), (b), (c) and (d) shows the photothermal images of four different areas of Au/BaTiO$_3$ nanocomposite film having Au/Ba molar ratio of 1.6/100. The photothermal image of four well separated areas looks similar, which shows the uniformity of the sample with respect to the concentration of the gold nanoparticle. Figure 5.8 (a), (b), (c) and (d) shows the photothermal image of four different areas chosen on the Au/BaTiO$_3$ nanocomposite film having Au/Ba molar ratio of 2.5/100. The image shows a 40 μm x 40 μm area of the sample. Figure 5.9 (a), (b), (c) and (d) shows the photothermal image of four different areas chosen on the Au/BaTiO$_3$ nanocomposite film having Au/Ba molar ratio of 4.8/100. The image shows a 40 μm x 40 μm area of the sample. All the images are acquired by employing a pump power of 3 mW and probe power of 1 mW. A modulated beam having wavelength 532 nm is used as the pump beam and a CW beam having wavelength 632 nm is used as probe beam in this study also. BaTiO$_3$ nanoparticles do not absorb any of these wavelengths of light and are not detected in the images. Gold nanoparticles on the other hand absorb 532 nm wavelength and gives images through photothermal effect. The red spots in the images shown in figure 5.6, 5.7, 5.8 and 5.9 are thus attributed to gold nanoparticles. We

further confirmed this by taking the photothermal image of BaTiO$_3$ thin film. There were no spots detected in the photothermal image of BaTiO$_3$ thin film. Photothermal microscopy thus independently verify the presence of gold nanoparticle in the dielectric film and help us to identify the density and distribution of particles inside the film.
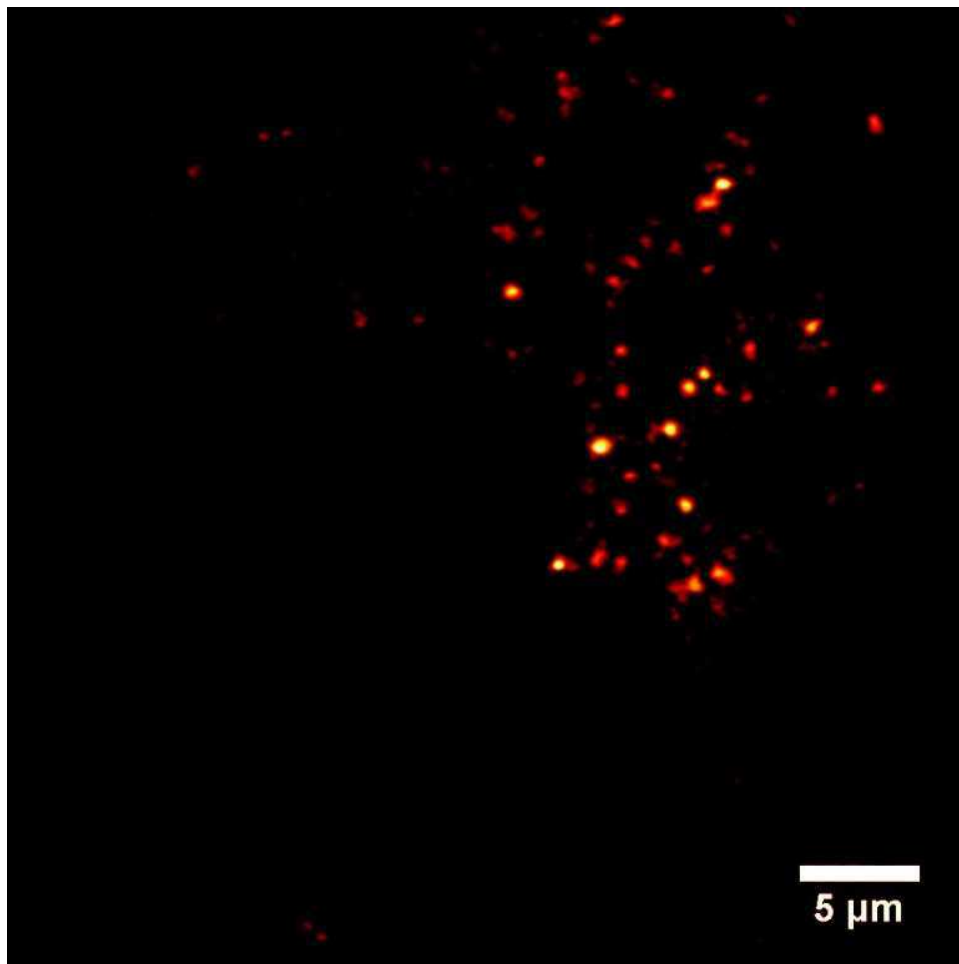
Fig. 5.6: Photothermal image of Au/BaTiO$_3$ films having Au/Ba molar ratio of 1.6/100 prepared without optimizing the dilution and uniformity. The red dots in the films shows the presence of gold nanoparticles in the film. These photothermal images are used to optimize the concentration of precursor solution and preparation methods. The images are acquired by employing 3 mW pump power and 1 mW probe power.
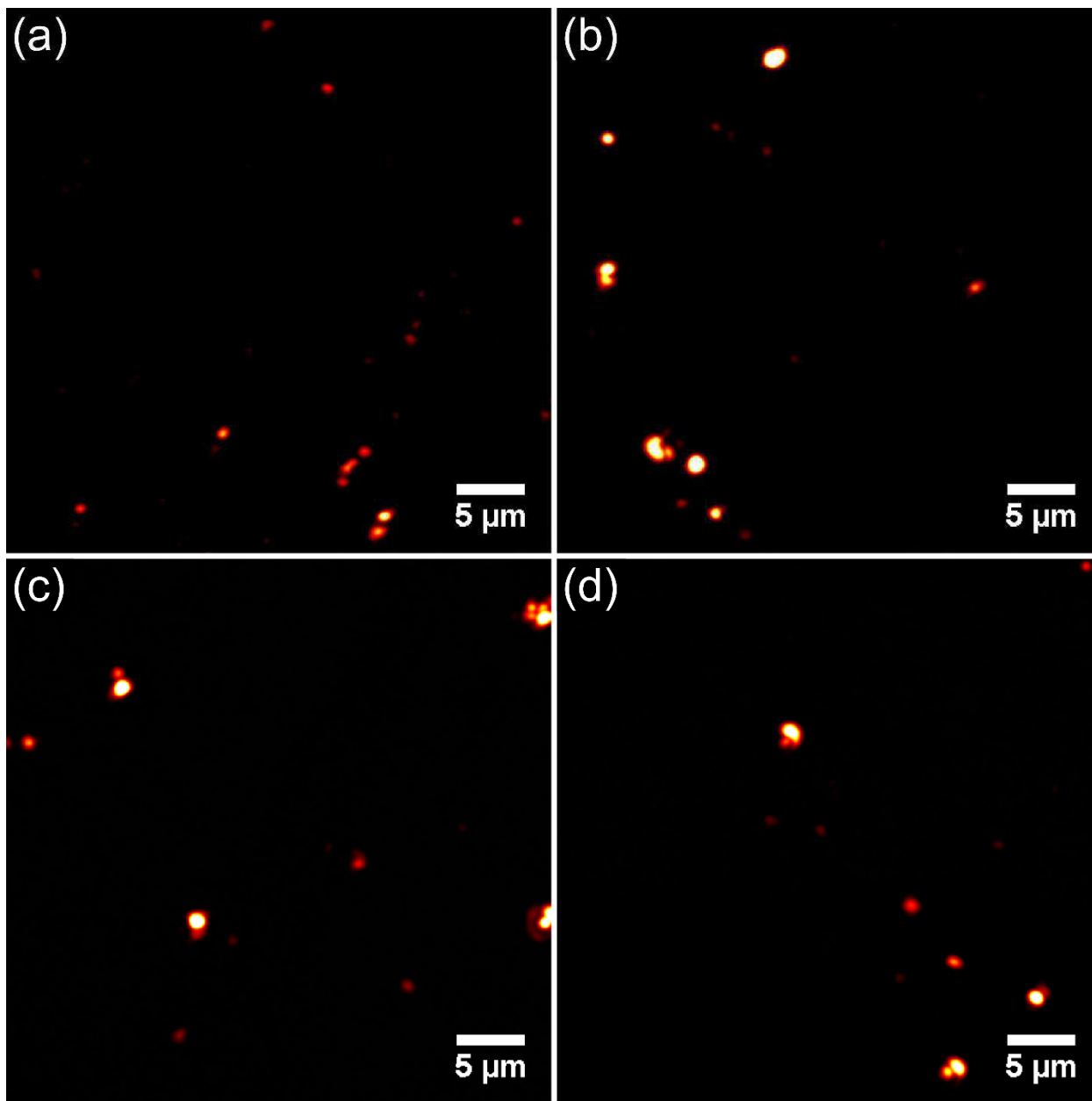
Fig. 5.7: Photothermal image of Au/BaTiO$_3$ nanocomposite films prepared by sol-gel technique with Au/Ba molar ratio of 1.6/100. (a), (b), (c) and (d) shows four different areas of the sample randomly chosen to check the uniformity of the sample. Each figure shows 512 pixel x 512 pixel image taken on an area of 40 μm x 40 μm in 20 s. The pixel integration time is 80 μs and pixel size is 80 nm. The pump and probe powers used for imaging are 3 mW and 1 mW respectively.
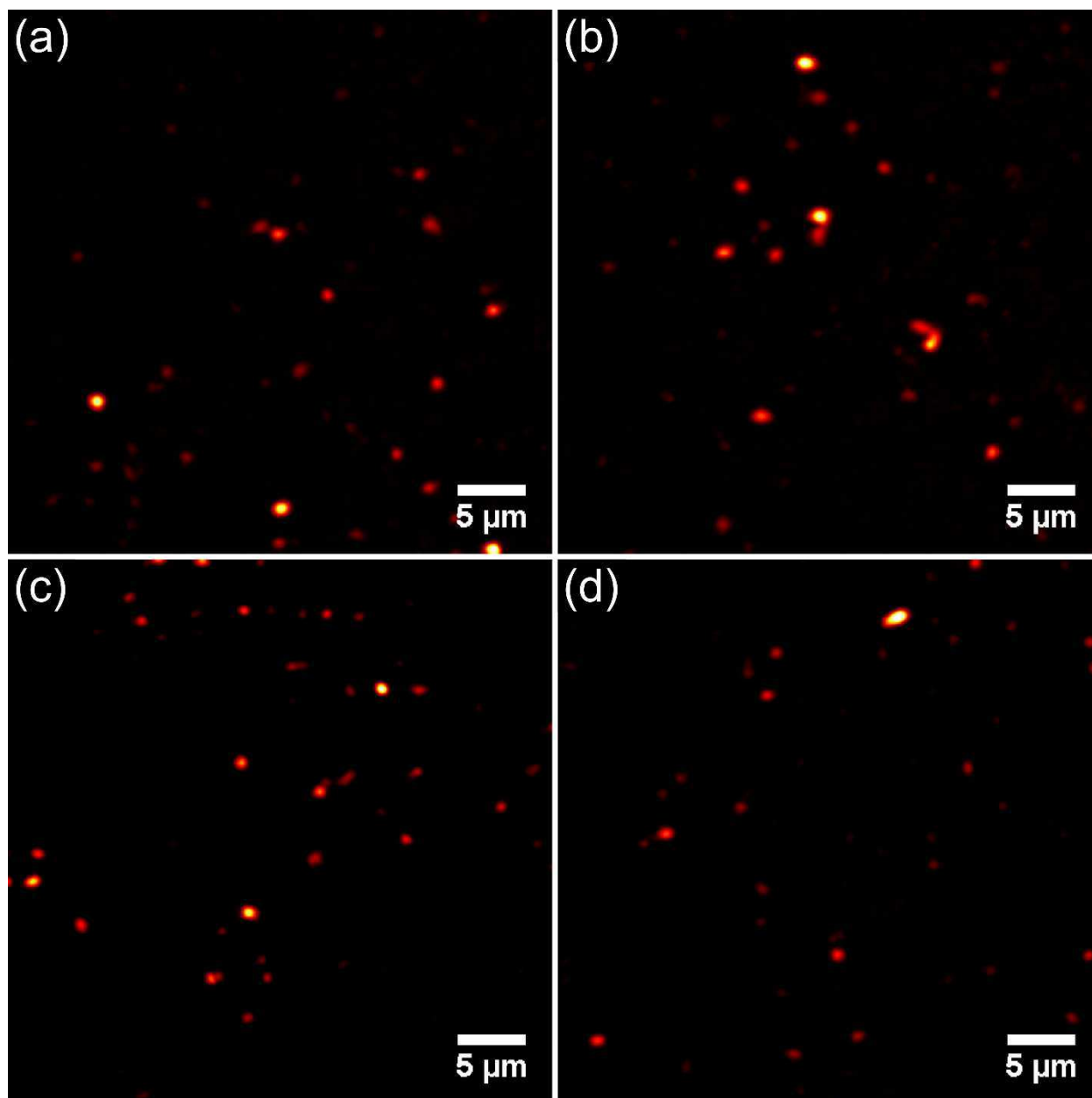
Fig. 5.8: Photothermal image of Au/BaTiO$_3$ nanocomposite films having a Au/Ba molar ratio of 2.5/100. (a), (b), (c) and (d) are photothermal image of four different area of Au/BaTiO$_3$ nanocomposite films. All four images show similar density of gold nanoparticles in the film. 3 mW of pump power and 1 mW of probe power is used to acquire images. A pixel integration time of 80 μs and pixel size of 80 nm is used for making a 512 pixel x 512 pixel image of an area 40 μm x 40 μm of the sample.
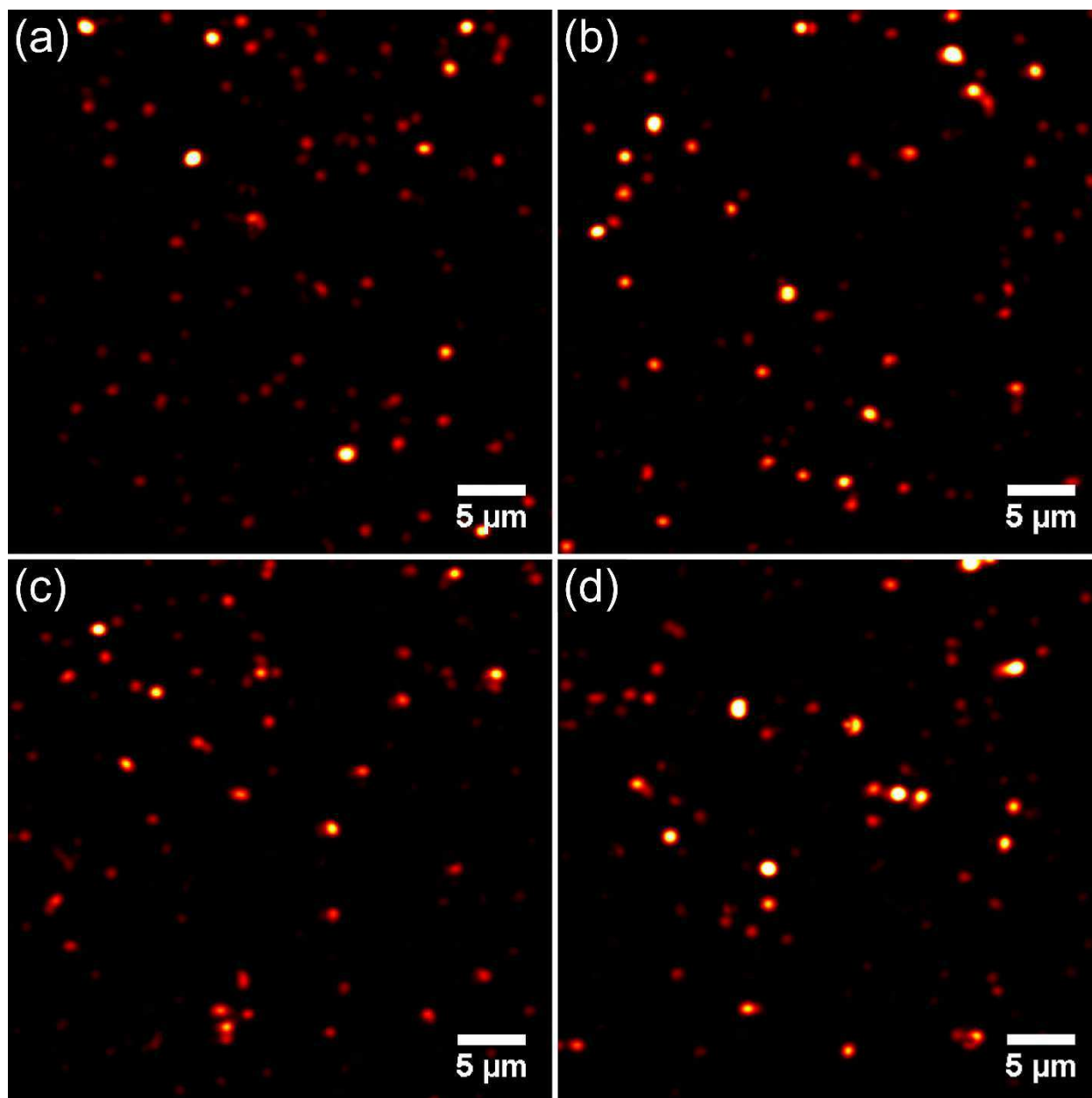
Fig. 5.9: Photothermal image of Au/BaTiO₃ nanocomposite film having Au/Ba molar ratio of 4.8/100. Four different areas (a), (b), (c) and (d) depicts photothermal image of a 40 μm x 40 μm area of the Au/Ba nanocomposite film. All four images show similar distribution of gold nanoparticles in the films. 3 mW of pump power and 1 mW of probe power is used to acquire the photothermal images.

The photothermal images of the Au/BaTiO₃ nanocomposite films give a good qualitative idea of the distribution of gold nanoparticle in the Au/BaTiO₃ nanoparticle films. The photothermal

images of all four randomly chosen areas of Au/BaTiO$_3$ nanocomposite of a particular Au/Ba molar ratio gives similar images. This shows the uniformity of the Au/BaTiO$_3$ nanocomposite films. The gold nanoparticles are evenly distributed in the films, which is a respectable feature in a low-cost sol-gel synthesis method. It helps in the systematic study of the optical properties of the nanocomposites. We further tried to get a qualitative idea about the concentration of gold nanoparticles in the Au/BaTiO$_3$ nanocomposite films by counting the number of spots in the photothermal image. The average number of spots found in the photothermal image of Au/BaTiO$_3$ nanocomposite films having Au/Ba concentration of 1.6/100, 2.5/100, 4.8/100 are 25, 54 and 107 respectively. The values show proportionate increase in the density of gold nanoparticles in concurrence with the Au/Ba molar ratio employed in the synthesis. The small deviation may be due to the small area under consideration.

5.6 Summary

A photothermal microscope is developed to image single, non-fluorescent gold nanoparticles by optical techniques. Gold nanoparticles in water with size as small as 5 nm are detected by the photothermal microscope. Photothermal microscope is successfully employed as characterization tool for characterizing Au/BaTiO$_3$ nanocomposite thin films. Photothermal images of different well separated areas of Au/BaTiO$_3$ nanocomposite films having a particular Au/Ba molar ratio is taken and studied. The images show uniformity in the distribution of gold nanoparticles inside Au/BaTiO$_3$ nanocomposite films. A good qualitative understanding of the distribution of gold nanoparticles in the BaTiO$_3$ matrix is obtained from this study. We further studied the concentration of gold nanoparticles in the Au/BaTiO$_3$ nanocomposite films. We compared the concentration of gold nanoparticles in the films as the number of spots in the photothermal image. We found that the concentration of gold nanoparticles was in agreement with the concertation estimated from the sample preparation. Photothermal microscopy thus independently verify the presence of gold nanoparticle in the dielectric film and help us to identify the density and distribution of particles inside the film.

Chapter 6: Two-photon photothermal microscopy: Biomolecular imaging using BaTiO₃ nanoparticle labels

6.1 Introduction

The ability to detect nanoparticles with high signal to noise ratio in a scattering environments qualify photothermal microscopy to be a potential alternative to fluorescent microscopy, particularly promising from the point of view of biomolecular imaging and biomedical applications. However, photothermal microscopy in its present form makes use of linear optical absorption and is not inherently confocal. Further, the usage of gold nanoparticles as a label necessitates the use of visible light having wavelength around 500 nm as pump beam. This wavelength is not ideal for biomolecular imaging, especially in experiments that involve deep tissue imaging, due to the absorption in biological tissues which ranges from 350 nm to 650 nm. These drawbacks of conventional photothermal microscopy advocate the use of two-photon excitation induced thermal effects as a contrast mechanism in biological imaging. Optical absorption in two-photon excitation microscopy is restricted to the focal plane of the microscope. Hence two-photon excitation microscopy is inherently confocal and would allow deeper penetration. Advantages of two-photon excitation fluorescence microscopy in three dimensional and deep tissue imaging have already been demonstrated [6,7,207]. Recently, Abeyasinghe *et al*. successfully employed two-photon excited fluorescence near-field scanning optical microscopy to image and study monolayer protected gold quantum dots composed of 25 gold atoms [208]. Applicability of two-photon excited photothermal microscopy in direct imaging of micrometer sized red blood cells containing heme proteins has been demonstrated recently [209,210]. However, many of the components of a complex biological system absorbs infrared radiation through two-photon absorption resulting in similar thermal profiles. To avoid this one may have to use very low pump powers limiting the applicability of the above technique to specific systems. One may overcome these difficulties by identifying and employing an appropriate nonlinear optical label possessing good thermal relaxation properties. Further this approach of using a photostable nanoparticle label will be particularly useful in live cell experiments that involve tracking of bimolecular transport.

In this chapter we report on the development of a new nonlinear optical microscope based on two-photon absorption induced photothermal effect capable of detecting individual non-fluorescent nanoparticles with high sensitivity. The confocal microscope, named two-photon photothermal microscope, uses near infrared excitation at high repetition rates and thus would be of interest in deep tissue imaging. High photostability, biocompatibility and the large third order nonlinearity, reported in the previous chapter, make $BaTiO_3$ nanoparticles an ideal label for two-photon photothermal microscope. We demonstrate the capability of the microscope by imaging single $BaTiO_3$ nanoparticles in a scattering environment at fast time scales with a pixel dwell time of 80 µs. We also present 3-dimensional images of $BaTiO_3$ nanoparticles embedded HeLa cells acquired using the two-photon photothermal microscope.

6.2 Two-photon photothermal microscope

Two-photon photothermal microscopy is a pump-probe detection technique where a pump beam excites a nanoparticle sample through two photon absorption. In the experiment we make use of the large third order nonlinear optical susceptibility of $BaTiO_3$ nanoparticles to excite them by means of two-photon absorption using a near infrared wavelength beam whose energy is half the energy difference between the transition levels. $BaTiO_3$ being weakly fluorescent, the two-photon absorption phenomena create a temperature profile around the particle by a non-radiative relaxation process. The corresponding refractive index variation is detected using a non-resonant probe beam. The collinear pump and probe beams are raster scanned over the sample to map the thermal profile of the sample and thus to image a nanoparticle sample. With this technique we can detect $BaTiO_3$ nanoparticles in the size range of 20-100 nm at fast time scales with 80 µs pixel dwell time. The technique has the potential to be a viable alternative to confocal fluorescence microscopy.

Two-photon excited laser scanning photothermal microscopy has several advantages in biological imaging over and above conventional photothermal microscopy. Unlike conventional photothermal microscopy, the technique is inherently confocal and would allow for three-dimensional sectioning of the sample. Because there is no absorption in the out of focus areas, it assures more penetration into the specimen and thus allows deep tissue imaging. Further since near infrared wavelengths are used in the experiment there will be less scattering and thus less loss. A

variety of ferroelectric materials like $BaTiO_3$ and $SrTiO_3$ have shown good nonlinear optical properties.
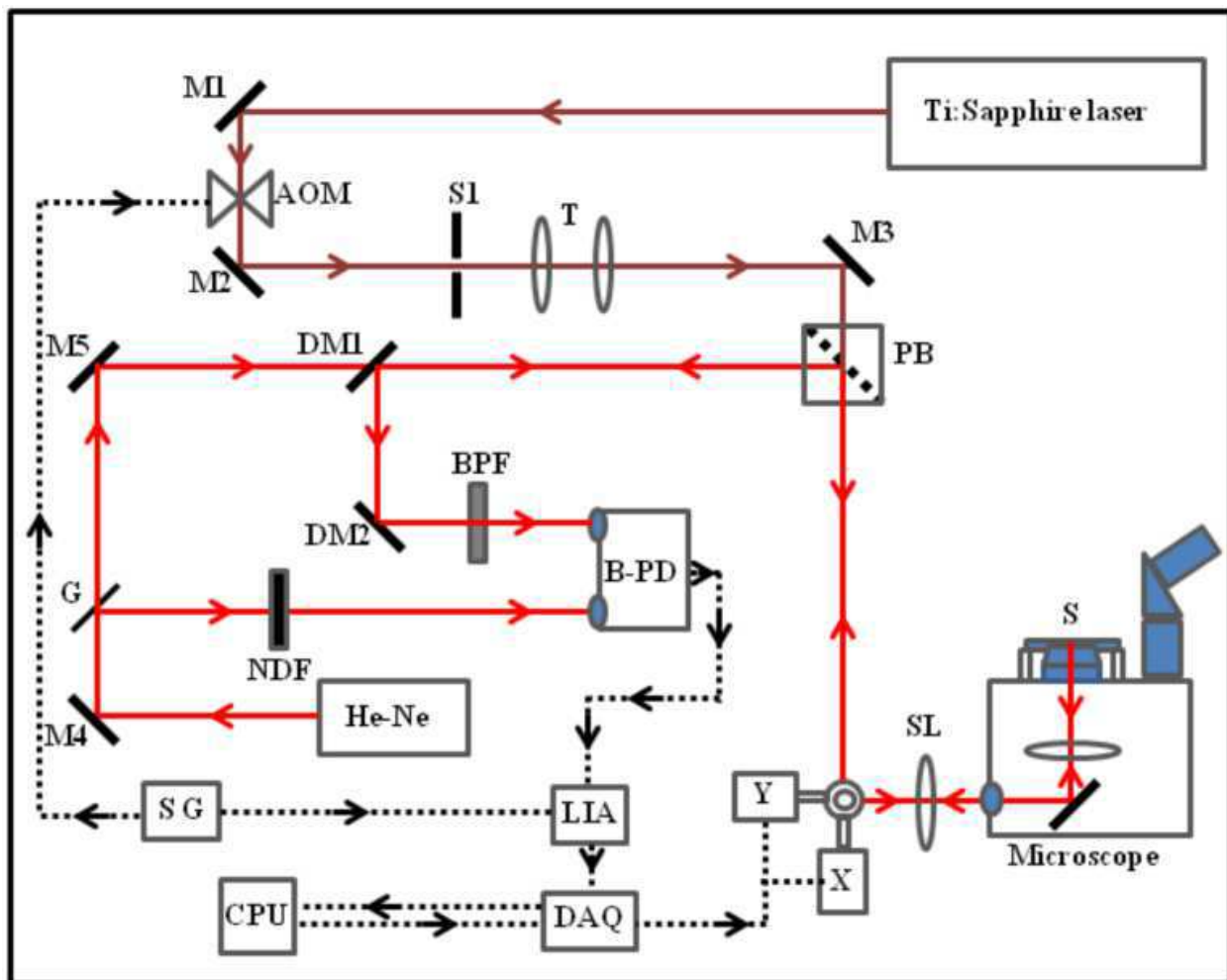
Fig. 6.1: Schematic of laser scanning two-photon photothermal microscope. M: Mirror, AOM: Acousto Optic Modulator, S1: Aperture, T: Telescope, PB: Polarizing Beam splitter, X&Y: Scan Mirrors, SL: Scan Lens, S: Sample, G: Glass slide, NDF: Neutral Density Filter, B-PD: Balanced Photo Receiver, BPF: Band Pass Filter, DM: Dichroic Mirror, DAQ: Data Acquisition card, CPU: Computer, LIA: Lock-In Amplifier, SG: Signal Generator. Continuous line shows the optical path and dotted line represents the electrical signal path.

$BaTiO_3$ nanoparticles, used as a label in the experiments reported in this work, exhibit large two-photon absorption cross section near infrared region and is a biocompatible material that can be easily conjugated with biomolecules of interest [92,135,211]. Further, as an added advantage,

BaTiO$_3$ is low cost, and large variety of preparation techniques are available for in-house synthesis of the nanoparticles [77,83]. The suitability of BaTiO$_3$ nanoparticles in biological imaging has already been demonstrated and is used as a probe in the second harmonic generation (SHG) microscopy [95]. Hsieh *et al.* demonstrated harmonic holographic microscopy with BaTiO$_3$ as second harmonic radiation imaging probes for high resolution 3D imaging of mammalian cells [211]. Culic-Viskota *et al.* successfully employed BaTiO$_3$ as SHG nano probe in the *in vivo* imaging of zebrafish embryos [96]. However, we may note that nanoparticles with cubic crystallization are not suitable for second harmonic generation microscopy because of the inversion symmetry.

Two-photon photothermal microscopy is set up on vibration isolation table (Newport) and standard optical mounts are used to fix all the optical components on the table. Figure 6.1 shows the optical layout of two-photon photothermal microscope. Here we have used a near infrared ~120 fs mode-locked Ti: sapphire laser (Mira 900, Coherent) operating at 76 MHz as the pump laser to excite the sample through two-photon absorption. The wavelength of the laser is tuned to 710 nm to coincide with the two-photon absorption band of BaTiO$_3$. A 632 nm He-Ne laser (Thorlabs, HNL150L) is used as the probe beam. The pump beam is modulated at 115 kHz by an acousto optic modulator (AOM, 1205C-1, Isomet). A polarizing beam splitter combines both pump and probe beam and directs it towards the scan mirrors. The scan lens kept in front of the scan mirrors focuses the pump and probe beam to the conjugate focal plane of an inverted microscope (IX 71, Olympus, 60X, NA 1.25 objective) on which the samples as prepared are mounted. Back scattered probe beam from the sample returns along the same pathway is directed to a large area balanced photo receiver (2307-M, New Focus) by the polarizing beam splitter and two dichroic mirrors (DM1 and DM2). Back scattered pump beam is further filtered off by keeping an interference band pass filter (BPF) (632 ± 10 nm, CVI Melles Griot) in front of the detector. The output of the photo receiver is given to a 200 MHz dual phase lock-in amplifier (SR-844, Stanford Research Systems). A two-dimensional image is obtained by raster scanning the laser beam over the sample with the help of a galvanometric scanner (6215H, Cambridge Technology Enterprises). The three-dimensional sectioning is achieved by moving the microscope objective along the Z-direction. A data acquisition card (NI USB-6251) along with National Instrument LabVIEW software is used for data acquisition as well as for controlling the scan mirrors.

6.3 Sample preparation

In this experiment we use two sets of particles to demonstrate two-photon photothermal imaging 1) commercially purchased (Sigma-aldrich, Product No. 467634) BaTiO$_3$ nanoparticle having cubic structure and an average size of 70 nm and 2) BaTiO$_3$ nanoparticles having an average size of 20 nm synthesized in the laboratory using sol-gel technique. The latter particles have a tetragonal crystal structure as verified by X-ray diffraction technique. The samples for microscopic studies are prepared from a dilute solution of BaTiO$_3$ nano powder in ethanol. 5 mg of BaTiO$_3$ powder is added to 15 ml of ethanol and sonicated for 30 minutes to form a clear solution. This solution is filtered using a 220 nm filter and spin coated on a 22×22 mm cleaned microscopic coverslip at 4000 rpm for 30 seconds. The spinning speed and concentration of BaTiO$_3$ nanoparticles is optimized in such a way that a uniform thin layer of well isolated nanoparticles is formed. Water is added on top of the prepared coverslip before taking the images.

6.4 Results and discussion

Two-photon absorption involves transition of a system from the ground state to a higher lying state by the simultaneous absorption of two photons from an incident radiation field. The rate of two-photon absorption is proportional to the square of the instantaneous intensity I and the optical loss due to absorption is described by the differential equation [212]

$$\frac{dI}{dz} = -\alpha_0 I - \alpha_2 I^2 \tag{6.1}$$

where α_0 is the linear absorption coefficient which in this case arise only from the impurities present, if any. The two-photon absorption coefficient α_2 in this expression is a macroscopic parameter characterizing the material and is related to the imaginary part of the third order nonlinear optical susceptibility $\chi^{(3)}$ by the relation

$$\alpha_2 = \frac{3\omega}{2n_0^2 \epsilon_0 c^2} Im\left(\left(\chi^{(3)}\right)\right) \tag{6.2}$$

where ϵ_0 is permittivity of free space, n is refractive index of the medium, c is speed of light, λ is the wavelength of light and $\omega = 2\pi/\lambda$. If N is the number density of molecules involved in the interaction, the transition rate due to the two-photon absorption process, $R = \sigma_2 I^2/\hbar\omega$ where $\sigma_2 = \hbar\omega\alpha_2/N$ is defined as the two-photon absorption cross section [212]. For a non-fluorescent

material, we may assume that most of the absorbed energy due to two-photon excitation is converted into heat and the nanoparticle would act as a point source of heat. It has been shown that gold nanorods having absorption in the near IR wavelength region efficiently converts absorbed light to heat and this property has been used in photothermal therapy [213].

If the pump beam is modulated sinusoidally at a frequency Ω, then the absorbed power will vary as $P_0[1 + \cos(\Omega t)]$ where the average absorbed power P_0 is proportional to the two-photon absorption cross section and the square of the pump power, P_{pump}. The dissipation of this energy into the medium will cause a temperature profile,

$$\Delta T(r,t) \propto \sigma_2 P_{Pump}^2 / 4\pi\kappa r \left[1 + \cos(\Omega t - r/r_{th}) e^{-r/r_{th}}\right] \tag{6.3}$$

where r is the distance from the particle, $r_{rh} = \sqrt{2\kappa/\Omega C}$ is a characteristic length for heat diffusion, k being the thermal conductivity of the surrounding medium and C its heat capacity. This temperature profile will lead to a time varying refractive index profile $\Delta n(\mathrm{r,t}) = \Delta T(\mathrm{r,t}) \, \partial n/\partial\mathrm{t}$ in the medium. A non-resonant probe beam interacting with this refractive index profile will result in a scattered field which can be used to map the thermal profile of the nanoparticle. In the experimental geometry employed, part of the incident probe field is reflected from sample-coverslip interface. This reflected probe field E_R interferes with the back scattered probe beam E_s. The back scattered probe field is detected through its beatnote at the modulation frequency Ω using a lock-in amplifier. Berciaud *et al.* [214] has carried out a detailed analysis of the polarization variations arising from local susceptibility fluctuations using the theory of light scattering [215]. As per this model the two-photon photothermal signal measured would be proportional to P_{phi} where

$$P_{phi} = n \, \frac{\partial n}{\partial t} \frac{f(\Omega)}{C\lambda_{probe}^2 w_0} \, \sigma_2 P_{Pump}^2 P_{Probe} \tag{6.4}$$

where P_{pump} and P_{pobe} are power of pump beam and probe beam respectively, w_0 is the probe beam focal radius and λ_{probe} is the wavelength of the probe beam. Here the size of the BaTiO$_3$ nanoparticle is much smaller than the wavelength of the incident probe beam and hence the angular distribution of the scattered light is symmetric with respect to the focal plane. Since the spatial extension of the induced susceptibility profile is of microscopic dimensions we may assume that

the frequency dependence of the signal $f(\Omega)$ can be approximated to $1/\Omega$ at high pump modulation frequencies.
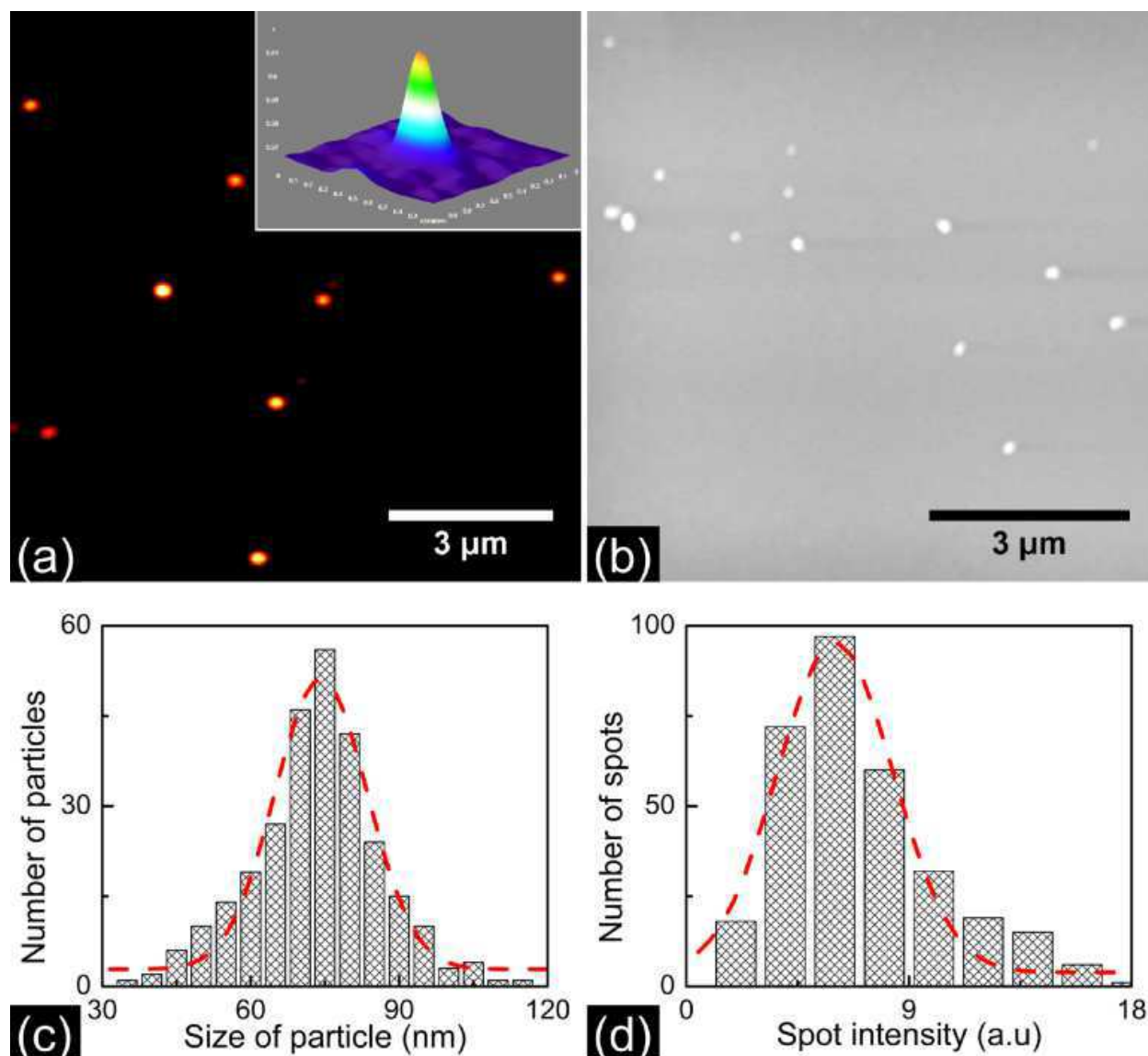
Fig. 6.2: (a) Two-photon photothermal image of the 70 nm BaTiO$_3$ nanoparticles spin coated on a coverslip at 4000 rpm for 30 s. The inset shows the pseudo 3D image of single BaTiO$_3$ corresponding to the thermal profile generated. (b) Scanning electron microscopy image of BaTiO$_3$ having an average size of 70 nm prepared same as above. The figure shows single isolated BaTiO$_3$ nanoparticles on the coverslip. (c) Particle size distribution histogram of BaTiO$_3$ nanoparticle measured from the SEM images. The dotted line shows a Gaussian curve fit. (d) Two-photon photothermal intensity distribution histogram of BaTiO$_3$ nanoparticles.
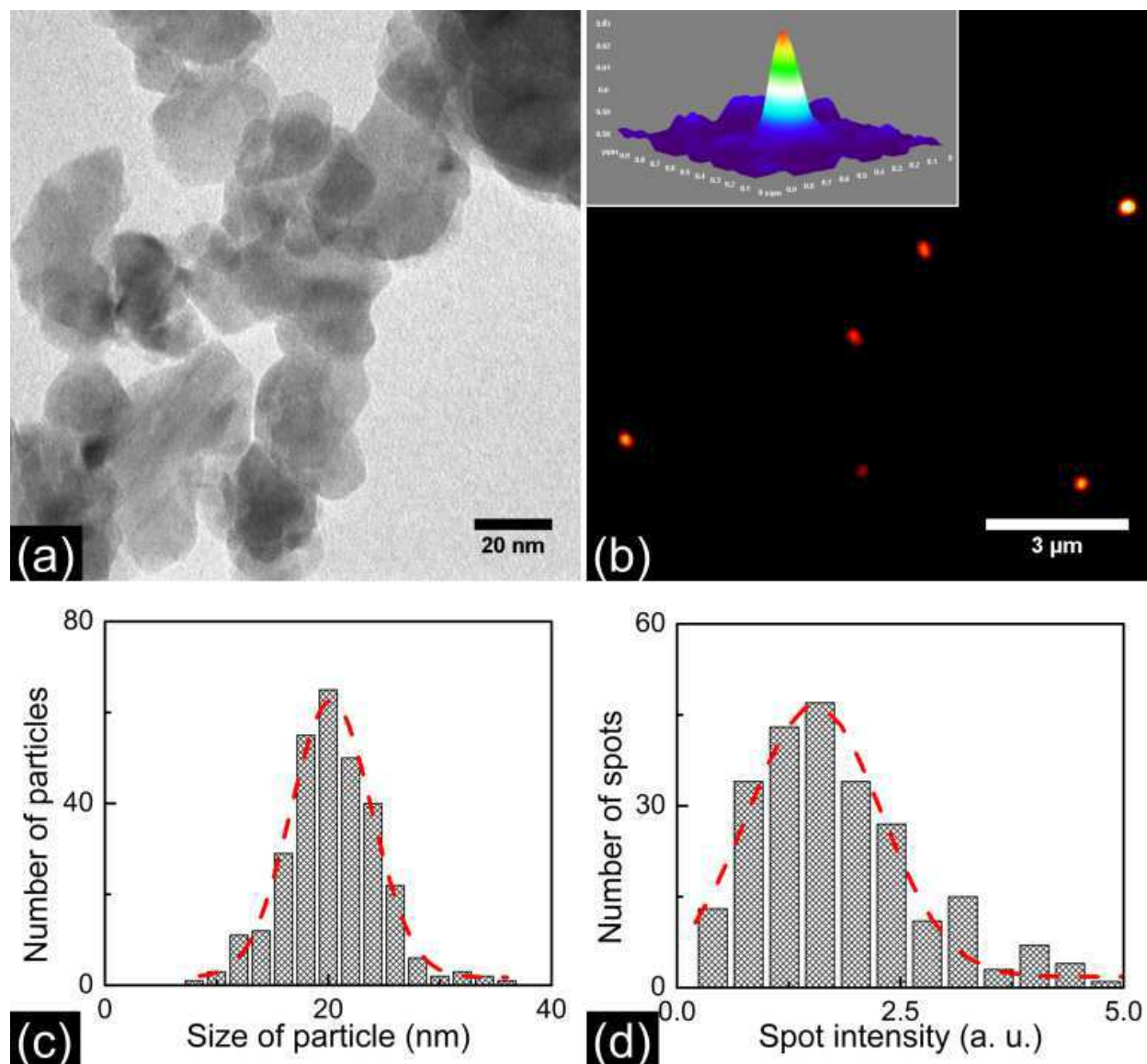
Fig. 6.3: (a) TEM image of BaTiO₃ nanoparticles prepared by sol-gel technique. (b) Photothermal image of 20 nm BaTiO₃ nanoparticles spin coated on a coverslip at 4000 rpm for 30 s. The pump power and probe power used are 8 mW and 0.8 mW respectively. Inset shows pseudo 3D image of single 20 nm BaTiO₃ nanoparticle. The SNR in the images shown is 19. (c) Particle size distribution of BaTiO₃ nanoparticle measured from the TEM images. The dotted line shows a Gaussian curve fit. The average size of BaTiO₃ nanoparticles is 20 nm. The percentage distribution in size is found to be 18 ± 2 %.(d) Two-photon photothermal intensity histogram of BaTiO₃ nanoparticles. The percentage distribution in intensity is found to be 49 ± 6 %.

Figure 6.2(a) shows the two-photon photothermal image of 70 nm $BaTiO_3$ nanoparticles acquired using the microscope as described in the methods section. The inset depicts the pseudo 3D image of one of the 8 particles seen in the figure. The images are acquired using pump pulses having energy of 80 picojoules (6 mW of average power). 0.8 mW of probe power is employed. A 500 x 500 pixel image is acquired in 20 s corresponding to a pixel integration time of 80 μs. The SNR in the images shown is 47. Here SNR is calculated by taking the ratio of the two-photon photothermal signal peak intensity in the image to the standard deviation in the background. While taking the image it was verified that the signal disappears when either of the beams is blocked thereby making sure that no scattered image is detected. In order to make sure that we are imaging single nanoparticles we compared the photothermal images with the scanning electron microscopy (SEM) images of an identically prepared sample. Figure 6.2(b) depicts the SEM image of a sample containing 70 nm $BaTiO_3$ nanoparticles, prepared with the same spin speed as that employed for acquiring the photothermal images. The figure shows that well isolated single nano size particles are formed on the coverslip at the 4000 rpm spin speed employed for preparing the sample. Figure 6.2(c) depict the size distribution of the nanoparticles as determined from the analysis of SEM images. The average particle size determined from the particle size distribution curve is 70 nm. The percentage distribution in size is found to be 13 ± 2 %. In order to further confirm that we are indeed detecting single nanoparticles, we compared the intensity distribution of the particles in the image to that of the size distribution of the synthesized particles. Since the photothermal intensity should scale with the volume of the particles, the corresponding photothermal intensity distribution is expected to be three times that of the particle size distribution. Figure 6.2(d) shows the two-photon photothermal intensity histogram of 70 nm $BaTiO_3$ particle. The percentage distribution in intensity is 41 ± 5 % in agreement with expected value. We further repeated the experiment with smaller nanoparticles synthesized in the laboratory. Figure 6.3(a)shows the transmission electron microscopy (TEM) image of these $BaTiO_3$ nanoparticles. In figure 6.3(b) we show the two-photon photothermal image of a thin film of $BaTiO_3$ nanoparticles having an average size of 20 nm spin coated on a coverslip at a spin speed of 4000 rpm. The inset shows the pseudo 3D image of a single $BaTiO_3$ nanoparticle corresponding to the thermal profile generated. The SNR in the images shown is 19. In Figure 6.3(c) we depict the particle size distribution as determined from the analysis of the TEM images. The average size of $BaTiO_3$nanoparticles is 20 nm. The percentage distribution

in size is found to be 18 ± 2 %. Figure 6.3(d) shows the two-photon photothermal intensity histogram. As expected the percentage distribution in intensity is found to be 49 ± 6 %.
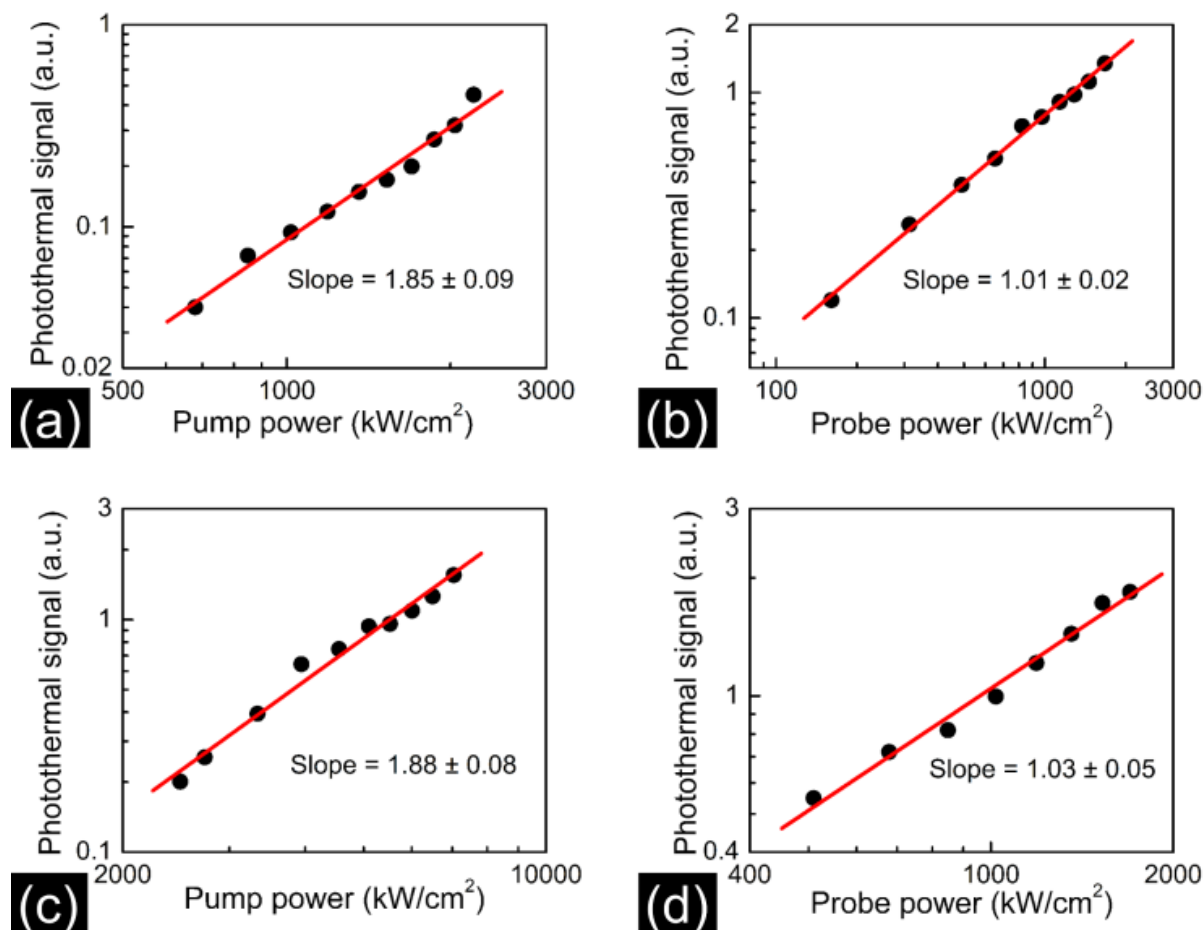
Fig. 6.4: (a) Pump and (b) Probe power dependence of two-photon photothermal signal measured for 70 nm BaTiO$_3$ nanoparticle. The probe power employed in (a) is 0.8 mW and the pump power employed in (b) is 6 mW. (c), (d) shows the pump and probe power dependence of two-photon photothermal signal measured for 20 nm BaTiO$_3$ nanoparticle respectively. The probe power employed in (c) is 0.8 mW and the pump power employed in (d) is 8 mW. The signal varies quadratically with the pump power and linearly with the probe power.

In order to verify the power dependence predicted by equation (6.4) we focused the pump and probe beams on a single nanoparticle and looked at the photothermal intensity as function of incident power. Figure 6.4 (a), (b) shows the pump and probe power dependence of two-photon photothermal signal measured for 70 nm BaTiO$_3$ nanoparticle. The best fit line to the data in Figure

6.4(a) has a slope of 1.85 ± 0.09 which is close to the value of 2 predicted by equation (6.4). Figure 6.4(b) shows that the photothermal signal intensity depends linearly on probe power. Figure 6.4 (c), (d) shows the pump and probe power dependence of two-photon photothermal signal measured for 20 nm $BaTiO_3$ nanoparticle respectively. Similar pump and probe power dependence is observed for both sets of particles.

6.5 Biomolecular imaging

The applicability of two-photon photothermal microscopy in bioimaging is demonstrated by imaging PLL coated $BaTiO_3$ nanoparticle internalized HeLa cells. HeLa cells were cultured in Dulbecco's Modified Eagle's Medium (DMEM) with 10% Fetal Bovine Serum (FBS) and 1% penicillin streptomycin at 37 °C in 5 % CO_2. The cells are cultured in a T25 (25 cm^2) cell culture flask. The thickness of the T25 flask is larger than the working distance of the 60X objective (0.17mm) used in the study. So, an imaging chamber is customized to use in the microscope with 60X objective as follows. Sterile plastic petri dish with 35 mm diameter and 1 mm depth is used to make an imaging chamber. A 6.0 mm hole is drilled in the petri dish and a microscope coverslip is attached to the bottom part of the petri dish by using parafilm as the adhesive. The parafilm and coverslip kept at the bottom side of the petri dish is heated with the blue flame from a gas burner to stick the coverslip permanently. The imaging chamber customized are washed in ethanol and sterilized in UV light in a biosafety cabinet. For nanoparticle internalization study ~20,000 cells were seeded in imaging chamber and incubated for 24 hours. After incubation for 24 hours at 37^0C in 5% CO_2, culture media is removed, and cells were carefully rinsed with PBS solution (pH 7.4). Then a colloidal solution of $BaTiO_3$ nanoparticles in culture media (5µg/mL) was added to the imaging chamber and incubated for next 6 hours. Two-photon photothermal imaging is carried out after 6 hours of incubation time.

To use $BaTiO_3$ nanoparticles as a bio-label, we must first check its biocompatibility. The biocompatibility studies can be performed in different ways. One can check the cytotoxicity or the metabolic activity after the internalization of the nanoparticles. In the present study we have employed a colorimetric assay to test the metabolic activity after the nanoparticle internalization. The biocompatibility of $BaTiO_3$ nanoparticles are studied in HeLa cells by a well-known MTT (3-(4,5- dimethylthiazole-2-yl)-2,5-diphenyl tetrazolium bromide) assay. MTT is a yellow colored tetrazolium dye, 3-(4,5- dimethylthiazole-2-yl)-2,5-diphenyl tetrazolium bromide. In MTT assay

we quantify NAD(P)H-dependent cellular oxidoreductase enzymes produced by the cells which gives a measure of the metabolic activity of the living cells. The MTT dye enters the cell and passes into the mitochondria where it is reduced to an insoluble dark purple colored formazan by the mitochondrial succinate dehydrogenase enzyme. Then the formazan is solubilized by proper reagents. The concentration of this solution is measured spectrophotometrically. Since reduction of MTT can occur in metabolically active cells, the color change is an indication of the level of activity and hence a measure of the viability of the cells.

The entrance of nanoparticles into the cytoplasm depends up on the charge of the nanoparticles. Hsieh *et al.* studied the inflow of BaTiO$_3$ nanoparticles into the cells and found that the rate of flow of BaTiO$_3$ improved highly when it is coated with Poly L Lysine (PLL). In the present study of biocompatibility, we have used BaTiO$_3$ nanoparticles coated with PLL. The coating of BaTiO$_3$ nanoparticles with PLL is carried out as detailed below. A stable dispersion of BaTiO$_3$ nanoparticles is prepared in PLL with Phosphate Buffered Saline (PBS)[92]. 1mg of BaTiO$_3$ is added in to 1ml of 0.1% PLL in PBS solution and sonicated for 12 hours resulting 1mg/ml PLL coated BaTiO$_3$ nanoparticle. For MTT assay 20,000 cells were seeded in each well of the 96 well plate and incubated for 24 hours. After 24 hours of incubation, cells were treated with modified culture media containing various concentrations of BaTiO$_3$ nanoparticle (2.5 µg/ml , 5 µg/ml, 10 µg/ml, 20 µg/ml) and incubated for another 24 hours. Afterwards cells were incubated with MTT having concentration of 0.5mg/ml for 4 hours. Once MTT reduction is done supernatant is aspirated followed by treating the sample with 100 µl of dimethyl sulphoxide (DMSO). The absorbance was measured at a wavelength of 570 nm using a 96 well plate micro plate reader. In all the experiments, control test was done on untreated cells. All the experiments were done in triplicate and three independent tests were conducted in different days.

Statistical analysis is performed to study results of the MTT assay to conclude the effect PLL coated BaTiO$_3$ nanoparticles on the metabolic activity of HeLa cells. Analysis of variance (ANOVA) along with student's t-test is widely used to study the statistical significance of MTT assay. ANOVA is a collection of statistical methods to study difference in group means and variation among and between groups. Student's t-test compares two different group means and tells whether their difference is significant or not. In student's t test a null hypothesis is made first for significance and then calculate the probability for the truth of the null hypothesis based on the

group means and its variation. Statistical analysis of MTT assay is done by analysis of variance (ANOVA) followed by Student's t-test by setting $p < 0.05$ as significant and marked with asterisk in the graph. The statistical analysis is performed in excel by using the single factor ANOVA and paired two sample for means for t-test. MTT assay result is taken from the spectrophotometer as optical density of the wells. The optical density of the untreated cells is considered as 100% viable cells and the percentage of live cells for each concentration is calculated by dividing with the optical density of the untreated cells. Here the MTT performed in triplets for each concentration is considered as a group and different concentration of $BaTiO_3$ gives different groups. First the significance in the group mean of result of MTT assay for each concentration performed in different days are tested among them. Then the significance of the MTT results for different concentration is also tested. The null hypothesis in the present case is set as the results are significant. In the t-test the probability value $p<0.05$ is set as the significant. The results are reported as mean± standard error of the mean (SEM). Figure 6.5 shows the image of resulting 96 well plate after the MTT assay. The color of the solution is proportional to the metabolic activity of the cells. One set of measurement is from the well A1 to B9 corresponding to different concentration of PLL coated $BaTiO_3$ nanoparticles.

Fig. 6.5: The resulting 96 well plate after MTT assay.

Cell viability after nanoparticles incubation and after irradiation with pump powers up to 10 mW was tested by trypan blue exclusion method. Trypan blue exclusion assay, one of the best possible assay for to check the viability of cell after the exposure with laser beam. Trypan blue is a blue colored azo dye, live cells do not allow this dye molecule to enter in to the cell through the intact cell membrane. So, if we treat cell line under study with Trypan blue, the dead cells will be stained by the dye and healthy live cells exclude the dye. So the cell viability can be measured by counting the unstained cells with the help of a microscope or with the other cell counting instruments. The cells remain viable at these power levels, no visible damage or entry of the dye into the cytoplasm is observed. The pump energy employed in the imaging reported here is only 0.03 nano joules (3mW average power). We have repeatedly imaged the same set of cells 10-15 times to check whether the cells are getting affected. Even after repeated imaging, the cells remain intact and provide reproducible images.

To verify the applicability of the two-photon photothermal microscope in live cell imaging and to check the capability of the microscope in acquiring images in the presence of scattering media, we imaged $BaTiO_3$ nanoparticles internalized in a biological cell. HeLa cells are seeded in the imaging chamber and cultured for 24 hours using standard protocol as described in the methods section. The cells are then incubated in culture media having Poly-L-Lysine (PLL) coated $BaTiO_3$ nanoparticle for 6 hours [92]. Figure 6.6(a) shows the wide field microscope image of HeLa cells seeded with $BaTiO_3$ nanoparticles. Figure 6.6(b) shows the corresponding two-photon photothermal image of the cell made by stacking different axial(Z) sections. The sections are taken after moving the microscope objective 2 µm at each step. The sections are combined by ImageJ software to make a 3D image. The figure confirms that the two-photon photothermal microscope can indeed provide high quality images of live cells. In order to check the cell viability after addition of $BaTiO_3$ nanoparticle, a cytotoxicity measurement using (3-(4,5- dimethylthiazole-2-yl)-2,5-diphenyl tetrazolium bromide) assay was carried out. Figure 6.7 depicts the results of MTT assay performed in HeLa cells treated with PLL coated $BaTiO_3$ nanoparticles having a size of 20 nm. No significant decrease in MTT reduction is observed up to 5µg/ml of PLL coated $BaTiO_3$ nanoparticle concentration. While a significant decrease in MTT reduction of 16% ($p < 0.05$) is observed for 10µg/ml concentration. A sharp decrease in MTT reduction is found ($p < 0.01$) for 20µg/ml of $BaTiO_3$ nanoparticle treated cells.
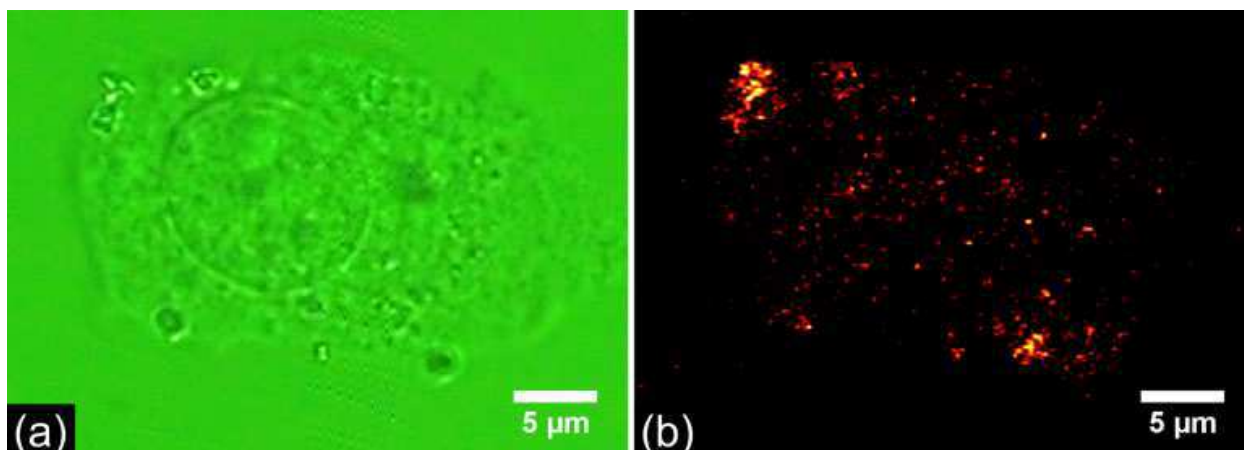
Fig. 6.6: (a) Wide field image of the HeLa cell with PLL coated 20 nm BaTiO$_3$ nanoparticles. (b) Corresponding 3D image of HeLa cells made from different axial sections of 2 μm interval taken with two-photon photothermal microscope. Pump and probe powers used are 3 mW and 0.8 mW respectively at the sample.
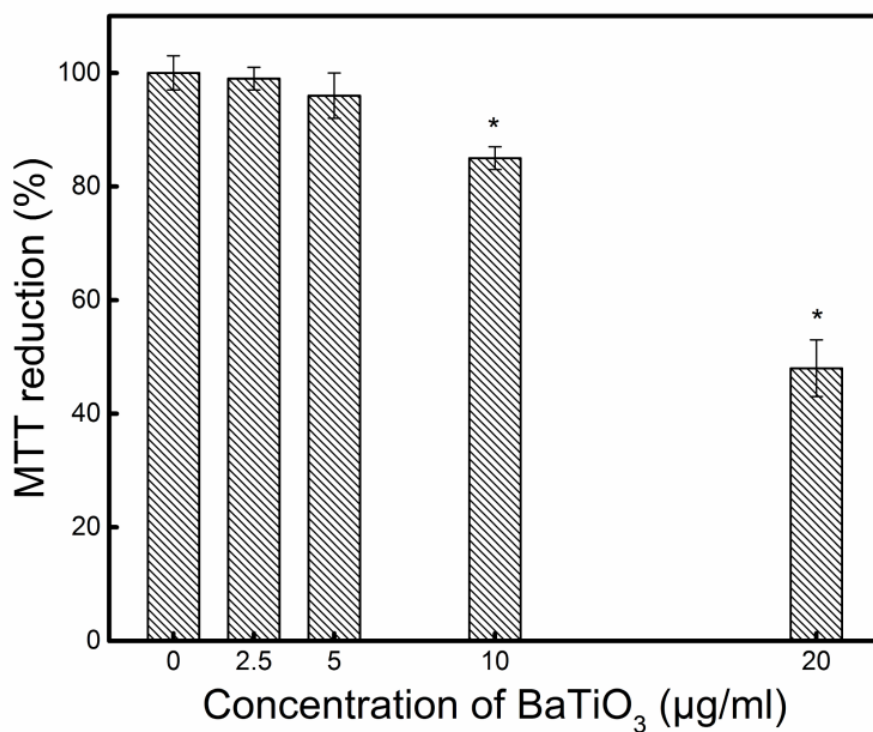
Fig. 6.7: Effect of PLL coated BaTiO$_3$ nanoparticles on the metabolic activity of HeLa cell as measured by MTT assay for various concentrations. Data is represented as mean ± standard error mean of three independent experiments. P < 0.05 is indicated with a*.

6.6 Summary

In summary a new nonlinear optical microscopic technique based on two-photon absorption induced photothermal effect capable of detecting individual non-fluorescent nanoparticles is developed. The two-photon photothermal microscope makes use of high repetition rate, near infrared laser pulses of pico jule energy as the heating beam in a pump-probe measurement scheme. The microscope is successfully employed to acquire images of $BaTiO_3$ nanoparticles in the size range of 20 nm to 70 nm with high sensitivity. $BaTiO_3$ is a highly photostable and biocompatible material having femtosecond response time and could provide a potential label for imaging. The near infrared excitation wavelengths employed by the microscope are less toxic to living cells. Further it provides a larger penetration depth and high SNR in imaging due to lower scattering. The microscope is inherently confocal making it a potential alternative tool for three-dimensional imaging in a scattering environment. The applicability of this technique in biology is demonstrated by imaging $BaTiO_3$ nanoparticles internalized in HeLa cells. Detection of nanometer sized single particles using photothermal microscopy incorporated with two-photon absorption has promising applications in deep tissue imaging in biological research and clinical diagnostics. Two-photon absorption being a third order process, the technique can be employed to detect and characterize nanoparticles regardless of its symmetry. Thus the applications of the two-photon photothermal microscope developed here are not limited to biological imaging, the microscope can be used as a potential non-invasive technique to detect and characterize nanosize objects in general.

Chapter 7: Summary and conclusions

In this work we have examined the nonlinear optical properties of $BaTiO_3$ nanoparticles from the point of view of applications in the area of biomolecular imaging. $BaTiO_3$ nanoparticles possess many attractive optical and dielectric properties and possess large values of third order nonlinear optical susceptibility. $BaTiO_3$ is a dielectric belonging to the perovskite family and is a biocompatible material having high photostability, an essential requirement for a biomolecular label. Our study demonstrates the potential of $BaTiO_3$ nanoparticles as a biomolecular label that would allow long term observation of a biological system. Further, in this work we introduce a new nonlinear optical imaging technique named two-photon photothermal microscope that makes use of high repetition rate infrared laser pulses.

Monodisperse $BaTiO_3$ nanoparticles of different sizes are successfully synthesized using a sol-gel method. The size control is achieved by varying a single experimental parameter, namely the annealing temperature. The cost-effective method of synthesis of monodisperse $BaTiO_3$ nanoparticles we employed is particularly attractive from the point of view of applications in nanophotonic devices such as detectors, sensors and capacitors.

The crystal structure of $BaTiO_3$ nanoparticles is characterized by X-ray diffractometer. The size and shape of the synthesized $BaTiO_3$ nanoparticles are analyzed by a transmission electron microscope. Linear optical absorption edge and bandgap of $BaTiO_3$ nanoparticles are measured by a UV-VIS-NIR spectrophotometer. The nonlinear optical absorption in $BaTiO_3$ nanoparticles are studied by using a single beam open aperture Z-scan technique. For this purpose, an automated Z-scan measurement system is developed in the laboratory. A femtosecond mode-locked Ti:sapphire laser system (Mira 900, Coherent) operating at 76 MHz, with a pulse width of 120 fs and at a wavelength of 800 nm is used for the Z-scan study. The two-photon absorption coefficient estimated from the Z-scan transmittance curve is of the order of 10^{-11} m/W and is found to increase with decrease in the size of $BaTiO_3$ nanoparticles.

We observed that the nonlinear optical absorption in $BaTiO_3$ nanoparticle films can be enhanced by doping with small amount of gold nanoparticles. The gold nanoparticles of average size 25 nm, synthesized by citrate reduction method are used as dopants. Au/$BaTiO_3$ nanocomposite thin films

with different Au/Ba molar ratios are prepared successfully by sol-gel technique and characterized by X-ray diffraction, UV-VIS-NIR absorption spectroscopy and high-resolution transmission electron microscopy. The two photon absorption coefficient of the composite films is determined by the single beam open aperture Z-scan method at a wavelength of 532 nm using 7 ns pulses from a frequency-doubled Q-Switched Nd:YAG laser. Au/BaTiO$_3$ nanocomposites shows enhanced nonlinear optical absorption with the increase of gold nanoparticle concentration in qualitative agreement with that predicted for the Maxwell-Garnet geometry. In the present work we have restricted the fill fraction of gold nanoparticle to 4.6 % due to coagulation of the sample which is a limitation of the current synthesis procedure. It is possible to further increase the fill fraction by suitably modifying sample preparation methods and efforts are on to achieve this.

A photothermal microscope is developed to image single gold nanoparticles and to characterize the Au/BaTiO$_3$ thins films. This helped in understanding the distribution of gold nanoparticle inside BaTiO$_3$ nanoparticle matrix for different concentration of gold nanoparticles. Photothermal detection of nonfluorescent nanoparticles has found applications in biomolecular imaging and cancer therapy. In this work we demonstrate capabilities of the photothermal microscopy as a characterization technique for material science. The photothermal images of Au/BaTiO$_3$ nanocomposite films with different molar ratio of Au/Ba is taken and the density and distribution gold nanoparticle in Au/BaTiO$_3$ film is compared. This method provides a nondestructive tool to test the presence of gold in microchips, integrated circuits and thin film photovoltaic cells (solar cells) and would be useful in the area of nanoelectronics.

Optical microscopic technique plays a vital role in biology. There is continued research effort and interest in developing new labels and microscopic techniques that would allow long term observation of biological systems. In this work we successfully developed a nonlinear optical microscope that uses BaTiO$_3$ nanoparticles as a reliable biomolecular label by making use of its photothermal and nonlinear optical properties. The two-photon photothermal microscope employs high repetition rate, near infrared laser pulses of pico-Joule energy as the heating beam in a pump-probe measurement scheme. The microscope is successfully employed to acquire images of BaTiO$_3$ nanoparticles in the size range of 20 nm to 70 nm with high sensitivity. The near infrared excitation wavelengths employed by the microscope are less toxic to living cells and provides a larger penetration depth in tissues due to lower scattering. The microscope is inherently confocal

making it a potential alternative tool for three-dimensional imaging in a scattering environment. The applicability of this technique in biology is demonstrated by imaging $BaTiO_3$ nanoparticles internalized in HeLa cells. Detection of nanometer sized single particles using photothermal microscopy incorporated with two-photon absorption has promising applications in deep tissue imaging in biological research and clinical diagnostics. Two-photon absorption being a third order process, the technique can be employed to detect and characterize nanoparticles regardless of its symmetry.

The major achievements of this thesis work are enumerated below,

1. $BaTiO_3$ nanoparticles of sizes 12 nm, 20 nm, 37 nm, 50 nm, 90 nm are successfully prepared by sol-gel technique. Particle size of the $BaTiO_3$ is controlled by a single synthesis parameter, namely the annealing temperature.
2. The $BaTiO_3$ nanoparticles are characterized by X-ray diffractometer, UV-VIS-NIR absorption spectrometer and transmission electron microscopy.
3. The third order nonlinear optical absorption coefficient of $BaTiO_3$ nanoparticles of different sizes are measured by an open aperture Z-scan technique. The results are summarized in the table below.

S. No.	Annealing Temperature (^oC)	TEM Particle size (nm)	Linear optical absorption edge (nm)	Band gap (eV)	Two-photon absorption coefficient (β) (x 10^{-11} m/W)
1	650	12 ± 2	371	3.21	3.68 ± 0.05
2	700	20 ± 4	368	3.24	5.65 ± 0.08
3	800	37 ± 7	366	3.26	6.50 ± 0.06
4	900	50 ± 8	364	3.29	8.20 ± 0.09
5	1000	90 ± 17	361	3.31	11.00 ± 0.08

4. $Au/BaTiO_3$ nanocomposite thin films with different Au/Ba molar ratios are prepared successfully by sol-gel technique and characterized by X-ray diffraction, UV-VIS-NIR absorption spectroscopy and high-resolution transmission electron microscopy.

5. The third order nonlinear optical coefficient of Au/BaTiO$_3$ nanocomposite thin films are measured by an open aperture Z-scan technique. The two-photon absorption coefficient of these films increases linearly with the increase in the concentration of gold nanoparticles. The result is summarized in the table below

Sample	Au/Ba Ratio	β
1	0%	$(1.0 \pm 0.1) \times 10^{-9}$ m/W
2	1.6%	$(1.5 \pm 0.2) \times 10^{-9}$ m/W
3	2.5%	$(2.0 \pm 0.1) \times 10^{-9}$ m/W
4	4.8%	$(3.2 \pm 0.2) \times 10^{-9}$ m/W

6. A photothermal microscope is developed to detect gold nanoparticles of size as small as 5 nm. We demonstrate that, apart from being a potential biomolecular imaging tool, photothermal microscopy provides a nondestructive characterization tool that can detect the presence and distribution of gold nanoparticles. We used the technique to characterize Au/BaTiO$_3$ nanocomposite films and to compare the gold nanoparticle distribution in different samples.

7. A new nonlinear optical microscopic technique, named as two-photon photothermal microscopy, based on two-photon absorption induced photothermal effect capable of detecting individual nonfluorescent nanoparticles is developed. The microscope is successfully employed to acquire images of BaTiO$_3$ nanoparticles in the size range of 20 nm to 70 nm with high sensitivity

8. The applicability of two-photon microscope in biomolecular imaging is demonstrated by imaging BaTiO$_3$ nanoparticles internalized Hela cells. A three-dimensional image of BaTiO$_3$ nanoparticles internalized HeLa cells is formed by taking serial sections at 2 μm intervals. The biocompatibility of BaTiO$_3$ nanoparticle is studied by using MTT assay and it was found that BaTiO$_3$ nanoparticles are safe to use in cells up to a concentration of 10 μg/ml.

Nonlinear optics is a vast area of research and in this thesis we have characterized and demonstrated the applications of a model system of perovskite nanoparticles in a specific context. These nanoparticles could find applications in a variety of photonics applications

which are yet to be explored. We have only demonstrated the potential of the nonlinear photothermal microscopy in biomolecular imaging, and efforts are being on to use the technique in different real life applications.

References

[1] J.B. Pawley, Handbook of Biological Confocal Microscopy, Springer, 1995. https://books.google.co.in/books?id=16Ft5k8RC-AC.

[2] B. Matsumoto, Cell Biological Applications of Confocal Microscopy, Elsevier Science, 2003. https://books.google.co.in/books?id=Ogc_GlNJ90YC.

[3] G.S. Kino, T.R. Corle, Confocal Scanning Optical Microscopy and Related Imaging Systems, Elsevier Science, 1996. https://books.google.co.in/books?id=tNJX4wwZPaAC.

[4] E.E. Hoover, J.A. Squier, Advances in multiphoton microscopy technology, Nat Photon. 7 (2013) 93–101. doi:10.1038/nphoton.2012.361.

[5] B.R. Masters, Confocal Microscopy and Multiphoton Excitation Microscopy: The Genesis of Live Cell Imaging, SPIE Press, 2006. https://books.google.co.in/books?id=frZ43VkbGXoC.

[6] F. Helmchen, W. Denk, Deep tissue two-photon microscopy, Nat Meth. 2 (2005) 932–940. doi:10.1038/nmeth818.

[7] Two-Photon Excitation Fluorescence Microscopy, Annual Review of Biomedical Engineering. 2 (2000) 399–429. doi:10.1146/annurev.bioeng.2.1.399.

[8] S.W. Bae, W. Tan, J.-I. Hong, Fluorescent dye-doped silica nanoparticles: new tools for bioapplications, Chem. Commun. 48 (2012) 2270–2282. doi:10.1039/C2CC16306C.

[9] T. Repenko, A. Rix, S. Ludwanowski, D. Go, F. Kiessling, W. Lederle, A.J.C. Kuehne, Bio-degradable highly fluorescent conjugated polymer nanoparticles for bio-medical imaging applications, Nature Communications. 8 (2017) 470. doi:10.1038/s41467-017-00545-0.

[10] X. Michalet, F.F. Pinaud, L.A. Bentolila, J.M. Tsay, S. Doose, J.J. Li, G. Sundaresan, A.M. Wu, S.S. Gambhir, S. Weiss, Quantum Dots for Live Cells, in Vivo Imaging, and Diagnostics, Science. 307 (2005) 538. doi:10.1126/science.1104274.

[11] O.S. Wolfbeis, An overview of nanoparticles commonly used in fluorescent bioimaging, Chem. Soc. Rev. 44 (2015) 4743–4768. doi:10.1039/C4CS00392F.

[12] Q.A. Acton, Advances in Nanotechnology Research and Application: 2012 Edition, ScholarlyEditions, 2012. https://books.google.co.in/books?id=DXqRUwZ0nnYC.

[13] D. Boyer, P. Tamarat, A. Maali, B. Lounis, M. Orrit, Photothermal imaging of nanometer-sized metal particles among scatterers., Science (New York, N.Y.). 297 (2002) 1160–3. doi:10.1126/science.1073765.

[14] V. Zharov, D. Lapotko, Photothermal sensing of nanoscale targets, in: Review of Scientific Instruments, 2003: pp. 785–788.

[15] X. Huang, I.H. El-Sayed, W. Qian, M.A. El-Sayed, Cancer cell imaging and photothermal therapy in the near-infrared region by using gold nanorods, Journal of the American Chemical Society. 128 (2006) 2115–2120.

[16] A. Gaiduk, M. Yorulmaz, P. V Ruijgrok, M. Orrit, Room-temperature detection of a single molecule's absorption by photothermal contrast, Science. 330 (2010) 353–6.

[17] G. Ajoy, Optics, Tata McGraw-Hill Education, 2005.

[18] B. Herman, K. Jacobson, Optical microscopy for biology: proceedings of the International Conference on Video Microscopy held in Chapel Hill, North Carolina, June 4-7, 1989, Wiley-Liss, 1990. https://books.google.co.in/books?id=-EDwAAAAMAAJ.

[19] B. Herman, J.J. Lemasters, Optical Microscopy: Emerging Methods and Applications, Academic Press, 1993. https://books.google.co.in/books?id=pVHwAAAAMAAJ.

[20] D.B. Murphy, Fundamentals of Light Microscopy and Electronic Imaging, Wiley, 2002. https://books.google.co.in/books?id=sBMIick3fVUC.

[21] J.W. Lichtman, J.A. Conchello, Fluorescence microscopy, Nat Meth. 2 (2005) 910–919. doi:10.1038/nmeth817.

[22] F.L. Pedrotti, L.M. Pedrotti, L.S. Pedrotti, Introduction to Optics, Cambridge University Press, 2017. https://books.google.co.in/books?id=VU9TDwAAQBAJ.

[23] M. Pluta, Advanced light microscopy, PWN, 1988. https://books.google.co.in/books?id=j2XwAAAAMAAJ.

[24] W.C. McCrone, L.B. McCrone, J.G. Delly, Polarized light microscopy, Ann Arbor Science Publishers, 1978. https://books.google.co.in/books?id=MDPwAAAAMAAJ.

[25] J.B. Pawley, Handbook of Biological Confocal Microscopy, Springer, 1995. https://books.google.co.in/books?id=16Ft5k8RC-AC.

[26] B.R. Masters, P. So, Handbook of Biomedical Nonlinear Optical Microscopy, Oxford University Press, 2008. https://books.google.co.in/books?id=4mki1ThMgGYC.

[27] M. Nirmal, B.O. Dabbousi, M.G. Bawendi, J.J. Macklin, J.K. Trautman, T.D. Harris, L.E. Brus, Fluorescence intermittency in single cadmium selenide nanocrystals, Nature. 383 (1996) 802–804. doi:10.1038/383802a0.

[28] J.E. Lee, N. Lee, H. Kim, J. Kim, S.H. Choi, J.H. Kim, T. Kim, I.C. Song, S.P. Park, W.K. Moon, T. Hyeon, Uniform Mesoporous Dye-Doped Silica Nanoparticles Decorated with Multiple Magnetite Nanocrystals for Simultaneous Enhanced Magnetic Resonance Imaging, Fluorescence Imaging, and Drug Delivery, Journal of the American Chemical Society. 132 (2010) 552–557. doi:10.1021/ja905793q.

[29] R.P. Bagwe, C. Yang, L.R. Hilliard, W. Tan, Optimization of Dye-Doped Silica Nanoparticles Prepared Using a Reverse Microemulsion Method, Langmuir. 20 (2004) 8336–8342. doi:10.1021/la049137j.

[30] D. Tuncel, H.V. Demir, Conjugated polymer nanoparticles, Nanoscale. 2 (2010) 484–494. doi:10.1039/B9NR00374F.

[31] N.C. Verma, S. Khan, C.K. Nandi, Single-molecule analysis of fluorescent carbon dots towards localization-based super-resolution microscopy, Methods and Applications in Fluorescence. 4 (2016) 044006. http://stacks.iop.org/2050-6120/4/i=4/a=044006.

[32] S.-T. Yang, L. Cao, P.G. Luo, F. Lu, X. Wang, H. Wang, M.J. Meziani, Y. Liu, G. Qi, Y.-P. Sun, Carbon Dots for Optical Imaging in Vivo, Journal of the American Chemical Society. 131 (2009) 11308–11309. doi:10.1021/ja904843x.

[33] S.-T. Yang, X. Wang, H. Wang, F. Lu, P.G. Luo, L. Cao, M.J. Meziani, J.-H. Liu, Y. Liu, M. Chen, Y. Huang, Y.-P. Sun, Carbon Dots as Nontoxic and High-Performance Fluorescence Imaging Agents, The Journal of Physical Chemistry C. 113 (2009) 18110–18114. doi:10.1021/jp9085969.

[34] S.B. Rizvi, S. Ghaderi, M. Keshtgar, A.M. Seifalian, Semiconductor quantum dots as fluorescent probes for in vitro and in vivo bio-molecular and cellular imaging, Nano Reviews. 1 (2010) 10.3402/nano.v1i0.5161. doi:10.3402/nano.v1i0.5161.

[35] K.D. Wegner, N. Hildebrandt, Quantum dots: bright and versatile in vitro and in vivo fluorescence imaging biosensors, Chem. Soc. Rev. 44 (2015) 4792–4834. doi:10.1039/C4CS00532E.

[36] K. Aslan, I. Gryczynski, J. Malicka, E. Matveeva, J.R. Lakowicz, C.D. Geddes, Metal-enhanced fluorescence: an emerging tool in biotechnology, Current Opinion in Biotechnology. 16 (2005) 55–62. doi:https://doi.org/10.1016/j.copbio.2005.01.001.

[37] S. Berciaud, L. Cognet, G.A. Blab, B. Lounis, Photothermal heterodyne imaging of individual nonfluorescent nanoclusters and nanocrystals, Physical Review Letters. 93 (2004).

[38] W. Martienssen, H. Warlimont, Springer Handbook of Condensed Matter and Materials Data, Springer Berlin Heidelberg, 2006. https://books.google.co.in/books?id=TnHJX79b3RwC.

[39] H.S. Nalwa, Handbook of Low and High Dielectric Constant Materials and Their Applications, Two-Volume Set, Elsevier Science, 1999. https://books.google.co.in/books?id=X2yK7HvrvaIC.

[40] M.E. Lines, A.M. Glass, Principles and Applications of Ferroelectrics and Related Materials, OUP Oxford, 1977.

[41] M.F. Ahmer, A.M. Asiri, S. Zaidi, Electrochemical Capacitors: Theory, Materials and Applications, Materials Research Forum LLC, 2018. https://books.google.co.in/books?id=6UhLDwAAQBAJ.

[42] A. Rosa, D. Tulli, P. Castera, A.M. Gutierrez, A. Griol, M. Baquero, B. Vilquin, F. Eltes, S. Abel, J. Fompeyrine, P. Sanchis, Barium titanate (BaTiO3) RF characterization for application in electro-optic modulators, Opt. Mater. Express. 7 (2017) 4328–4336. doi:10.1364/OME.7.004328.

[43] B. Li, T. Jiao, Nano/Micro-Structured Materials for Energy and Biomedical Applications: Latest Developments, Challenges and Future Directions, Springer Singapore, 2018. https://books.google.co.in/books?id=uUtLDwAAQBAJ.

[44] S. Selvarajan, N.R. Alluri, A. Chandrasekhar, S.-J. Kim, BaTiO3 nanoparticles as biomaterial film for self-powered glucose sensor application, Sensors and Actuators B: Chemical. 234 (2016) 395–403. doi:https://doi.org/10.1016/j.snb.2016.05.004.

[45] Z. Yan, Y. Guo, G. Zhang, J.-M. Liu, High-Performance Programmable Memory Devices Based on Co-Doped BaTiO3, Advanced Materials. 23 (n.d.) 1351–1355. doi:10.1002/adma.201004306.

[46] L. Holtmann, G. Kuper, E. Krätzig, G. Godefroy, Photovoltaic holographic recording in BaTiO3:Fe, Ferroelectrics. 126 (1992) 51–56. doi:10.1080/00150199208227034.

[47] Y. Fan, X. Huang, G. Wang, P. Jiang, Core–Shell Structured Biopolymer@BaTiO3 Nanoparticles for Biopolymer Nanocomposites with Significantly Enhanced Dielectric Properties and Energy Storage Capability, J. Phys. Chem. C. 119 (2015) 27330–27339. doi:10.1021/acs.jpcc.5b09619.

[48] N. Samardzic, T. Kojic, J. Vukmirovic, D. Tripkovic, B. Bajac, Vladimir Srdic, G. Stojanovic, Performance analysis of resistive switching devices based on BaTiO 3 thin films, IOP Conference Series: Materials Science and Engineering. 108 (2016) 012046. http://stacks.iop.org/1757-899X/108/i=1/a=012046.

[49] J. Li, J. Claude, L.E. Norena-Franco, S.I. Seok, Q. Wang, Electrical Energy Storage in Ferroelectric Polymer Nanocomposites Containing Surface-Functionalized BaTiO3 Nanoparticles, Chem. Mater. 20 (2008) 6304–6306. doi:10.1021/cm8021648.

[50] S.C. Mukhopadhyay, A. Lay-Ekuakille, A. Fuchs, New Developments and Applications in Sensing Technology, Springer Berlin Heidelberg, 2011. https://books.google.co.in/books?id=iufo-3hVT18C.

[51] H.-J. Noh, S.-G. Lee, S.-P. Nam, Y.-H. Lee, Pyroelectric properties of arrayed BaTiO3 system thick film for uncooled IR detector, Materials Research Bulletin. 45 (2010) 339–342. doi:https://doi.org/10.1016/j.materresbull.2009.12.029.

[52] F. Eltes, D. Caimi, F. Fallegger, M. Sousa, E. O'Connor, M.D. Rossell, B. Offrein, J. Fompeyrine, S. Abel, Low-Loss BaTiO3–Si Waveguides for Nonlinear Integrated Photonics, ACS Photonics. 3 (2016) 1698–1703. doi:10.1021/acsphotonics.6b00350.

[53] R.K. Goyal, Nanomaterials and Nanocomposites: Synthesis, Properties, Characterization Techniques, and Applications, CRC Press, 2017. https://books.google.co.in/books?id=X3JQDwAAQBAJ.

[54] N. Vijay, F.M. M, D.A. A, Thin Films On Silicon: Electronic And Photonic Applications, World Scientific Publishing Company, 2016. https://books.google.co.in/books?id=DpP4DAAAQBAJ.

[55] C.A. Stanciu, M. Cernea, E.C. Secu, G. Aldica, P. Ganea, R. Trusca, Lanthanum influence on the structure, dielectric properties and luminescence of BaTiO3 ceramics processed by spark plasma sintering technique, Journal of Alloys and Compounds. 706 (2017) 538–545. doi:https://doi.org/10.1016/j.jallcom.2017.02.258.

[56] L.V. Maneeshya, P.V. Thomas, K. Joy, Visible PL Emission from Erbium Doped BaTiO3 thin Films Deposited by RF Magnetron Sputtering, Materials Today: Proceedings. 2 (2015) 992–996. doi:https://doi.org/10.1016/j.matpr.2015.06.023.

[57] W.F. Zhang, Y.B. Huang, M.S. Zhang, Z.G. Liu, Nonlinear optical absorption in undoped and cerium-doped BaTiO3 thin films using Z-scan technique, Applied Physics Letters. 76 (2000) 1003–1005. doi:10.1063/1.125920.

[58] F.A. Ismail, R.A.M. Osman, M.S. Idris, Review on dielectric properties of rare earth doped barium titanate, AIP Conference Proceedings. 1756 (2016) 090005. doi:10.1063/1.4958786.

[59] Y. Okino, H. Shizuno, S. Kusumi, H. Kishi, Dielectric Properties of Rare-Earth-Oxide-Doped B a T i O 3 Ceramics Fired in Reducing Atmosphere, Japanese Journal of Applied Physics. 33 (1994) 5393. http://stacks.iop.org/1347-4065/33/i=9S/a=5393.

[60] Y.-X. Li, X. Yao, X.-S. Wang, Y.-B. Hao, Studies of dielectric properties of rare earth (Dy, Tb, Eu) doped barium titanate sintered in pure nitrogen, Ceramics International. 38 (2012) S29–S32. doi:https://doi.org/10.1016/j.ceramint.2011.04.042.

[61] V.V. Mitic, Z.S. Nikolic, V.B. Pavlovic, V. Paunovic, M. Miljkovic, B. Jordovic, L. Zivkovic, Influence of Rare-Earth Dopants on Barium Titanate Ceramics Microstructure and Corresponding Electrical Properties, Journal of the American Ceramic Society. 93 (n.d.) 132–137. doi:10.1111/j.1551-2916.2009.03309.x.

[62] Y. Hakuta, H. Ura, H. Hayashi, K. Arai, Continuous Production of BaTiO3 Nanoparticles by Hydrothermal Synthesis, Ind. Eng. Chem. Res. 44 (2005) 840–846. doi:10.1021/ie049424i.

[63] D. Hennings, S. Schreinemacher, Characterization of hydrothermal barium titanate, Journal of the European Ceramic Society. 9 (1992) 41–46. doi:https://doi.org/10.1016/0955-2219(92)90075-O.

[64] R. Bacsa, P. Ravindranathan, J.P. Dougherty, Electrochemical, hydrothermal, and electrochemical-hydrothermal synthesis of barium titanate thin films on titanium substrates, Journal of Materials Research. 7 (1992) 423–428. doi:10.1557/JMR.1992.0423.

[65] W. Zhu, S.A. Akbar, R. Asiaie, P.K. Dutta, Sintering and Dielectric Properties of Hydrothermally Synthesized Cubic and Tetragonal B a T i O 3 Powders, Japanese Journal of Applied Physics. 36 (1997) 214. http://stacks.iop.org/1347-4065/36/i=1R/a=214.

[66] A. Kareiva, S. Tautkus, R. Rapalaviciute, J.-E. Jørgensen, B. Lundtoft, Sol-gel synthesis and characterization of barium titanate powders, Journal of Materials Science. 34 (1999) 4853–4857. doi:10.1023/A:1004615912473.

[67] C. Lemoine, B. Gilbert, B. Michaux, J.-P. Pirard, A. Lecloux, Synthesis of barium titanate by the sol-gel process, Journal of Non-Crystalline Solids. 175 (1994) 1–13. doi:https://doi.org/10.1016/0022-3093(94)90309-3.

[68] M. Veith, S. Mathur, N. Lecerf, V. Huch, T. Decker, H.P. Beck, W. Eiser, R. Haberkorn, Sol-Gel Synthesis of Nano-Scaled BaTiO3, BaZrO3 and BaTi0.5Zr0.5O3 Oxides via Single-Source Alkoxide Precursors and Semi-Alkoxide Routes, Journal of Sol-Gel Science and Technology. 17 (2000) 145–158. doi:10.1023/A:1008795419020.

[69] H. Zheng, K. Zhu, Q. Wu, J. Liu, J. Qiu, Preparation and characterization of monodispersed BaTiO3 nanocrystals by sol–hydrothemal method, Journal of Crystal Growth. 363 (2013) 300–307. doi:https://doi.org/10.1016/j.jcrysgro.2012.11.019.

[70] K.K. Lee, Y.C. Kang, K.Y. Jung, J.H. Kim, Preparation of nano-sized BaTiO3 particle by citric acid-assisted spray pyrolysis, Journal of Alloys and Compounds. 395 (2005) 280–285. doi:https://doi.org/10.1016/j.jallcom.2004.11.033.

[71] K.-Y. Chen, Y.-W. Chen, Preparation of barium titanate ultrafine particles from rutile titania by a hydrothermal conversion, Powder Technology. 141 (2004) 69–74. doi:https://doi.org/10.1016/j.powtec.2004.03.002.

[72] H. Xu, L. Gao, J. Guo, Preparation and characterizations of tetragonal barium titanate powders by hydrothermal method, Journal of the European Ceramic Society. 22 (2002) 1163–1170. doi:https://doi.org/10.1016/S0955-2219(01)00425-3.

[73] M.L. Moreira, G.P. Mambrini, D.P. Volanti, E.R. Leite, M.O. Orlandi, P.S. Pizani, V.R. Mastelaro, C.O. Paiva-Santos, E. Longo, J.A. Varela, Hydrothermal Microwave: A New Route to Obtain Photoluminescent Crystalline BaTiO3 Nanoparticles, Chem. Mater. 20 (2008) 5381–5387. doi:10.1021/cm801638d.

[74] S.-G. Kwon, B.-H. Park, K. Choi, E.-S. Choi, S. Nam, J.-W. Kim, J.-H. Kim, Solvothermally synthesized tetragonal barium titanate powders using H2O/EtOH solvent, Journal of the European Ceramic Society. 26 (2006) 1401–1404. doi:https://doi.org/10.1016/j.jeurceramsoc.2005.02.003.

[75] H. Bai, X. Liu, Low temperature solvothermal synthesis, optical and electric properties of tetragonal phase BaTiO3 nanocrystals using BaCO3 powder, Materials Letters. 100 (2013) 1–3. doi:https://doi.org/10.1016/j.matlet.2013.02.106.

[76] Y.T. Wu, X.F. Wang, C.L. Yu, E.Y. Li, Preparation and Characterization of Barium Titanate (BaTiO3) Nano-Powders by Pechini Sol-Gel Method, Materials and Manufacturing Processes. 27 (2012) 1329–1333. doi:10.1080/10426914.2012.663148.

[77] S. O'Brien, L. Brus, C.B. Murray, Synthesis of Monodisperse Nanoparticles of Barium Titanate: Toward a Generalized Strategy of Oxide Nanoparticle Synthesis, Journal of the American Chemical Society. 123 (2001) 12085–12086. doi:10.1021/ja011414a.

[78] Y. Peng, Q. Peng, S. Liu, Preparation of Barium Titanate Nanopowder through Thermal Decomposition of Peroxide Precursor and Its Formation Mechanism, Chinese Journal of Chemistry. 27 (n.d.) 2291–2295. doi:10.1002/cjoc.200990384.

[79] S. Kim, M. Lee, T. Noh, C. Lee, Preparation of barium titanate by homogeneous precipitation, Journal of Materials Science. 31 (1996) 3643–3645. doi:10.1007/BF00352772.

[80] A. Shi, W. Yan, Y. Li, K. Huang, Preparation and characterization of nanometer-sized barium titanate powder by complex-precursor method, Journal of Central South University of Technology. 15 (2008) 334. doi:10.1007/s11771-008-0063-2.

[81] W.-S. Jung, J. Park, Y. Park, D.-H. Yoon, Effects of impurities on the properties of BaTiO3 synthesized from barium titanyl oxalate, Ceramics International. 36 (2010) 1997–2002. doi:https://doi.org/10.1016/j.ceramint.2010.03.033.

[82] W. Maison, R. Kleeberg, R.B. Heimann, S. Phanichphant, Phase content, tetragonality, and crystallite size of nanoscaled barium titanate synthesized by the catecholate process: effect of calcination temperature, Journal of the European Ceramic Society. 23 (2003) 127–132. doi:https://doi.org/10.1016/S0955-2219(02)00071-7.

[83] H.-J. Gläsel, E. Hartmann, D. Hirsch, R. Böttcher, C. Klimm, D. Michel, H.-C. Semmelhack, J. Hormes, H. Rumpf, Preparation of barium titanate ultrafine powders from a monomeric metallo-organic precursor by combined solid-state polymerisation and pyrolysis, Journal of Materials Science. 34 (1999) 2319–2323. doi:10.1023/A:1004533926099.

[84] B. Mojić-Lanté, R. Djenadic, V.V. Srdić, H. Hahn, Direct preparation of ultrafine BaTiO3 nanoparticles by chemical vapor synthesis, Journal of Nanoparticle Research. 16 (2014) 2618. doi:10.1007/s11051-014-2618-5.

[85] J.J. Lee, K.J. Park, K.H. Hur, S.C. Yi, S.M. Koo, Synthesis of Ultrafine and Spherical Barium Titanate Powders Using a Titania Nano-Sol, Journal of the American Ceramic Society. 89 (n.d.) 3299–3301. doi:10.1111/j.1551-2916.2006.01220.x.

[86] B. Ji, D. Chen, X. Jiao, Z. Zhao, Y. Jiao, Preparation and electrical properties of nanoporous BaTiO3, Materials Letters. 64 (2010) 1836–1838. doi:https://doi.org/10.1016/j.matlet.2010.05.026.

[87] L.R. Prado, N.S. de Resende, R.S. Silva, S.M.S. Egues, G.R. Salazar-Banda, Influence of the synthesis method on the preparation of barium titanate nanoparticles, Chemical Engineering and Processing: Process Intensification. 103 (2016) 12–20. doi:https://doi.org/10.1016/j.cep.2015.09.011.

[88] T.K. Mandal, Characterization of tetragonal BaTiO3 nanopowders prepared with a new soft chemistry route, Materials Letters. 61 (2007) 850–854. doi:https://doi.org/10.1016/j.matlet.2006.06.006.

[89] R. Ashiri, A. Moghtada, A. Shahrouzianfar, R. Ajami, K. Joy, Low Temperature Synthesis of Carbonate-Free Barium Titanate Nanoscale Crystals: Toward a Generalized Strategy of Titanate-

Based Perovskite Nanocrystals Synthesis, Journal of the American Ceramic Society. 97 (n.d.) 2027–2031. doi:10.1111/jace.13023.

[90] V. Bansal, P. Poddar, A. Ahmad, M. Sastry, Room-Temperature Biosynthesis of Ferroelectric Barium Titanate Nanoparticles, J. Am. Chem. Soc. 128 (2006) 11958–11963. doi:10.1021/ja063011m.

[91] G. Ciofani, A. Menciassi, Piezoelectric Nanomaterials for Biomedical Applications, Springer Berlin Heidelberg, 2012. https://books.google.co.in/books?id=PKwlrW-CrxUC.

[92] G. Ciofani, S. Danti, S. Moscato, L. Albertazzi, D. D'Alessandro, D. Dinucci, F. Chiellini, M. Petrini, A. Menciassi, Preparation of stable dispersion of barium titanate nanoparticles: Potential applications in biomedicine, Colloids and Surfaces B: Biointerfaces. 76 (2010) 535–543. doi:http://dx.doi.org/10.1016/j.colsurfb.2009.12.015.

[93] C.-L. Hsieh, R. Grange, Y. Pu, D. Psaltis, Bioconjugation of barium titanate nanocrystals with immunoglobulin G antibody for second harmonic radiation imaging probes, Biomaterials. 31 (2010) 2272–2277. doi:http://dx.doi.org/10.1016/j.biomaterials.2009.11.096.

[94] O. Matar, O.M. Posada, N.S. Hondow, C. Wälti, M. Saunders, C.A. Murray, R.M.D. Brydson, S.J. Milne, A.P. Brown, Barium Titanate Nanoparticles for Biomarker Applications, Journal of Physics: Conference Series. 644 (2015) 012037. http://stacks.iop.org/1742-6596/644/i=1/a=012037.

[95] D. Staedler, T. Magouroux, Hadji Rachid, C. Joulaud, J. Extermann, S. Schwung, S. Passemard, C. Kasparian, G. Clarke, M. Gerrmann, R.L. Dantec, Y. Mugnier, D. Rytz, D. Ciepielewski, C. Galez, S. Gerber-Lemaire, L. Juillerat-Jeanneret, L. Bonacina, J.-P. Wolf, Harmonic Nanocrystals for Biolabeling: A Survey of Optical Properties and Biocompatibility, ACS Nano. 6 (2012) 2542–2549. doi:10.1021/nn204990n.

[96] J. Ĉulić-Viskota, W.P. Dempsey, S.E. Fraser, P. Pantazis, Surface functionalization of barium titanate SHG nanoprobes for in vivo imaging in zebrafish, Nat. Protocols. 7 (2012) 1618–1633. doi:10.1038/nprot.2012.087.

[97] C.-L. Hsieh, Y. Pu, R. Grange, G. Laporte, D. Psaltis, Imaging through turbid layers by scanning the phase conjugated second harmonic radiation from a nanoparticle, Opt. Express. 18 (2010) 20723–20731. doi:10.1364/OE.18.020723.

[98] R. Grange, T. Lanvin, C.-L. Hsieh, Y. Pu, D. Psaltis, Imaging with second-harmonic radiation probes in living tissue, Biomedical Optics Express. 2 (2011) 2532–2539. doi:10.1364/BOE.2.002532.

[99] F.S. Pavone, P.J. Campagnola, Second Harmonic Generation Imaging, CRC Press, 2016. https://books.google.co.in/books?id=EiTOBQAAQBAJ.

[100] C. Dempsey, I. Lee, K. Cowan, J. Suh, Coating barium titanate nanoparticles with polyethylenimine improves cellular uptake and allows for coupled imaging and gene delivery, Colloids and Surfaces. B, Biointerfaces. 112 (2013) 108–112. doi:10.1016/j.colsurfb.2013.07.045.

[101] A. Bagchi, S.R.K. Meka, B.N. Rao, K. Chatterjee, Perovskite ceramic nanoparticles in polymer composites for augmenting bone tissue regeneration, Nanotechnology. 25 (2014) 485101. http://stacks.iop.org/0957-4484/25/i=48/a=485101.

[102] J.P. Ball, B.A. Mound, J.C. Nino, J.B. Allen, Biocompatible evaluation of barium titanate foamed ceramic structures for orthopedic applications, Journal of Biomedical Materials Research Part A. 102 (n.d.) 2089–2095. doi:10.1002/jbm.a.34879.

[103] G. Ciofani, S. Danti, D. D'Alessandro, S. Moscato, M. Petrini, A. Menciassi, Barium Titanate Nanoparticles: Highly Cytocompatible Dispersions in Glycol-chitosan and Doxorubicin Complexes for Cancer Therapy, Nanoscale Research Letters. 5 (2010) 1093. doi:10.1007/s11671-010-9607-0.

[104] E. FarrokhTakin, G. Ciofani, G.L. Puleo, G. de Vito, C. Filippeschi, B. Mazzolai, V. Piazza, V. Mattoli, Barium titanate core – gold shell nanoparticles for hyperthermia treatments, International Journal of Nanomedicine. 8 (2013) 2319–2331. doi:10.2147/IJN.S45654.

[105] Y. Pu, M. Centurion, D. Psaltis, Harmonic holography: a new holographic principle, Appl. Opt. 47 (2008) A103–A110. doi:10.1364/AO.47.00A103.

[106] E. Kim, A. Steinbrück, M.T. Buscaglia, V. Buscaglia, T. Pertsch, R. Grange, Second-Harmonic Generation of Single BaTiO3 Nanoparticles down to 22 nm Diameter, ACS Nano. 7 (2013) 5343–5349. doi:10.1021/nn401198g.

[107] R. Le Dantec, Y. Mugnier, G. Djanta, L. Bonacina, J. Extermann, L. Badie, C. Joulaud, M. Gerrmann, D. Rytz, J.P. Wolf, C. Galez, Ensemble and Individual Characterization of the Nonlinear Optical Properties of ZnO and BaTiO3 Nanocrystals, J. Phys. Chem. C. 115 (2011) 15140–15146. doi:10.1021/jp200579x.

[108] S. Ramakanth, S. Hamad, S.V. Rao, K.C.J. Raju, Magnetic and nonlinear optical properties of BaTiO3 nanoparticles, AIP Advances. 5 (2015) 057139. doi:10.1063/1.4921480.

[109] R.A. Ganeev, M. Suzuki, M. Baba, M. Ichihara, H. Kuroda, Low- and high-order nonlinear optical properties of BaTiO3 and SrTiO3 nanoparticles, J. Opt. Soc. Am. B. 25 (2008) 325–333. doi:10.1364/JOSAB.25.000325.

[110] W. Shi, Z. Chen, N. Liu, H. Lu, Y. Zhou, D. Cui, G. Yang, Nonlinear optical properties of self-organized complex oxide Ce:BaTiO3 quantum dots grown by pulsed laser deposition, Applied Physics Letters. 75 (1999) 1547–1549. doi:10.1063/1.124750.

[111] G. Yang, W. Wang, L. Yan, H. Lu, G. Yang, Z. Chen, Z-scan determination of the large third-order optical nonlinearity of Rh:BaTiO3 thin films deposited on MgO substrates, Optics Communications. 209 (2002) 445–449. doi:http://dx.doi.org/10.1016/S0030-4018(02)01676-0.

[112] Y. Guang, W. Huan-Hua, T. Guo-Tai, J. An-Quan, Z. Yue-Liang, Y. Guo-Zhen, C. Zheng-Hao, Large Third-Order Nonlinear Optical Susceptibility of Rh-Doped BaTiO 3 Thin Films Prepared by Pulsed Laser Deposition, Chinese Physics Letters. 18 (2001) 1598. http://stacks.iop.org/0256-307X/18/i=12/a=317.

[113] B.G. Yust, N. Razavi, F. Pedraza, Z. Elliott, A.T. Tsin, D.K. Sardar, Enhancement of nonlinear optical properties of BaTiO3 nanoparticles by the addition of silver seeds, Opt. Express. 20 (2012) 26511–26520. doi:10.1364/OE.20.026511.

[114] G. Yang, W. Wang, Y. Zhou, H. Lu, G. Yang, Z. Chen, Linear and nonlinear optical properties of Ag nanocluster/BaTiO3 composite films, Applied Physics Letters. 81 (2002) 3969–3971. doi:10.1063/1.1522832.

[115] Y. Guang, W. Wei-Tian, Y. Guo-Zhen, C. Zheng-Hao, Enhanced Nonlinear Optical Properties of Laser Deposited Ag/BaTiO 3 Nanocomposite Films, Chinese Physics Letters. 20 (2003) 924.

[116] S. Otsuki, K. Nishio, T. Kineri, Y. Watanabe, T. Tsuchiya, Optical Properties of Gold-Dispersed Barium Titanate Thin Films Prepared by Sol-Gel Processing, Journal of the American Ceramic Society. 82 (1999) 1676–1680. doi:10.1111/j.1151-2916.1999.tb01985.x.

[117] Y. Yang, J. Shi, W. Huang, S. Dai, L. Wang, Preparation and optical properties of gold nanoparticles embedded in barium titanate thin films, Journal of Materials Science. 38 (2003) 1243–1248. doi:10.1023/A:1022865905812.

[118] T. Ning, C. Chen, Y. Zhou, H. Lu, H. Shen, D. Zhang, P. Wang, H. Ming, G. Yang, Third-order optical nonlinearity of gold nanoparticle arrays embedded in a BaTiO3 matrix, Appl. Opt. 48 (2009) 375–379. doi:10.1364/AO.48.000375.

[119] A.I. Ryasnyanskiy, B. Palpant, S. Debrus, U. Pal, A.L. Stepanov, Nonlinear optical properties of gold nanoparticles dispersed in different optically transparent matrices, Physics of the Solid State. 51 (2009) 55–60. doi:10.1134/S1063783409010065.

[120] W. Wei-Tian, Y. Guang, C. Zheng-Hao, Z. Yue-Liang, L. Hui-Bin, Y. Guo-Zhen, Large third-order optical nonlinearity in Au nanometre particle doped BaTiO 3 composite films near the resonant frequency, Chinese Physics. 11 (2002) 1324. http://stacks.iop.org/1009-1963/11/i=12/a=320.

[121] W.T. Wang, Z.H. Chen, G. Yang, D.Y. Guan, G.Z. Yang, Y.L. Zhou, H.B. Lu, Resonant absorption quenching and enhancement of optical nonlinearity in Au:BaTiO3 composite films by adding Fe nanoclusters, Applied Physics Letters. 83 (2003) 1983–1985. doi:10.1063/1.1606876.

[122] W. Wang, G. Yang, W. Wu, Z. Chen, Effects of the morphology and nanostructure on the optical nonlinearities of Au:BaTiO3 nanocomposite films, Journal of Applied Physics. 94 (2003) 6837–6840. doi:http://dx.doi.org/10.1063/1.1625082.

[123] W. Wang, G. Yang, Z. Chen, Y. Zhou, H. Lu, G. Yang, Iron nanoparticles in amorphous BaTiO3 thin films with large third-order optical nonlinearity, Journal of Applied Physics. 92 (2002) 7242–7245. doi:http://dx.doi.org/10.1063/1.1524709.

[124] W. Wei-Tian, Y. Guang, D. Ping, Z. Yue-Liang, C. Zheng-Hao, Fe-doped BaTiO 3 Thin Films with Large Third-Order Nonlinear Optical Susceptibility, Chinese Physics Letters. 19 (2002) 1122. http://stacks.iop.org/0256-307X/19/i=8/a=328.

[125] S. Schlag, H.-F. Eicke, Size driven phase transition in nanocrystalline BaTiO3, Solid State Communications. 91 (1994) 883–887. doi:https://doi.org/10.1016/0038-1098(94)90007-8.

[126] S. of P.I. Engineers, Functional Integration of Opto-electro-mechanical Devices and Systems, SPIE, 2002. https://books.google.co.in/books?id=OCZTAAAAMAAJ.

[127] Y.K.V. Reddy, Synthesis and Characterization of BaTiO3 and SrTiO3 Thin Film Capacitors with RuO2 Electrodes, 2006. https://books.google.co.in/books?id=bvuNtgAACAAJ.

[128] C.B. Carter, M.G. Norton, Ceramic Materials: Science and Engineering, Springer New York, 2007. https://books.google.co.in/books?id=aE_VQ8I24OoC.

[129] J. Cooper, A fast-response pyroelectric thermal detector, Journal of Scientific Instruments. 39 (1962) 467. http://stacks.iop.org/0950-7671/39/i=9/a=308.

[130] Sung-Soo Lim, Myung-Soo Han, Suk-Ryong Hahn, Sung-Gap Lee, Dielectric and Pyroelectric Properties of (Ba,Sr,Ca)TiO 3 Ceramics for Uncooled Infrared Detectors, Japanese Journal of Applied Physics. 39 (2000) 4835. http://stacks.iop.org/1347-4065/39/i=8R/a=4835.

[131] P. Günter, J.P. Huignard, Photorefractive Materials and Their Applications 2: Materials, Springer New York, 2007. https://books.google.co.in/books?id=LD9gdfKeFHQC.

[132] F. Eltes, D. Caimi, F. Fallegger, M. Sousa, E. O'Connor, M.D. Rossell, B. Offrein, J. Fompeyrine, S. Abel, Low-Loss BaTiO3–Si Waveguides for Nonlinear Integrated Photonics, ACS Photonics. 3 (2016) 1698–1703. doi:10.1021/acsphotonics.6b00350.

[133] M. Singh, H.M. Haverinen, P. Dhagat, G.E. Jabbour, Inkjet Printing—Process and Its Applications, Advanced Materials. 22 (n.d.) 673–685. doi:10.1002/adma.200901141.

[134] O. Bisi, S. italiana di fisica, S.U. Campisano, L. Pavesi, Silicon-based Microphotonics: from Basics to Applications, IOS Press, 1999. https://books.google.co.in/books?id=hcXDAQAAQBAJ.

[135] C.-L. Hsieh, R. Grange, Y. Pu, D. Psaltis, Bioconjugation of barium titanate nanocrystals with immunoglobulin G antibody for second harmonic radiation imaging probes, Biomaterials. 31 (2010) 2272–2277. doi:http://dx.doi.org/10.1016/j.biomaterials.2009.11.096.

[136] Giada Graziana Genchi and Attilio Marino and Antonella Rocca and Virgilio Mattoli and Gianni Ciofani, Barium titanate nanoparticles: promising multitasking vectors in nanomedicine, Nanotechnology. 27 (2016) 232001. http://stacks.iop.org/0957-4484/27/i=23/a=232001.

[137] P.W. Hawkes, Advances in Imaging and Electron Physics, Elsevier Science, 2010. https://books.google.co.in/books?id=1PVAynWGo6kC.

[138] W. Sun, W. Liu, J. Li, Effects of chloride ions on hydrothermal synthesis of tetragonal BaTiO3 by microwave heating and conventional heating, Powder Technology. 166 (2006) 55–59. doi:https://doi.org/10.1016/j.powtec.2006.05.007.

[139] H.-J. Gläsel, E. Hartmann, D. Hirsch, R. Böttcher, C. Klimm, D. Michel, H.-C. Semmelhack, J. Hormes, H. Rumpf, Preparation of barium titanate ultrafine powders from a monomeric metallo-organic precursor by combined solid-state polymerisation and pyrolysis, Journal of Materials Science. 34 (1999) 2319–2323. doi:10.1023/A:1004533926099.

[140] V. Vinothini, P. Singh, M. Balasubramanian, Synthesis of barium titanate nanopowder using polymeric precursor method, Ceramics International. 32 (2006) 99–103. doi:https://doi.org/10.1016/j.ceramint.2004.12.012.

[141] W.-S. Cho, Structural evolution and characterization of BaTiO3 nanoparticles synthesized from polymeric precursor, Journal of Physics and Chemistry of Solids. 59 (1998) 659–666. doi:https://doi.org/10.1016/S0022-3697(97)00227-8.

[142] W.-S. Cho, E. Hamada, Synthesis of ultrafine BaTiO3 particles from polymeric precursor: their structure and surface property, Journal of Alloys and Compounds. 266 (1998) 118–122. doi:https://doi.org/10.1016/S0925-8388(97)00446-5.

[143] B.Y. Mgbemeje EA Akhtar SM, K. CD, Influence of Annealing Temperatures on the Structural, Morphological,Crystalline and Optical properties of BaTiO3 and SrTiO3 Nanoparticles, Journal of Material Sciences & Engineering. 5 (2016) 1–6. doi:10.4172/2169-0022.1000277.

[144] H. Han, D. Ghosh, J.L. Jones, J.C. Nino, X.M. Chen, Colossal Permittivity in Microwave-Sintered Barium Titanate and Effect of Annealing on Dielectric Properties, Journal of the American Ceramic Society. 96 (n.d.) 485–490. doi:10.1111/jace.12051.

[145] J. Li, K. Inukai, Y. Takahashi, W. Shin, Synthesis and size control of monodispersed BaTiO3–PVP nanoparticles, Journal of Asian Ceramic Societies. 4 (2016) 394–402. doi:https://doi.org/10.1016/j.jascer.2016.09.001.

[146] K. Nogi, M. Hosokawa, M. Naito, T. Yokoyama, Nanoparticle Technology Handbook, Elsevier, 2012. https://books.google.co.in/books?id=LlbaX0tM2dIC.

[147] Y.K.V. Reddy, D. Mergel, S. Reuter, V. Buck, M. Sulkowski, Structural and optical properties of BaTiO 3 thin films prepared by radio-frequency magnetron sputtering at various substrate temperatures, Journal of Physics D: Applied Physics. 39 (2006) 1161. http://stacks.iop.org/0022-3727/39/i=6/a=023.

[148] S. Kim, S. Hishita, Preparation and Characterization of BaTiO3 Thin Films on MgO-buffered Si(100) Substrates by RF Sputtering, Journal of Materials Research. 12 (1997) 1152–1159. doi:10.1557/JMR.1997.0159.

[149] R. Nawathey, R.D. Vispute, S.M. Chaudhari, S.M. Kanetkar, S.B. Ogale, Pulsed laser deposition of barium titanate films on silicon, Solid State Communications. 71 (1989) 9–12. doi:https://doi.org/10.1016/0038-1098(89)90162-2.

[150] G. Niu, B. Gautier, S. Yin, G. Saint-Girons, P. Lecoeur, V. Pillard, G. Hollinger, B. Vilquin, Molecular beam epitaxy growth of BaTiO3 thin films and crucial impact of oxygen content conditions on the electrical characteristics, Thin Solid Films. 520 (2012) 4595–4599. doi:https://doi.org/10.1016/j.tsf.2011.10.182.

[151] J.R. Slack, J.C. Burfoot, Flash evaporation of ferroelectric thin films, Thin Solid Films. 6 (1970) 233–237. doi:https://doi.org/10.1016/0040-6090(70)90122-7.

[152] J.R. Slack, J.C. Burfoot, Electrical properties of flash evaporated ferroelectric BaTiO 3 thin films, Journal of Physics C: Solid State Physics. 4 (1971) 898. http://stacks.iop.org/0022-3719/4/i=8/a=016.

[153] D.L. Kaiser, M.D. Vaudin, G. Gillen, C.-S. Hwang, L.H. Robins, L.D. Rotter, Growth and characterization of barium titanate thin films prepared by metalorganic chemical vapor deposition, Journal of Crystal Growth. 137 (1994) 136–140. doi:https://doi.org/10.1016/0022-0248(94)91261-0.

[154] N. Ishizawa, H. Banno, M. Hayashi, S.E. Yoo, M. Yoshimura, Preparation of BaTiO 3 and SrTiO 3 Polycrystalline Thin Films on Flexible Polymer Film Substrate by Hydrothermal Method, Japanese Journal of Applied Physics. 29 (1990) 2467. http://stacks.iop.org/1347-4065/29/i=11R/a=2467.

[155] H. Kumazawa, K. Masuda, Fabrication of barium titanate thin films with a high dielectric constant by a sol–gel technique, Thin Solid Films. 353 (1999) 144–148. doi:https://doi.org/10.1016/S0040-6090(99)00427-7.

[156] H. Matsuda, N. Kobayashi, T. Kobayashi, K. Miyazawa, M. Kuwabara, Room-temperature synthesis of crystalline barium titanate thin films by high-concentration sol–gel method, Journal of Non-Crystalline Solids. 271 (2000) 162–166. doi:https://doi.org/10.1016/S0022-3093(00)00101-0.

[157] M.N. Kamalasanan, S. Chandra, P.C. Joshi, A. Mansingh, Structural and optical properties of sol-gel-processed BaTiO3 ferroelectric thin films, Applied Physics Letters. 59 (1991) 3547–3549. doi:10.1063/1.105653.

[158] R. Ashiri, A. Nemati, M.S. Ghamsari, Crack-free nanostructured BaTiO3 thin films prepared by sol–gel dip-coating technique, Ceramics International. 40 (2014) 8613–8619. doi:https://doi.org/10.1016/j.ceramint.2014.01.078.

[159] T. Hayashi, N. Ohji, K. Hirohara, T. Fukunaga, H. Maiwa, Preparation and Properties of Ferroelectric BaTiO 3 Thin Films by Sol-Gel Process, Japanese Journal of Applied Physics. 32 (1993) 4092. http://stacks.iop.org/1347-4065/32/i=9S/a=4092.

[160] L. Huang, Y. Dai, H. Xiao, X. Pei, W. Chen, Structure and ferroelectric property of low concentration iron-doped sol–gel BaTiO3 thin films, Ceramics International. 42 (2016) 9046–9050. doi:https://doi.org/10.1016/j.ceramint.2016.02.162.

[161] Y.-H. Kuo, S. Nah, K. He, T. Hu, A.M. Lindenberg, Ultrafast light-induced symmetry changes in single BaTiO3 nanowires, J. Mater. Chem. C. 5 (2017) 1522–1528. doi:10.1039/C6TC04448D.

[162] L. Curecheriu, M.M. Vijatović Petrović, J.D. Bobić, B.D. Stojanović, Nonlinear properties of antimony-doped BaTiO3 ceramics, Applied Physics A. 119 (2015) 681–686. doi:10.1007/s00339-015-9013-7.

[163] C. Ma, J. Yan, Y. Wei, P. Liu, G. Yang, Enhanced second harmonic generation in individual barium titanate nanoparticles driven by Mie resonances, J. Mater. Chem. C. 5 (2017) 4810–4819. doi:10.1039/C7TC00650K.

[164] M. Sheik-Bahae, A. A. Said, T. H. Wei, D. J. Hagan, E. W. Van Stryland, Sensitive measurement of optical nonlinearities using a single beam, IEEE Journal of Quantum Electronics. 26 (1990) 760–769. doi:10.1109/3.53394.

[165] D. Weaire, B.S. Wherrett, D.A.B. Miller, S.D. Smith, Effect of low-power nonlinear refraction on laser-beam propagation in InSb, Opt. Lett. 4 (1979) 331–333. doi:10.1364/OL.4.000331.

[166] Kuzyk, Characterization Techniques and Tabulations for Organic Nonlinear Optical Materials, CRC Press, 1998.

[167] C.W. Beier, M.A. Cuevas, R.L. Brutchey, Effect of Surface Modification on the Dielectric Properties of BaTiO3 Nanocrystals, Langmuir. 26 (2010) 5067–5071. doi:10.1021/la9035419.

[168] S. Kohiki, S. Takada, A. Shimizu, K. Yamada, H. Higashijima, M. Mitome, Quantum-confinement effects on the optical and dielectric properties for mesocrystals of BaTiO3 and SrBi2Ta2O9, Journal of Applied Physics. 87 (2000) 474–478. doi:10.1063/1.371886.

[169] B.-H. Fan, J.-W. Zha, D. Wang, J. Zhao, Z.-M. Dang, Size-dependent low-frequency dielectric properties in the BaTiO3/poly(vinylidene fluoride) nanocomposite films, Applied Physics Letters. 100 (2012) 012903. doi:10.1063/1.3673555.

[170] K. Suzuki, K. Kijima, Optical Band Gap of Barium Titanate Nanoparticles Prepared by RF-plasma Chemical Vapor Deposition, Japanese Journal of Applied Physics. 44 (2005) 2081. http://stacks.iop.org/1347-4065/44/i=4R/a=2081.

[171] A. Rudzki, D.R. Evans, G. Cook, W. Haase, Size dependence of harvested BaTiO3 nanoparticles on the electro-optic and dielectric properties of ferroelectric liquid crystal nanocolloids, Appl. Opt. 52 (2013) E6–E14. doi:10.1364/AO.52.0000E6.

[172] R.W. Boyd, R.J. Gehr, G.L. Fischer, J.E. Sipe, Nonlinear optical properties of nanocomposite materials, Pure and Applied Optics: Journal of the European Optical Society Part A. 5 (1996) 505.

[173] J.E. Sipe, R.W. Boyd, Nonlinear susceptibility of composite optical materials in the Maxwell Garnett model, Phys. Rev. A. 46 (1992) 1614–1629. doi:10.1103/PhysRevA.46.1614.

[174] N.N. LEPESHKIN, W. KIM, V.P. SAFONOV, J.G. ZHU, R.L. ARMSTRONG, C.W. WHITE, R.A. ZUHR, V.M. SHALAEV, OPTICAL NONLINEARITIES OF METAL-DIELECTRIC COMPOSITES, Journal of Nonlinear Optical Physics & Materials. 08 (1999) 191–210. doi:10.1142/S021886359900014X.

[175] J.C.M. Garnett, Colours in Metal Glasses and in Metallic Films, Philosophical Transactions of the Royal Society of London A: Mathematical, Physical and Engineering Sciences. 203 (1904) 385–420. doi:10.1098/rsta.1904.0024.

[176] M. G. Papadopoulos, A. J. Sadlej, J. Leszczynski, Non-Linear Optical Properties of Matter, Springer Netherlands, 2006.

[177] T. Woldu, B. Raneesh, P. Sreekanth, M.V.R. Reddy, R. Philip, N. Kalarikkal, Size dependent nonlinear optical absorption in BaTiO3 nanoparticles, Chemical Physics Letters. 625 (2015) 58–63. doi:http://dx.doi.org/10.1016/j.cplett.2015.02.020.

[178] S. Ramakanth, S. Hamad, S. Venugopal Rao, K.C. James Raju, Magnetic and nonlinear optical properties of BaTiO3 nanoparticles, AIP Advances. 5 (2015). doi:http://dx.doi.org/10.1063/1.4921480.

[179] R.A. Ganeev, M. Suzuki, M. Baba, M. Ichihara, H. Kuroda, Low- and high-order nonlinear optical properties of BaTiO3 and SrTiO3 nanoparticles, J. Opt. Soc. Am. B. 25 (2008) 325–333. doi:10.1364/JOSAB.25.000325.

[180] C.-L. Hsieh, R. Grange, Y. Pu, D. Psaltis, Three-dimensional harmonic holographic microcopy using nanoparticles as probes for cell imaging, Opt. Express. 17 (2009) 2880–2891. doi:10.1364/OE.17.002880.

[181] D. Staedler, T. Magouroux, Hadji Rachid, C. Joulaud, J. Extermann, S. Schwung, S. Passemard, C. Kasparian, G. Clarke, M. Gerrmann, R. Le Dantec, Y. Mugnier, D. Rytz, D. Ciepielewski, C. Galez, S. Gerber-Lemaire, L. Juillerat-Jeanneret, L. Bonacina, J.-P. Wolf, Harmonic Nanocrystals for Biolabeling: A Survey of Optical Properties and Biocompatibility, ACS Nano. 6 (2012) 2542–2549. doi:10.1021/nn204990n.

[182] M.M. Bijeesh, P.K. Shakhi, S. Arunkarthick, G.K. Varier, P. Nandakumar, Confocal imaging of single BaTiO3 nanoparticles by two-photon photothermal microscopy, Scientific Reports. 7 (2017) 1643. doi:10.1038/s41598-017-01548-z.

[183] W.F. Zhang, Y.B. Huang, M.S. Zhang, Z.G. Liu, Nonlinear optical absorption in undoped and cerium-doped BaTiO3 thin films using Z-scan technique, Applied Physics Letters. 76 (2000) 1003–1005. doi:http://dx.doi.org/10.1063/1.125920.

[184] P Senthilkumar and S Dhanuskodi and Anitta Rose Thomas and Reji Philip, Enhancement of nonlinear optical and temperature dependent dielectric properties of Ce:BaTiO 3 nano and submicron particles, Materials Research Express. 4 (2017) 085027. http://stacks.iop.org/2053-1591/4/i=8/a=085027.

[185] G. Ma, W. Sun, S.-H. Tang, H. Zhang, Z. Shen, S. Qian, Size and dielectric dependence of the third-order nonlinear optical response of Au nanocrystals embedded in matrices, Opt. Lett. 27 (2002) 1043–1045. doi:10.1364/OL.27.001043.

[186] Y. Liu, D. Li, R.Y. Zhu, G.J. You, S.X. Qian, Y. Yang, J.L. Shi, Third-order nonlinear optical response of Au-core CdS-shell composite nanoparticles embedded in BaTiO3 thin films, Applied Physics B. 76 (2003) 435–439. doi:10.1007/s00340-002-1068-4.

[187] S.-J. Ding, F. Nan, D.-J. Yang, X.-L. Liu, Y.-L. Wang, L. Zhou, Z.-H. Hao, Q.-Q. Wang, Largely Enhanced Saturable Absorption of a Complex of Plasmonic and Molecular-Like Au Nanocrystals, Scientific Reports. 5 (2015) 9735.

[188] S.L. Smitha, K.G. Gopchandran, N. Smijesh, R. Philip, Size-dependent optical properties of Au nanorods, Progress in Natural Science: Materials International. 23 (2013) 36–43. doi:http://dx.doi.org/10.1016/j.pnsc.2013.01.005.

[189] G.S. He, W.-C. Law, A. Baev, S. Liu, M.T. Swihart, P.N. Prasad, Nonlinear optical absorption and stimulated Mie scattering in metallic nanoparticle suspensions, The Journal of Chemical Physics. 138 (2013). doi:http://dx.doi.org/10.1063/1.4773340.

[190] V. Liberman, M. Sworin, R.P. Kingsborough, G.P. Geurtsen, M. Rothschild, Nonlinear bleaching, absorption, and scattering of 532-nm-irradiated plasmonic nanoparticles, Journal of Applied Physics. 113 (2013). doi:http://dx.doi.org/10.1063/1.4790798.

[191] R. Philip, P. Chantharasupawong, H. Qian, R. Jin, J. Thomas, Evolution of Nonlinear Optical Properties: From Gold Atomic Clusters to Plasmonic Nanocrystals, Nano Letters. 12 (2012) 4661–4667. doi:10.1021/nl301988v.

[192] K. Wang, H. Long, M. Fu, G. Yang, P. Lu, Size-related third-order optical nonlinearities of Au nanoparticle arrays, Opt. Express. 18 (2010) 13874–13879. doi:10.1364/OE.18.013874.

[193] K. Wang, H. Long, M. Fu, G. Yang, P. Lu, Intensity-dependent reversal of nonlinearity sign in a gold nanoparticle array, Opt. Lett. 35 (2010) 1560–1562. doi:10.1364/OL.35.001560.

[194] R. Sreeja, P.M. Aneesh, A. Aravind, R. Reshmi, R. Philip, M.K. Jayaraj, Size-Dependent Optical Nonlinearity of Au Nanocrystals, Journal of The Electrochemical Society. 156 (2009) K167–K172. doi:10.1149/1.3184188.

[195] W. Wang, G. Yang, Z. Chen, H. Lu, Y. Zhou, G. Yang, X. Kong, Nonlinear refraction and saturable absorption in Au:BaTiO3 composite films, Appl. Opt. 42 (2003) 5591–5595. doi:10.1364/AO.42.005591.

[196] E.W.V. Stryland, M. Sheik-Bahae, A.A. Said, D.J. Hagan, Characterization of nonlinear optical absorption and refraction, Progress in Crystal Growth and Characterization of Materials. 27 (1993) 279–311. doi:http://dx.doi.org/10.1016/0960-8974(93)90026-Z.

[197] V.M. Shalaev, E.Y. Poliakov, V.A. Markel, Small-particle composites. II. Nonlinear optical properties, Phys. Rev. B. 53 (1996) 2437–2449. doi:10.1103/PhysRevB.53.2437.

[198] D. Boyer, P. Tamarat, A. Maali, B. Lounis, M. Orrit, Photothermal Imaging of Nanometer-Sized Metal Particles Among Scatterers, Science. 297 (2002) 1160. doi:10.1126/science.1073765.

[199] V. Zharov, D. Lapotko, Photothermal sensing of nanoscale targets, Review of Scientific Instruments. 74 (2003) 785–788. doi:http://dx.doi.org/10.1063/1.1520322.

[200] A. Gaiduk, M. Yorulmaz, P.V. Ruijgrok, M. Orrit, Room-Temperature Detection of a Single Molecule's Absorption by Photothermal Contrast, Science. 330 (2010) 353. doi:10.1126/science.1195475.

[201] M. Selmke, F. Cichos, Photothermal Single Particle Rutherford Scattering Microscopy, Phys. Rev. Lett. 110 (2013) 103901. doi:10.1103/PhysRevLett.110.103901.

[202] S. Berciaud, L. Cognet, G.A. Blab, B. Lounis, Photothermal Heterodyne Imaging of Individual Nonfluorescent Nanoclusters and Nanocrystals, Phys. Rev. Lett. 93 (2004) 257402. doi:10.1103/PhysRevLett.93.257402.

[203] X. Huang, I.H. El-Sayed, W. Qian, M.A. El-Sayed, Cancer Cell Imaging and Photothermal Therapy in the Near-Infrared Region by Using Gold Nanorods, J. Am. Chem. Soc. 128 (2006) 2115–2120. doi:10.1021/ja057254a.

[204] L. Tong, Q. Wei, A. Wei, J.-X. Cheng, Gold Nanorods as Contrast Agents for Biological Imaging: Optical Properties, Surface Conjugation and Photothermal Effects†, Photochemistry and Photobiology. 85 (2009) 21–32. doi:10.1111/j.1751-1097.2008.00507.x.

[205] I.H. El-Sayed, X. Huang, M.A. El-Sayed, Selective laser photo-thermal therapy of epithelial carcinoma using anti-EGFR antibody conjugated gold nanoparticles, Cancer Letters. 239 (2006) 129–135. doi:http://dx.doi.org/10.1016/j.canlet.2005.07.035.

[206] L. Tong, Y. Zhao, T.B. Huff, M.N. Hansen, A. Wei, J.-X. Cheng, Gold Nanorods Mediate Tumor Cell Death by Compromising Membrane Integrity, Advanced Materials. 19 (2007) 3136–3141. doi:10.1002/adma.200701974.

[207] E.E. Hoover, J.A. Squier, Advances in multiphoton microscopy technology, Nat Photon. 7 (2013) 93–101. doi:10.1038/nphoton.2012.361.

[208] N. Abeyasinghe, S. Kumar, K. Sun, J.F. Mansfield, R. Jin, T. Goodson, Enhanced Emission from Single Isolated Gold Quantum Dots Investigated Using Two-Photon-Excited Fluorescence Near-Field Scanning Optical Microscopy, Journal of the American Chemical Society. 138 (2016) 16299–16307. doi:10.1021/jacs.6b07737.

[209] S. Lu, W. Min, S. Chong, G.R. Holtom, X.S. Xie, Label-free imaging of heme proteins with two-photon excited photothermal lens microscopy, Applied Physics Letters. 96 (2010). doi:http://dx.doi.org/10.1063/1.3308485.

[210] J. Moger, N.L. Garrett, D. Begley, L. Mihoreanu, A. Lalatsa, M.V. Lozano, M. Mazza, A. Schatzlein, I. Uchegbu, Imaging cortical vasculature with stimulated Raman scattering and two-photon photothermal lensing microscopy, Journal of Raman Spectroscopy. 43 (2012) 668–674. doi:10.1002/jrs.3156.

[211] C.-L. Hsieh, R. Grange, Y. Pu, D. Psaltis, Three-dimensional harmonic holographic microcopy using nanoparticles as probes for cell imaging, Opt. Express. 17 (2009) 2880–2891. doi:10.1364/OE.17.002880.

[212] R.W. Boyd, Nonlinear Optics, Elsevier Science, 2003. https://books.google.co.in/books?id=3vHb7WGXmSQC.

[213] K.P. Mary, I. Oubou, C. Shepherd, Z. Nager, C. Anderson, L. Pagliaro, Photothermal Therapy Using Gold Nanorods and Near-Infrared Light in a Murine Melanoma Model Increases Survival and Decreases Tumor Volume, Journal of Nanomaterials. 2014 (2014) 8. doi:10.1155/2014/450670.

[214] S. Berciaud, D. Lasne, G.A. Blab, L. Cognet, B. Lounis, Photothermal heterodyne imaging of individual metallic nanoparticles: Theory versus experiment, Phys. Rev. B. 73 (2006) 045424. doi:10.1103/PhysRevB.73.045424.

[215] B. Chu, Laser Light Scattering, Academic Press, 1974. https://books.google.co.in/books?id=tyZRAAAAMAAJ.

Publications and presentations

RESEARCH PUBLICATIONS

1. **M.M. Bijeesh**, P.K. Shakhi, Geetha K. Varier and P. Nandakumar, "Tuning the nonlinear optical absorption in Au/BaTiO3 nanocomposites with gold nanoparticle concentration" Optics and Laser Technology, 102, 2018, 207–212

2. **M. M. Bijeesh**, P. K. Shakhi, S. Arunkarthick, Geetha K. Varier and P. Nandakumar, "Confocal imaging of single BaTiO3 nanoparticles by two-photon photothermal microscopy" Scientific Reports, 2017, 7, 1643

3. S. Arunkarthick, **M. M. Bijeesh**, Anand Satya Vetcha, Nishith Rastogi, P. Nandakumar and Geetha K. Varier. "Design and construction of a confocal laser scanning microscope for biomolecular imaging". Current Science, 2014, 107 (12), 1965-1969. (IF– 0.833).

4. S. Arunkarthick, **M. M. Bijeesh**, Geetha K. Varier, Meenal Kowshik andP. Nandakumar. "Laser Scanning Photothermal Microscopy: Fast Detection and Imaging of Gold Nanoparticles". Journal of Microscopy, 2014, 256 (2), 111-116. doi:10.1111/jmi.12164. (IF – 2.15).

5. **M. M. Bijeesh**, S. Arunkarthick, K. Arvind, R. Nishith, Geetha K. Varier, Meenal Kowshik and P. Nandakumar. "Construction of Simple Confocal Microscope". Kiran, 2011, 22 (1), 26-28.

6. S. Arunkarthick, **M. M. Bijeesh**, Geetha K. Varier,Meenal Kowshik ,and P. Nandakumar. "Passive permeability and effective pore size of HeLa cell nuclear membranes" Cell Biol Int. 2016, 40(9):991-8.

PUBLICATIONS IN CONFERENCES (PAPER/POSTER PRESENTATIONS)

1. **M. M. Bijeesh**, P. K. Shakhi, K. Varier Geetha, and P. Nandakumar "Two-Photon Photothermal Microscopy: Biomolecular Imaging Using Nonfluorescent Nanoparticle Labels" Focus on Microscopy-2018, Singapore Expo, Singapore, March 25-28, 2018.

2. **M. M. Bijeesh,** S. Arunkarthick, Geetha K. Varier and P. Nandakumar. Nonlinear refractive index measurements of $BaTiO_3$ by the Z - scan technique, DAE-BRNS National Laser Symposium (NLS-22), MIT, Manipal University, Manipal, Karnataka, January 8-11, 2014.

3. **M. M. Bijeesh**, S. Arunkarthick, Arvind Krishnan, Nishith Rastogi, Geetha K. Varier, Meenal Kowshik and P. Nandakumar. "Construction of Simple Confocal Microscope" DAE-BRNS National Laser Symposium, RRCAT, Indore, December 1-4, 2010.

4. P. K. Shakhi, **M. M. Bijeesh**, K. Varier Geetha and P. Nandakumar Intensity Modulated Confocal Laser Scanning Microscopy (IMCLSM), Focus on Microscopy-2018, Singapore Expo, Singapore, March 25-28, 2018.

5. S. Arunkarthick, **M. M. Bijeesh**, Geetha K. Varier, Meenal Kowshik and P. Nandakumar. "Studies on Biomolecular Transport through Nuclear Membranes using a Home Built Confocal Laser Scanning Microscope", 18th International Microscopy congress (IMC-2014), Prague, Czech Republic, September 7-12, 2014.

7. S. Arunkarthick, **M. M. Bijeesh**, Geetha K. Varier, Meenal Kowshik and P. Nandakumar. "Permeability studies on nuclear membranes using confocal laser 138 | Publications and Presentations scanning microscopy", DAE-BRNS National Laser Symposium (NLS-22), MIT,Manipal University, Manipal, Karnataka, January 8-11, 2014.

8. S. Arunkarthick, **M. M. Bijeesh**, Geetha K. Varier, Meenal Kowshik and P. Nandakumar. "Optical microscopic studies on biomolecular transport through nuclear membranes", 37th All India Cell Biology Conference on "Cell Dynamics and Cell Fate", InStem, Bangalore, December 22- 24, 2013.

9. S. Arunkarthick, **M. M. Bijeesh**, Geetha K. Varier, Meenal Kowshik and P. Nandakumar. "Studies on Nuclear Transport of FITC Labelled Dextran Using Confocal Laser Scanning Microscopy", International Conference on Biotechnology and Human Welfare, SASTRA University and M S Swaminathan Research Foundation, Tamil Nadu, during December 6-8, 2013.

10. S. Arunkarthick, **M. M. Bijeesh**, Geetha K. Varier, Meenal Kowshik and P. Nandakumar. "Photothermal Laser Scanning Microscopy", Focus on Microscopy 2013, Maastricht, The Netherlands during March 24 - March 27, 2013.

11. S. Arunkarthick, **M. M. Bijeesh**, Geetha K. Varier, Meenal Kowshik and P. Nandakumar. "Nuclear Transport Study Using Home Built Confocal LaserScanning Microscopy" 4th Bangalore Microscopy Course, National Centre for Biological Sciences (NCBS), TIFR, Bangalore, during September 23-30, 2012.

12. S. Arunkarthick, **M. M. Bijeesh**, Geetha K. Varier, Meenal Kowshik and P. Nandakumar. "Laser scanning photothermal microscopy", Optics Within Life Sciences (OWLS-2012), Genoa, 4-6, July 2012.

WORKSHOPS / SYMPOSIUM PARTICIPATED

1. DAE-BRNS National Laser Symposium (NLS-19), organized at Raja Ramanna Centre for Advanced Technology (RRCAT), Indore – 452 013 during December 1-4, 2010.
2. Biophotonics, a national level short course conducted by Indian Laser Association at Raja Ramanna Centre for Advanced Technology, Indore on November 29-30, 2010.
3. Imaging at Nanoscale, an International Workshop organized by IIT Bombay at the time of ICONSAT'2010, on 17th February 2010.

AWARDS AND RECOGNITIONS

1. Qualified "National Eligibility Test (NET)" conducted by Council of Science and Industrial research (CSIR), Government of India, 2010
2. Received a Best Poster Award for the poster titled "Construction of simple Confocal Microscope" presented during the DAE-BRNS National Laser Symposium (NLS-19) held at RRCAT, Indore during December 1-4, 2010.

FELLOWSHIPS

1. **Junior Research Fellowship** received from Defence Research and Development Organization (DRDO) from October 2009 to February 2012.
2. Institute **Senior Research Fellowship** received from Birla Institute of Technology and Science (BITS) from March 2012 to February 2017.
3. Senior Research Fellowship received from Department of Biotechnology (DBT) funded project from April 2017 to till date.

BIODATA OF CANDIDATE

Bijeesh M M was born on 29th May 1987 in Calicut, Kerala, India to Chandran V and Syamala C. He completed his Bachelor's degree in Physics from St. Joseph's College, Devagiri, Calicut, Kerala, India during 2004-2007. He completed his master's degree in Physics from Cochin university of science and technology (CUSAT), Cochin, Kerala, India in 2009. In October 2009 he joined BITS Pilani K K Birla Goa campus as a Junior Research Fellow in a DRDO funded project "Studies on the nonlinear optical properties of gold nanoparticles embedded $BaTiO_3$ thin films. He completed the prescribed course work for the Ph.D. program in May, 2011 and passed the qualifying examination in October, 2011. Then he started his graduate study in Physics at Birla Institute of Technology and Science, Pilani with the proposed thesis title "Linear and Nonlinear Optical Characterization of $BaTiO_3$ Nanoparticles and their Applications in Two-Photon Photothermal Microscopy".

He received the best poster award during 19th National Laser Symposium in RRCAT, Indore, India. He qualified the National Eligibility Test (NET) for lectureship in December 2009 in the subject Physical sciences, conducted by CSIR, Govt. of India.

BIODATA OF SUPERVISOR

Prof. P Nandakuamr is currently working as an Associate Professor in Physics at BITS Pilani K. K. Birla Goa campus. He completed his Ph. D in Physics from Indian Institute of Technology Madras in the year 1999 on the topic of 'Optical properties of semiconductor quantum dots' under the supervision of Prof. Y.V.G.S. Murthy and Prof. C. vijayan. After his Ph.D he worked for one year as a CSIR research associate at Indian Institute of Science, Bangalore with Prof. P. K. Das. After that he worked as a Visiting Research Fellow with Prof. A. Monkman at the University of Durham, UK. Thereafter he worked at the Weizmann Institute of Science, Israel for two years with Prof. Yehiam Prior on 'coherent control of chemical reactions' using a 30 femto-second laser beam. Next two years he worked at the University of Stuttgart, Germany with Dr. Andreas Volkmer on 'Coherent Raman Micro-spectroscopy'. There he developed a Raman scattering Microscope based on stimulated Raman loss detection, for noninvasive point-by-point vibrational mapping of chemical and biological samples with high sensitivity and without the requirement for labeling of the sample. He joined the department of Physics at BITS Pilani K. K. Birla Goa campus as a faculty member in the year 2005. His current research interests include nonlinear optics, quantum optics, Biomolecular nuclear transport, optical microscopy and application in Biophysics.